Characterization of response properties in the mouse lateral geniculate nucleus

Jiaying Tang

February 2015

A thesis submitted for the degree of
Doctor of Philosophy of Imperial College London
Diploma of Imperial College (DIC) London

Department of Bioengineering
Imperial College London
SW7 2AZ

Supervisor: Dr. Simon Schultz

Statement of originality

I hereby declare that the work presented in this thesis is my own, aside from the following that was performed by Silvia C. Ardila Jiménez:

MATLAB scripts for: hand-mapping of receptive field; the Flymouse interface for visual stimulus (customized from the Flyfly that developed by Motion Vision Group at Uppsala University, http://www.flyfly.se/about.html); computation of different properties of single cells and power spectrum from local field potentials.

I am appreciative of the help from the aforementioned aspects.

Jiaying Tang

Copyright Declaration

Abstract

The lateral geniculate nucleus (LGN) has been increasingly recognized to actively regulate information transmission to primary visual cortex (V1). Although efforts have been devoted to study its morphological and functional features, the full array of response characteristics in mouse LGN as well as their dependency on subjective state have been relatively unexplored.

To address the question we recorded from mouse LGN with multisite-electrode-arrays (MEAs). From a dataset with 185 single units, our results revealed several exceptional response features in mouse LGN. We also demonstrated that subtypes, such as ON-/OFF-centre and transient/sustained cells exhibited functionally distinctive features, which might indicate parallel projections. To further compare response features from the full extent of mouse LGN, we developed a three-dimension (3D) LGN volume through histological approach. This volume explicitly captures morphological features of mouse LGN and provides the preciseness to classify location of single neuron into the anterior/middle/posterior LGN. Based on this categorization, we showed that response features were not regionally restricted within mouse LGN.

We further examined neural activity with subjects in high or low isoflurane states. The distinct features in LFPs between the two states indicated that adjusting isoflurane concentration could provide a reliable and controllable experimental model to explore the state-dependent neural activity in mouse visual system. Subsequently, our results demonstrated that properties, including response latency, contrast sensitivity and spatial frequency properties were modulated by isoflurane concentration.

Our current work suggests that mouse LGN can dynamically regulate information transmission to the cortex using numerous mechanisms, including responding mode, modulation of neuronal responses according to subjects' states.

Acknowledgements

First and foremost I would like to acknowledge my supervisor Simon R Schulz, for his encouragement, support and immense knowledge every step through my way as his student. He patiently guided me into the fascinating world of visual neuroscience and helped me to shape ideas along the way. I would like to thank him for encouraging me to perform independent research and also providing me with collaborating opportunity to gain the best outcomes.

I would like to express my deepest thanks to Silvia C. Ardila Jiménez, for being the computational superhero in this study. Without her, I would not be able to complete my PhD project. I would like to thank her for every code debugging, brainstorming and warm hug to support and encourage me along the way.

Thank you to Elena Phoka and Isable Delgado Ruz, who patiently led me into the field of experimental neuroscience and generously shared with me their professional experiences. Thank you to Aleksandra Berditchevskaia for teaching me histological procedures and inspiring me on the development of staining protocol.

I would like to thank Tomaso Muzzu, for being helpful on rig setting up. I would like to thank Susanna Mitolo, for being such an amazing mate in rebuilding the rig, and sharing those good and bad moments in work and life. Thank you to Subhojit Chakraborty, for his precious advice on my thesis, and valuable comments on and beyond my project. Thank you to Sarah Jarvis, for her feedback on my thesis correction and encouragement throughout writing-up period. I would like to thank all of the colleagues in Schultz lab, for providing suggestions and comments on my work, and being a wonderful group of people.

Thank you to members in Dr. Paul Chadderton's group. Matthew Brown and Caroline Golden, thank you for helping me de-nosing the rig; Susu Chen, thanks for encouragements and amazing Chinese-style breakfast that brightened up my days.

Thank you to Jiaqi Huang, for his patience and kindness, for spending those late nights with me in lab on problem shooting, and also discussions and inspirations from blowfly neuroscience. Thank you to Martina Wicklein, for her suggestive feedback on my thesis. Also, thank you to Ben Hardcastle and Kit Longden for being great neuroscientists on the other side of the lab.

Thank you to Amanda Wilson, for teaching me procedures towards brain reconstruction, and sparing time with me working out the best protocol. Thank you to Stephen Rothery, for his advice on confocal imaging and post-processing. Thank you to Gary Jones and Satpal Sangha, for offering precious help in my rig set-up design and always putting up with me for the pressing time.

Qingyi Wu, thank you in particular for always being there for me, thanks for the support and understanding over these years. Thank you for being you and letting me be me.

Thank you to Dr. Hua Zhang for being an indispensable part in my studies and life, “in the dew of little things, the heart finds its morning and is refreshed”.

Thank you to the great friends that I met in London and around: Min Chen, Dr. Zhigen Wu, Dr. Bo Han, Dr. Liang Ma, Dr. Di Wu, Dr. Gang Yao, Dr. Yaozu Xiang, Dr. Nan Zhang, Wenjie Cui, Chao Gao, Mengmeng Yang, William Wu. Thank you for those beers and chats, and also laughs and tears. The memory will never fade.

Finally, I would like to thank my parents. Thank you for their calmness and wisdom, for their endless love and understanding, and giving me strength to reach out for stars.

Table of Contents

List of Figures

List of Tables

Abbreviation

Ach	Acetylcholine
DA	Dopamine
DAPI	Diamidino-2-phenylindole
DMSO	Dimethyl sulfoxide
DoG	Difference of Gaussian
DS	Direction Selective
DSI	Direction Selective Index
DSRGC	Direction-selective Retinal Ganglion Cell
ECoG	Electrocorticography
EEG	Electroencephalography
EPSP	Excitatory Postsynaptic Potential
FITC	Fluorescein Isothiocyanate
FOV	Field Of View
GABA	Gamma Amino Butyric Acid
K	Koniocellular
LFP	Local Field Potential
LGN	Lateral Geniculate Nucleus
LPN	Lateral Posterior Nucleus
LT	Low Threshold
LTS	Low Threshold Spikes
M	Magnocellular
MEA	Multi-electrode-array

MEG	Magnetoencephalography
MGN	Medial Geniculate Nucleus
MRI	Magnetic Resonance Imaging
NE	Norepinephrine
OS	Orientation Selective
OSI	Orientation Selective Index
P	Parvocellular
PBS	Phosphate Buffered Saline
PFA	Paraformaldehyde
PSTH	Poststimulus Time Histogram
REM	Rapid-eye-movement
RGC	Retinal Ganglion Cell
RHOD	Rhodamine
SC	Superior Colliculus
SEM	Standard Error Of The Mean
STA	Spike Triggered Averaging
TRN	Thalamic Reticular Nucleus
V1	Primary Visual Cortex
2D	Two-dimensional
3D	Three-dimensional
5-HT	Serotonin
°C	Celsius Degrees

CHAPTER 1

Introduction

The lateral geniculate nucleus (LGN), a structure of the thalamus, is increasingly regarded as a "smart-gating" operator of the visual pathway. It faithfully relays information from the retina to the visual cortex, and also supports different "gating outcomes" stemming from various non-retinal inputs. Therefore, characterizing response properties of LGN will help in understanding visual information processing. This chapter starts with a general description of the thalamus, and the classification of its main nuclei as first or second order, followed by a brief introduction to two types of afferents, drivers and modulators. In Section 1.2, I outline the anatomical organization of LGN with the examples of monkey and cat LGN – two well-explored visual thalamic nuclei – and compare them with new evidence from the mouse. After outlining the properties of burst/tonic firing modes and receptive field structures of LGN neurons, I evaluate our current understanding of the functional significance of corticothalamic feedback to LGN, both at the level of single cells and neuronal ensembles. I further summarize the physiological characterization of single-cell response features of mouse LGN and relate this to other species, such as the macaque monkey and cat. Subsequently, I review recent research about the temporal codes of neuronal groups, particularly that of synchronized oscillations. Moreover, I present the characteristics of two extremes of a continuum of cortical states, namely synchronized and desynchronized states, and review current knowledge about potential mechanisms of these states and their functional roles. In the final section, I provide an outline of this thesis, with major findings and their implications.

1.1 The thalamus

The thalamus is a dual-lobed cluster of grey matter nuclei located at the junction of the brain stem and the two cerebral hemispheres. The major part is the dorsal thalamus, which includes approximately 15 relay nuclei that project to the cerebral cortex (Figure 1.1A). Relay cells constitute approximately 75% of the cell population and play a dominant role in

information processing. The rest are local interneurons that primarily involve in inhibiting their respective targets by releasing the neurotransmitter- gamma amino butyric acid (GABA) (Spreafico et al., 1994; Arcelli et al., 1997; Sherman and Guillery, 1998; Sherman, 2004). The ventral thalamus, adjacent to the dorsal thalamus, comprises mainly of the thalamic reticular nucleus (TRN). The TRN sends inhibitory GABAergic axons to relay cells in the dorsal thalamus (the term "thalamus" is used to refer the dorsal thalamus in this study).

As illustrated from the rat brain (Figure 1.1A), thalamic nuclei can be categorized into two groups on the basis of the afferent fibres they receive from, "first order nuclei" receive primary ascending afferent fibres that can be differentiated by their origins and their intrathalamic synaptic relationships. For instance, LGN, the ventral posterior, the ventral part of the medial geniculate nucleus and the anterior thalamic nucleus in the first order group receive visual, somatosensory, auditory and mammillary primary afferents respectively. In contrast, "higher order nuclei" receive most or all of their "primary afferents" from pyramidal cells in layer 5 of the cortex and participate in transmitting information about the output of one cortical area to another cortical area (Guillery, 1995; Sherman and Guillery, 1998; Theyel et al., 2010).

The "primary ascending afferents", commonly referred to drivers, are thought to transmit essential information from peripheral receptors to the brain. In addition to drivers, the other type of afferents to the thalamus is the modulator, whose synapses constitute the vast majority of inputs to a given thalamic neuron in every thalamic nucleus studied to date. However, the modulators are capable of altering the effectiveness of the drivers but do not significantly change the general pattern of the message (Sherman and Guillery, 1998; Guillery and Sherman, 2002; Varela, 2014). This functional variance parallels the differences in cross-correlograms, specifically, driver inputs normally have a sharp peak rising out of a low baseline that indicates a faithful transfer of signals, whereas modulator inputs have a broad peak against a noisy baseline representing a less faithful relay (Sherman and Guillery, 2002). Modulators form a heterogeneous group of afferents to the thalamus although they share some similar anatomical and functional characteristics across nuclei. The majority of modulators come either from cortical layer 6 (glutamatergic afferents) or the brain stem (e.g. the hypothalamus, and dopaminergic, cholinergic, serotonergic afferents), and can function directly or through an inhibitory relay in the TRN or local thalamic interneurons (Sherman and Guillery, 1998; Varela, 2014) (Figure 1.1B).

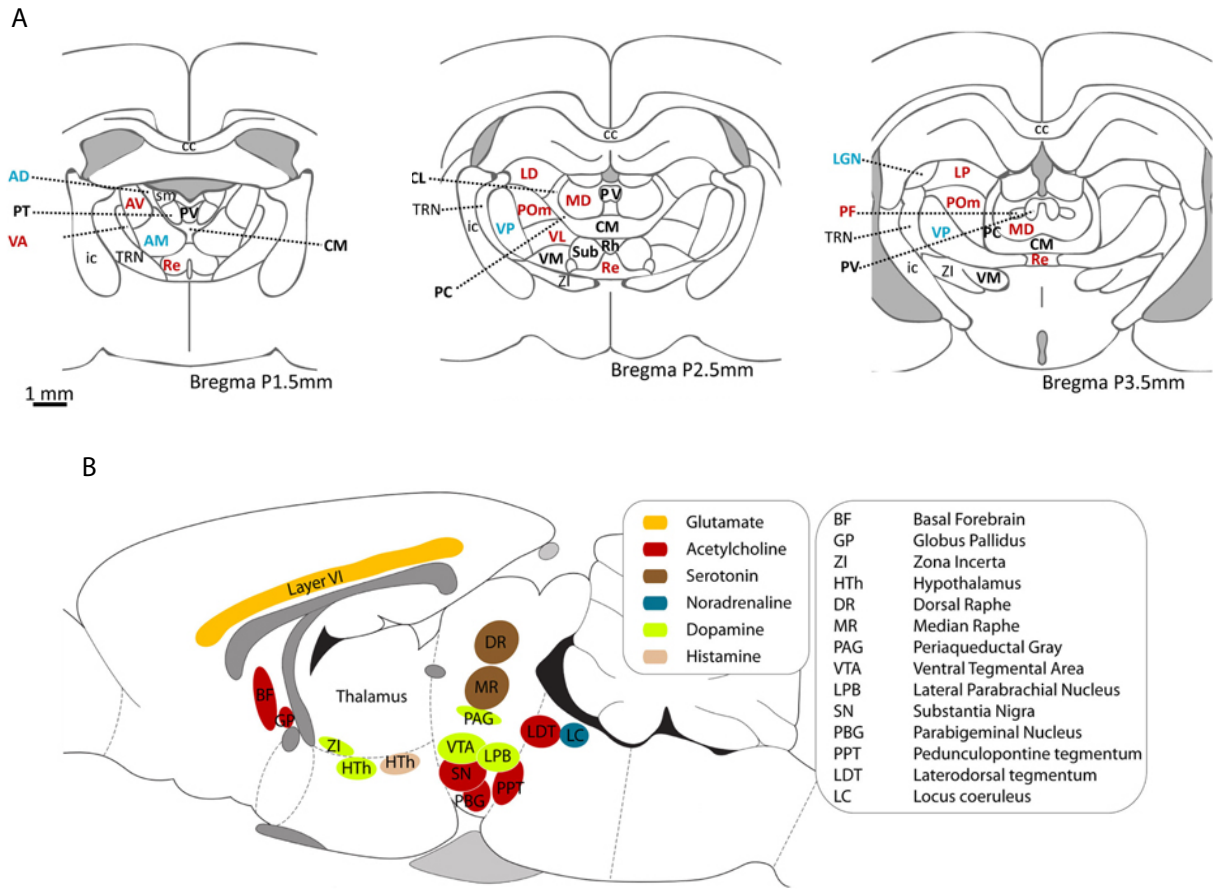

Figure 1.1 Thalamic nuclei and modulator afferents to the thalamus in a rodent brain. A. Schematic illustration of the thalamic nuclei in the rat from three different planes along the anterior-posterior axis and corresponding abbreviated names. First order nuclei are labelled in blue, higher order in red, and nuclei that have not been classified in first or higher orders are shown in black. First order nuclei: AD, anterior dorsal nucleus; AM, anterior medial nucleus; VP, ventral posterior nucleus; LGN, lateral geniculate nucleus. Higher order nuclei: POm, posterior medial nucleus; VA, ventral anterior nucleus; Re, reuniens nucleus; MD, mediodorsal nucleus; PF, parafascicular nucleus; LP, lateral posterior nucleus; LD, laterodorsal nucleus; AV, anterior ventral nucleus; VL, ventral lateral nucleus. Unclassified: VM, ventral medial nucleus; Sub, nucleus submedius; Rh, rhomboid nucleus; PT, paratenial nucleus; PV, paraventricular nucleus; CL, central lateral nucleus; CM, central medial nucleus; PC, paracentral nucleus; ZI, zona incerta; TRN, thalamic reticular nucleus. Note that the schematic do not include the medial geniculate nucleus (most posterior), which constitutes a first order region (the ventral portion) and higher order regions (dorsal portion). B. Locations of brain regions that provide modulator afferents to the thalamus, and primary neurotransmitter used in each region is coded in a different colour. Adapted from Varela (2014).

Virtually all sensory information (visual, auditory, somatosensory etc.) except olfaction firstly pass through specific thalamic nucleus before reaching the corresponding area or group of areas of the cerebral cortex for further processing, and yet the thalamus has mostly been regarded as a simple passive relay. However, recent evidence of structural and functional organization, and distinct properties of thalamic drivers and modulators point strongly to the role of thalamus in actively integrating inputs and relaying to the cortex. Therefore, studying the physiology of relay cells in the thalamus is critical to figure out the

computational functions of thalamic neurons and, ultimately, how signal is being processed along the sensory pathway. Among all the thalamic nuclei, LGN has served as an ideal candidate to study the role of thalamus in information processing. The reasons are that most of its cellular mechanisms and the principles of thalamo-cortical connectivity are comparable to the properties of other thalamic nuclei (Sherman, 2005). In addition, visual sensory information is easier to access and manipulate than others.

1.2 LGN

1.2.1 Visual pathway

Visual pathway refers to the journey that visual information takes from the retina to the primary visual cortex (V1) through LGN. Specifically, as illustrated in Figure 1.2, information from the external world is first detected by rods and cones and then transferred to the retinal ganglion cells (RGCs) in the form of chemical and electrical signals. The information leave the eyes via the optic nerve, and axons mostly originating from the nasal part of the retina cross at the optic chiasm to project contralaterally. After the chiasm, the axons, renamed as the optic tract, wrap around the midbrain to LGN in the thalamus or the superior colliculus (SC). The LGN efferents proceed through the deep white matter of the brain as optic radiations to ultimately reach V1. Although there is a small binocular region in rodents that receives thalamocortical inputs from both hemispheres, the majority of neurons in V1 are stimulated by the contralateral eye due to the lateral placements of the eyes (Dräger, 1975; Mangini and Pearlman, 1980).

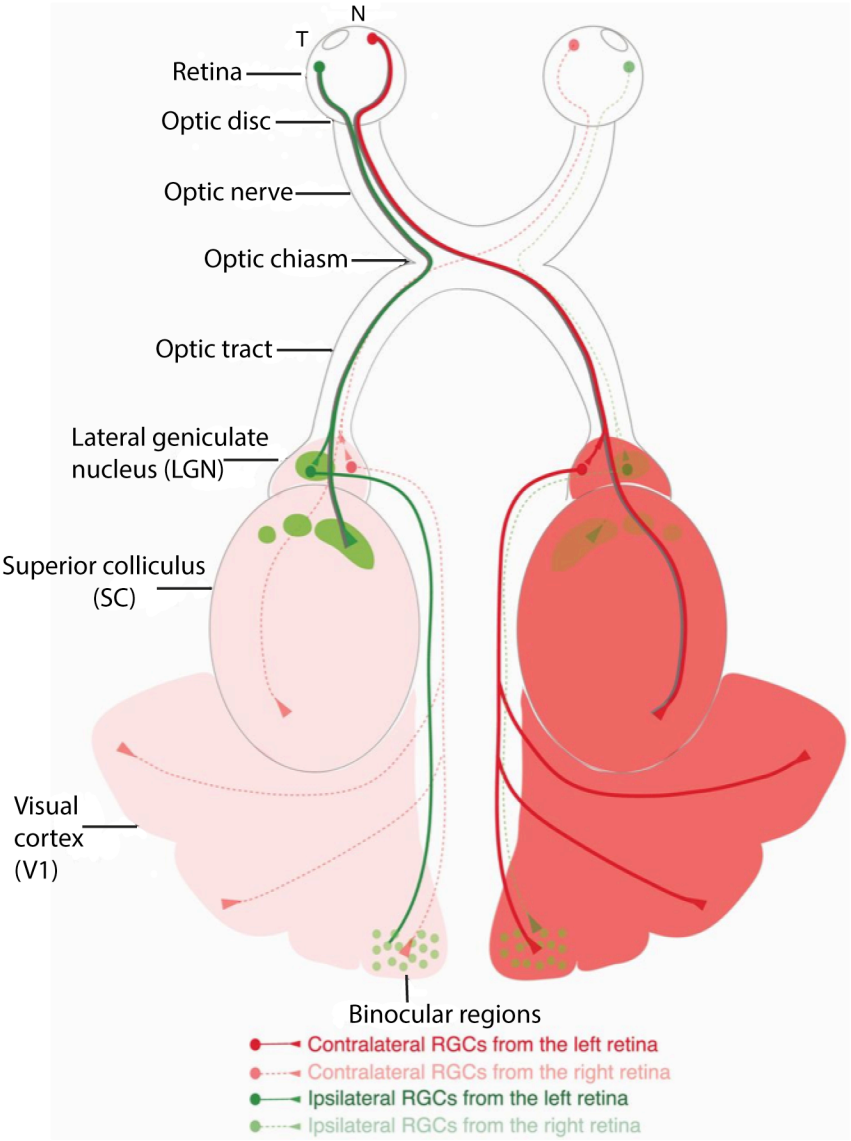

Figure 1.2 Schematic representation of the organization of the contralateral and ipsilateral visual pathway in the mouse. RGC axons leave the eyes via the optic nerve, and axons mostly originating from the nasal part of the retina cross at the optic chiasm and project contralaterally. After the chiasm, the axons, renamed as the optic tract, project to the main visual targets: the LGN in the thalamus (main target) or the superior colliculus (SC). Visual information is transmitted by relay neurons in the thalamus to V1. V1 in the mouse is mostly monocular, yet there is s small binocular region that receives thalamocortical inputs from both hemispheres. Adapted from Erskine and Herrera (2014).

Within the visual pathway, LGN is situated in a strategic position, a strait through which majority of retinal afferents must pass to reach V1. LGN had been traditionally viewed as a passive relay station on the basis of highly specified RGC axons projecting to LGN, as well as similar receptive field properties of RGCs and LGN relay neurons. Nevertheless, pioneering investigations in the early 1980s demonstrated that thalamic neurons could fire spikes in one of two modes, burst or tonic (Deschenes et al., 1982; Llinas and Jahnsen, 1982).

Furthermore, burst or tonic responsive mode was found to relate to the instantaneous attentional demands (Livingstone and Hubel, 1981; Steriade et al., 1993). This dual firing mode is one of numerous evidence that has emerged in recent years suggesting that LGN is able to filter and introduce more complexity to retinal information before it reaches V1. LGN is therefore able to determine what, when and how information is passed to V1 (Saalmann and Kastner, 2011), and examining the physiological properties of LGN can help in better understanding of higher visual function.

1.2.2 Structural parallel pathways in LGN

It is widely accepted that RGC signals are optimized to represent efficiently the visual world, while the visual information is extracted and processed by V1 to create a coherent percept (Van Essen et al., 1992; Callaway, 2005). The major strategy applied towards compact visual representation is parallel projections within the visual system (Dacey et al., 2003), which is apparently reflected in the clear laminar segregation of LGN. Such structural parallel projection has been established in species including humans, macaque monkeys, squirrels, cats, tree shrews, ferrets and rats (Kass et al., 1972a; Humphrey et al., 1985; Casagrande and Norton, 1991; Van Hooser et al., 2003; Briggs and Usrey, 2011). This section takes the monkey and cat LGN - the two most thoroughly studied visual thalamic nuclei across species – as examples, and presents their anatomy and functional implications, followed by studies on parallel projection in mouse LGN.

In the macaque monkey LGN (Figure 1.3), three classes of neurons – the magnocellular (M), parvocellular (P) and koniocellular (K) neurons - originate from parasol, midget RGCs and less common RGC types, respectively. Furthermore, they demonstrate clear laminar segregations in LGN, with M- cells occupying the two most ventral layers (layer 1 and 2), P-cells dominating the four dorsal layers (layer 3 to 6), and K- cells inhabiting the intercalated layers between and below each of the M- and P- layers (Leventhal et al., 1981; Perry et al., 1984; Rodieck and Watanabe, 1993). In addition to the clear anatomical segregation within LGN, there is strong evidence to show that M-, P- and K- pathways remain as parallel processing streams terminating in V1. Explicitly, M- axons target cortical layer 4Cα, P-axons target layer 4Cβ, and K- axons target layer 1 and 4A. Moreover, feedback from cortical layer 6 to LGN also indicates layer-specification: cells located in the upper third of layer 6 project entirely to the P- layers, whilst cells within the lower third project mostly to

the M- layers and possibly the K-layers (Figure 1.3B) (Hendrickson et al., 1978; Livingstone and Hubel, 1982; Blasdel and Lund, 1983; Hendry and Yoshioka, 1994).

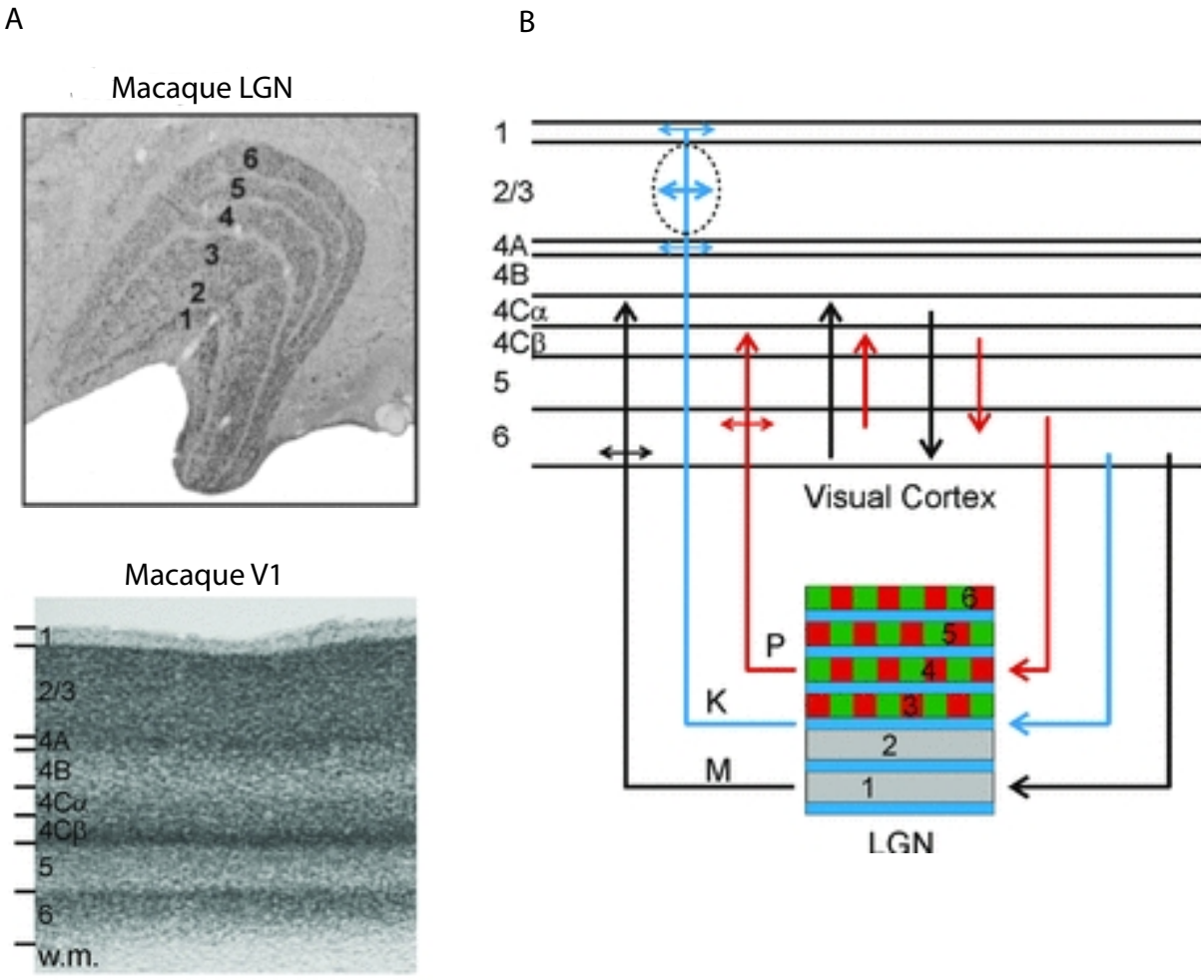

Figure 1.3 Anatomy and connections between LGN and V1 in the primate. A. Top, Laminar segregation of macaque monkey LGN, magnocellular (M-) cells occupy the two most ventral layers (layer 1 and 2), parvocellular (P-) cells dominate the four dorsal layers (layer 3 to 6), and koniocellular (K-) cells inhabit the intercalated layers between and below each of the M- and P- layers. B. Schematic representation of structural connection between LGN and V1. Within LGN, the M- layers (layer 1 and 2) are shown in grey, the P- layers (layer 3 to 6) are shown in green and red grids, and the K- layers (occupy below each of the M- and P-layers) are shown in blue. M- axons target layer 4Cα, P- axons target cortical layer 4Cβ, and K- axons target layer 1 and 4A. Feedback from cortical layer 6 to the LGN is layer-specified as well. Explicitly, cells in the upper third of layer 6 project entirely to the P- layers, whilst cells in the lower third project mostly to the M- layers and possibly the K-layers. Modified from Briggs and Usrey (2011).

Similarly, in cat LGN, another well-studied thalamic nuclei, three distinguishable classes, named as X-, Y- and W- cells, are found to originate from structurally and functionally distinct but analogous classes of RGCs. Morphologically, X-, Y- and W- cells differ greatly in their dendritic arborisations and soma sizes (Stanford et al., 1981). Additionally, each subtype of retinogeniculate axons represents distinct patterns of termination in the cellular

layers, with X- and Y- cells being intermingled in the major geniculate layers (layers A and A1), while W- cells mostly occupying layer C within LGN (Kaas et al., 1972a; Sherman and Spear, 1982; Casagrande and Norton, 1991). As illustrated in Figure 1.4, these parallel channels further lead to separate axonal projections to cortical layers, and the segregation of separate projection is most obvious in cortical layer 1 and 6, which receive exclusive projections from layer C and A of LGN respectively. It is also apparent that in cortical layer 4, the layer A geniculate projections mostly dominate the gap between the two thinner tiers of the layer C projections (Figure 1.4) (LeVay and Gilbert, 1976; Xu and Casagrande, 2004; Kaplan, 2004).

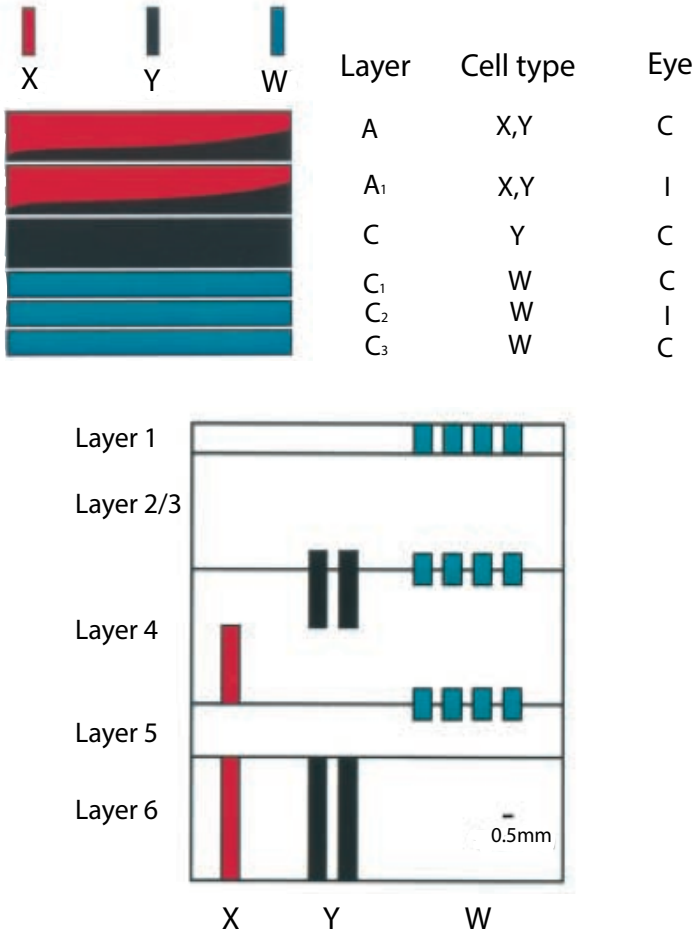

Figure 1.4 Schematic representation of LGN laminae A, A1 and C, and their feedforward projections to cortical layers in the cat. Cat LGN is organized in three main layers. X- (red) and Y- (black) cells are intermingled in layer A and A1, whereas W-cells (blue) occupy a separate set of layer within LGN, named as layer C. Cortical layer 1 and 6 receive restricted projections from geniculate layer A and C respectively. In cortical layer 4, the layer A geniculate projections mostly occupy the gap between the two thinner tiers of the layer C projections. Modified from Alonso (2002).

In mice, studies have identified that several classes of RGCs comprise separate channels, representing unique morphological and functional features, as well as different arrangements of connectivity and projections (Huberman et al., 2008, Kim et al., 2008, 2010; Siegert et al., 2009). Nevertheless, it is generally accepted that these separate retinal channels are not preserved in a parallel manner onto recipient neurons in LGN, where relay cells display a uniform cell type classification in the mouse. This notion has recently been challenged by a morphological characterization study by Krahe et al. (2011). Recording from biocytin-filled neurons in mouse LGN enabled the classification of relay cells into X- (biconical), Y- (symmetrical) and W- (hemispheric) subgroups according to their dendritic architecture (Figure 1.5A). Moreover, by injecting anterograde tracer, these researchers reported that each distinct group exhibited a eye-specific domain: X- cells illustrated a high density in the monocular segment adjacent to the LGN's ventral border; Y- cells dispersed evenly within the central core that also received afferents from the ipsilateral eye; W- cells tended to occupy the perimeter of LGN (Figure 1.5B) (Krahe et al., 2011). This evidence raises the fascinating hypothesis that on structural evidence alone mouse LGN might be far more sophisticated than previously thought.

In addition to these aforementioned anatomical parallel properties, relay cells in monkey and cat LGN also vary notably in cell physiology and functional properties. For instance, axonal conduction velocity of retinal afferents, receptive field features and responses to spatial/temporal frequencies show marked differences (Sur and Sherman, 1982; Jeffries et al., 2013). However, comprehensive characterization of functional features, particularly correlation to the cell morphology and distribution, lacks in-depth examination in mouse LGN. In the subsequent sections, some general physiological characteristics of thalamic relay neurons, including burst/tonic properties and receptive fields, will first be reviewed and summarized. This will be followed by an evaluation of functional properties based on studies in the cat and monkey, as well as comparison with the current knowledge of mouse LGN.

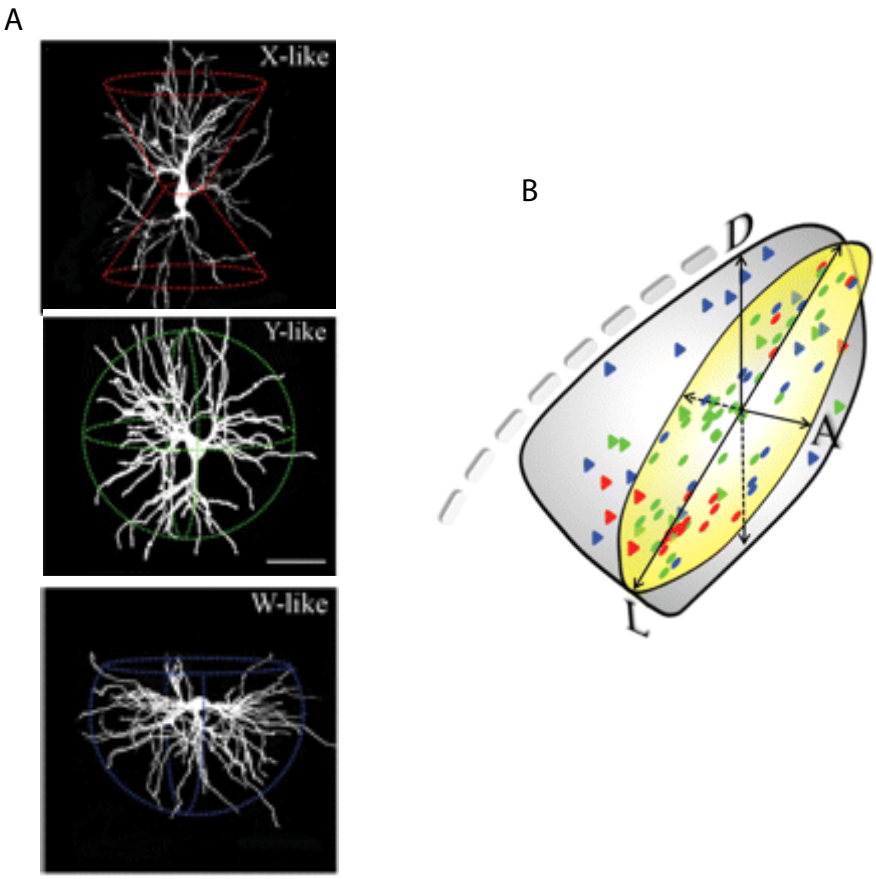

Figure 1.5 The characterization of mouse LGN relay cells from a morphological study. A. Examples of distinguishable subgroups categorized as X- (biconical), Y- (symmetrical) and W- (hemispheric) cells from top to bottom, according to dendritic reconstruction from confocal microscopy. B. Schematic demonstrates the regional specification of distinct cell subgroups within mouse LGN, colours corresponding to specific cell type as in A. This figure is modified from Krahe et al. (2011).

1.2.3 Burst and tonic modes

All relay cells are able to respond to excitatory inputs in one of two distinct modes, burst or tonic. This ability is determined by the inactivation or de-inactivation of I_T, which is a low-threshold (LT) inward T type Ca^{2+} current specifically observed in relay cells (reviewed in Sherman, 2001; Sherman and Guillery, 2001; Sherman, 2005). In the state where I_T is inactivated at relatively depolarized membrane potentials (>55 mV) (Figure 1.6A), the relay cell generates a stream of conventional action potentials that stays as long as there is suprathreshold activation, and represents the tonic response mode. However, I_T is de-inactivated when the membrane potential is hyperpolarized for 100 msec or more. Cell stimulation then produces an all-or-none depolarizing waveform, known as a low-threshold spike (LTS). This LTS is accompanied by a high frequency cluster of action potentials (typically 2 to 6), recognized as the burst-firing mode (Figure 1.6B). Switching between the

burst and tonic mode occurs irregularly from every several 100 msec to several seconds, accompanied by slow changes in baseline membrane potential.

This membrane potential dependent characteristic leads to distinct intrinsic physiological properties as well as functional roles in information relay between the two firing modes. In contrast to those in the tonic mode, the excitatory postsynaptic potentials (EPSPs) link indirectly with action potentials via the all-or-none mechanism in the burst mode. Consequently, larger EPSPs do not elicit higher firing rates, and the input-output relationship is a nonlinear step function for burst firing, whereas tonic firing pattern is almost linear with higher level of spontaneous activity (Figure 1.6C and D) (Sherman, 2001).

Functionally, it has been established that both modes transmitted approximately equal levels of information (Reinagel et al., 1999). Nevertheless, due to the intrinsic cellular properties, the quality of information differs between modes. Specifically, with a higher signal-to-noise ratio, burst-firing patterns are better suited to activate thalamo-cortical synapses than tonic firings (Swadlow and Gusev, 2001). The burst firing may therefore be more useful to alert the cortex when there is a sudden change in the stimulus (Fanselow et al., 2001). As the tonic mode exhibits better linear summation, it is able to support a higher fidelity of information transmission and more detailed analysis of the current situational state (Shermann, 2001; Sherman, 2005). It is thus reasonable to speculate from these mechanisms that burst firing serves as a "wake-up call" for periods during which relay cell responses are relatively suppressed, as may be seen during inattention, drowsiness, or when an alerting animal directs its attention elsewhere. Under these circumstances, a novel visual stimulus to an LGN relay cell can trigger a burst firing that "wakes up" V1 and lead the relay cell to switch to the tonic mode. Consequently, the information about the new stimulus can be relayed more linearly and faithfully (Sherman, 2005).

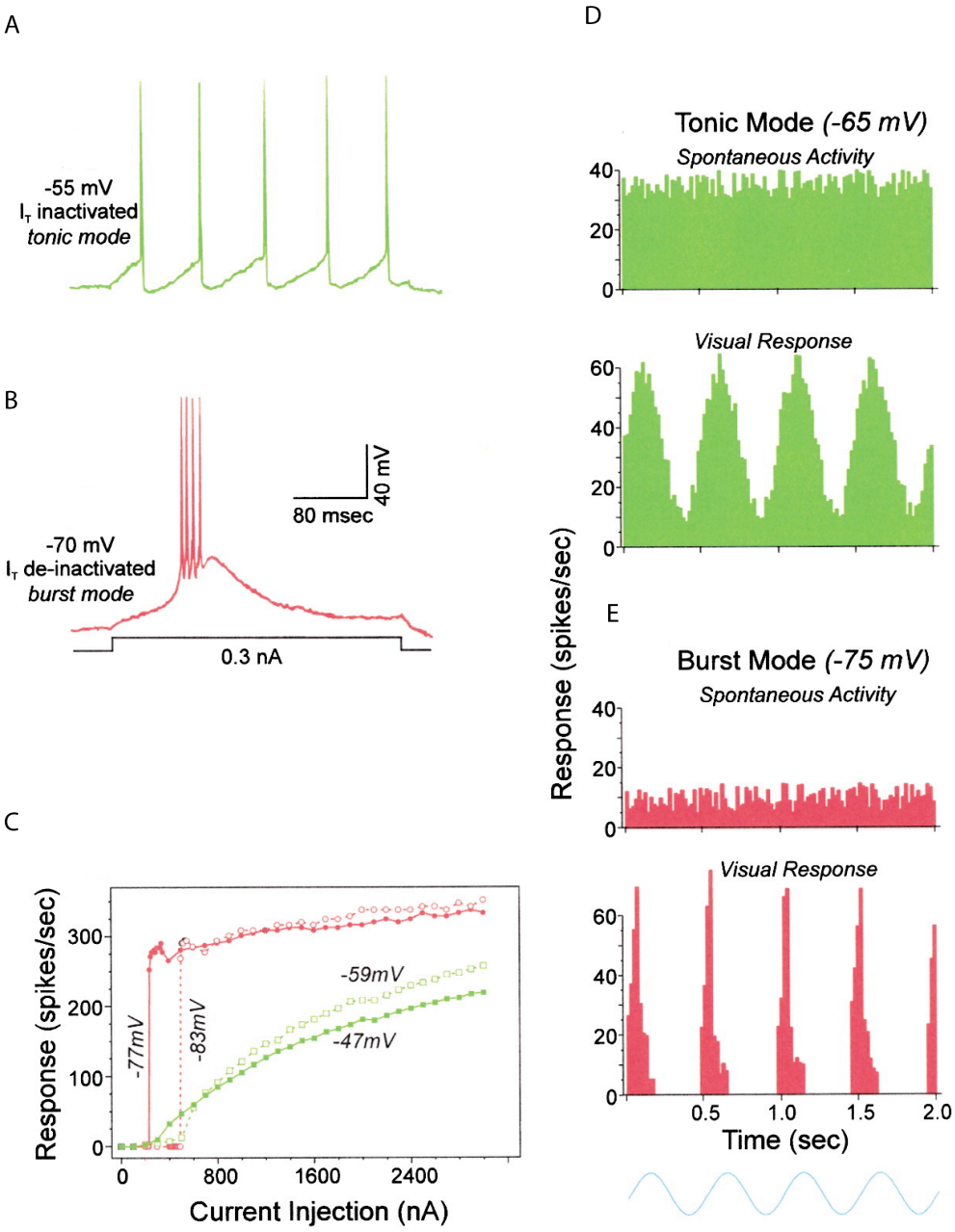

Figure 1.6 Properties of tonic and burst response modes. All examples were intracellularly recorded from relay cells in cat LGN (*in vitro*). A and B. Voltage dependency of low-threshold spike (LTS). At the membrane potential of -55 mV, the cell is relatively depolarized and I_T is inactivated, thus the cell responds in the tonic mode (A). At the membrane potential of -70 mV, the cell is relatively hyperpolarized and I_T is de-inactiveted, cell stimulation produces an LTS, which is accompanied by a cluster of four action potentials. This is the burst mode (B). C. Initial responses of neurons in A and B to different levels of current injection from different levels of original membrane potentials. In the condition of the de-inactivated I_T resulting in the burst response (-77 mV and -83 mV), the cell responds in a nonlinear step function. In the condition of the inactivated I_T that produces the tonic firing (-47 mV and -59 mV), the cell responds almost linearly. D. Responses to sinusoidal gratings (bottom blue) of a relay cell in the tonic mode (top, green) and burst (bottom, red) mode. In contrast to the burst mode, the spontaneous activity in the tonic mode is relatively higher and displays a sinusoidal profile that corresponds to the visual stimulus. This figure is adapted from Guillery and Sherman (2002).

1.2.4 Receptive fields

The pioneering work of Hubel and Wiesel (1961, 1962) half a century ago established the basic characteristics of receptive fields in the cat visual system, and the classical receptive fields in the retina and LGN showed an approximately circular centre-surround spatial structure. Particularly, the ON-/OFF-centre cells referred to neurons that responded to the increment/decrement in light presented to the centre of their receptive fields respectively. The ground-breaking work of Hubel and Wiesel marked the beginning of a productive era of research in receptive field properties, and the fundamental spatial organization of receptive fields have been extensively advanced by later investigations. Some neurons in the primate LGN are achromatic and respond only to luminous intensity. Others could be regulated by specific colours due to separate retinal inputs, for instance, P- cells receive inputs from only L- and M-cones that cover the long- and middle- wavelength ranges of the spectrum, while the other group receive inputs from S- cones (Wiesel and Hubel, 1966; Reid and Shapley, 2002; reviewed in Solomon and Lennie, 2007).

Apart from the above-mentioned classical centre-surround receptive fields, a larger inhibitory extra-classical receptive field has been observed in primate LGN (Hubel and Wiesel, 1961, 1962). Properties (origins, shapes, responses to visual stimuli and functions) of extra-classical receptive fields are less clear and further studies will help to reconcile discrepancies. Nevertheless, it is now commonly accepted that the extra-classical receptive field is an important element of receptive fields in primate LGN and has functional significance in information processing (Webb et al., 2005; Angelucci and Bressloff, 2006; Jeffries et al., 2014).

Compared to the extensive studies conducted on the monkey and cat LGN, thus far, our current understanding in mouse LGN response properties mostly come from two investigations (Grubb and Thompson, 2003; Piscopo et al., 2013). In the study by Grubb and Thompson (2003), only centre-surround LGN neurons with linear spatial summation were reported. However, it has to be noted that in this study with white noise visual stimulus and reverse correlation based mapping approach, receptive fields of nearly one third of the cells recorded could not be constructed and were therefore excluded from analysis. In the other, more recent, characterization study, the majority of neurons exhibited circular receptive

fields (Piscopo et al., 2013) as described in the mouse retina (Chalupa and Williams, 2008) and LGN (Grubb and Thompson, 2003). Moreover, two striking features, selectivity to directions of motion and suppression by contrast, were revealed by applying a clustering algorithm on all of the neurons recorded (Piscopo et al., 2013). These heterogeneities in receptive field properties and responses to visual stimuli suggest that LGN play a dynamic role in visual information processing. This study also inspired further investigations to reveal an exhaustive characterization of mouse LGN.

The receptive field structure becomes increasingly complex at the cortical stage of the visual pathway. Hubel and Wiesel (1959, 1961, 1962, 1965) initially distinguished cortical neurons into two main categories - simple and complex, according to receptive field structures. Briefly, the receptive fields of simple cells have separate ON- and OFF- subareas similar to those in LGN, while receptive fields of complex cells cover a much more heterogeneous population in the cortex. As exemplified from the three columns in Figure 1.7, the receptive field of simple cells shows elongated and parallel ON and OFF subareas besides circular ones. At the cortical level, the subregions of receptive fields from simple cells in the mouse share many similarities seen in other species, although relatively smaller in size (Figure 1.7).

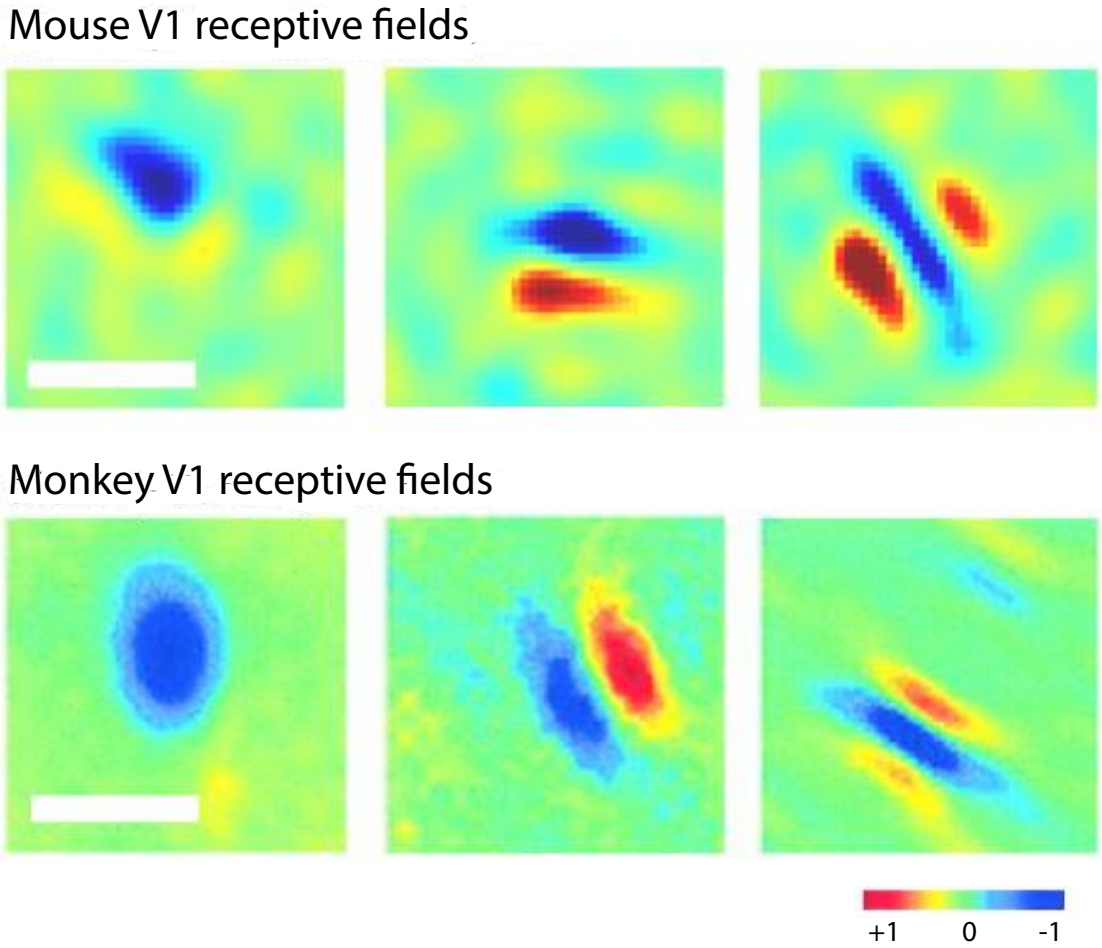

Figure 1.7 Three examples of receptive field structures of simple cells in mouse V1 (upper row) and monkey V1 (lower row). Note that the scale bar is 20 deg for mouse V1, whereas for monkey V1, the scale bar is 1 deg. Red and blue represent ON and OFF subareas respectively. The three examples from the mouse and monkey V1 show that receptive field of individual simple cells from these two species have similar spatial structure despite the differences in spatial resolution. Modified from Huberman and Niell (2012).

1.2.5 Corticothalamic feedback

Among various afferents to LGN, the retina, regarded as the "driver" input, merely accounts for 5%~10% synapses onto the LGN relay neurons (Ahmed et al., 1994; Latawiec, 2000), whereas most of the synapses are from non-retinal neurons, including cortical layer 6, the TRN and local interneurons, which can all be considered as modulators (Sherman and Guillery, 2001; Guillery and Sherman, 2002). Specifically, the TRN and local interneurons act as inhibitory inputs. By contrast, feedback from layer 6 of V1 is the major component of the non-retinal-excitatory inputs (Figure 1.8).

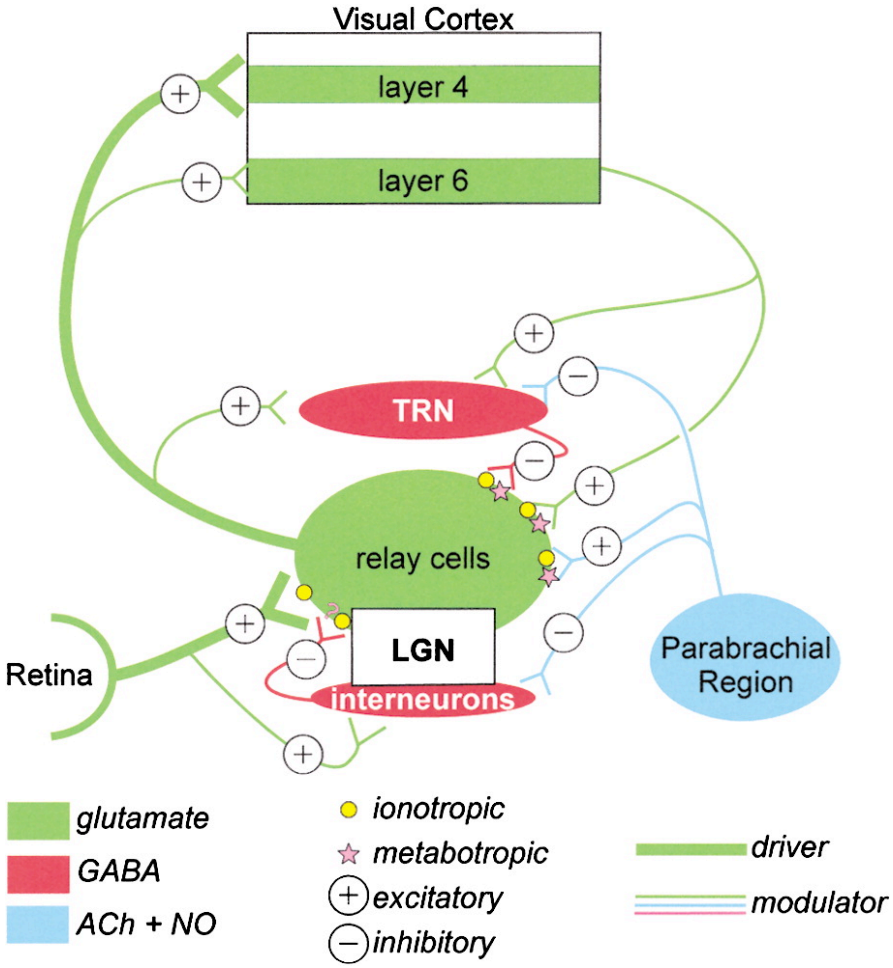

Figure 1.8 Schematic representation of synaptic circuitry in cat LGN. The driver inputs to LGN is ascending retinal afferents, while the modulator inputs include GABAergic inhibitory inputs from the TRN and local interneurons, glutamatergic feedback from cortical layer 6, as well as cholinergic inputs from the parabrachial region of the midbrain. This figure is adapted from Guillery and Sherman (2002).

Among various modulators, cortical feedback plays a "gatekeeping" role in regulating information processing in the visual pathway. In addition to comprising nearly 30% of the synaptic inputs to LGN relay cells, the same layer 6 cortical neurons also send excitatory synaptic inputs to layer 4 in V1, where LGN efferents project (Wilson, 1993; Van Horn et al., 2000; Sherman and Guillery, 2002). These extensive connections display a strong level of retinotopy (Cudeiro and Sillito, 2006). Accumulating evidence has shown that cortical feedback could aid thalamic responses at both single cell and population levels in the following ways.

One major feature of the impact of cortical feedback on LGN cell responses is an enhancement of the spatial focus of receptive fields. Numerous experimental data has suggested that in situation where moving stimuli covered both the centre and the surround

receptive fields of an LGN relay cell, feedback could enhance surround antagonism and thereby the centre excitatory zone can focus more on the stimuli (Murphy and Sillito, 1987; Jones and Sillito, 1991; reviewed in Sillito and Jones, 2002). Cortical feedback, as a consequence, has the capacity to sharpen receptive field borders of LGN and increase the sensitivity of relay cells in spatial domain.

Apart from the influence on the strength of thalamic receptive fields, cortical feedback has been shown to enhance the reliability of LGN responses to visual stimuli. For instance, it was reported experimentally that feedback could remarkably increase the precision of LGN responses to repeated presentations of visual stimuli (Andolina et al., 2007). Along these lines, a growing body of recent studies has shown that cortical feedback might control the transition of burst/tonic modes by adjusting I_T. Specifically, by activating metabotropic receptors (Figure 1.8), cortical inputs to LGN produce sustained EPSPs to inactivate I_T, thereby switching relay cells to the tonic mode (Sherman, 2001; Alitto et al., 2005; Denning and Reinagel, 2005). Additionally, it has been indicated that cortical feedback generates conductance noise within LGN that can serve to mix the burst and tonic firings. This mix generates a more linear thalamocortical summation that leads to higher precision in information transmission (Wolfart et al., 2005).

In temporal terms, cortical feedback can reduce the temporal dispersion of neural events in LGN, thereby leading to improved temporal precision (Wörgötter et al., 1998). More interestingly, accumulating studies have identified distinct subclasses of layer 6 cortical neurons operating at multiple speeds on the basis of axonal conduction latencies and were therefore able to dynamically modulate LGN responses over multiple time scales (Harvey, 1978; Swadlow and Weyand, 1987; Briggs and Usrey, 2007).

There is also abundant evidence suggesting that the cortical feedback could selectively enhance the gain of LGN responses at single cell level (Cano et al., 2006, see review in Briggs and Usrey, 2008). Additional studies have been carried out to probe the role of cortical feedback at a global level. Verified by both *in vitro* electrophysiological and computational studies, corticothalamic inputs could induce correlated firing in LGN relay cells via a redistribution of spike timing (Destexhe et al., 1999; Bal et al., 2000). This synchronous response in turn resulted in increased gain of the input to V1 (Briggs and Usrey, 2008). It has been further reported that cortical feedback could be modulated by subjects'

state (wakefulness or sleep), and this modulation likely contributed to synchronized coherence within the thalamus-cortex neural circuitry (reviewed in Steriade, 2006).

1.2.6 Mouse LGN

LGN in the mouse has been largely neglected for visual research over the past decades. This is mainly due to its small brain volume, as well as different organizational principles compared to higher mammals (e.g. the layer segregation). Additionally, because of the mouse's nocturnal characteristics, its visual acuity is poor compared to other species. There are at least three obvious reasons, nevertheless, to study its structural and functional characteristics.

Firstly, compared with cats and primates, mouse visual pathway is an order or two smaller in magnitude (Remtulla and Hallett, 1985). To some extent, it brings challenges in precisely targeting LGN, which is located relatively deep in the brain. The smaller brain size may be an advantage in covering large spatial scale for physiological characterization, as for example, the V1 across all layers or the entire LGN in dorso-ventral axis can be easily accessed by single penetration of multi-site electrodes (Huberman and Niell, 2011). Secondly, in contrast to carnivores, LGN is the only thalamic nucleus in rodents that has GABAergic local interneurons (Sherman and Guillery, 2009). As a consequence of this feature, it is of growing interest to evaluate functional properties of mouse LGN and relate to those from other species, which may lead to an enhanced functional understanding of interneurons in general. Thirdly, highly developed techniques of genetic manipulations in mice, such as Cre-expressor lines and molecular agents for *in vivo* labeling (Luo et al., 2008), provide powerful tools to address many open questions to elucidate information processing in the visual network.

As reviewed in Section 1.2.2, the visual path at the thalamic level is segregated into three major divisions in the monkey and cat, in terms of the architecture. The divisions are also reflected in functional properties. Take monkey LGN as an example, M- neurons are normally achromatic, have relatively larger classical receptive field centres and prefer higher temporal frequencies. P- cells have colour-opponent structure, relatively smaller classical receptive field centres and prefer lower temporal frequencies, while most K- cells display blue-on or blue-off classical receptive field structure, and a considerable portion of K- cells (34%) can not be triggered by grating stimuli, compared to 9% of M- and 6% of P- cells

(Hendry and Reid, 2000; Usrey and Reid, 2000; Xu et al., 2001; Jacobs, 2008; Martin et al., 1997; Tailby et al., 2008). Cellular physiology and response features also vary among comparable pathways within cat LGN: Y- cells show the fastest conduction velocities, large receptive field size and nonlinear spatial summation; X- cells display intermediate conduction velocities, small receptive field size and linear spatial summation; W- cells are a diverse group that show both linear and nonlinear spatial summation, and very slow conduction velocities (reviewed in Orban, 1984; Sherman and Guillery, 2001).

In contrast to these well-explored response properties in monkey and cat LGN, studies from Grubb and Thompson (2003, 2005) served as the only delicate characterizations of mouse LGN available until very recently. According to their observations, relay cells showed an identical cell type classification, and overall intrinsic physiology of individual LGN neurons was comparable to those of other mammals, including burst/tonic response modes and classical centre-surround receptive fields. Compared to other species with regards to receptive fields and response properties, as listed in Table 1.1, mouse LGN neurons exhibit larger receptive field centre sizes (~11 deg in diameter) that is similar to those measured in mouse RGCs (Chalupa and Williams, 2008). However, in macaque LGN, receptive field size is normally smaller than 1 deg. Consequently, neurons show extremely poor spatial acuity at the thalamic stage in mice (around 0.2 c/deg), as receptive field size acts as an indication of spatial acuity. In macaque LGN, though, spatial acuity is up to 40 c/deg (Derrington and Lennie, 1984). However, peak temporal frequency and contrast gain of mouse LGN are comparable with those reported from other species (Table 1.1).

Table 1.1 Comparison of single cell response properties in LGN across species.

		RF diameter (deg)	SF cutoff (c/deg)	Peak TF (Hz)	Contrast C_{50} (%)
Mouse		11	0.18	3.95 ± 0.24	32.53 ± 2.18
Squirrel	X	1.54 ± 0.1	3.9	6	-
	Y	1.94 ± 0.3			
Cat	X	0.40 ± 0.04	2.7 ± 0.8	4.75 ± 0.42	-
	Y	1.47 ± 0.19	1.1 ± 0.5		-
Macaque	P	0.138	40	6.76 ± 3.24	46.6 ± 1.6
	M	0.224		7.94 ± 4.80	14.6 ± 1.1

RF=receptive filed; SF=spatial frequency; TF=temporal frequency (Mouse data from Grubb and Thompson, 2003; Squirrel data from Jacobs et al., 1982 for SF cutoff, with the rest from Van Hooser, 2003; cat data from Mukherjee and Kaplan, 1995 for peak TF, from Saul and Humphrey, 1990 for RF diameter, from Sireteanu and Hoffmann, 1979 for SF cutoff; all based on nonlagged cells; macaque data from Levitt, 2001 for RF diameter and peak TF, from Derrington and Lennie, 1984 for SF cutoff; from Alitto et al., 2001 for contrast C_{50}; to note that data from subtypes is not provided as no significant difference has been found).

Aside from the characterization of these aforementioned properties, evidence of diverse visual representations in LGN has gained growing interest over the past decade. High selectivity for the direction (selective to one direction of motion) or orientation (selective to two opposite directions of motion) of visual stimuli was long believed to be computed at the cortical level (Albright, 1984). As proposed in the initial feed-forward model by Hubel and Wiesel (1962), simple cells in V1 receive inputs from several LGN neurons simultaneously that result in elongated ON/OFF subfields. Due to this receptive field property, simple cells can be triggered by moving bars or flashes at preferred directions within their receptive fields. There also exists a subtype of RGCs named as direction-selective RGCs (DSRGCs) that respond preferably to directions of motion. This group of DSRGCs had long been thought to project exclusively to brain areas other than LGN (Simpson, 1984), and thus led to the persistent view that direction/orientation selectivity was computed from untuned thalamic inputs.

Recent studies in transgenic mice, however, have shown that at least two separate functional subtypes of DSRGCs project their axons in restricted regions of LGN (Kim et al., 2008, 2010; Huberman et al., 2008, 2009). Such observations raise the conjecture that in addition to the well-established ON-/OFF- pathway, mouse LGN is capable of processing more sophisticated features, such as direction selectivity. By applying two-photon calcium imaging in the superficial mouse LGN, Marshel et al. (2012) showed the functional presence of relay cells selectively responding to motion in the anterior-posterior axis. Interestingly, this pattern was in accordance with superficially restricted projections of posterior DSRGCs (Huberman et al., 2009) and deeply restricted projections of ON-OFF downward and OFF upward DSRGCs (Kim et al., 2010). Although limited to the superficial LGN (almost 75μm), study by Marshel et al. (2012) established a structural-functional relationship within mouse LGN that supported an active role of LGN neurons in conveying information of direction selectivity, contrary to previous classical models (Hubel and Wiesel, 1962).

Shortly after this study, another two researches investigated direction/orientation selectivity in mouse LGN (Piscopo et al., 2013; Zhao et al., 2013). Moving a step forward from showing the existence of direction/orientation selectivity, these two studies addressed potential origins and functional influence of the direction/orientation selectivity in cortical computation. Specifically, Piscopo and colleagues (2013) reported that neurons with direction/orientation selectivity displayed far higher density in the posterior LGN, compared to the anterior and middle regions, which was in agreement with the area where DSRGCs projected. Nonetheless, similar regional preference of direction/orientation selective (DS/OS) cells was not observed from experiments performed by Zhao et al. (2013). Excluding the influence from cortical feedback through pharmacological approach, these investigators raised alternative assumptions to account for the prevalence of direction/orientation selectivity in mouse LGN (nearly 60% of cells sampled), such as the summation of two RGCs that had spatial offset. Zhao et al. (2013) further compared the orientation selectivity in LGN to that in V1, and found a much-improved selectivity in the cortex, with higher proportion of cells and considerably sharper tuning width. This implied that V1 was not simply identical to LGN in direction/orientation selectivity, and left the functional role of LGN for direction/orientation selectivity in cortical processing as an open question. A few studies have sought to address this issue, however, hypotheses including LGN cells with direction/orientation selectivity functioning as a scaffold (Rochefort et al., 2011) or

providing parallel input to V1 (Hendry and Yoshioka, 1994) still need experimental verification.

Above all, the establishment of direction/orientation selectivity from previously mentioned studies provides new insights into the functional role of mouse LGN in visual information processing. Perhaps most important is the growing appreciation for the view that mouse LGN can compute and manipulate sophisticated features rather than merely relaying visual information. Nonetheless, mechanisms underlying such selectivity still remain unclear. By taking advantage of genetic techniques to map synaptic connections and manipulate cell activity, it may be possible in the near future to explore further this avenue. Moreover, comprehensive characterization of the direction/orientation selectivity including the origins may contribute to the understanding of other properties (e.g. receptive field and linearity) in mouse LGN. Combined with information of the cell distribution within LGN, it is imperative to investigate whether these features represent functional distinct pathways in the mouse, similar to those that have been established in the monkey and cat.

1.3 State-dependent neuronal activity

1.3.1 Neuronal synchronization

In previous sections, the main focus was on response properties of individual neurons, which were represented as changes in the firing rates. However, at any one moment, many neuronal groups are active in the brain. It would therefore be unwise to dismiss the potentially rich source of information available in the temporal codes of neuronal groups.

In higher mammals, neuronal network activities are commonly obtained with non-invasive techniques that record from superficial layers of the cortex, such as electroencephalography (EEG), magnetoencephalography (MEG) and electrocorticography (ECoG). Neuronal activity from deeper locations in non-human species can be explored by inserting micro-electrodes (metal, silicon or glass micropipettes) into the brain to record local field potentials (LFPs) (Buzsaki et al., 2012). Much like EEG, the LFP reflects the compound activity from multiple postsynaptic potentials and provides an integrated electrical signal recorded from a small neuronal volume (Mitzdorf, 1985).

Neuronal activities around an electrode can temporally coordinate into a series of alternating membrane potentials, giving rise to LFP oscillations (Frederick et al., 2014). Synchronized

oscillations can lead to increased efficiency in information transmission. Explicitly, it is more likely for synchronized pre-synaptic neurons to drive post-synaptic neurons. In addition, synchronized activities of pre- and post-synaptic cells, such that action potentials of a pre-synaptic cell arrive during phases of reduced inhibition of a post-synaptic cell, increases the probability of the action potentials being relayed (Womelsdorf et al., 2007; Gregoriou et al., 2009; Saalmann, 2014). The synchronized activity can occur in low- (delta, theta and alpha) and high- (beta and gamma) frequency bands. It provides temporal coordination of information transmission across brain regions and supports spike-timing dependent plasticity (Varela et al., 2001; Engle et al., 2001; Buzsaki and Draguhn, 2004).

Singer and colleagues (Eckhorn et al., 1988; Gray et al., 1989; Engle et al., 1991; Singer and Gray, 1995) initially demonstrated that action potentials aligned with the oscillatory rhythm in the beta and gamma range (20~80 Hz) in the cortex such that neurons participating in the same oscillatory rhythm synchronized their discharges with high temporal precision. An important link was thus revealed between synchronized oscillation and cortical computation, often referred to, in short, as the binding-by-synchronization hypothesis. These pioneering studies have sparked intense research on mechanistic underpinnings and functional interactions of neuronal synchronization over the past two decades.

The synchronization at gamma band (> 30 Hz), compared to other lower bands, has received the most intensive investigations thus far. After being firstly reported in V1 of anesthetized cats and monkeys (Gray et al., 1989; Gray and Singer, 1989; Engle et al., 1991), it was found in other neocortical areas as well as non-neocortical regions, such as the hippocampus in numerous species, spanning from rodents to humans (Kreiter and Singer, 1996; Fries et al., 1997, 2001, 2001, 2008b; Womelsdorf et al., 2006, 2007; Adjamian et al., 2004; Hoogenboom et al., 2006; Montgomery and Buzsaki, 2007; Montgomery et al., 2008).

In spite of this general existence, gamma-band synchronization exhibits great specificity as well. Besides moving gratings or bars, gamma-band synchronization could also be induced by viewing smoothly changing shapes (Taylor et al., 2005) and stationary squares (Rols et al., 2001). Further, it is especially strong for salient stimuli, increasing with increase in stimulus size, contrast and spatial integrity (Gieselmann and Thiele, 2008; Henrie and Shapley, 2005; Zhou et al., 2008) or during awake and active states (Munk et al., 1996; Fries et al., 2001; Womelsdorf et al., 2006). Additionally, as shown in V1 (Bertini et al., 2004) and somatosensory cortex (Roopun et al., 2006), gamma-band synchronization is much stronger

in superficial layers than in infragranular layers. The above-mentioned evidences imply that gamma-band synchronization varies across experimental conditions in a meaningful way, indicating the computations that the brain needs to perform in such instances (Salinas and Sejnowski, 2001; Fries, 2009). Functionally, it is now clear that the gamma-band synchronization is dynamically involved in selective attention (Tallon-Baudry et al., 2005; Gregoriou et al., 2009; Chalk et al., 2010), visuomotor coordination (Bressler et al., 1993), working memory (Tallon-Baudry et al., 1998; Pesaran et al., 2002) and associative learning (Miltner et al., 1999).

Just as gamma band, the synchronization at other frequency ranges, including delta (0.5~3.5 Hz), theta (4~7 Hz), alpha (8~12 Hz) and beta (13~30 Hz) (Engle and Fries, 2010), also strongly interweaves with sensory and cognitive functions. Rhythmic activity in delta band is thought to generate from thalamo-cortical and neocortical networks (Steriade, 1999). The delta activity is commonly found during deep sleep (Steriade, 1999), and plays a key role in large-scale cortical integration (Bruns and Eckhorn, 2004) as well as in learning and reward mechanism (Knyazev, 2007). Theta-band synchronization is associated with the integration of the limbic activity of the brainstem, the hypothalamus and the neocortex (Kirk and Mackay, 2003). Furthermore, it has been found that theta-frequency synchronization accompanies gamma-band activity through inter-areal phase coupling, in various attentional and memory functions (Fell et al., 2001, 2003; Sederberg et al., 2003, 2006).

Interestingly, alpha-band activity participates in attentional processing in the form of spatially selective desynchronization (Womelsdorf and Fries, 2007). In other words, alpha-frequency synchronization typically reflects the absence of attended or task-relevant inputs in brain areas, as well as in working memory function (Fries et al., 2001; Muller et al., 2004; Bauer et al., 2006; Palva and Palva, 2007). Beta-band synchronization has been proposed to signal the tendency to maintain the status quo in the sensorimotor system or cognitive state. More specifically, it is dependent on the expectancy of a forthcoming event, and would be enhanced if the maintenance of the current state was intended or predicted, than if a change was expected (Engel and Fries, 2010). A growing body of studies in humans has reported that beta- and gamma- band synchronizations appear in conjunction and fluctuate simultaneously under various mental conditions, leading to the assumption that these two rhythmic activities should be considered as a single entity (reviewed in Steriade, 2005). Taken together, these selectivity-distributed synchronizations provide links between single

neurons and cell assemblies, and govern the most general dynamics in the brain at all sensory and cognitive levels with different attributes. Such a mechanism can provide for cerebral integration.

However, it is important to note that in the intact brain, there is no "pure" rhythm that can be constrained to a single area, and the neuronal electrical activity at population level generates complex wave sequences consisting of cross-areal synchronizations at multiple frequency bands (Steriade, 2001). The variety is owing to compound electrophysiological and connectivity features involving relay cells in the thalamus, the TRN, and cortical neurons as well as modulatory projections such as the brainstem (Steriade, 2005). To examine patterns and functional roles of the synchronization within sensory circuitry, the frequency ranges presented above could be meaningfully categorized into two subdivisions. One is the global processing pattern, which refers to synchronization at slow frequencies (delta, theta and alpha) and distributes over relatively larger brain areas. The other is the local mode, representing those synchronizations that are higher in frequency (beta and gamma bands), lower in amplitude and more restricted to local areas (Knyazev, 2007; Engel and Fries, 2010).

Due to differences in spatial interaction patterns, global synchronization is considered to integrate spatially wide distribution of neural populations, by phase coupling and synchronizing coherence (two signals exhibiting a consistent correlation in phase and amplitude) (Thatcher et al., 1986, 1987; Nunez, 1995). Also, slow rhythms are more likely to reflect states of low arousal, such as deep sleep or anesthesia. Conversely, local synchronization has been suggested to be functionally involved in diverse perceptual or cognitive processes within a limited topographic brain area (Kolev et al., 1999). In addition, local synchronization acts as an indication of enhanced arousal brain state (Steriade et al., 1993; Alkire et al., 2008). Growing evidence demonstrates that global and local synchronizations operate in close interactions with each other. This robust conjunction might reflect that fast rhythms in local circuit are under modulation from large-scale networks operating in lower frequencies (top-down integration), or it might indicate a bottom-up mechanism for propagation of local activities to other brain areas (Demiralp et al., 2007).

In the visual system, it has been proposed that LGN neurons are capable of synchronizing their discharges with high temporal precision because of synchronized input from the retina (Neuenschwander and Singer, 1996). These synchronous LGN responses in turn are particularly effective in driving cortical cells (Alonso et al., 1996) and are also mediated by

corticofugal projections (Sillito et al., 1994). Synchronization at cortical level results from two independent but interacting mechanisms: first, a transient retinal feedforward synchronization at high frequency; and second, an intracortical mechanism, which operates at a lower frequency range and induces more sustained synchronization (Castelo-Branco et al., 1998).

As reviewed in Section 1.2.5, within the thalamic-cortico-thalamic closed loop, the cortical feedback comprises a massive bundle of fibers and provides nearly 30% of the synaptic inputs to LGN relay cells. Besides influencing the spatial strength of receptive fields in LGN, the corticothalamic projections has also been regarded to be involved in the generation and synchronization of fast (20~50 Hz) as well as slow (<15 Hz) oscillatory activities in the thalamocortical network, characterizing activated and sleep-like states respectively (Steriade, 1997). From *in vivo* multi-site recordings in the cat, in activated states (waking or internal signaling during dreaming), it was shown that layer 6 corticothalamic neurons were good candidates to reset weakly synchronized thalamic population activities into robust coherence (Steriade, 1997). During quiescent sleep, however, the corticothalamic projections could effectively support long-range thalamocortical synchronization of thalamic-generated rhythms, such as sleep spindles (7~14 Hz) and delta waves (1~4 Hz) (Contreras et al., 1997; Steriade, 1997).

To sum up, the complex wave sequences comprising of cross-areal synchronizations at different frequency bands in intact brains of living animals are instrumental for promoting selective neuronal communications. Apart from studies on processing synchronization mechanisms in primates and cats, an intriguing trend has begun to investigate the functional implication of rhythmic activity in rodents with the help of modern multi-electrode-arrays (MEAs) and optical techniques, especially with animals in synchronized/desynchronized cortical states. A brief introduction of the two states, and a summary of what is known about their relevance with synchronous activity as well as the influence on neuronal activity at single cell level will be presented in the following section.

1.3.2 Cortical states in rodents

It has been classically accepted that the network of sensory processing has relatively fixed input-output relationships. An increasing number of experimental studies have suggested that both networks and their component neurons could respond differently to an identical

stimulus, depending on their state. The network state is reflected as coherent structure in the activity of multiple interconnected single neurons, and not driven by any specific stimulus (Fontanini and Katz, 2008).

The most conspicuous changes in the brain state occur during sleep-wake transitions. Further, sleep can be separated into two types: rapid-eye-movement (REM) sleep with vivid dreams and non-REM sleep with lack of sensation (Hobson, 2005). During periods of wakefulness, brain states can also be dynamically modulated on demand of specific tasks and switch rapidly from quiet, inattentive to alert, vigilant states, which is critical for the survival of the animal. The transitions of states are commonly accompanied by significant variations in the neuronal population activity, which can be measured electrophysiologically (Lee and Dan, 2012). During alert periods and REM sleep, the cortex operates in a "desynchronized" state in which rhythmic activities at low frequency are suppressed. During quiescence or non-REM sleep, the cortex operates in a "synchronized" state, featured by strong low-frequency synchronization (Steriade and McCarley, 2005). However, it has to be noted that cortical state reveals a continuum, instead of a bimodal switch between extreme synchronized and desynchronized states (Okun et al., 2010).

Figure 1.9 shows other different patterns of neuronal ensemble activity between the two cortical states. In the synchronized state (top panel in Figure 1.9), all neuronal classes respond robustly (coloured rasters) during the active phase, whereas the firing becomes decreased or absent during the silent phase. These phases are accompanied by corresponding depolarization and hyperpolarization in intracellular potentials (red, top). The cortical LFPs (black trace) features high-frequency activity in the active phase and smooth dome-shaped positive waves in the silent phase. By contrast, the spontaneous fluctuation is not seen in the desynchronized state, and low-frequency fluctuations in LFPs as well as membrane potentials are suppressed (bottom panel in Figure 1.9) (Harris and Thiele, 2009).

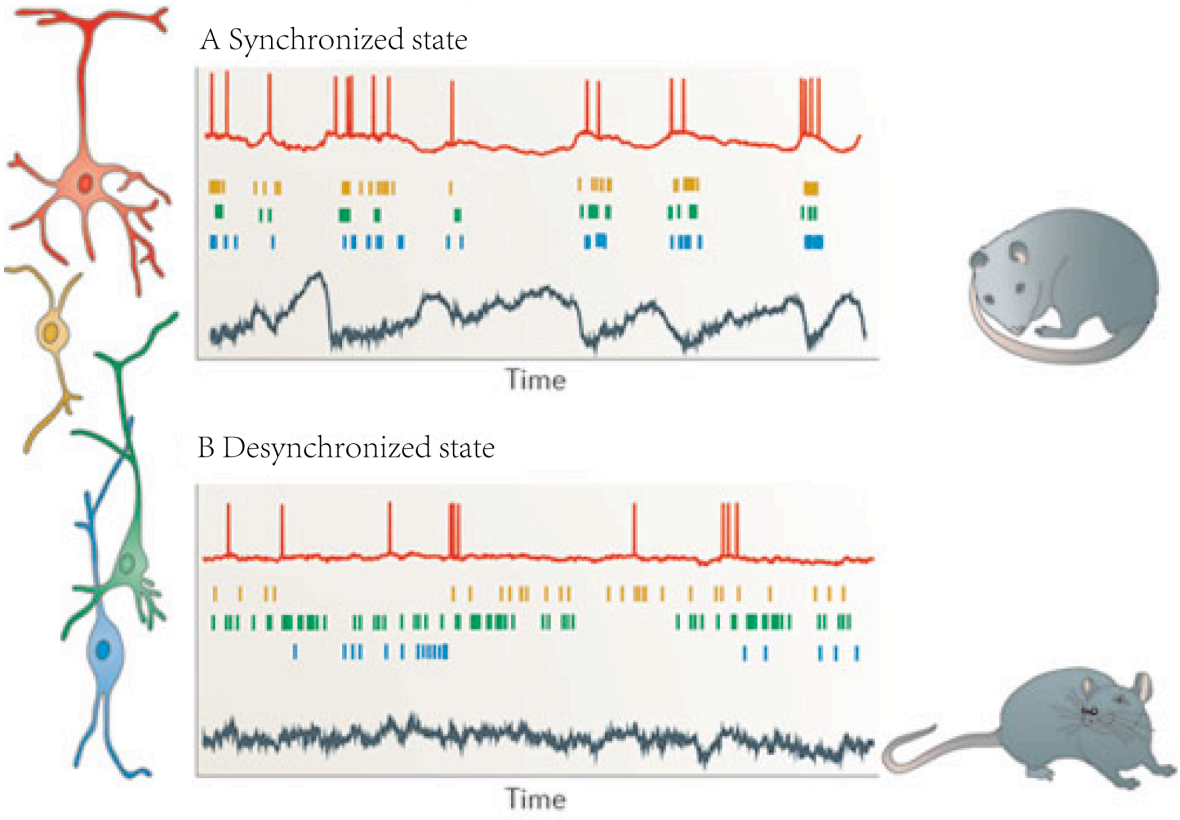

Figure 1.9 Cartoon illustration of different patterns of ensemble neuronal activity seen in two extremes of continuum cortical states in the awake rodent. A. In a synchronized state, all neuronal classes respond robustly (coloured rasters) during the active phase, whereas firing activity is decreased or absent during the silent phase. These phases are accompanied with corresponding depolarization and hyperpolarization in intracellular potentials (red, top). Cortical LFPs (black, bottom) show that slow negative waves are accompanied by high-frequency activity in the active phase, with smooth dome-shaped positive waves in the silent phase. This type of activity is often seen in quiescence or slow-wave (non-REM) sleep (right). B. In a desynchronized state, spontaneous fluctuation is far weaker than that in the synchronized state, and also fluctuations at low frequency in LFPs and membrane potentials are not seen. This type of activity is often seen in waking and behaving animals (right). This figure is adapted from Harris and Thiele (2012).

Numerous studies have been performed to address two fundamental questions concerning cortical states: what mechanisms control cortical states, and what is the function of each state? It has been proposed that several mechanisms might contribute to state transitions, such as cortico-cortical connections (Li et al., 2009), and sustained thalamic glutamatergic inputs as well as increased activity of subcortical cholinergic nuclei (Harris and Thiele, 2011). As mentioned earlier, burst and tonic firings are two distinct response modes of thalamic neurons in different brain states, with burst firing during quiescence or non-REM and tonic firing during alertness (Sherman, 2005; Bezdudnaya et al., 2006 Stoelzel et al., 2009). Experimental evidence has demonstrated that local application of a cholinergic agonist could

effectively prompt tonic firing of thalamic relay cells, and subsequently lead to the desynchronization of the cortical area that received the inputs (Hirata and Castro-Alamancos, 2010). Interestingly, several other studies showed that thalamic lesion did not prevent desynchronized cortical activity (Buzsaki et al., 1988; Fuller et al., 2011; Constantinople and Bruno, 2011). These observations may indicate that an intact thalamus is not a necessity for the maintenance and shift of cortical states; modulation of thalamic activity, however, is sufficient to alert cortical states (Lee and Dan, 2012).

Functionally, the effect of cortical states on sensory responses at cortical level appears to be complex: the state could reduce (sudden puncture stimuli), enhance or have no impact (temporally extended or rapidly repeated stimuli) on cortical responses, depending on specific type of stimulus (summarized in Harris and Thiele, 2011). Interestingly, a growing body of evidence indicates that the state-dependent variances of sensory responses are reflected in subcortical areas as well. Particularly, during the synchronized state, relay neurons in the thalamus reveal an increased tendency to fire in the burst mode (Sherman, 2001). While during the desynchronized state, increased baseline (tonic) responses of thalamic neurons are able to cause depression of thalamocortical synapses, which would reduce the potentiality for sensory adaptation and thus lead to efficient sensory information processing (Castro-Alamancos, 2004). Further, a number of attempts have been made to examine and compare response properties of the primate and cat LGN, with the subjects in distinct states, such as alertness and anaesthesia (Cano et al., 2006; Alitto et al., 2011; Hei et al., 2014; Bastos et al., 2014). However, the role of the cortical state on response properties in mouse LGN remains largely unexplored, and more work is needed to address this issue.

1.4 Purpose and outline of this thesis

Motivated by previous work summarized in this chapter, the main goal of this project was to electrophysiologically characterize response properties of mouse LGN mainly at single cell level and further explore the influence of anaesthesia depths on such properties. To achieve this goal, the aim was to record from the full-extent of mouse LGN with MEAs and investigate neuron responses to a battery of visual stimuli. Additionally, LFPs were examined in mouse LGN and V1, with the animals in two different states, differentiated by isoflurane concentration. The variances of LGN response properties in the two states were subsequently assessed.

Chapter 2 of this thesis provides detailed description of the experimental preparations and procedures towards the electrophysiological recording, along with a summary of stimulus parameters and data processing. Specifically, the first step was to design and optimize the experimental setup, and to ensure reliable approaches to mouse LGN. Towards this end, a mouse nose cone for inhalation anaesthesia, and a rotatory rail mounted under the monitor to provide smooth rotation while keeping the distance to the animal eye fixed were developed. Also, a 16-channel audio splitter was custom-designed and manufactured to be compatible with the data acquisition system. The splitter offered the possibility to monitor real-time neuronal activity, which was essential for hand mapping of receptive field. In addition, a precise and repeatable LGN targeting protocol was developed, which played a crucial role in recording from different coordinates within mouse LGN.

In chapter 3, we discuss a broad range of response properties observed in mouse LGN cells that displayed centre-surround receptive fields, both in aspects of volumes and response parameters. We re-investigated properties that were in agreement with earlier studies in this field (Grubb and Thompson, 2003; Piscopo et al., 2013), which served as a reference before comparing other parameters and investigating novel features. Successively, we established a number of novel properties at single cell level, for instance, non-responsive cells to gratings, low-pass and high-pass temporal tuning features. We also identified the prevalence of cells that responded selectively to directions of motion in mouse LGN, and additional examinations on other properties of these cells added to the weight of understanding on their origins. Moreover, it was revealed that some functional subtypes, such as ON-/OFF- centre and transient/sustained cells showed distinctive response patterns. In sum, these results can facilitate in determining stimulus parameters that triggering the largest responses in mouse LGN for future studies. More importantly, the characterization of unexpected properties and evidence of parallel projections broaden our understanding of the functionality of this nucleus and reflect that more elaborate features can be encoded subcortically than previously thought.

Chapter 4 explores the modulatory effects of the depth of anaesthesia on response properties of mouse LGN neurons. To address this issue, electrophysiological recordings were performed on mouse LGN and V1 simultaneously with the animal under high or low concentration of isoflurane. We observed that the LFPs in V1 showed distinct patterns between the high and low isoflurane states that resembled the synchronized and

desynchronized cortical states respectively. Using the power ratio in theta (4~8 Hz) against delta (1~4 Hz) bands to differentiate the high and low isoflurane states, we show that changing levels of anaesthesia can be a good model for the "state-dependence" studies. Furthermore, our current study provides the first in-depth investigation on state-dependent properties of mouse LGN and reveals that when the animal is under low isoflurane state, the response latency decreases, and the contrast sensitivity increases, also the neurons tend to be more responsive to the gratings moving at higher spatial frequencies.

In Chapter 5 we discuss ways to visually recover electrode tracks and clarify electrode locations. We developed a series of histological protocols to reconstruct a mouse LGN volume for the first time. The LGN volume successfully demonstrated a close to perfect alignment and satisfactory match to original images, and was also able to identify subtle morphological changes of LGN. Combined with confocal-imaged electrode tracks, it helped to classify locations of electrode tracks and corresponding neurons recorded from to be in the anterior, middle or posterior LGN. This volume provides a powerful tool to map single neuron location within LGN and explore the relationship between cell distribution and response properties.

Finally, Chapter 6 summarises the main findings and outline future directions to expand on this project.

CHAPTER 2

Methods

In this chapter, experimental preparations and procedures used in this project for the *in vivo* electrophysiological recording will be described. Subsequently, a summary of parameters for visual stimuli as well as data analysis methods will be presented to characterize single cell response properties in mouse LGN.

2.1 Animals

Experiments were performed on adult (age 2~4 months) wild type female C57Bl/6 mice (Harlan, UK). The animals were used in strict accordance with protocols approved by UK Home Office project and personal licenses. The mice were kept in Imperial College animal facility under a 12-hour light/dark cycle. All electrophysiological recordings were carried out during the dark phase of the cycle.

2.2 Anaesthesia

Several factors that were taken into account for anaesthetic selection will be discussed in this section, followed by anaesthesia protocols used in this study. The novel feature of anaesthesia protocol is the development of a nose cone to minimize the block of visual field while delivering the anaesthetic agent to the animal (Figure 2.1).

2.2.1 Anaesthetic selection

We primarily adapted anaesthesia protocols from the mouse V1 research by Gandhi et al. (2008). Isoflurane, the agent in this study, is a type of inhalation anaesthetic that has rapid induction ability and maintains stable mean arterial blood pressure and heart rate (Szczesny et al., 2004). It has gained increasing application in mouse visual pathway studies (Gandhi et al., 2008; Smith and Häusser, 2010; Piscopo et al., 2013).

Furthermore, isoflurane allows easy and quick control of the depth of anaesthesia, enabling

to record from both deep and light anesthetized states from the same subject. This feature has been applied in this study to characterize neuronal responses during different animal states (Chapter 4).

Additionally, in combination with isoflurane, we administered chlorprothixene as a preanesthetic sedative, to reduce apprehension and favour stress-free induction. It also helped to lower concentration of isoflurane used for both induction and maintenance. Moreover, a small dose of atropine was administered after anaesthesia induction to reduce bronchial and salivary secretions (Stokes et al., 2009).

2.2.2 Nose cone

Standard off-shelf breathing mask seals around the face of the animal, it reduces the amount of anaesthetic gases that might leak into the room, but also covers the visual field to a great extent, which interferes with the visual stimuli presented to the mouse in this project. To resolve this issue, a nose cone was customized to deliver isoflurane and O_2 to the animal. The nose cone fitted with the experimental setup, and more importantly covered only the mouth and nose of the mouse without blocking the visual field of view.

The nose cone was a cylinder (approximately 1.5 cm in diameter) made of acrylic that fitted to the incisor adaptor. Gas was delivered to the mouse through a tube (0.5 cm in diameter) connecting the bottom of the nose cone (Figure 2.1).

Due to the small diameter of the nose cone, superfluous gas was retrieved using a scavenging unit (Harvard Apparatus, UK) that connected to another tube mounted on the side of the stereotaxic apparatus (Figure 2.1).

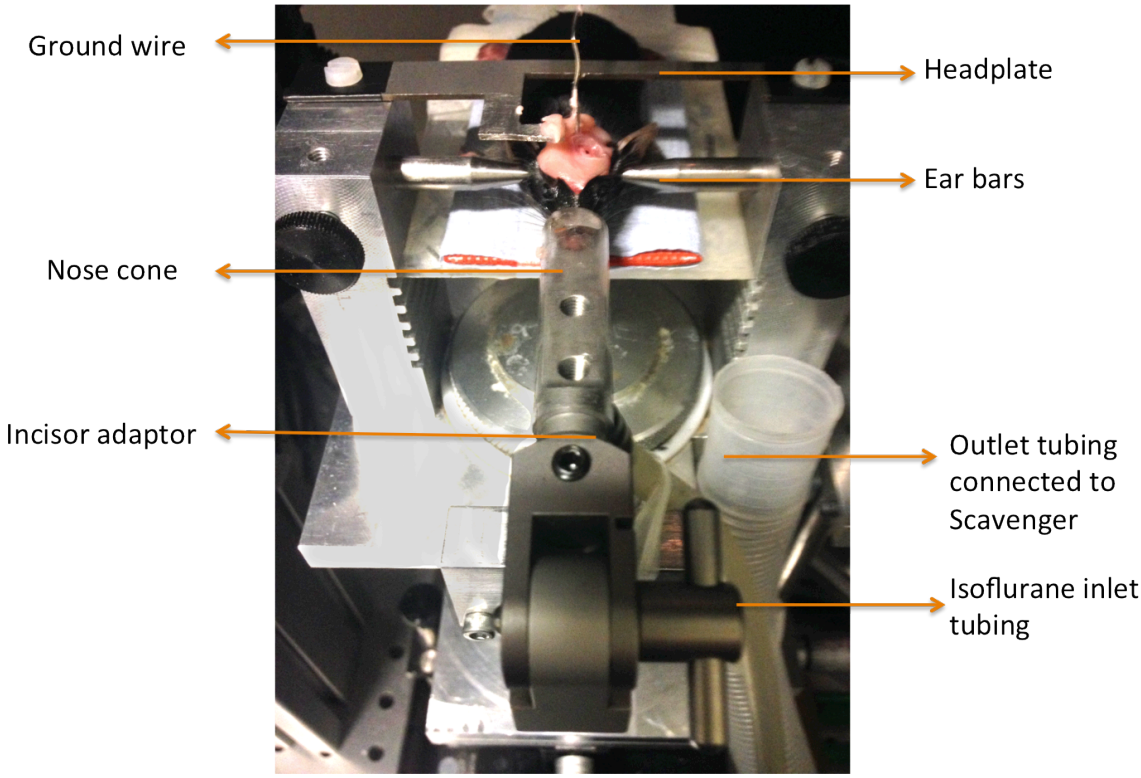

Figure 2.1 Surgery setup. Main components are marked in the figure. The mouse was secured with ear bars and incisor adaptor on the stereotaxic apparatus. Isoflurane and O_2 were delivered to the animal through the nose cone. Redundant anaesthetic was retrieved by outlet tubing connected to the scavenging unit.

2.2.3 Anaesthesia protocol

The mouse was sedated with an intraperitoneal injection of chlorprothixene (Sigma-Aldrich, UK), at a dose of 0.5 mg/kg. After 10~15 min, the animal was transferred to the stereotaxic apparatus and positioned onto the incisor adaptor, facing the experimenter. The tongue was gently pulled out and aside with small dull forceps, which helped to reduce breathing problems.

Surgical anaesthesia was induced with 3% isoflurane in O_2, and maintained with 1~1.5% isoflurane in O_2 (Harvard Apparatus, UK) through the nose cone. Dexamethasone (2mg/Kg) (Organon, UK) and atropine (0.3mg/Kg, 20% in distilled water) (Animalcare, UK) were applied to improve breathing and reduce secretions, respectively (Niell and Stryker, 2008). Both of these were administered subcutaneously in the scruff at the back of the animal's neck.

During experiments (preparation, surgery and recording), respiratory rate (150~200 per min for mouse), paw pinch withdrawal reflexes and presence of whisker movements of animals

were monitored regularly. Body temperature was monitored and maintained at 37 ± 0.5 ˚C with an electronic rectal thermometer and a feedback-controlled heat mat (Harvard Apparatus). Skull and brain tissue were kept moist with sterile phosphate buffered saline (PBS) throughout the experiment.

2.3 *In vivo* electrophysiology

Methods for *in vivo* electrophysiology will be described in the following section. The procedure starts with fixation of ear bars and craniotomy for ground wire, followed by LGN coordinate targeting. The latter is a critical step because of the small volume and deep location of this nucleus in the mouse brain. Finally, neuronal activities were recorded with MEAs. Histological and imaging protocols will be described in Section 5.2.

2.3.1 Fixation of skull and ground wire

The stereotaxic apparatus where the mouse was placed was secured and the animal was ensured to face straight forward, both during surgery and recording. These were achieved by two small-customized aluminium pieces mounted through a bar on the edge of the stereotaxic apparatus (Figure 2.2).

Before the start of surgery, a thin layer of silicon eye oil (viscosity 100cSt, Sigma-Aldrich) was applied on the animal's eyes. This was applied often throughout the experiment to prevent corneal dehydration while maintaining clear optical transmission. Furthermore, to protect the animal's eyes from microscope light, a small piece of black acrylic was screwed to one side of the stereotaxic apparatus and it covered the eyes until recording.

Ear bars were placed into the ear canals and tightened into place on both sides with proper pressure to hold the head in position without causing breathing difficulties and intracranial pressure increase. The fur on the skull was shaved and the skin was cleaned with 70% ethanol. Afterwards, the scalp was removed with scissors in a midline incision to expose the skull bone. The subcutaneous and muscle tissue were cleared from the skull surface with cotton swabs and fine surgical scissors and retracted.

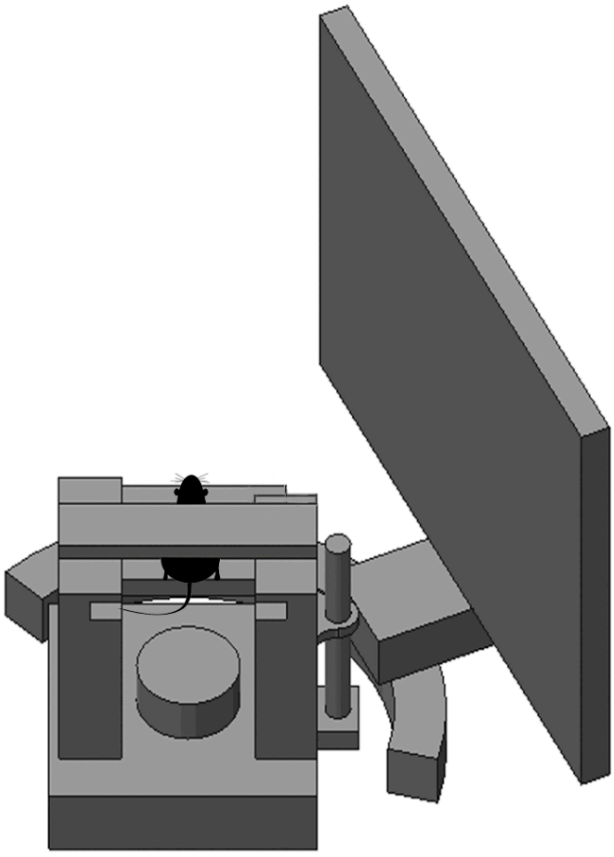

Figure 2.2 Illustration of the stereotaxic setup. The top platform where the mouse sits is rotatable for surgery purpose. Bars on right side function to ensure the top platform is straight forward during experiment. The monitor-to-mouse distance is kept at 25 cm with a rotatory track at the bottom.

To place the ground wire, a craniotomy of ~0.05 mm in diameter was performed over the cerebellum with a hand-held drill (Osada Success 40). The drill bit was moved horizontally at a speed of 30,000 rotation/min while applying a slight pressure downward. Dura was carefully perforated and removed with a small needle (27G).

2.3.2 LGN coordinate targeting

For the purpose of stereotaxic targeting of mouse LGN, two landmarks on mouse skull were used: the Bregma point (cross of the coronal and sagittal sutures) and the Lambda point (cross of the sagittal and lambdoid sutures) (Cetin et al., 2006).

To achieve the horizontal leveling of the mouse's head (in the caudal-to-rostral direction), the Bregma and Lambda points were first marked with marker pens on the skull. An aluminum needle with very fine tip was mounted onto a micromanipulator (Scientifica, UK). The needle was lowered to touch both Bregma and Lambda points and their Z coordinates

were compared. The screw at the incisor adaptor was adjusted accordingly until the difference of these two coordinates was less than 0.05 mm on Z plane.

Similarly, for the leveling of the animal's head in the medial-to-lateral direction, points 1.5mm lateral to Bregma point on both left and right hemispheres were chosen and their Z coordinates were measured. Positions of the ear bars in the mouse ear canals were gently adjusted until the difference of these two coordinates was less than 0.05 mm.

Subsequently, a coordinate that was 2.15 mm lateral and 2.6 mm posterior from Bregma was chosen as the targeted recording site. The actual coordinate was scaled in cases where the Bregma-Lambda distance differed considerably from 4.2 mm, which is the average Bregma-Lambda distance (Paxinos and Franklin, 2008). The targeted site was identified with marker pen on skull.

For recordings aimed for the anterior and the posterior LGN, the target coordinates were 2.15 mm lateral and 2.2 mm posterior from the Bregma for the anterior LGN, and 2.15 mm lateral and 3.0 mm posterior from the Bregma for the posterior LGN.

2.3.3 Locating electrode and recording from mouse LGN

A rubber ring ~3 mm in diameter was placed onto the marked site and glued with Histoacryl (B.Braun). A ground wire (customized, silver-plated) was placed onto the brain surface through the previously drilled hole and a headplate was screwed on the stereotaxic apparatus. Dental cement was subsequently used to cover the skull and secure the headplate and ground wire in place, leaving out the space inside the rubber ring. Once the dental cement cured, the ear bars were removed and the mouse was kept in place with the headplate.

The stereotaxic platform was then rotated, with the mouse facing the monitor. Bars on the right side of the platform were re-secured to ensure the animal was facing straight ahead (Figure 2.2). The eye opposite to the monitor was covered with eye ointment and then black tape on top to prevent confounding effects of binocularity on the experiments.

The silicon MEA (A1x16-Poly2-5mm-50s-177-A16, NeuroNexus) was connected to electrode adaptor (ADPT-HS-18-N2T-16A, Neuralynx) and headstage pre-amplifier (HS-18, Neuralynx). All these were mounted on the micromanipulator through a customized electrode adaptor holder.

The electrode was firstly moved to the marked recording site on skull surface and the coordinates in X-, Y- and Z-axes were recorded to guarantee precise targeting. The electrode was moved back to the recorded coordinates 2~3 times during craniotomy to ensure the marked site did not shift due to drilling.

The craniotomy was performed by moving the drill bit along the inner edge of the rubber ring, slowly and with slight pressure downwards. Drilling was stopped when the bone became very thin (blood vessels were visible or cracks appeared). Skull area within the rubber well was kept moist with PBS to prevent the brain being over-heated by drilling. The piece of thinned bone was carefully removed with a 27G needle and #5 forceps. The dura was perforated and gently torn apart with a 27G needle held at a flat angle to expose brain tissue.

Before inserting the electrode, PBS on brain surface was dried with soft tissue. Afterwards, the electrode was moved back to the previously targeted coordinates. Amplifier (Lynx-8, Neuralynx) and digital data acquisition system (Power 1401 and Spike 2, version 7, from Cambridge Electronic Design, UK) were set to gain at 6000 and filtering from 300 to 9000 Hz for all the 16 channels, with sample frequency at 20 kHz.

The electrode was lowered vertically at a speed of approximately 50 μm/sec. As soon as the lowest recording site on electrode surface touched the brain, a sudden decrease in the baseline amplitude on corresponding channel on Spike 2 software would be observed, from 5000 mv to 200~250 mv. The electrode was then inserted into the brain at a speed of 2~3 μm/sec. Before reaching the LGN, from 2,000~2,200 μm depth below the pia, the electrode usually went through one band 400~500 μm wide with extremely high density of hippocampal activities.

LGN was usually found at a depth of 2,500 ~ 3,200 μm from the pia surface, characterized by robust visual responses, either to gratings or to white/black squares. Within this range of depth, weak visual responses usually indicated the electrode was too medial and was recording from lateral posterior nucleus (LPN). Whereas robust responses to sound stimuli suggested that the electrode was too posterior and was recording from medial geniculate nucleus (MGN). In cases of mis-targeting, the electrode would be slowly retrieved and re-targeted based on the brain atlas. Number of penetrations in one subject was restricted to three to maintain neuronal viability.

Once the electrode could be confirmed to be in LGN, with most channels obtaining reliable visual responses, the electrode was allowed to settle in position for 30 min to obtain stable single-unit recordings.

During recording, both LFPs and spikes were recorded. For channels to record LFPs, the extracellular signals were filtered from 0.1 to 9000 Hz and sampled at 20 kHz.

The rig was built with aluminium sheets on two sides, top and back to form a Faraday cage for the purpose of minimizing noise artifacts and keeping the light out. All recordings were performed in a dark room. A conductive fabric curtain (Wavetame, UK) was applied to cover the front of the rig during recording to further block out light from computer displays. As a result, the monitor that presented stimuli to the animal was the only source of illumination to the animal.

The animal's anaesthesia level, brain condition and optical quality were monitored throughout the recording session. An entire recording session generally took 2 ~ 2.5 hours. If the mouse condition remained stable, another session would be carried out, either at a different anaesthesia level or a different recording site (at least 100 μm away from the 1st penetration). At the end of recording, the animal was terminated with perfusion (Section 5.2).

2.4 Stimulus presentation

This section starts with an introduction of the monitor set up. A brief overview of the 16-channel audio splitter and hand mapping of receptive field will then be described. Parameters of all visual stimuli used to characterize neuronal response features will be described in Section 2.4.4.

2.4.1 Monitor setup

Stimuli were displayed on a Samsung SyncMaster 2233RZ monitor (22" LCD monitor, with 120 Hz refresh rate). This type of monitor was chosen based on the advantages of LCD monitors with luminance accuracy and low electromagnetic emission. More importantly, this specific model of LCD monitor has been reported to possess temporal reliability for visual research (Wang and Nikolic, 2011). The monitor was gamma corrected and stimuli were displayed on a scale of 255 pixels. The mean luminance (127 pixels) was 46.93 cd/m^2.

The monitor was placed 25 cm from the animal, the same distance as used in other electrophysiological studies in mouse visual system (Niell and Stryker, 2008; Piscopo et al., 2013). The monitor centre was set at the same height as mouse's eye, meaning the viewing angle was approximately ~50 deg on each side, ~30 deg above and below. This height of the monitor was fixed. The monitor's original position was set as a plane perpendicular to the mouse's eye. The monitor was mounted on a custom-made 90 deg rotate rail (with radius of 25 cm). This rail enabled smooth and stable monitor rotation during recording to cover visual field of as many cells as possible. This smooth rotation had advantages in minimizing electrode shift or mechanical damage, and in maintaining visual stimuli at the same distance to the animal's eye. Another monitor (HP Compaq LA2205wg) of same dimension was mirrored for the purpose of hand mapping of receptive field.

To obtain synchronized stimulus impulses, a photodiode circuit board was custom made. Primarily, a sensor (LCM555CN) was attached on one bottom corner of the Samsung monitor where a small square flashed whenever stimulus changed. Digital output of the photodiode was sent to the data acquisition system, to precisely indicate start and end time of each stimulus trial and also help to double check that no single frame was dropped.

2.4.2 16-channel audio splitter

A 16-channel audio splitter was custom manufactured to work with the data acquisition system. Its main purpose was to enable us to listen to real-time cell firing activity, which was of significant importance in hand mapping of receptive field. In addition, it served as a direct indicator of cells' responses when LFPs were recorded, when it was impossible to observe spikes on-line from Spike 2.

The main component of the audio splitter was a 16-channel-Multiplexer (MPC506AP). Together with amplifiers (LM2902N), buffers (1N926B-diode) and four binary switches (Figure 2.3), the audio splitter served easy selection of one specific channel among 16 channels to hear simultaneously spiking activities of cells from that channel. Additionally, it featured threshold adjustment depending on the actual signal-to-noise ratio and no additional noise/artefacts were generated.

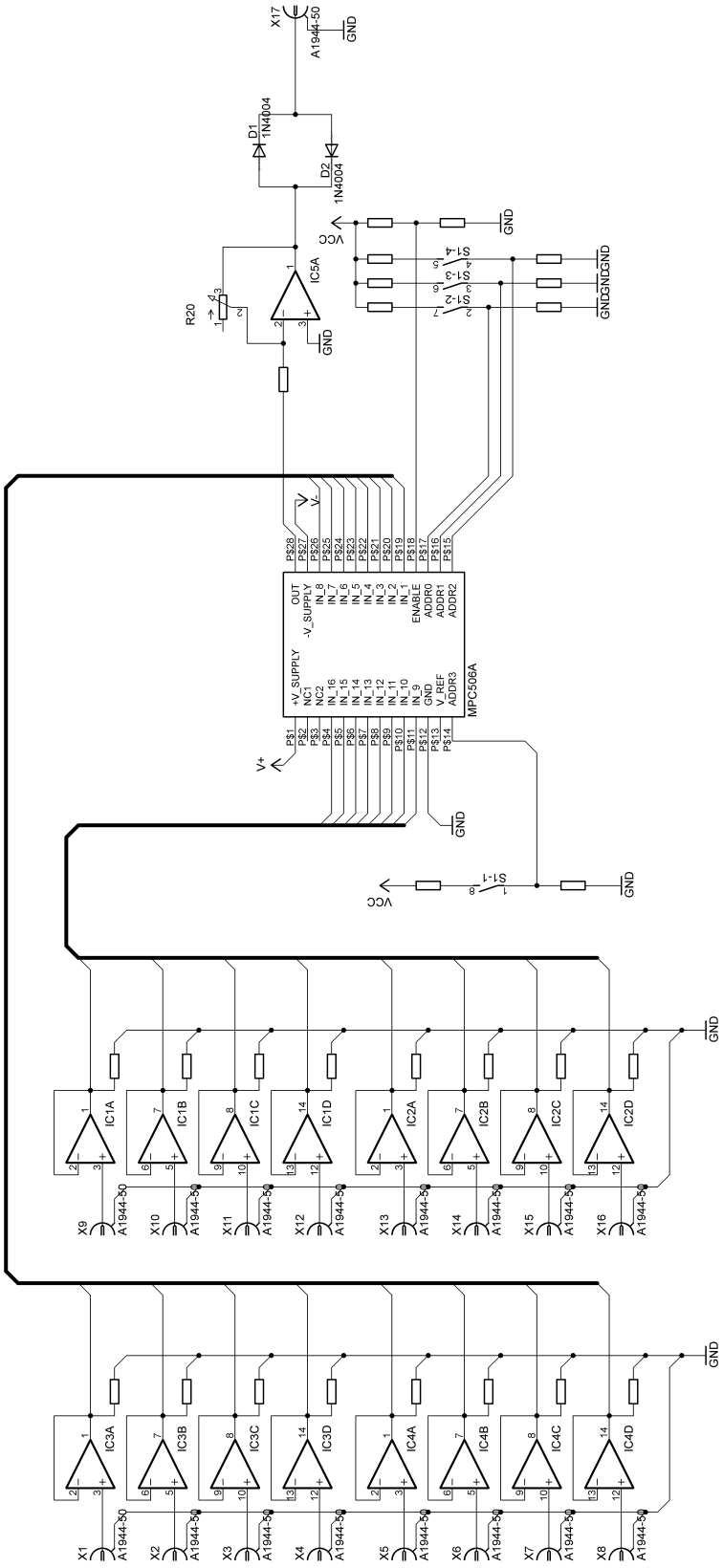

Figure 2.3 Schematic of 16-channel audio splitter. It consists of a 16-channel multiplexer, amplifiers, buffers and binary switches. This audio splitter is compatible with the data acquisition system.

2.4.3 Hand mapping of receptive field

Hand mapping of visual receptive field, a classical protocol in visual neuroscience research, served as an electrophysiological prerequisite for this project. First, it functioned as a verification of electrode's precise targeting in LGN before stimulus presentation. Second, the monitor's position could be adjusted accordingly if receptive fields of a few channels were found on the edge of the monitor. In most of the recordings, hand mapping was carried out in 2~3 nonadjacent channels and the whole procedure took approximately 20 min.

Two types of stimuli were applied for hand mapping: Expo (an interface of visual stimuli, developed by Peter Lennie at New York University, https://sites.google.com/a/nyu.edu/expo/) and customized MATLAB based hand-mapping software. One channel with a high signal-to-noise ratio and robust visual triggered responses was selected from the audio splitter. Then a ~15 deg white/black square was chosen from Expo and moved manually across the monitor, stopping when stimulus related responses could be identified from the audio splitter. Stimulus' information (size, position) was then recorded. The second mapping software was applied to feature small-step movement in any direction and white-black flip. These features provided more specific and detailed receptive field information. A video of receptive-field hand mapping could be found in this link.

(https://www.youtube.com/watch?v=a5wxqru70gU&feature=youtu.be).

2.4.4 Visual stimulus

All stimuli for electrophysiological characterization purpose were presented with Flymouse. The Flymouse was customized from a MATLAB Psychophysics Toolbox based interface developed by Motion Vision Group at Uppsala University (http://www.flyfly.se/about.html).

A battery of stimuli was generated to characterize a wide category of response features in mouse LGN. We presented sinusoidal monochromatic gratings covering the full extent of the monitor. Parameters of each grating are listed in Table 2.1. Apart from sinusoidal gratings, flicker and contrast noise movie were also presented to LGN cells.

Flicker: Full-screen black or white flashes with duration of 600 msec were presented. Each black and white session was interleaved with a total of 800 repetitions.

Contrast-modulated noise movie: we applied the same stimulus as the one used in published papers from Niell's group (2008, 2013) and implemented into our Flymouse interface. It was a spatiotemporal movie multiplied by a 0.1 Hz sinusoidally varying contrast modulation to prevent response adaptation. The movie was inverted from a random three-dimensional spectrum in the Fourier domain, with spatial frequency spectrum drop off as $A(f) \sim 1/(f+fc)$ ($fc=0.05$ c/deg) and with a cutoff at 0.16 c/deg, and temporal frequency spectrum flattened with a sharp low-pass cutoff at 10 Hz (Figure 2.4). Each session began with a 5 min presentation of grey background and 5 min of the movie. The whole session was presented four times with a total duration of 40 min, which was enough to trigger sufficient number of spikes (Niell and Stryker, 2008; Piscopo et al., 2013).

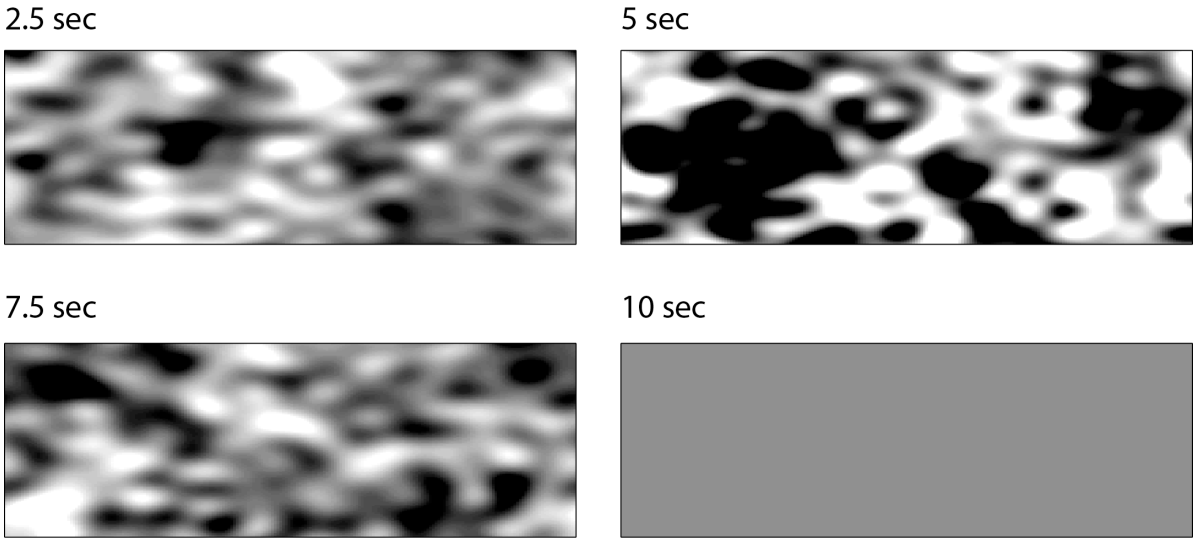

Figure 2.4 Contrast noise movie stimulus. From top left to bottom right: segments taken from 2.5, 5, 7.5 and 10 sec from one session.

Table 2.1 Stimulus information of sinusoidal gratings.

Stimulus / Parameters	**Spatial Frequency**	**Temporal Frequency**	**Contrast**	**Direction**
spatial frequency (c/deg)	0.02; 0.03; 0.04; 0.06; 0.08; 0.12; 0.16; 0.32; 0.64; 0.96	0.03	0.03	0.03
temporal frequency (Hz)	1	0.3; 0.4; 0.6; 1.2; 1.6; 2.4; 3.2; 4.8; 6.4; 9.6	1	1
Contrast (%)	98.0	98.0	10.0; 19.6; 39.2; 58.8; 78.4; 98.0	98.0
Direction (deg)	0	0	0	0; 45; 90; 135; 180; 225; 270; 315
total number of trials	60	40	60	48
duration of each trial (sec)	7	14	7	7
number of repeation of each trial	6	4	10	6
Pseudorandom sequence	Yes	Yes	Yes	Yes
1s blank screen before & after each trial	Yes	Yes	Yes	Yes

2.5 Data processing

Firstly, in this section, methods of data filtering and single-unit inclusion criteria will be shown. Subsequently, analysis protocols to characterize each response property will be described.

2.5.1 Spike-sorting and cell inclusion

Histology and confocal imaging were performed after recording (detailed procedures and results described in Chapter 5). If electrode sites were found outside the edge of LGN, then units from those sites were excluded from subsequent analysis.

Single-units were identified and isolated by custom routines in MATLAB (MathWorks) and Klusta-Kwik (Harris et al., 2000). With Klusta-Kwik, continuous raw data was first band-pass filtered, and spikes were detected based on voltage thresholds and spike waveforms, relevant features of the spike shapes were then extracted. This was followed by clustering, which was to group clusters with similar features. This was the final step of manual supervision and validation, and was performed on Klusters (a cluster cutting application) through all channels.

Quality of single unit separation was checked based on clear refractory period, cross-correlogram and discriminated feature vectors with other clusters (Figure 2.5).

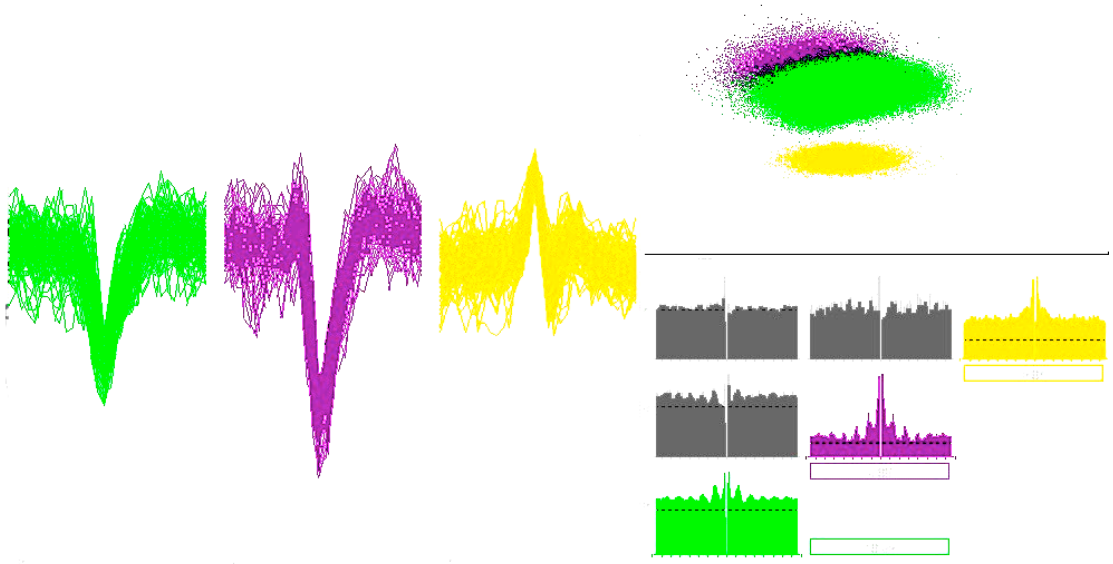

Figure 2.5 A representative result of manual spike sorting with Klusters of one channel that recorded from mouse LGN. Left panel is wave shape of three individual clusters. Top right panel shows amplitude feature. Bottom right panel shows their cross-correlgrams (in grey) and auto-correlgrams (green, purple and yellow correspondingly), the dashed lines represent individual cell's spontaneous response level. Each of the three clusters displays a clear refractory period. Although there was some overlap between green and purple clusters in amplitude, their waveform features were different.

In addition, stability of single units was assessed to exclude cases where electrode shifts or other mechanical damages occurred: units suffered from significant amplitude or waveform changes, or stopped responding during stimuli presentation. Such events were all eliminated from the data pool. Subsequent analyses were carried out with custom-written MATLAB routines.

2.5.2 Data analysis

Spontaneous and evoked firing rates: Spontaneous firing rate was calculated by averaging responses within all presentations of blank screen at mean luminance across sinusoidal gratings. Evoked activity level was measured as the maximal responses to grating stimuli.

Receptive field properties: Receptive field structures were computed based on contrast noise movie stimulus. Total number of spikes was firstly calculated and binned in response to each stimulus frame. Then spontaneous activity was removed from the overall response.

Spike triggered averaging (STA) was used to extract receptive field information. The STA procedure first involves detecting and collecting frames where a spike was elicited at a certain temporal offset, and follows with averaging and normalizing those frames to create a map. In the particular example displayed in Figure 2.6A, checkerboard frames that triggered

responses were collected (named as a, b etc.). The colour map in the bottom row illustrated the progression of computational normalization with an increasing number of checkerboard frames (1, 2, 5 till 100), and consequently an ON-centre cell was depicted. Receptive field reconstruction was finalized by fitting data to the two-dimensional (2D) Gaussian function, as sketched in Figure 2.6B, the narrower positive region in red represented the excitatory area, whereas the wider negative region in blue was the inhibitory area, the interaction strengths of these two shown in black and formed the classical Mexican Hat receptive field profile for an ON- centre cell (Jeffries et al., 2014).

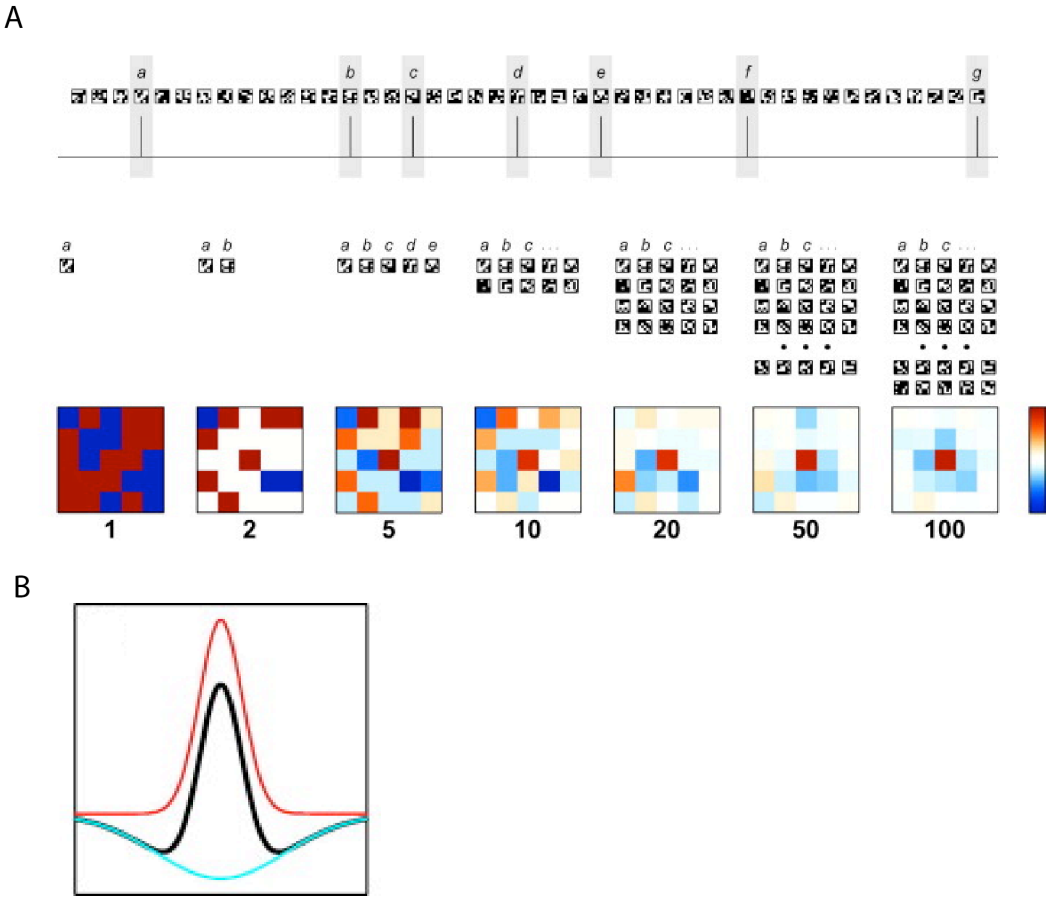

Figure 2.6 Receptive field computation. A. Diagram of STA method. Top row: Stimulus frames (5*5 checkerboard) that elicited neuronal responses were detected and named as a, b, c etc. Middle and bottom rows: Detected frames were averaged and normalized. The colour map displayed a transition as number of frames increased from 1 to 100. An ON-cell was computed from the example. B. The classical Mexican Hat profile. This was generated from the 2D Gaussian function. The narrower region in red shows the excitatory area, and the broader region in blue shows the inhibitory area. The black represents the sum of these two and forms the centre-surround structure for an ON-cell. This figure is adapted from published work from Jeffries et al. 2014.

To characterize responses to drifting gratings, a fast Fourier transform was applied to the data and converted them to response amplitudes (spikes/s) and phases (in degrees) of harmonics of stimulus modulation frequency (Grubb and Thompson, 2003).

Spatial frequency tuning characterization: Spatial frequency tuning properties were assessed by presenting vertical drifting gratings of various spatial frequencies ranging from 0.02 to 0.96 c/deg. Gratings were presented at 1 Hz temporal frequency and 98% contrast. Spatial frequency curve (spatial frequency versus F1 response amplitude) was fitted with a difference of Gaussian (DoG) equation (Rodieck, 1965; So and Shapley, 1981).

$$R(\nu) = b + (k_c - b) \cdot (e^{-(\pi \cdot r_c \cdot \nu)^2} - k_s \cdot e^{-(\pi \cdot r_s \cdot \nu)^2}) \quad (1)$$

where R is F1 response amplitude, ν is spatial frequency, b is baseline response amplitude, k_c and k_s are the areas under the receptive field centre's and surround's Gaussian function respectively, r_c and r_s are radii of the centre and surround Gaussian functions respectively, at the point each mechanism reaches 1/e of its peak.

Also, a cell's preferred spatial frequency and cutoff (taken as the high spatial frequency at which response amplitude reached 1% of its maximum) (Grubb and Thompson, 2003) were calculated directly from the DoG fitted curve because the curve could provide a smooth fit to the raw data.

Temporal frequency tuning characterization: Temporal frequency tuning properties were calculated with sinusoidal gratings of a series of temporal frequencies from 0.3 to 9.6 Hz, at 0.03 c/deg spatial frequency and 98% contrast. The tuning curve (temporal frequency versus F1 response amplitude) was fitted with a theoretical two half-Gaussians function (Grubb and Thompson, 2003).

$$R(\omega) = b_1 + (a - b_1) \cdot e^{-[(p-\omega)/s]^2} \; for \; \omega < p \quad (2)$$

$$R(\omega) = b_2 + (a - b_2) \cdot e^{-[(p-\omega)/s]^2} \; for \; \omega > p \quad (3)$$

where R is F1 response amplitude, b_1 and b_2 are the baselines on the low- and high-frequency sides of the curve respectively, a is the response amplitude at optimal temporal frequency, ω is temporal frequency, p is peak temporal frequency, s is the Gaussian spread.

A cell's optimal temporal frequency, $high_{50}$ and low_{50} (representing the high and low temporal frequencies at which response amplitudes were 50% of its maximum respectively), and tuning bandwidth (difference between low_{50} and $high_{50}$) were readily accessible from the fitted tuning.

Contrast sensitivity property: Contrast sensitivity property was examined by showing cells with drifting grating at 0.03 c/deg spatial frequency and 1Hz temporal frequency with varying contrasts. Plots of stimulus contrast versus F1 cell response amplitude were fitted with a hyperbolic function (Albrecht and Hamilton, 1982).

$$R(c) = b + (R_{\max} - b) \cdot \frac{c^n}{c^n + h^n} \tag{4}$$

where R is F1 response amplitude, c is contrast, $R_{\max}$ is maximum response, h is the contrast at which R reached 50% of $R_{\max}$, n is rate of change.

We measured the contrast gain as the slope of a tangent to the curve where cell response amplitude was 20% of its value at 100% contrast. In addition, we calculated C_{50} that was viewed as the contrast at which response amplitude fell to 50% of its value at 100% contrast.

DS/OS property: Stimulus applied was a drifting grating moving at eight evenly spaced directions, at 0.03 c/deg spatial frequency, 1 Hz temporal frequency and 98% contrast. Spontaneous activity was first subtracted from the overall responses. DS/OS preference and index were calculated with standard metric based on the circular variance.

$$\frac{\Sigma F(\theta) e^{2i\theta}}{\Sigma F(\theta)} \textit{ for OSI and } \frac{\Sigma F(\theta) e^{i\theta}}{\Sigma F(\theta)} \textit{ for DSI} \tag{5}$$

DS/OS index (DSI/OSI) is given by the absolute amplitude of this value, and the complex phase (or half the complex phase for orientation selectivity) gave the preferred orientation/direction. Cells with DSI >0.33 or OSI >0.6 were defined as DS or OS cells.

Linearity: Linearity was computed from the same stimulus characterizing spatial frequency tuning properties. Spontaneous activity was first subtracted. The discrete Fourier transform was then applied to a cell's averaged responses to drifting gratings at various spatial frequencies. F1/F0 was computed subsequently, which is the ratio of the first harmonic (response at the drift frequency) to the 0^{th} harmonic (mean response) (Skottun et al., 1991).

A high F1/F0 ratio indicates that the cell responds to sinusoidal grating with a sinusoidal output at the stimulus temporal frequency. Contrastingly, a low F1/F0 ratio represents a relatively continuous firing throughout the presentation of the grating. We define F1/F0=1 as the threshold for linearity.

Response latency was measured from responses to the drifting grating moving at various spatial frequencies and full-field flicker stimuli. The method used here was referred to as peak latency, referring to the latency to the peak of the neuronal responses in the PSTH that had 1-msec bins and included responses within stimulus presentations.

Transient/sustained property: This feature was characterized from neuronal responses to full-screen black/white flickers. Poststimulus time histogram (PSTH) was plotted from each cell's responses to repetitions of flickers. Transient/sustained index was calculated as the ratio of average response amplitude from cell response latency (lat) till 50 msec after response latency (lat+50msec) to response amplitude from lat+50msec on till end of stimulus duration. Sustained cells were categorized when the transient/sustained index fell below 1, indicating that cell responses were maintained over the entire duration of stimuli. Whereas transient cells were units with the transient/sustained index above 1, representing cells responding to sudden appearance of stimuli and activities were grouped after the onset of stimuli.

Finally, only cells with receptive fields reconstructed from STA technique were included in data pool for subsequent analysis.

2.5.3 Statistical analysis

Normality was assessed with a D'agostino-Pearson test in datasets that were large enough ($n>30$). Normal distribution data was described with mean ± standard error of the mean (S.E.M.) and compared with parametric test. Non-normal distribution data was presented in the format of median (25 percentile, 75 percentile), and the Mann-Whitney-Wilcoxon test was used for comparison within two groups, while for non-parametric comparison within three or more groups, Kruskai-Wallis test was applied. All comparison tests were two-tailed, and the level of significance was set at 0.05 unless specified. In figures, **** signifies $P<0.0001$, *** $P<0.001$, ** $P<0.01$, *$P<0.05$.

CHAPTER 3

Single cell response characterization in mouse LGN

3.1 Introduction

This chapter aims to provide comprehensive characterization of single cell response properties in mouse LGN, both in aspects of response types and anatomical volume. The first goal was to cover a broad range of response parameters, which was largely motivated by highly developed genetic techniques that has made the mouse a prime candidate to study visual information processing (Brecht et al., 2004; Luo et al., 2008). Along the visual pathway, LGN lies in a strategic position to actively play a role in information transmission from the retina to the cortex. However, studies carried by Grubb and Thompson (2003) and, more recently, by Piscopo et al. (2013) have served as the two major quantitative analyses available in this field. Therefore, a thorough electrophysiological investigation will enhance our understanding of the functionality of this nucleus. Our second goal was to explore if certain response type displays a regional preference within mouse LGN. This was prompted by the finding that the DS/OS cells, newly characterized in mouse LGN, were restricted to the area where DSRGCs projected (Piscopo et al., 2013). It will therefore be informative to further probe from a larger dataset the preferred directions of motion and precise cell locations of units that are selective to direction/orientation, and also evaluate if other response features are correlated with cell locations.

This chapter starts with a summary of the experimental procedure in Section 3.2 to address the abovementioned aims. Subsequently in Section 3.3, I firstly provide results on individual response property characterization, including receptive fields, spatial and temporal frequency tuning properties, contrast sensitivity, response latency, selectivity to direction/orientation and linearity. Then I present findings on several types of response properties, such as ON-

/OFF-, and transient/sustained, and those markedly different are described. Finally, by taking advantage of the LGN volume (described in Chapter 5) to map cell position, the location of each cell was categorized to belong to the anterior, middle or posterior LGN depending on the coordinate of the electrode that the cell was recorded from. Subsequently, we explored whether each specific response property was strongly correlated with the cell location. In addition to confirming many results from previous mouse LGN characterizations (Grubb and Thompson, 2003; Piscopo et al., 2013), we describe several novel response features: high-pass and low-pass response profiles in temporal frequency tuning curves. Furthermore, we report the prevalence of nonlinear cells and DS/OS cells in mouse LGN. Interestingly, DS/OS cells do not display regional bias within LGN. We also observe distinct response features carried by ON-/OFF- and transient/sustained subtypes that may imply parallel projections.

In Section 3.4, I provide a compendium of major findings, and relate the findings with other studies in the visual system of both mice and other species. Furthermore, I conclude this section with functional implications of mouse LGN at single cell level.

3.2 Methods

Experimental protocols were as described in Chapter 2. Extracellular recordings were made from isoflurane-anesthetized adult mice with 16-channel MEAs. A series of visual stimuli was presented to the animal for the purpose of fully characterizing its response features. Histology was carried out at the end of each experiment to recover electrode sites. Only sites successfully verified to be within LGN were included for subsequent analysis. Specifically, the electrode site was categorized to be located within the anterior, middle or posterior LGN based on the LGN volume (protocols and results presented in Chapter 5). Data analyses were performed off-line.

Normality of data (sample size >30) was assessed with the D'agostino-Pearson test. Data that had a normal distribution was described with mean ± S.E.M. and compared with the parametric test. Data that did not show normal distribution were presented in the format of medians with interquartile ranges, and the Mann-Whitney-Wilcoxon test was used for parameter comparison within two groups, whereas Kruskai-Wallis test was applied for non-parametric comparison within three or more groups. The level of significance was set at 0.05 unless stated otherwise in the text.

3.3 Results

In this section, a general description of the data obtained and analysed, followed by characterization of individual response features will be provided. Subsequently, features between ON- and OFF- centre cells, particularly those were statistically different, will be presented. Finally, in addition to the overall characterization, data recorded from the anterior, middle and posterior LGN will be compared separately to explore topographical-functional relevance.

3.3.1 Recording and data filtering

For each animal, the number of penetrations was limited to three to maintain viability of brain tissue. In total, from 20 mice 28 penetrations successfully targeted LGN. Single unit detecting and manual clustering were carried out only on channels that were histologically confirmed to reside within LGN. Generally, one to three single units with stable and constant responses throughout stimulus presentation could be acquired from one channel.

There were 189 well-isolated single units that displaying robust centre-surround receptive fields reconstructed from STA technique, varying from 3 to 12 single units across recordings. Among them, a small subset of cells (4/189, 2.1%) was not responsive to any episodic drifting grating stimuli. They were therefore excluded from subsequent analysis. Consequently, 185 single units from 20 mice were used to characterize response features.

Analysis of response properties was carried out on all units in the dataset. Taking account of location of electrode penetration in LGN that was confirmed by histology (Chapter 5), neuronal locations were categorized into the anterior, middle or posterior LGN and 41, 129 and 15 units were obtained from these three sub-locations respectively. Functional properties across sub-locations were also compared to investigate their relationship to anatomy and results are described later in this section.

3.3.2 Individual response property of mouse LGN

3.3.2.1 Spontaneous and evoked activities

Spontaneous activity was averaged from responses to blank (grey) screens at mean luminance (46.93 cd/m^2) in the absence of stimuli, whereas evoked activity was measured as the maximal responses to grating stimuli.

Distributions of spontaneous and evoked firings are illustrated in Figure 3.1A. Most of the single cells (149/185, 80.5%) fired at a frequency below 5 Hz during spontaneous condition, while the evoked response covered a broader range and went as high as 35 spikes/s. The evoked firing rates of majority of the cells (120/185, 64.9%) were above 5 spikes/s. Across the population, the median with interquartile ranges of spontaneous firing activity was 2.0 (0.9, 4.3) spikes/s, and the median with interquartile ranges of evoked response was 7.3 (3.7, 13.0) spikes/s. The evoked response was higher than the corresponding spontaneous activity of each LGN cell in the dataset (Figure 3.1B). Statistically, the evoked activity was approximately 125% higher than the baseline response (y=2.25x, 95% confidence interval 2.08~2.42, with R^2=0.3).

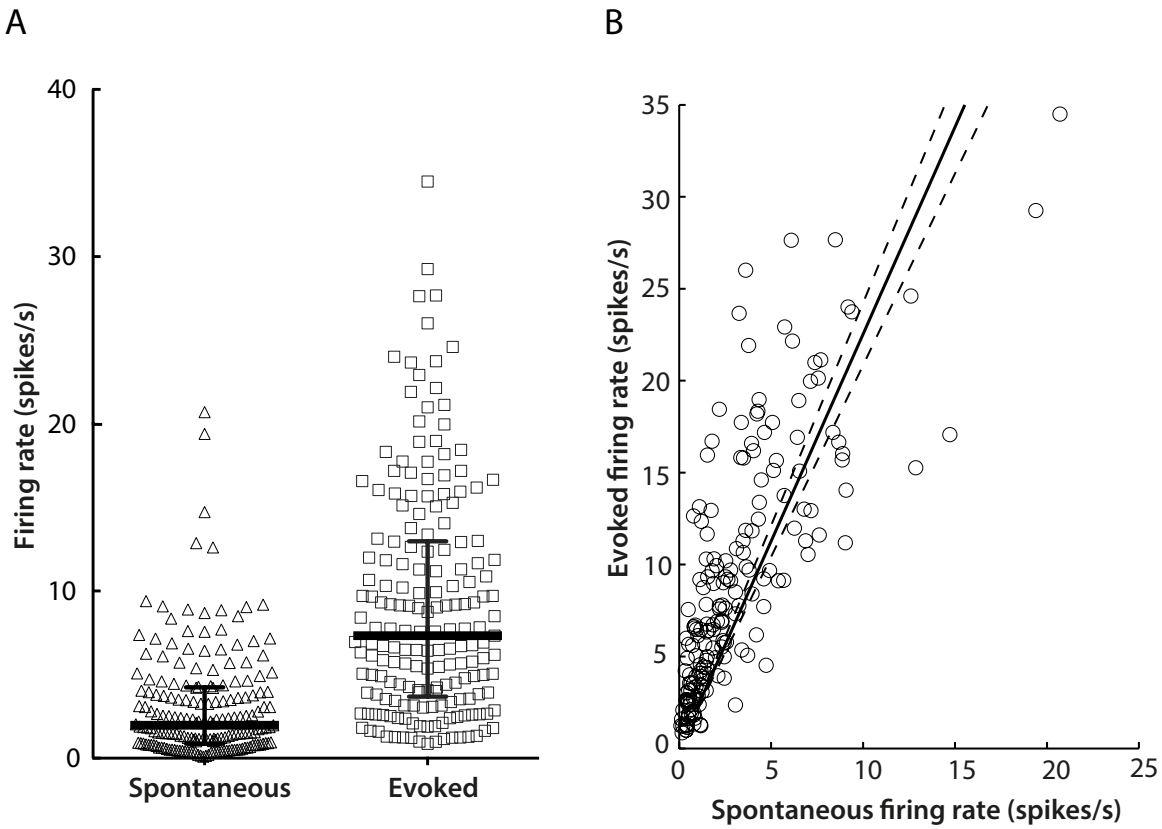

Figure 3.1 Spontaneous and evoked firing rates of mouse LGN neurons. A. Distributions of spontaneous (triangle) and evoked (square) firing rates of single cells. Medians with interquartile ranges (solid lines) are 2.0 (0.9,4.3) spikes/s and 7.3 (3.7,13.0) spikes/s for spontaneous and evoked firing rates. B. Correlation of spontaneous (x) and evoked (y) responses is y=2.25x, 95% confidence interval 2.08~2.42. R^2=0.31.

3.3.2.2 Centre-surround receptive field structure

LGN receptive field profiles were extracted from responses to contrast noise movie stimulus with STA technique (Section 2.4.4 and 2.5.2). All cells included in the dataset displayed classical centre-surround receptive field structures similar to previous LGN studies (Hubel and Wiesel, 1966; Grubb and Thompson, 2003).

In all the 185 units, single cells were separated into ON- (n=90; 48.6%) or OFF- (n=95; 51.4%) subclasses based on their STA polarities. Figure 3.2B demonstrates an example of STA spatial receptive fields from one recording. Receptive fields of seven simultaneously recorded neurons are illustrated, white for ON- and black for OFF-cells, with their corresponding waveforms shown in Figure 3.2C. The relative location and size of each neuron's receptive field are noticeable in comparison to the grey background that represents the monitor. Combined with histological visualization of the electrode track (Figure 3.2A), it is observable from this specific recording that these neurons displayed spatial alignment with the electrode configuration to a great extent: receptive field locations occupied the middle of

the monitor and moved towards the top as channels they represented moved more superficial in LGN.

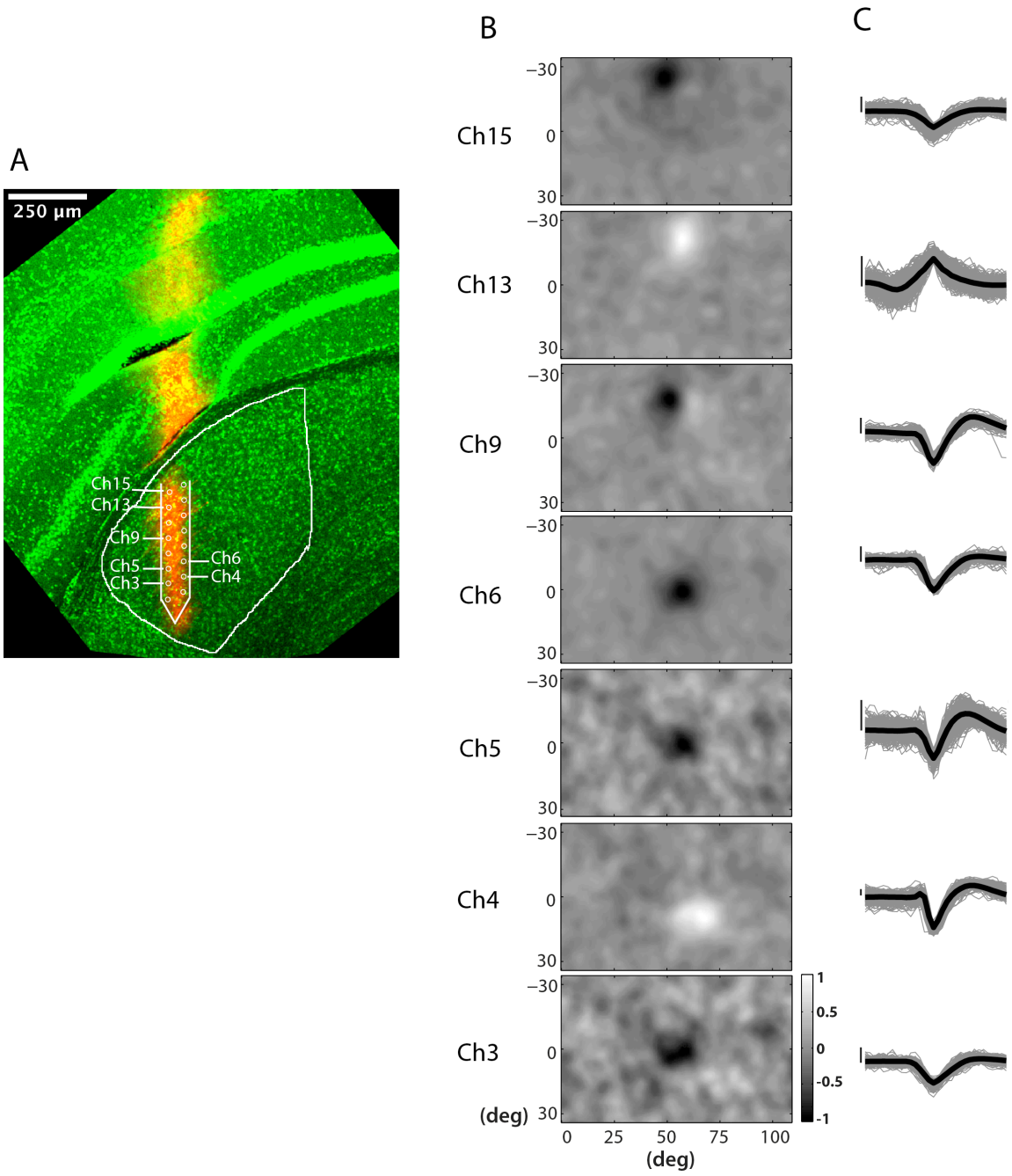

Figure 3.2 An example of spatial receptive field profile from one single recording. A. Confocal image of coronal sectioned brain slice (200 µm) from the same animal. The electrode was dyed with DiI/DMSO solution (red track), and the slice was stained with DAPI (Diamidino-2-phenylindole, displayed as green). The LGN boundary and electrode trace are outlined in white. Particularly, electrode sites that corresponded to the seven neurons recorded in (B) are illustrated with numbers. B. Two-dimensional profiles of centre receptive fields from seven units reconstructed with STA technique. The colour map is shown at the bottom right. The channel that each single unit recorded from is indicated on the left, and corresponds to the marks in the histological image (A). C. Waveforms of corresponding neurons shown in (B). The black lines on left side indicate 25 mV in length.

Figure 3.3A presents the location of centre receptive field of all isolated units within the monitor dimension, in both formats of the single cell (main panel) and population distributions (histograms at bottom and left). It could be observed that centre receptive field of majority of the cells locate within -30~0 deg (Y axis) and 40~100 deg (X axis) of the monitor, while the bottom centre displays a particular higher density (Figure 3.3A).

For each cell, the radius of centre receptive field was calculated along both horizontal- and vertical- axes. Radius was obtained by fitting the data to the DoG function and measured as the absolute value of response amplitude above 0.8. Cells with the radius ratio (taken as the radius on horizontal axis to the radius on the vertical axis) fell into the range between 0.7~1.3 were defined as circular cells, while those outside this range were categorized as non-circular cells (Figure 3.3B). Based on this criterion, 75.1% (139/185) units in the dataset displayed circular receptive fields. The radius was measured as the average between horizontal- and vertical-axes from cells with circular receptive fields. Within this population, there were 3.6% (5/139) units with receptive field radius exceeding 10 deg and going up to 11.5 deg as the maximum, and the median with interquartile ranges of receptive field centre radius was 6.5 (5.3, 8.1) deg.

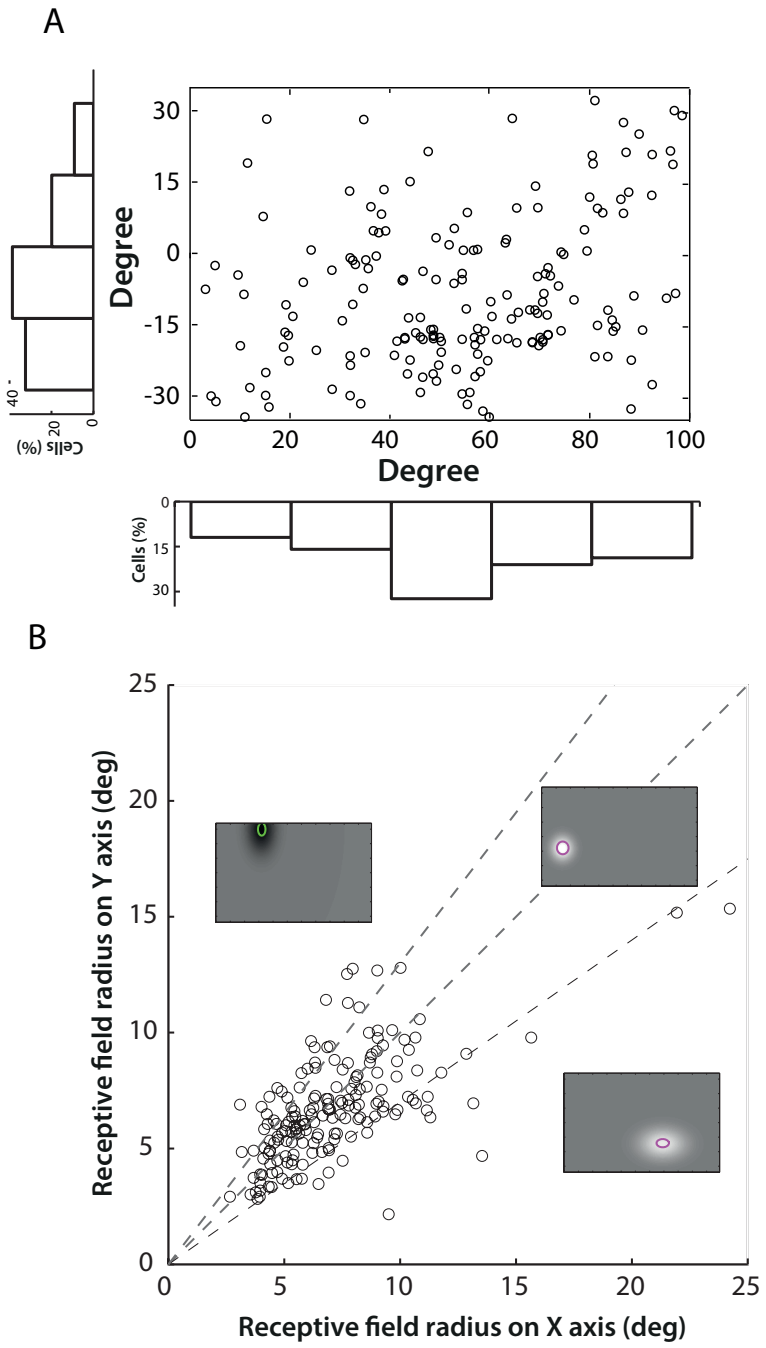

Figure 3.3 Receptive field centre location and size of the population dataset. A. Location of receptive field centre of all isolated single units. The main panel displays the receptive field location of each cell within the dimension of monitor in visual degree, and the histograms at left and bottom represent distributions of receptive field location on the vertical and horizontal axis respectively. B. Correlation of receptive field centre radius measured along vertical and horizontal axes. Radius was obtained by fitting the data to the DoG function and measured as the absolute value of response amplitude above 0.8 (receptive field size indicated as red for ON- centre cells and green for OFF- centre cells). Radius ratio was calculated as the radius on horizontal axis to that on the vertical axis. Cells with the ratio fell into the range between 0.7~1.3 (two dash lines, with the middle dash line indicating 1) were defined as circular cells, while those outside this range were categorized as non-circular cells. Three single-cell representatives shown were cells that fell into the three categories respectively: larger size on the vertical axis, circular and larger size on the horizontal axis.

3.3.2.3 Spatial frequency tuning properties

Spatial frequency tuning properties were calculated from neuronal responses to gratings of various spatial frequencies and fitted with a curve generated from the DoG equation (Rodieck, 1965; So and Shapley, 1981) (see Section 2.5.2). Within the population, 92 cells were well fitted and included in subsequent spatial frequency tuning property analysis.

At single cell level, the LGN cells generally display three types of spatial frequency tuning curves. The top representative shown in Figure 3.4A that defined as "low pass" filtering represents the most common response type: cell activity progressively decreased as the spatial frequency increased, starting from the lowest spatial frequency value. However, we could not distinguish whether cells in this category were truly responding as low pass filters or they actually preferred extremely low spatial frequency tunings (lower than 0.02 c/deg). Apart from this typical response, the middle representative in Figure 3.4A reveals a "band pass" response type: cell activity was maximal at approximately 0.04 c/deg and decreased rapidly as spatial frequency further increased. Moreover, the bottom representative in Figure 3.4A illustrates an example of a cell that responded best to far higher spatial frequency, over 0.10 c/deg. Particularly, the preferred spatial frequency of this cell was 0.15 c/deg with cutoff frequency (taken as the high spatial frequency at which response amplitude reached 1% of its maximum) at 0.45 c/deg.

Observed from the population distribution in Figure 3.4B, LGN cells preferred very low spatial frequency, half of the neurons in the dataset responding as "low-pass" filtering. The cutoff frequency, which represents the highest spatial frequency that LGN cells are capable of resolving, was low in mice. The cutoff frequency of majority of cells was below 0.40 c/deg (Figure 3.4C), and its median with interquartile ranges was 0.19 (0.11, 0.33) c/deg.

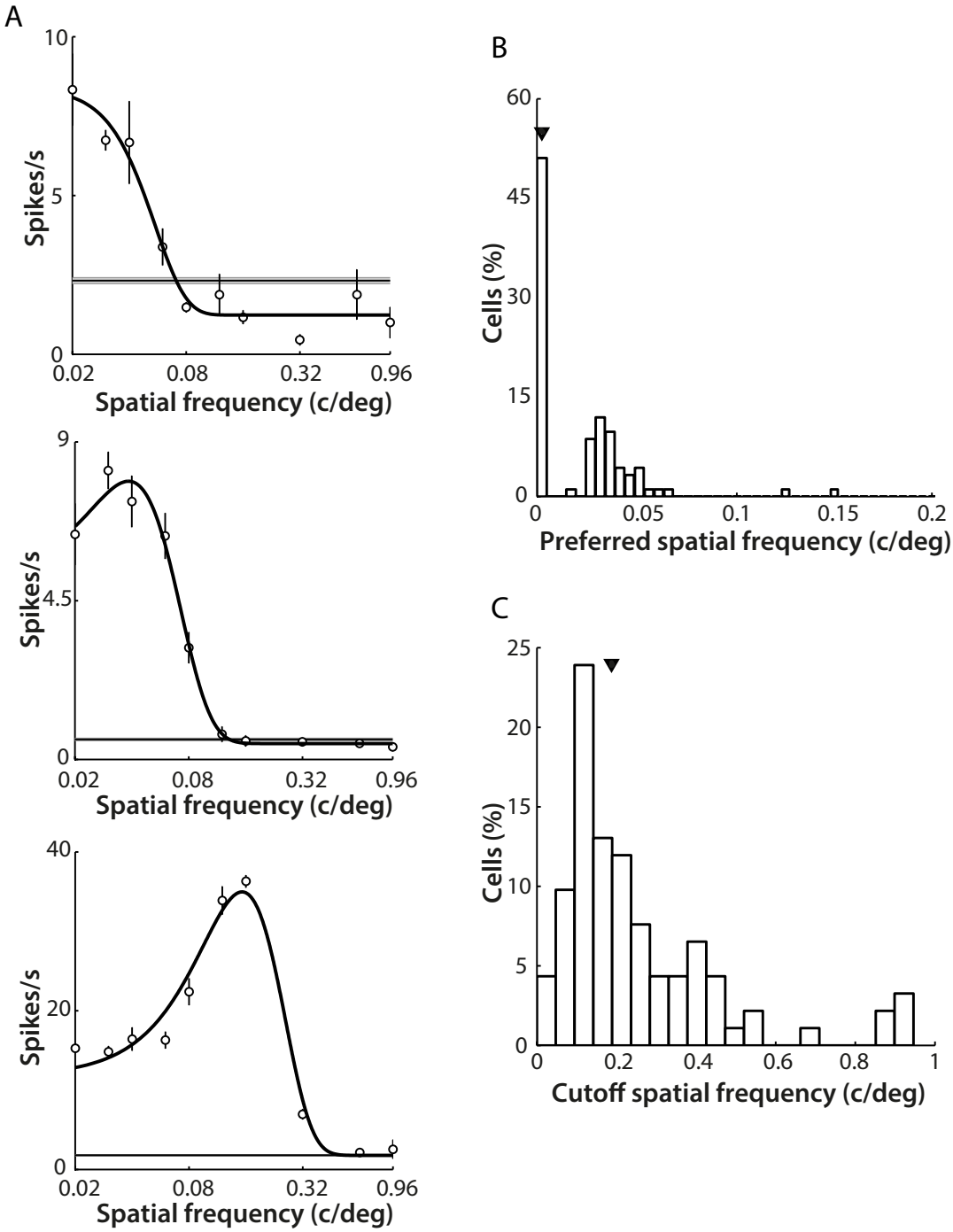

Figure 3.4 Spatial frequency tuning properties of mouse LGN cells. A. Examples of spatial frequency tuning of single cells. Open circles represent mean firing rates with S.E.M. across repetitive presentations of drifting gratings. Black curves show the best fits of these raw data to a DoG function (Rodieck, 1965; So and Shapley, 1981). Grey areas represent S.E.M. of spontaneous activity, with thinner lines indicating mean values. Note logarithmic scale of X-axis. Top, the most typical response as a cell firing in a "low-pass" pattern: increasing spatial frequency corresponded with decreasing activity; Middle, a representative cell responding in a "band-pass" pattern; Bottom, a representative with preferred spatial frequency over 0.10 c/deg. Parameters for all three units: top: cutoff 0.10 c/deg; middle: preferred 0.04 c/deg, cutoff 0.14 c/deg; bottom: preferred 0.15 c/deg, cutoff 0.45 c/deg. B. Distribution of preferred spatial frequency. The median (arrow) with interquartile ranges is 0.00 (0, 0.04) c/deg. C. Distribution of cutoff spatial frequency. The median (arrow) with interquartile ranges is 0.19 (0.11, 0.33) c/deg.

3.3.2.4 Temporal frequency tuning properties

Temporal frequency tuning properties were ascertained by fitting data to a 2-Gaussian-halves equation (Grubb and Thompson, 2003) (detailed in Section 2.5.2). 57 units fitted well across the dataset and were included in the analysis.

The temporal frequency tuning of individual LGN cells could be categorized into three main subtypes by visual inspection: low-pass, high-pass and band-pass. The first type referred to cells that responded in a similar pattern as the low-pass type in the spatial frequency tunings. In these cells, no definite "optimum" temporal frequency could be identified, and the response amplitude at extremely low temporal frequencies (<0.6 Hz) remained at a high plateau level (main panel in Figure 3.5A); yet in some cells, as exemplified in the main panel in Figure 3.5B, the response increased to its maximum and stayed at the plateau as temporal frequency went higher, which was interpreted as high-pass responsive type. Figure 3.6A shows a representative of the most typical band-pass response: firing activity increased steadily as the temporal frequency of drifting gratings increased, and responses peaked at around 3~4 Hz and decreased rapidly as temporal frequency increased further.

Among the population of neurons, there were three out of 57 cells (5.3%) that responded as "high-pass" filters, while two cells (3.5%) responded as "low-pass" filters and the rest (52/57, 91.2%) responded in "band-pass" pattern. $High_{50}$ and low_{50}, referred to the high and low temporal frequencies at which response amplitude was 50% of its maximum, were calculated for low-pass and high-pass filtering cells respectively. $High_{50}$ of the two low-pass units were 1.1 and 2 Hz (inset panel in Figure 3.5A), whereas low_{50} of the three high-pass responsive cells were 1.4, 2.0 and 3.1 Hz (inset panel in Figure 3.5B).

For the band-pass subpopulation, the mean ± S.E.M. of $high_{50}$ and low_{50} were 7.1 ± 0.2 Hz Hz and 1.0 ± 0.1 Hz (Figure 3.6B and C). The tuning bandwidth was calculated from the difference between $high_{50}$ and low_{50} of each cell, it distributed between 4.0 Hz ~ 7.0 Hz in most cells, with a mean ± S.E.M. of 5.5 ± 0.2 Hz (Figure 3.6E). Seen from the population distribution in Figure 3.6D, the preferred temporal frequency of band-pass filtering cells was in the range of 2.0 ~ 5.5 Hz, and its mean ± S.E.M. was 3.4 ± 0.1 Hz.

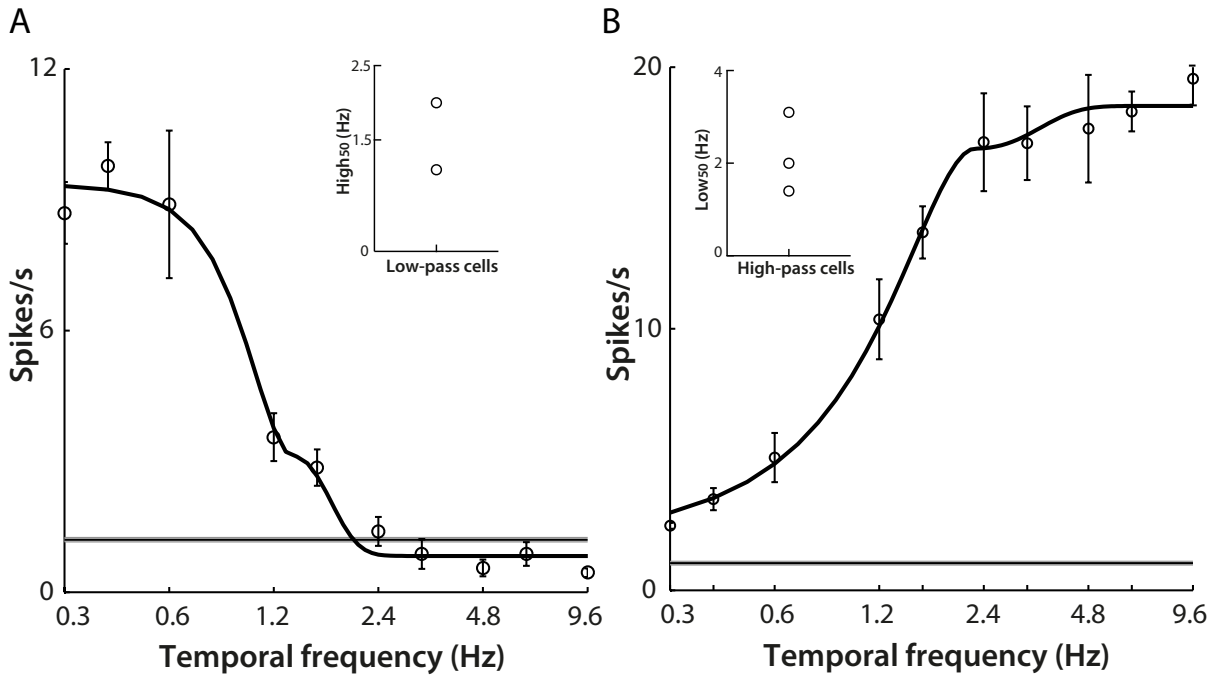

Figure 3.5 Low-pass and high-pass temporal frequency tuning properties. Main panels: A and B. Single cell examples of low-pass (A) and high-pass (B) temporal frequency tunings. Open circles represent mean firing rates with S.E.M. across repetitive presentations of drifting gratings. Black curves show the best fits of these raw data to a two half-Gaussian function (Grubb and Thompson, 2003). Grey areas represent S.E.M. of spontaneous activity, with thinner lines indicating mean values. Parameters for the two units: A. $high_{50}$ 1.1 Hz; B. low_{50} 1.4 Hz. Inset: $high_{50}$ of two low-pass cells, which are 1.1 and 2.0 Hz (A); low_{50} of three high-pass cells, which are 1.4, 2.0 and 3.1 Hz (B).

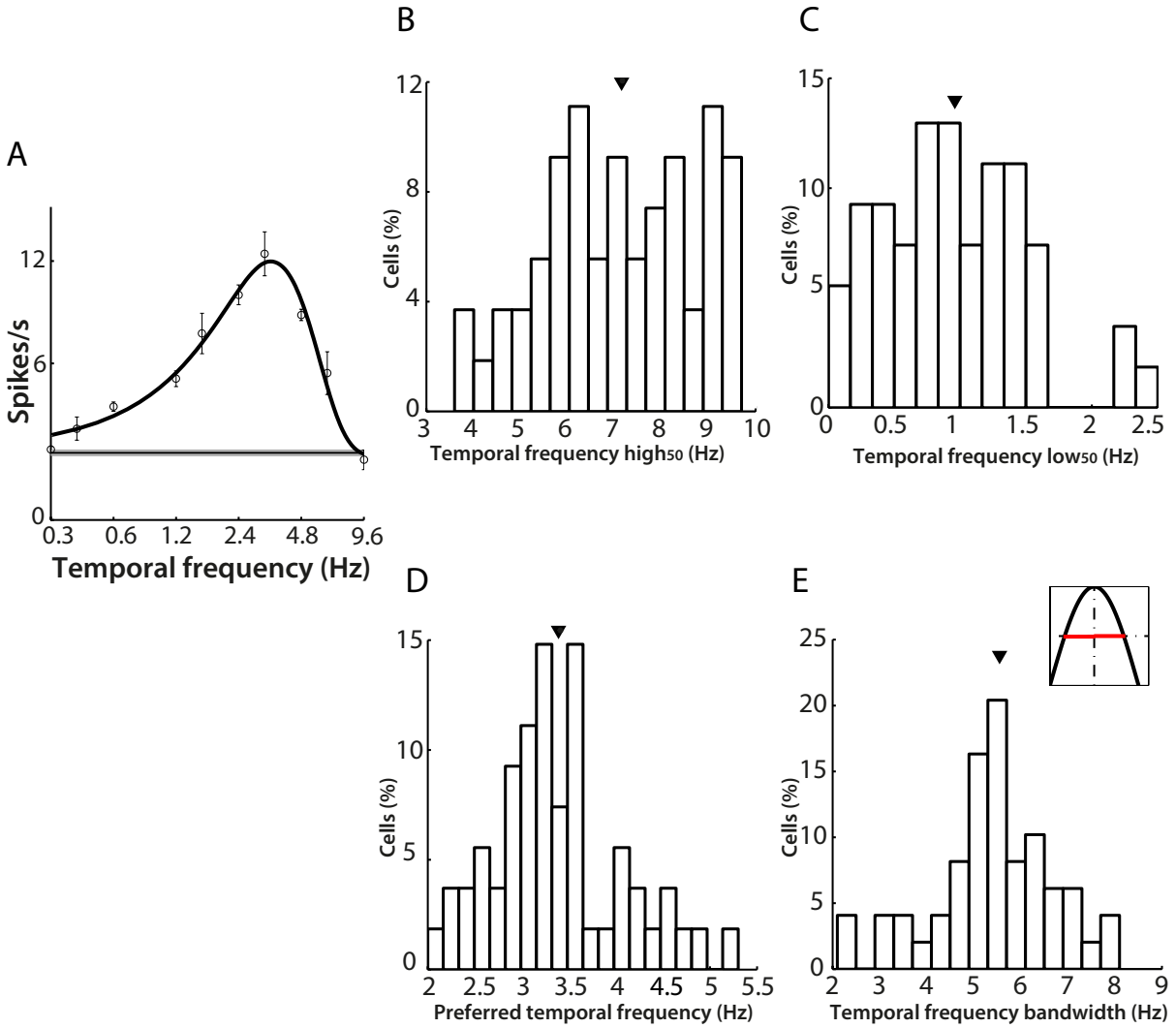

Figure 3.6 Band-pass temporal frequency tuning properties of neurons in mouse LGN. A. A representative cell with the most typical temporal frequency tuning that was defined as band-pass: cell activity decreased sharply after reaching peak at the preferred frequency. Open circles represent mean firing rates with S.E.M. across repetitive presentations of drifting gratings. Black curves show the best fits of these raw data to a two half-Gaussian function (Grubb and Thompson, 2003). Grey areas represent S.E.M. of spontaneous activity, with thinner lines indicating mean values. B-E. Parameters measured from band-pass subtypes that represented 91.2% (52/57) of all the neurons in the dataset. Arrows represent mean values. B. Distribution of $high_{50}$, and the mean ± S.E.M. is 7.1 ± 0.2 Hz. C. Distribution of low_{50}, and the mean ± S.E.M. is 1.0 ± 0.1 Hz. D. Distribution of preferred temporal frequency, and the mean ± S.E.M. is 3.4 ± 0.1 Hz. E. Distribution of tuning bandwidth, calculated as the difference between $high_{50}$ and low_{50} (illustrated as the range in red in the plot inset). Its mean ± S.E.M. is 5.5 ± 0.2 Hz.

3.3.2.5 Contrast response properties

To characterize contrast sensitivity, 131 of 185 cells were presented with drifting gratings of varying contrasts from 10.0% to 98.0% at 0.03 c/deg spatial frequency and 1 Hz temporal frequency. Among them, 128 units were successfully fitted with a hyperbolic function

(Albrecht and Hamilton, 1982), and therefore included in the contrast response property analysis.

Generally, response amplitudes of individual LGN cells increased with increasing stimulus contrasts. However, significant variations were exhibited from fitted tuning curves of individual cells. As illustrated in Figure 3.7, some cells increased their responses from very low contrasts but also saturated at relatively low contrasts (A), some cells displayed sigmoid response properties (B): response amplitude began to increase rapidly after a short period of slow increase at low contrasts. Additionally, some cells responded linearly and did not saturate even at the highest contrast (C). There were also cells that only displayed linear increase in response to gratings of higher contrasts (D).

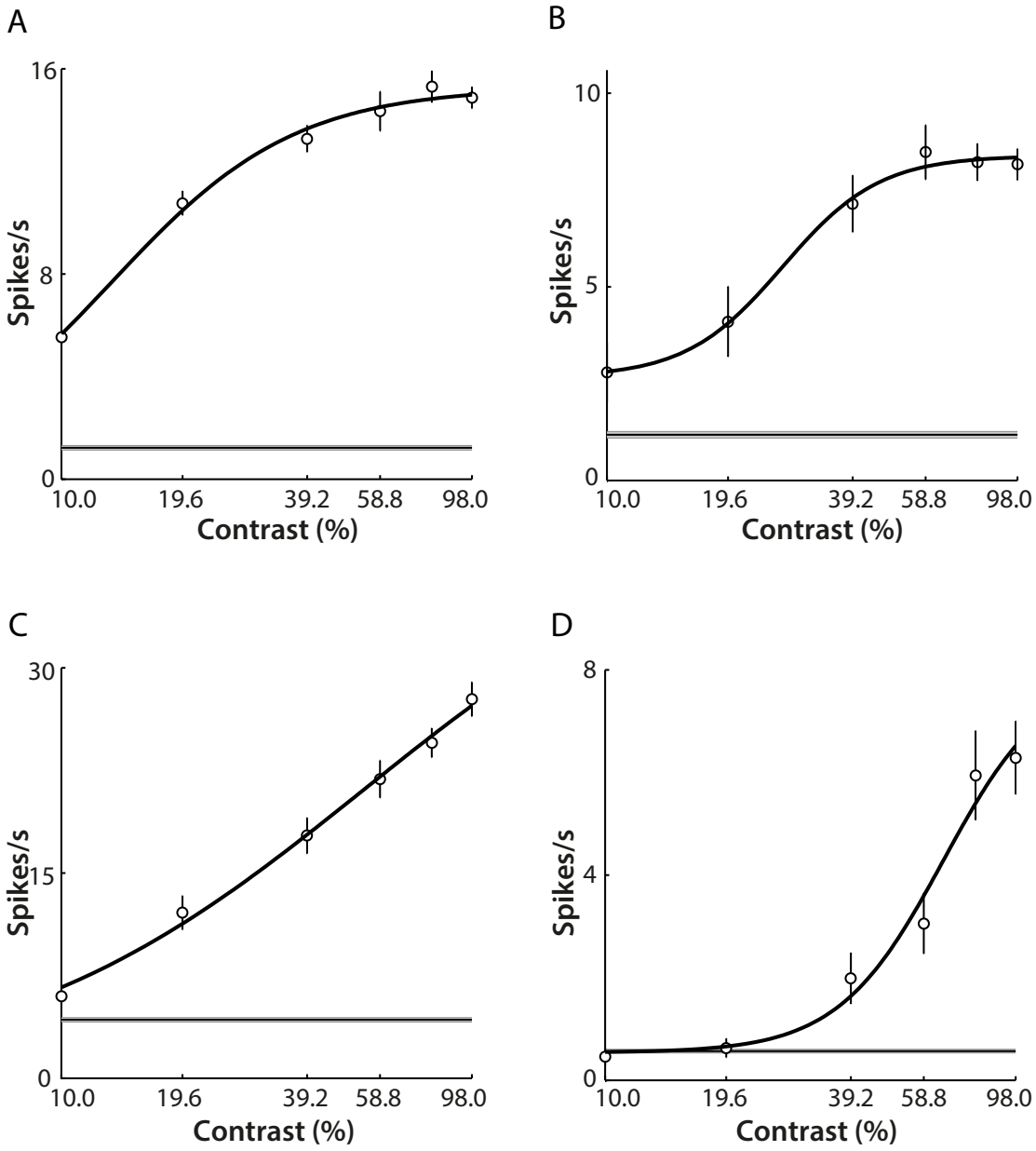

Figure 3.7 Examples of single cell contrast response tuning to drifting gratings of varying contrasts. Open circles represent mean firing rates with S.E.M. across repetitions of drifting gratings. Black curves show the best fits of these raw data to a hyperbolic function (Albrecht and Hamilton, 1982). Grey areas represent S.E.M. of spontaneous activity, with thinner lines indicating mean values. Note logarithmic scale of X-axis. Four types of responses were mainly observed among the population. (A) shows response amplitude of the cell increased sharply from very low contrast but also began to saturate at relatively lower contrast. (B) displays a sigmoid response curve: response amplitude began to increase rapidly after a short period of slow increase at low contrasts. (C) displays an almost linear increase in response amplitude with increasing contrasts. (D) displays linear increase only from higher contrast. Parameters for each of the four units: A: gain=0.99 spikes/s/%, C_{50}=13.1%; B: gain=0.68 spikes/s/%, C_{50}=27.2%; C: gain=1.52 spikes/s/%, C_{50}=54.3%; D: gain=1.19 spikes/s/%, C_{50}=66.7%.

Contrast gain and C_{50} were calculated to indicate overall contrast sensitivity across the sample data. The distribution of contrast gain (Figure 3.8A) mainly fell in the range from 0.5

to 1.5 spikes/s/%. The mean ± S.E.M. of contrast gain was 0.98 ± 0.04 spikes/s/%. C_{50}, an indication of the contrast where response amplitude fell to 50% of its value at 100% contrast, spread widely within the range from 10% to 90%, with mean ± S.E.M. at 51.1 ± 2.0 % (Figure 3.8B).

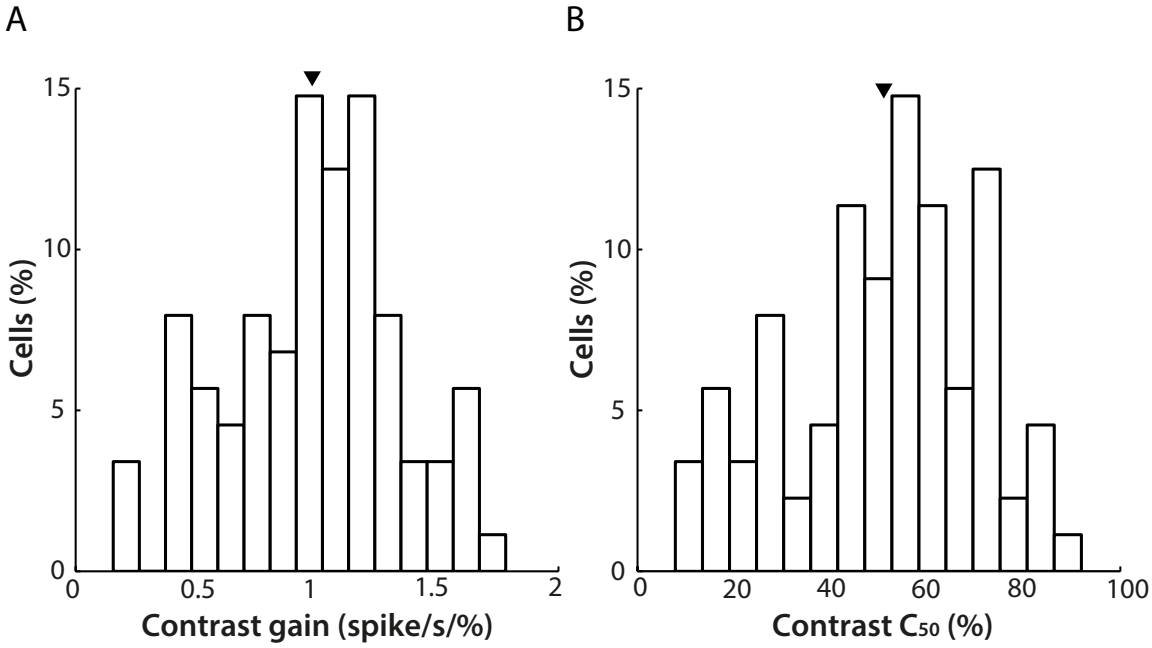

Figure 3.8 Contrast sensitivity properties at population level. A. Contrast gain of mouse LGN cells. The mean value (arrow) ± S.E.M. is 0.98 ± 0.04 spikes/s/%. B. C_{50} of mouse LGN cells. The mean value (arrow) ± S.E.M. is 50.1 ± 2.0 %.

3.3.2.6 Direction/orientation selectivity

Direction/orientation selectivity refers to neurons responding preferably to either one direction of motion (direction selectivity) or two opposing directions of motion (orientation selectivity). Direction/orientation selectivity property was computed from responses to drifting stimulus moving at a specific angle between 0 deg and 315 deg. 129 out of 185 cells across 19 recordings were presented with this stimulus.

Figure 3.9A and B demonstrate two examples of individual cells that were strongly tuned to direction (A) and posterior-anterior orientation (B), whilst activities of these responsive neurons were suppressed by opposing or orthogonal directions of motion. Population distributions of DSI and OSI are shown in Figure 3.9C and D. There were 7 cells categorized as DS cells (DSI index above 0.33, red dash line in Figure 3.9C) and 2 cells categorized as OS cells (OSI index above 0.6, red dash line in Figure 3.9D).

To measure the overall preferred directions of motion, we divided 0 to 360 deg evenly into 8 proportions and defined the four cardinal directions as superior (67.5~112.5 deg), inferior (247.5~292.5 deg), posterior (157.5~202.5 deg) and anterior (337.5~22.5 deg) (Figure 3.9E and F). The preferred directions of 85.7% LGN DS cells are closely tied to the four cardinal directions (5 out of 7 cells along the superior/inferior direction and 1 out of 7 cell along the posterior direction) (Figure 3.9E). For the two OS cells, the preferred orientations were biased towards the orientations along the superior-inferior axis and posterior-anterior axis respectively (Figure 3.9F).

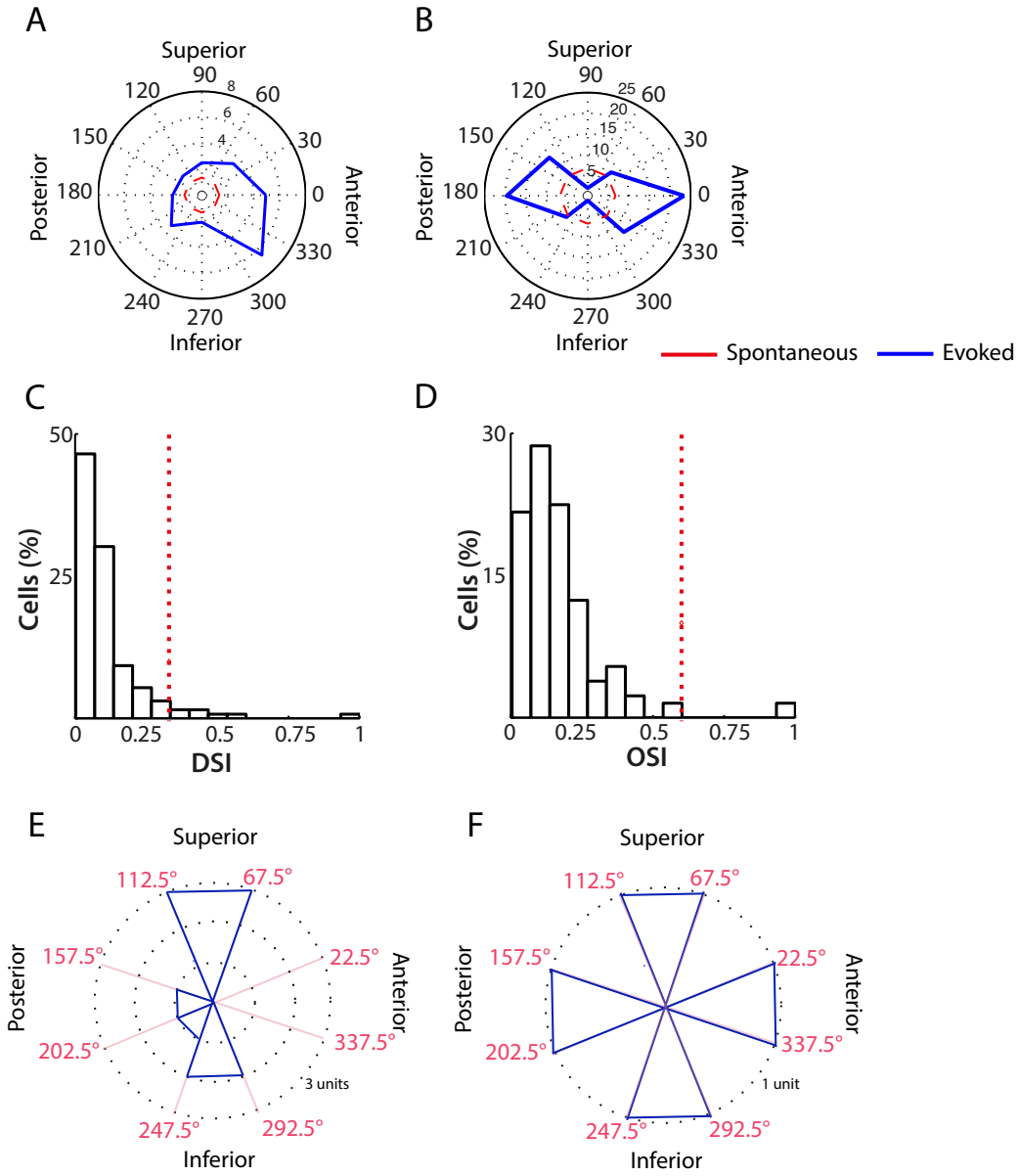

Figure 3.9 Direction/orientation selectivity in mouse LGN. A and B. Examples of single DS/OS neurons that responded preferentially to direction (A), anterior-posterior orientation (B). The radius indicates response amplitude (spikes/s). Red dash line represents level of spontaneous activity and blue solid line represents response amplitudes to all directions of motion. C and D. Population distributions of DSI and OSI. Red dash lines indicate index threshold for selective cells: 0.33 for direction selectivity and 0.6 for orientation selectivity. E and F. Distributions of preferred motion of direction (E) and orientation (F) of all DS (n=7) and OS (n=2) cells. Angles from 0 to 360 deg are evenly spaced into 8 proportions. The four cardinal directions are named as superior (67.5~112.5 deg), inferior (247.5~292.5 deg), posterior (157.5~202.5 deg) and anterior (337.5~22.5 deg). The radii indicate number of cells within DS or OS groups.

3.3.2.7 Response latency

We measured single cell response latency separately from full-field flicker and the grating stimulus that applied to characterize spatial frequency tuning properties. 123 out of 185 LGN cells were presented with flicker stimulus, while the number of cells successfully fitted to spatial frequency tunings was 92. Response latency was calculated from these cells.

Seen from the distributions (Figure 3.10), latencies spanned from less than 10 msec to up to nearly 400 msec to sinusoidal gratings (triangles) and full-field flickers (squares). The medians with interquartile ranges (indicated as solid lines in Figure 3.10) were 93 (52, 133) msec and 32 (12, 95) msec respectively. Although seen in Figure 3.10 that the latency distributions displayed substantial overlaps between the two different measurements, latency calculated from flicker stimulus was significantly lower than those from the grating stimuli (Mann-Whitney U test: $P<0.0001$).

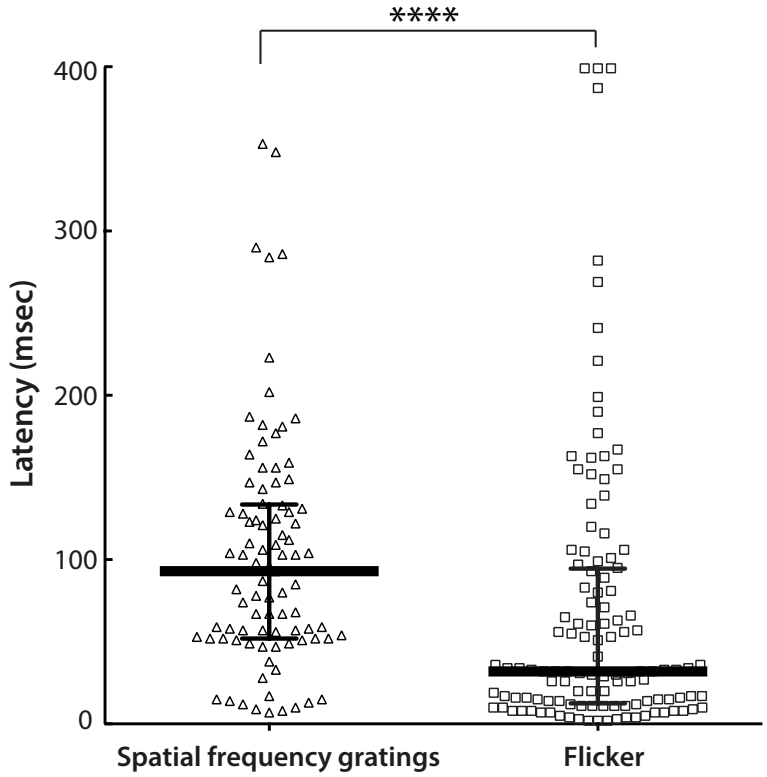

Figure 3.10 Distributions of response latency of mouse LGN neurons to gratings moving at various spatial frequencies and full-field flicker. Response latency of single units measured from gratings of changing spatial frequencies and flickers are represented as triangles and squares. The medians with interquartile ranges (solid lines) are 93 (52, 133) msec and 32 (12, 95) msec respectively. Latency calculated from flicker stimulus is significantly lower than those measured from gratings of different spatial frequencies, with Mann-Whitney U test: $P<0.0001$ (****).

3.3.2.8 Transient/sustained responsive property

Transient/sustained responsive property was characterized from responses to repetitions of full-field black or white flicker of 600 msec duration. Transient/sustained index was calculated as the ratio of average response amplitude from cell response latency (lat) till 50 msec afterwards (lat+50msec) to response amplitude from lat+50msec on till end of stimulus duration. Cells with index below 1 were defined as sustained responsive cells, implying responding consistently during the stimulus presentation. While cells with index above 1 were defined as transient responsive cells, implying cell only responding to sudden appearance of stimuli.

Figure 3.11A and B are examples of single transient and sustained cells' responses to the full-field flickers, in both of which the right columns represent PSTHs, while the left columns are raster plots across repetitions of trials. Cells of both transient/sustained modes responded strongly to flicker (ON- cells to white stimulation and OFF- cells to black stimulation). As observed from their PSTHs and rasters, transient cells responded dynamically only at the onset of stimulation, shortly afterwards activity decreased and some cells even turned silent. Cells responding in the sustained manner, however, did not exhibit post-excitatory suppression and fired continuously throughout the duration of stimulus presentation.

In total, 123 out of 185 LGN cells were presented with this stimulus. 92.7% (n=114) cells responded in the transient mode, with the remaining 7.3% cells responding in the sustained pattern. As shown in Figure 3.12, the transient/sustained index always fell in the range of 0 to 1 for cells showing sustained response, and spanned a broader range (1 to 11) for transient responsive cells.

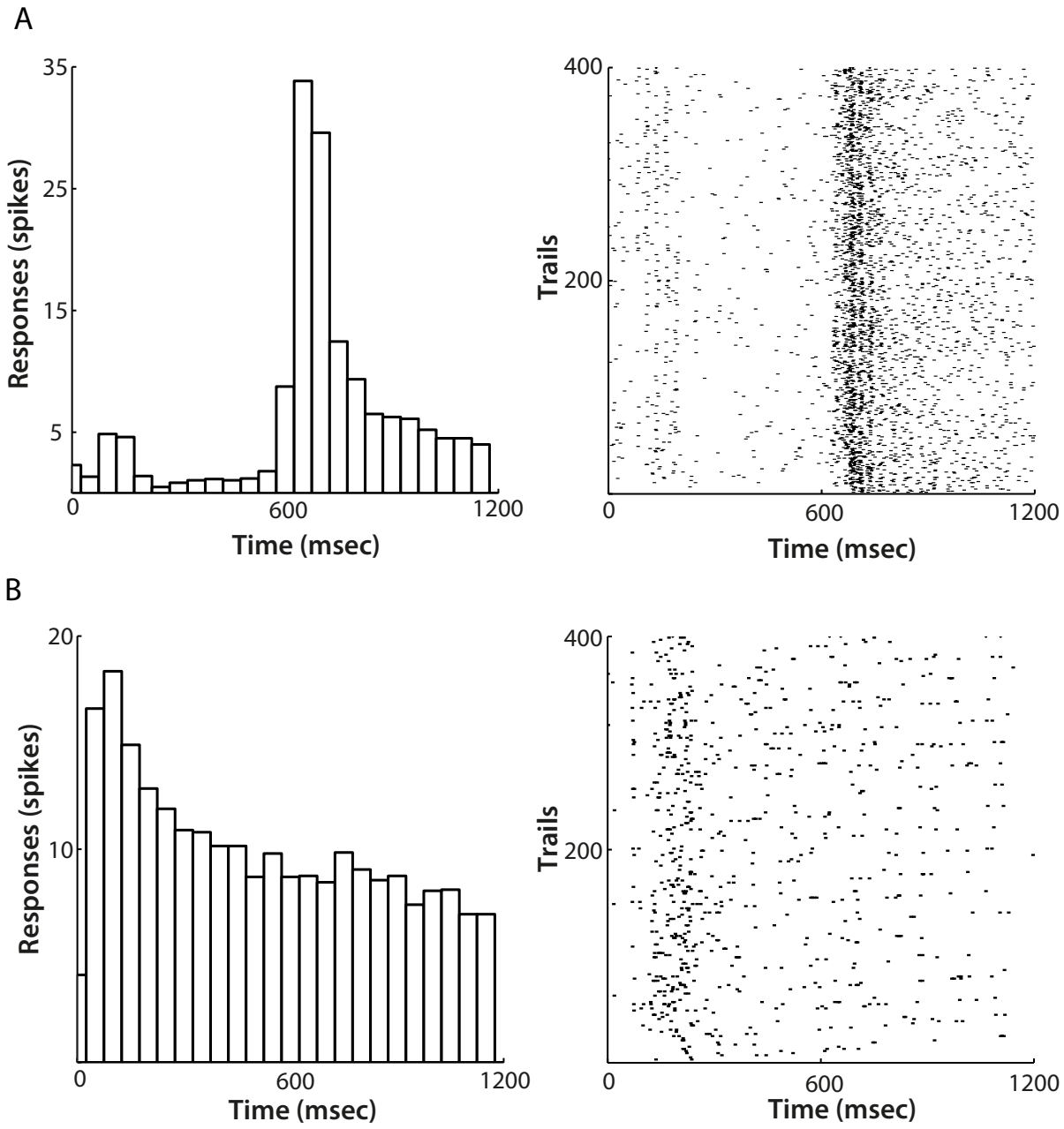

Figure 3.11 Response patterns of transient and sustained cells to full-field flicker stimulus. PSTH (left columns) and rasters (right columns) of single transient (A) and sustained (B) responsive cells. Full-field white stimulation started from 0 and persisted for 600 msec, while black stimulation started from 600 msec and persisted for another 600 msec. This white-black flicker was repeated for 400 trials. Parameters for these two cells: A. Transient/sustained index: 5.15; response latency to flicker 61 msec. B. Transient/sustained index: 0.95; response latency to flicker: 189 msec.

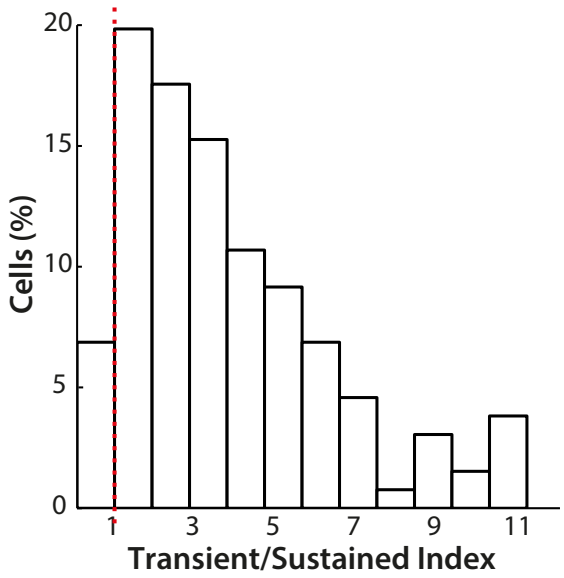

Figure 3.12 Distribution of transient/sustained index of neurons in mouse LGN. The red dashed line represents the threshold that divides cells into sustained (<1) and transient (>1). 114 out of 123 (92.7%) cells responded in the transient pattern.

3.3.2.9 Linearity

Linearity was assessed with sinusoidal gratings at various spatial frequencies with temporal frequency at 1 Hz. In our dataset, 92 cells were successfully fitted with DoG (Section 2.5.2). Linearity index (F1/F0) was calculated from these cells, cells with index >1 were defined as responding in linear mode.

Illustrated from the PSTH in Figure 3.13A, the nonlinear cell fired more continuously throughout the 7 sec presentation of grating stimulus moving at a specific spatial frequency, whereas the linear cell (Figure 3.13A top) showed a relative sinusoidal response corresponding to the temporal frequency of the stimulus. Such linear behaviour was present at all spatial frequencies used, for this representative and other linear cells in the dataset.

Overall, the majority of cells displayed nonlinear response pattern (79/92, 85.9%). The distribution of linearity index shown in Figure 3.13B was bimodal, one peak concentrated on low values below 0.1, and the other peak was in the range from 1.0 to 1.1.

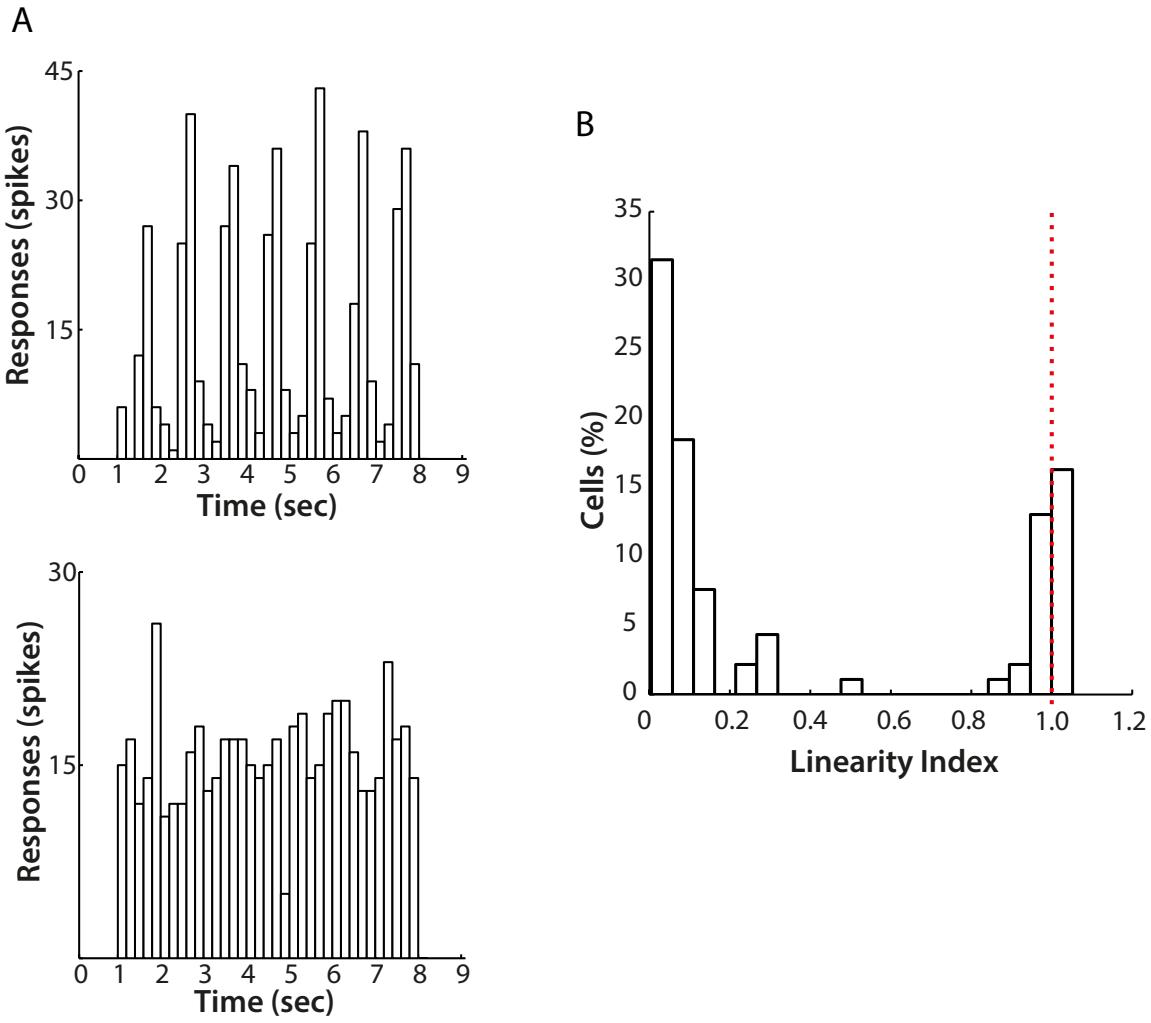

Figure 3.13 Linearity of mouse LGN cells. A. Activity of single linear (top) and non-linear (bottom) responsive cells across a 7 sec presentation of sinusoidal grating at the temporal frequency of 1 Hz. Responses were summed from repetition of 6 trials. Linearity index for Top: 1.11; Bottom: 0.16. B. The overall distribution of linearity index. Linearity and non-linearity was separated by threshold 1 that indicated as red dash line. Index <1 were non-linear cells (85.9% or 79/92), whereas cells with index >1 (14.1% or 13/92) responded in a more linear mode.

3.3.3 Response properties of subtypes in mouse LGN

Studies on parallel pathways have tended to identify structural and functional links between the component cells at successive stages along the visual path, such as different properties between neurons located in separate laminae in monkey LGN (Kaplan and Shapley, 1982). Mouse LGN is not laminated. However, as introduced in Chapter 1, it was recently revealed the prevalence of morphological X-/Y- like neurons within this nucleus (Krahe et al., 2011). We therefore sought to investigate functional subtypes of this nucleus, primarily ON-/OFF-centre cells, as well as linear/non-linear cells, transient/sustained responsive cells and cells with direction/orientation selectivity.

3.3.3.1 Response properties of ON-/OFF- centre cells

Our current data show that ON- and OFF- centre cells are comparable in fraction, with 48.6% (90/185) ON- centre cells and 51.4% (95/185) OFF-centre cells in the population (Figure 3.14A). Additionally, as shown in Figure 3.14B-D, ON- and OFF- cells overlapped considerably in receptive field sizes (ON- 6.7 (5.5, 8.0) deg, OFF- 5.9 (4.9, 7.9) deg), spontaneous (ON- 2.0 (0.8, 4.4) spikes/s, OFF- 1.9 (0.9, 3.9) spikes/s) and evoked (ON- 6.4 (3.4, 13.8) spikes/s and OFF- 7.6 (3.7, 11.8) spikes/s) (Mann-Whitney test: $P>0.05$).

Interestingly, with regard to both contrast parameters, ON- centre cells were more sensitive than their OFF- centre counterparts. Specifically, compared to OFF- centre cells, ON- centre cells illustrate significantly higher contrast gain (ON: 1.1 ± 0.05 spikes/s/%; OFF: 0.87 ± 0.06 spikes/s/%; *t*-test, $P<0.01$) (Figure 3.15A), and lower C_{50}s (ON: 47.3 ± 3.1%; OFF: 56.2 ± 3.3%; *t*-test, $P<0.05$) (Figure 3.15B).

In addition, over the temporal frequency tuning properties, OFF-centre cells showed higher degree of selectivity than their OFF-centre neighbours, possessing significantly higher preferred temporal frequency (ON-centre: 3.1 ± 0.1 Hz; OFF-centre: 3.6 ± 0.2 Hz. *t*-test, $P<0.01$) (Figure 3.16A), broader tuning bandwidth (ON-centre: 4.9 ± 0.3 Hz; OFF-centre: 6.5 ± 0.3 Hz. *t*-test, $P<0.001$) (Figure 3.16B) and higher low_{50}s (ON- centre: 0.7 ± 0.1 Hz; OFF-centre: 1.0 ± 0.1 Hz. *t*-test, $P<0.05$) (Figure 3.16D). The $high_{50}$s of these two subtypes stayed comparable (ON- centre: 7.2 ± 0.4 Hz; OFF-centre: 7.6 ± 0.3 Hz. *t*-test, $P>0.1$) (Figure 3.16C).

Apart from the abovementioned contrast sensitivity and temporal frequency tuning properties, ON- and OFF- centre cells were comparable in the rest response parameters that we characterized in this study, which included spatial frequency tuning properties, fractions of cells that exhibited direction/orientation selectivity, transient/sustained index and linearity.

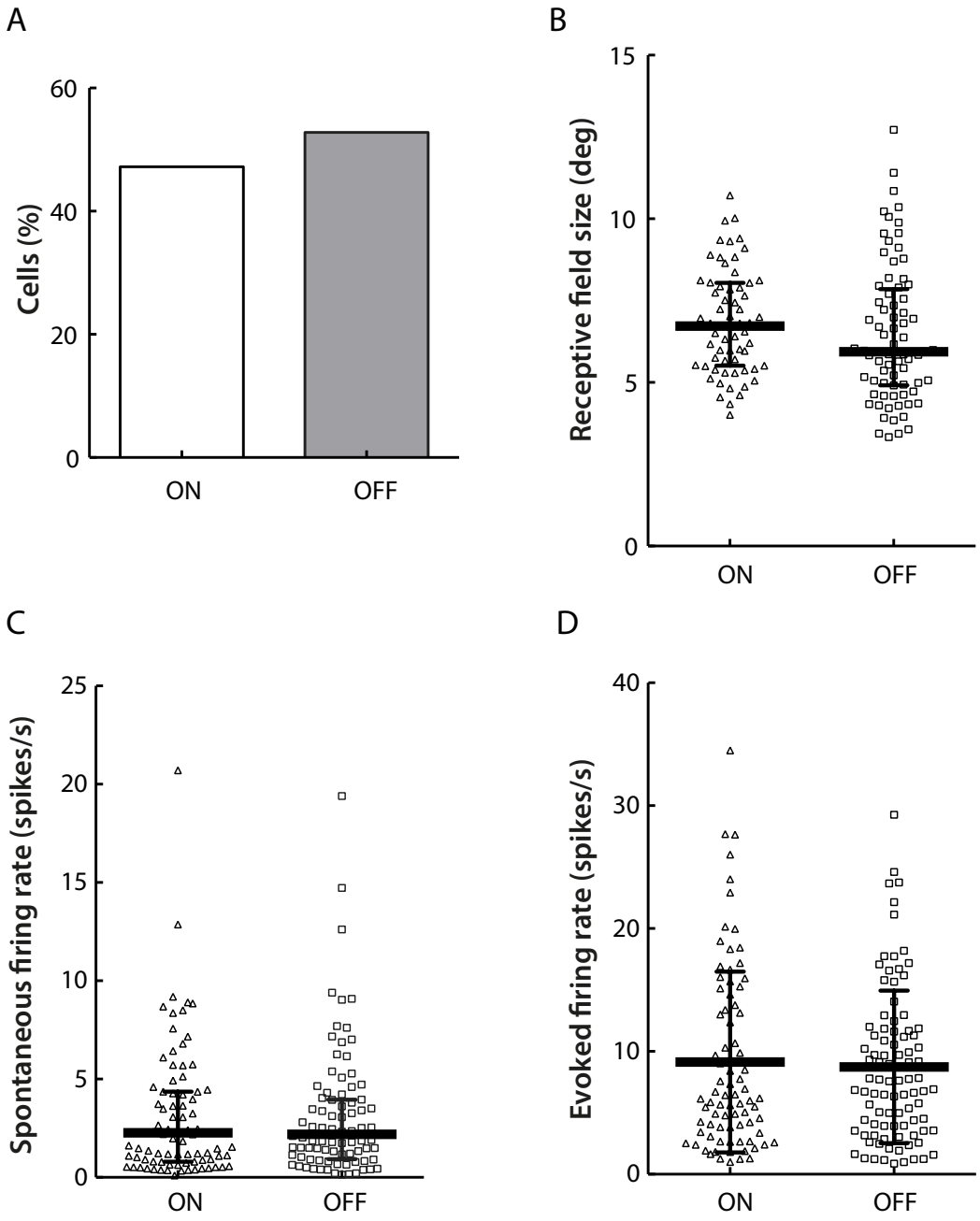

Figure 3.14 ON- and OFF- centre cells in mouse LGN are highly correlated in fraction, receptive field sizes and firing rates. A. 48.6% (90/185) and 51.4% (95/185) cells are ON- and OFF- centre cells respectively in the dataset. B-D. Distributions show that ON-cells (triangle) and OFF- cells (square) are comparable in receptive field sizes (B), spontaneous (C) and evoked firing rates (C) (Mann-Whitney test: $P>0.05$). The value of each single ON- or OFF-centre cell is presented as a triangle or square respectively. Parameters: Receptive field size, ON- 6.7 (5.5, 8.0) deg, OFF- 5.9 (4.9, 7.9) deg; Spontaneous firing rate, ON- 2.0 (0.8, 4.4) spikes/s, OFF- 1.9 (0.9, 3.9) spikes/s; Evoked firing rate, ON- 6.4 (3.4, 13.8) spikes/s and OFF- 7.6 (3.7, 11.8) spikes/s. Values are also presented in the format of medians with interquartile ranges that are shown in each plot.

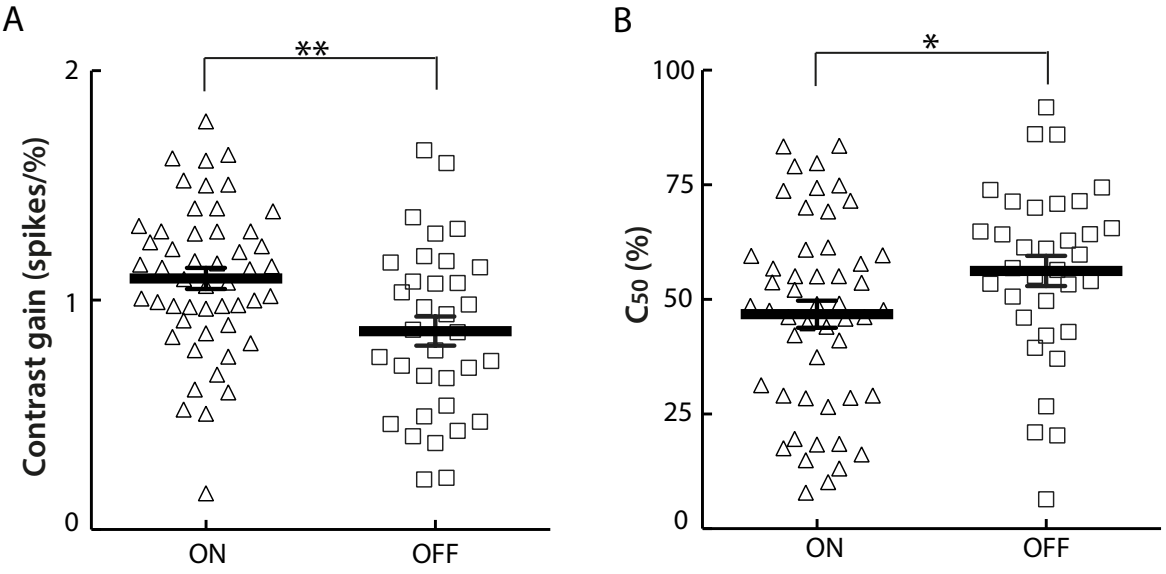

Figure 3.15 Contrast selectivity differences between ON- and OFF- centre cells in mouse LGN. A. ON-centre cells show significantly higher mean contrast gains than OFF-centre cells (*t*-test, $P<0.01$). ON-centre cells: 1.10 ± 0.05 spikes/s/%; OFF-centre cells: 0.87 ± 0.06 spikes/s/%. B. ON- centre cells show significantly lower mean C_{50}s than their OFF- centre counterparts (*t*-test, $P<0.05$). ON-centre cells: 47.3 ± 3.1%; OFF-centre cells: 56.2 ± 3.3%. The value of each single ON- or OFF-centre cell is presented as a triangle or square respectively. Values are presented as mean ± S.E.M. and are shown in A and B.

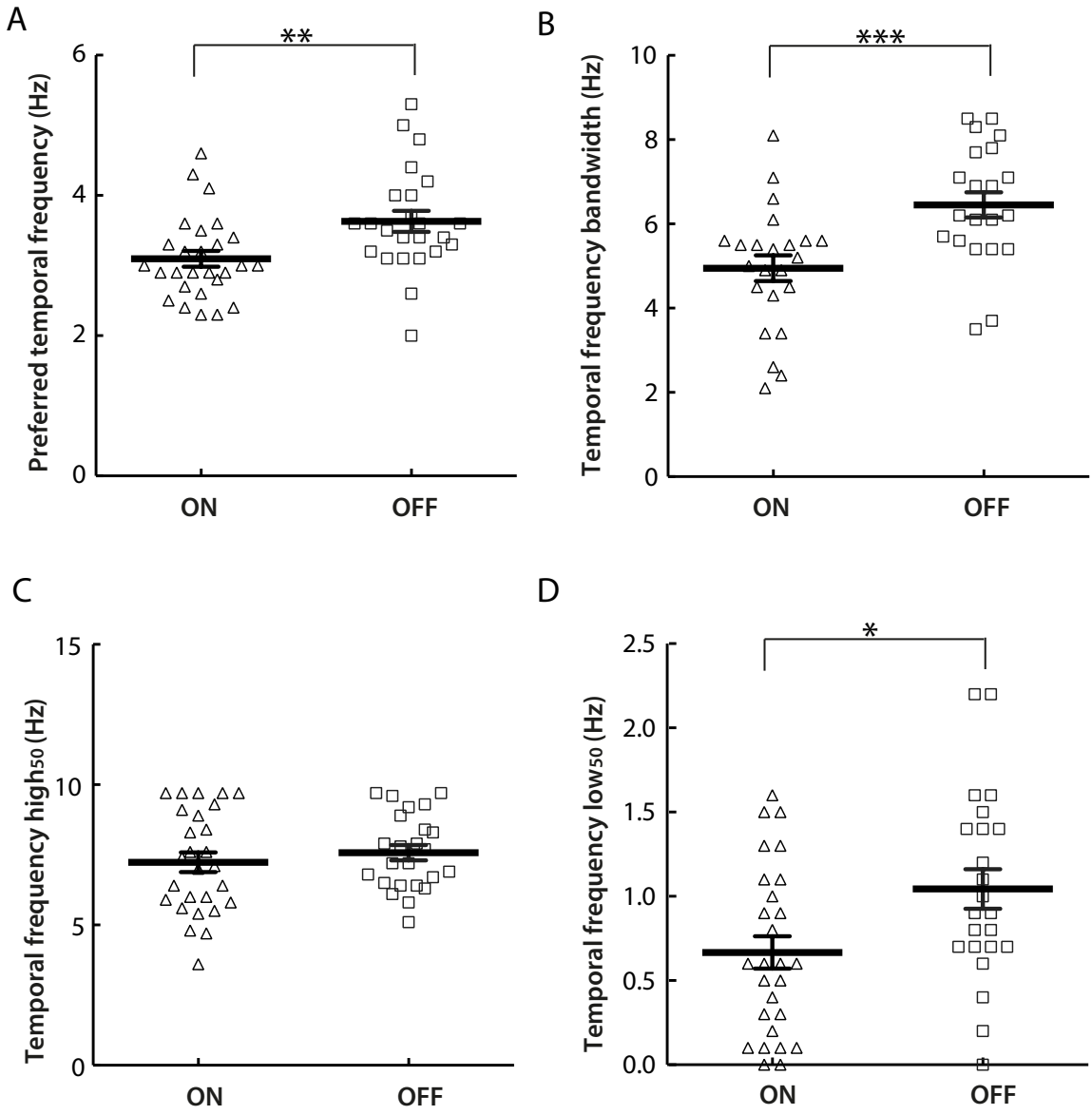

Figure 3.16 Comparison of temporal frequency properties between ON- and OFF- centre cells in mouse LGN. A. ON- centre cells show significantly lower mean preferred temporal frequencies than OFF-centre cells (*t*-test, $P<0.01$). ON-centre cells: 3.1 ± 0.1 Hz; OFF-centre cells: 3.6 ± 0.2 Hz. B. ON- centre cells show significantly lower mean temporal frequency bandwidths than OFF-centre cells (*t*-test, $P<0.001$). ON-centre cells: 4.9 ± 0.3 Hz; OFF-centre cells: 6.5 ± 0.3 Hz. C. Mean temporal frequency $high_{50}$s are comparable between ON- and OFF-centre cells (*t*-test, $P>0.1$). ON- centre cells: 7.2 ± 0.4 Hz; OFF-centre cells: 7.6 ± 0.3 Hz. D. ON-centre cells have significantly lower mean temporal frequency low_{50}s than OFF-centre cell (*t*-test, $P<0.05$). ON-centre cells 0.7 ± 0.1 Hz; OFF-centre cells: 1.0 ± 0.1 Hz. The value of each single ON- or OFF-centre cell is presented as a triangle or square respectively. Values are also presented in the format of mean ± S.E.M. that are shown in each plot.

3.3.3.2 Response properties of DS/OS cells

DS/OS cells were categorized as a single group and their response properties were compared with the rest non-DS/OS cells. Among the cells (9/129, 7.0%) that exhibited direction/orientation selectivity, no significant difference was observed in spontaneous/evoked response amplitudes and contrast sensitivity, compared to the non-DS/OS cells (Mann-Whitney test, $P>0.05$). In addition, receptive field characteristics of DS/OS cells, including radius and ON/OFF ratio remained consistent with the rest of the neurons analysed (Mann-Whitney test, $P>0.05$). We did not compare temporal frequency tuning properties, considering the number of cells that fitted to the 2-Gaussian-halves equation (Grubb and Thompson, 2003) (Section 2.5.2) was too small in the DS/OS group (n=2).

As summarized in Table 3.1, the peak (median=0.04 (0.01, 0.05) c/deg) and cutoff (median=0.28 (0.18, 0.36) c/deg) spatial frequency of the DS/OS cells were higher than that of the non-DS/OS cells. In addition, linearity was assessed from six DS/OS cells that had spatial frequency tuning successfully fitted by the DoG (Rodieck, 1965; So and Shapley, 1981) (Section 2.5.2), and all these neurons showed non-linear summation, with F1/F0<1. This might indicate the DS/OS units responded in a more continuous rather than a periodic mode during stimulus presentation. However, it has to be noted that due to the small sample size in the DS/OS group, statistical significance test could not be carried out between non-DS/OS and DS/OS cells and the comparison was based on observations of median values.

Table 3.1 Comparison of response properties that showed difference between non-DS/OS and DS/OS cells in mouse LGN.

		Non-DS/OS cells	DS/OS cells
Total No. of cells		176	9
	No. of cells fitted	86	6
SF	Preferred SF (c/deg)	0.00 (0, 0.03)	0.04 (0.01, 0.05)
	SF cutoff (c/deg)	0.19 (0.11, 0.33)	0.28 (0.18, 0.36)
No. of non-linear cells		70 (84.3%)	6 (100%)

SF: spatial frequency. Values are presented in the format of median (25 percentile, 75 percentile).

3.3.3.3 Response properties of other types

In addition to the ON/OFF and DS/OS cells described above, response features of another two major categorizations were examined.

We first looked into the transient and sustained responsive cells. As summarized in Table 3.2, transient responsive cells (114/123, 92.7%) displayed longer response latency calculated from sinusoidal gratings with varying spatial frequencies than their sustained responsive counterparts (9/123, 7.3%) (transient, 94 (53, 135) msec; sustained, 63 (29, 87) msec). In addition, transient responsive neurons tended to prefer lower spatial frequency cutoff (transient, 0.19 (0.08, 0.31) c/deg; sustained, 0.29 (0.16, 0.38) c/deg). The comparisons in these two parameters were relied on observations because of the small sample size of the sustained responsive cells (four cells that were successfully fitted by the DoG, Section 2.5.2). Moreover, our results suggested that transient responsive cells displayed poorer contrast sensitivity than sustained responsive ones (transient, 0.98 ± 0.04 spikes/s/%; sustained, 1.11 ± 0.02 spikes/s/%. Mann-Whitney test, $P<0.01$).

The remaining response properties of the transient responsive cells, including spontaneous/evoked firing rates, receptive field sizes, proportions of ON-/OFF- centre cells and linear/non-linear cells were not found to be statistically different from those of the sustained responsive cells.

Table 3.2. Response properties of transient and sustained responsive cells that are different.

	Transient	Sustained
No. of cells	114 (92.7%)	9 (7.3%)
Latency to SF (msec)	94 (53, 135)	63 (29, 87)
Spatial frequency cutoff (c/deg)	0.19 (0.08, 0.31)	0.29 (0.16, 0.38)
Contrast gain (spikes/s/%)	0.98 ± 0.04	1.11 ± 0.02

SF: sinusoidal gratings moving at changing spatial frequencies

Secondly, we compared response features between the linear and nonlinear neurons (summarized in Table 3.3). Within these two categorizes that included 92 cells in total, 5 cells responded preferably to direction/orientation. Interestingly, all these cells responded in a non-linear mode. Except for this difference in the fraction of DS/OS cells, linear and nonlinear cells were comparable on all the other parameters measured.

Table 3.3 Comparison of response properties between linear and non-linear responsive neurons in mouse LGN.

		Linear	Non-linear
Total No. of cells		13	79
Fraction of DS/OS cells (%)		0	6.3%
Firing rate	Spont (spikes/s)	1.8 (0.9, 3.9)	2.0 (0.9, 4.2)
	Evoked (spikes/s)	7.1 (3.4, 12.0)	7.4 (3.9, 13.3)
SF	Preferred SF (c/deg)	0.00 (0.00, 0.04)	0.00 (0.00, 0.04)
	SF cutoff (c/deg)	0.19 (0.11, 0.32)	0.19(0.10, 0.33)
	Latency (msec)	93 (51, 133)	93 (53, 135)
TF	Preferred TF (Hz)	3.5 ± 0.2	3.4 ± 0.1
	TF $high_{50}$ (Hz)	7.3 ± 0.2	7.1 ± 0.1
	TF low_{50} (Hz)	0.9 ± 0.1	1.0 ± 0.1
Contrast	Gain (spikes/s/%)	0.98 ± 0.03	0.98 ± 0.04
	C_{50} (%)	50.1 ± 1.9	50.0 ± 1.8

3.3.4 Response property dependence upon location within mouse LGN

To fully understand neuronal response features, electrophysiological characterizations were also aimed to span the entire extent of mouse LGN in this study. For this purpose, recordings were made from coordinates that were 2.2 mm, 2.6 mm and 3.0 mm posterior from the Bregma point, which were topographically categorized as the anterior, middle and posterior LGN respectively. Among the 185 single units in total that were included in the dataset, 41, 129 and 15 were classified as belonging to the anterior, middle or posterior LGN. This topographical categorization was verified by both targeted coordinates and histological electrode track visualization combined with the LGN volume (see Chapter 5).

Table 3.4 Comparison of properties of mouse LGN neurons across the anterior/middle/posterior location.

	Anterior	**Middle**	**Posterior**
Coordinate (mm posterior from Bregma point)	2.2	2.6	3.0
Numbers of single units	41	129	15
Fraction of ON- cells (%)	36.8	51.6	33.3
Receptive field radius (deg)	6.2 (5.8, 8.1)	6.2 (5.0, 7.9)	7.4 (5.4, 8.4)
Spontaneous firing rate (spikes/s)	2.2 (0.9, 3.9)	2.0 (0.9, 4.6)	1.4 (0.8, 2.4)
Evoked firing rate (spikes/s)	8.4 (5.6, 16.3)	6.8 (3.3, 12.4)	5.6 (2.7, 7.2)
Preferred SF (c/deg)	0.00 (0., 0.04)	0.00 (0., 0.04)	0.01 (0., 0.03)
SF cutoff (c/deg)	0.19(0.12,0.34)	0.20 (0.12, 0.32)	0.19 (0.15, 0.33)
Preferred TF (Hz)	3.4 ± 0.1	3.3 ± 0.2	3.4 ± 0.1
TF $high_{50}$ (Hz)	7.1 ± 0.2	7.0 ± 0.2	7.1 ± 0.2
TF low_{50} (Hz)	1.0 ± 0.1	1.1 ± 0.1	1.0 ± 0.1
Contrast gain (spikes/s/%)	0.83 ± 0.08	1.1 ± 0.05	0.9 ± 0.1
Contrast C_{50} (%)	59.1 ± 3.8	46.8 ± 2.7	53.7 ± 6.1
Fraction of linear cells (%)	13.1	16.0	14.9
Fraction of transient cells (%)	92.5	91.0	93.1

We started with comparing individual response property across locations (summarized in Table 3.4). The first variance in response property noticed was that the middle LGN had a higher fraction of ON-centre cells than the other two subregions (Anterior: ON- 36.8% (14/38); Middle: ON- 51.6% (65/126); Posterior: ON- 33.3% (4/12)) (Figure 3.17A).

Apart from the proportion of ON- centre cells, the receptive field size (Anterior 6.2 (5.8, 8.1) deg. Middle 6.2 (5.0, 7.9) deg. Posterior 7.4 (5.4, 8.4) deg. Kruskai-Wallis test, $P>0.1$) remained consistent across the subregions in LGN (Figure 3.17B). In addition, cells from the three subregions showed comparable spontaneous (Anterior 2.2 (0.9, 3.9) spikes/s. Middle 2.0 (0.9, 4.6) spikes/s. Posterior 1.4 (0.8, 2.4) spikes/s. Kruskai-Wallis test, $P>0.1$) (Figure 3.17C) as well as evoked firing rates (Anterior 8.4 (5.6, 16.3) spikes/s. Middle 6.8 (3.3, 12.4) spikes/s. Posterior 5.6 (2.7, 7.2) spikes/s. Kruskai-Wallis test, $P>0.1$) (Figure 3.17D).

Furthermore, neurons located in the middle LGN displayed higher contrast sensitivity than those from the anterior and posterior regions, possessing higher contrast gain (Anterior: 0.83 ± 0.08 spikes/s/%, Middle: 1.1 ± 0.05 spikes/s/%, Posterior: 0.9 ± 0.1 spikes/s/%. Kruskai-Wallis test, $P<0.05$) (Figure 3.18A) and lower C_{50} (Anterior: 59.1 ± 3.8%, Middle: 46.8 ± 2.7%, Posterior: 53.7 ± 6.1%. Kruskai-Wallis test, $P<0.05$) (Figure 3.18B).

Except for the differences in the contrast sensitivity, spatial frequency tuning properties were highly correlated (Kruskai-Wallis test, $P>0.1$). Additionally, cells from these three locations exhibited a comparable proportion of transient/sustained and linear/non-linear responses.

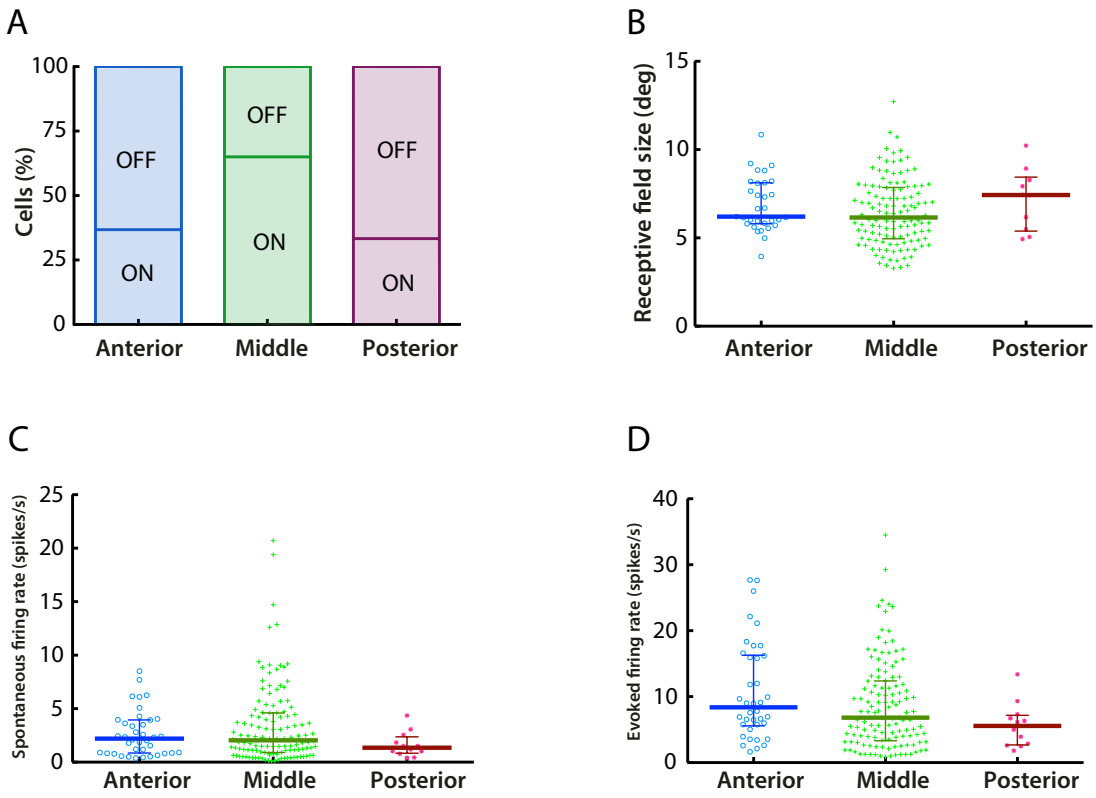

Figure 3.17 Cells located in the anterior, middle and posterior regions in mouse LGN are highly correlated in receptive field sizes and firing rates. A. Ratio of ON- and OFF- centre cells among locations. Anterior: ON- 36.8% (14/38), OFF- 63.2% (24/38). Middle: ON- 51.6% (65/126), OFF- 48.4% (61/126). Posterior: ON- 33.3% (4/12), OFF- 66.7% (8/12). B. Cells from the anterior, middle and posterior regions show comparable median centre receptive field sizes (Kruskai-Wallis test, P>0.1). Centre receptive field size: Anterior 6.2 (5.8, 8.1) deg. Middle 6.2 (5.0, 7.9) deg. Posterior 7.4 (5.4, 8.4) deg. C. Cells from the anterior, middle and posterior regions show comparable median spontaneous firing rates (Kruskai-Wallis test, P>0.1). Spontaneous firing rate: Anterior 2.2 (0.9, 3.9) spikes/s. Middle 2.0 (0.9, 4.6) spikes/s. Posterior 1.4 (0.8, 2.4) spikes/s. D. Cells from the anterior, middle and posterior regions show comparable median evoked firing rates (Kruskai-Wallis test, P>0.1). Evoked firing rate: Anterior 8.4 (5.6, 16.3) spikes/s. Middle 6.8 (3.3, 12.4) spikes/s. Posterior 5.6 (2.7, 7.2) spikes/s. The value of each single cell is represented as blue circle (anterior), green cross (middle) and magenta asterisk (posterior), and medians with interquartile ranges are shown as bars in each plot.

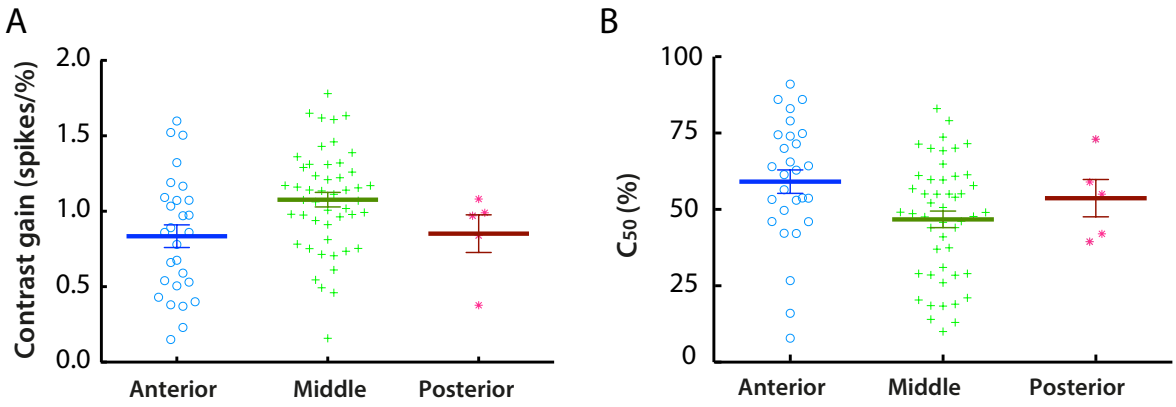

Figure 3.18 Contrast selectivity differs among cells from the anterior, middle and posterior regions in mouse LGN. A. Mean contrast gains are significantly different among three locations in LGN (Kruskai-Wallis test, $P<0.05$), and cells in the middle LGN have significantly higher values than cells in the anterior LGN (Dunn's multiple comparisons test). Contrast gain: Anterior 0.83 ± 0.08 spikes/s/%, Middle 1.1 ± 0.05 spikes/s/%, Posterior 0.9 ± 0.1 spikes/s/%. B. Mean C_{50}s are significantly different among three locations in LGN (Kruskai-Wallis test, $P<0.05$), and cells in the middle LGN have significantly lower values than cells in the anterior LGN (Dunn's multiple comparisons test). C_{50}: Anterior 59.1 ± 3.8%, Middle 46.8 ± 2.7%, Posterior 53.7 ± 6.1%. The value of each single cell is represented as blue circle (anterior), green cross (middle) and magenta asterisk (posterior), and medians with interquartile ranges are shown as bars in each plot. Due to small number of samples in the posterior region, Dunn's multiple comparisons test was run between values from the anterior and middle regions.

Subsequently, we looked into whether response properties related to cell location. The dataset was further categorized according to transient/sustained, linear/non-linear and DS/OS response properties, and features were investigated correspondingly. Due to the small number of cells obtained from the posterior LGN, we were unable to conduct statistical analysis on response properties from this location. Still, we did not notice any functional trends related to anatomy in the transient/sustained and linear/non-linear cells.

Cells responding preferably to directions of motion have been recently established in mouse LGN (Piscopo et al., 2013; Zhao et al., 2013), interestingly, these cells were found to be regionally restricted to the dorsal-lateral LGN, corresponding to where DSRGCs projected to (Piscopo et al., 2013). Therefore, we sought to investigate the relevance of direction/orientation preference to cell locations in this study as well.

To probe precisely the location of each DS/OS cell, we took advantage of the LGN volume by mapping confocal image of electrode track and electrode site with the three-dimensional (3D) LGN model, and therefore were able to decide the exact position of each cell in 3D (protocols and example results described in Chapter 5). This procedure was performed for all

of the recordings that had DS/OS cells and the summarized data was exported to MATLAB as shown in Figure 3.19. The bottom panel displays a side view of the LGN volume (pink), with all DS/OS cells categorized as locating within the anterior, middle or posterior LGN. This categorization of subregions resulted from dividing the LGN volume evenly into three along the anterior-posterior axis, and it is observed from the bottom panel that all units could be classified without ambiguity. The front view is presented in the top panel, demonstrating that positions of the DS/OS cells spanned the entire LGN along the ventral-dorsal axis. Nearly all of the units were in the middle of LGN on the medial-lateral axis, this was due to the design of electrode penetration. It is observable from Figure 3.19 that most DS/OS cells in the dataset were recorded from the middle LGN.

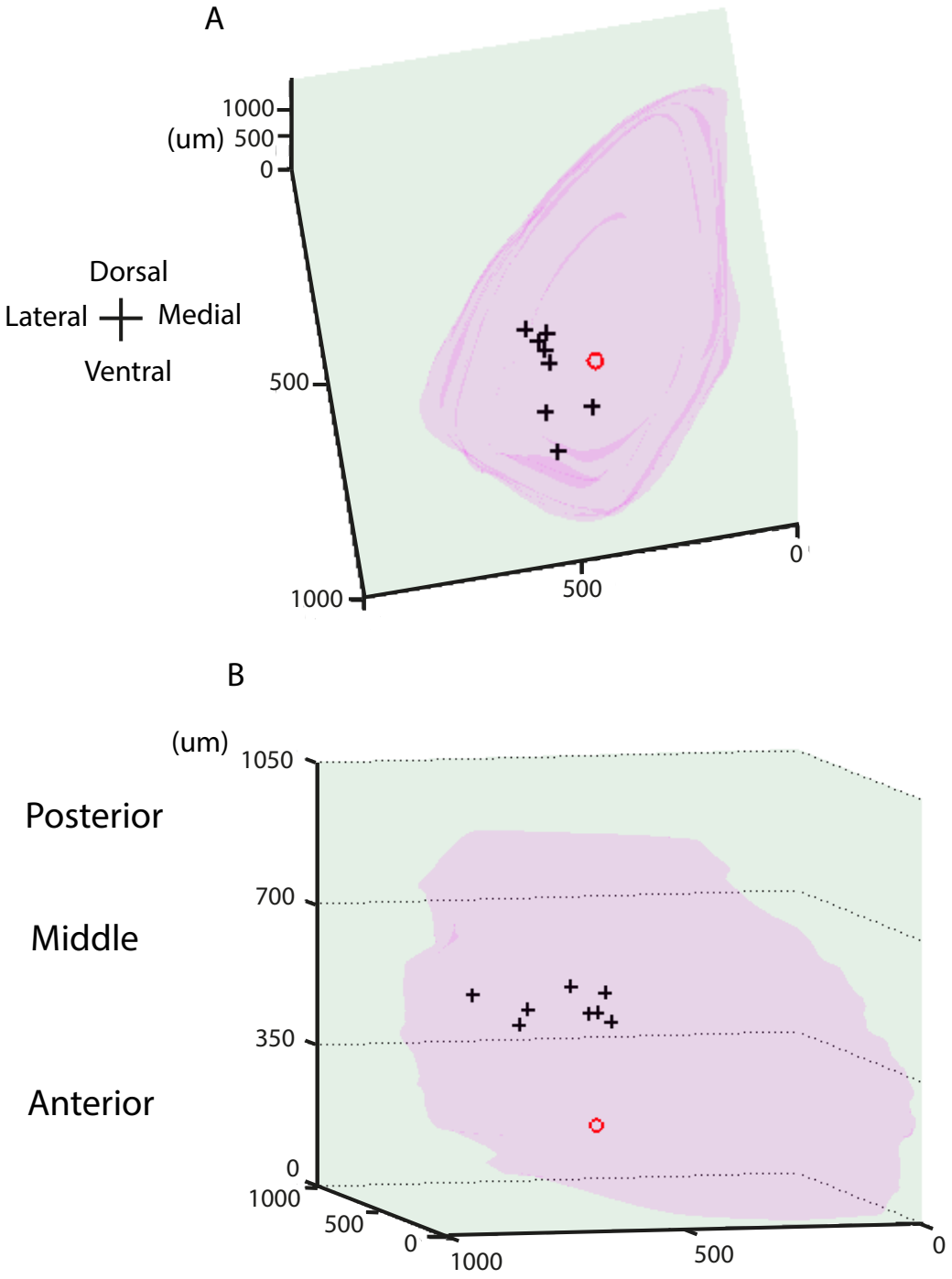

Figure 3.19 The location of each DS/OS unit within the LGN volume developed in Chapter 5. The location was decided by mapping confocal image of electrode track and electrode site with the LGN volume. The LGN volume (pink) was categorized as anterior, middle and posterior subregions. 1 and 8 DS/OS cells fell into the anterior and posterior region, which are illustrated as red circles and black cross respectively. Scales represent the actual dimensions in μm. Top panel and bottom panel show the front and side view of the location of each DS/OS cell within the LGN volume.

3.4 Summary and discussion

In this study, comprehensive response characterizations were conducted on mouse LGN cells that displayed centre-surround receptive fields, both in aspects of volumes and response parameters. We re-characterized features that were consistent with other mouse LGN electrophysiological studies (Grubb and Thompson, 2003; Piscopo et al., 2013), including receptive field properties, baseline spontaneous response amplitudes, spatial frequency tuning properties and sustained/transient responses of cells. This approach served as a reference point before the comparison of other parameters and investigation of novel features. At single cell level, a few novel individual response properties are established, including low-pass and high-pass in temporal frequency tuning curves. We identified the existence of DS/OS cells in mouse LGN and further explored locations of DS/OS cells within this nucleus, which added to the weight of understanding on DS/OS origins. We also report that ON- and OFF-centre subtypes exhibited functionally distinctive features. Consequently, these results can help to determine stimulus parameters effective for probing vision in mouse LGN in future studies. Moreover, the characterization of unexpected properties and evidence of parallel projections broaden our understanding on functionality of this nucleus and suggest that more sophisticated features might be encoded subcortically than previously thought.

This section relates our findings with other studies in visual system of both mice and other species, and the functional implications and limitations will also be discussed. I will start with a few general considerations in the experimental design that might contribute to the neuronal responsiveness and selectivity (Section 3.4.1). Subsequently, single cell response properties will be compared with other available investigations, particularly with regard to classical receptive fields, direction/orientation selectivity (Section 3.4.2). Next, I will evaluate the differences in response properties between ON-/OFF- centre cells and also assess the strength of functional parallel pathways that can be made from these observations (Section 3.4.3). I will also discuss constraints as well as potential improvements in Section 3.4.2 and 3.4.3 to extend current understanding on electrophysiological features of mouse LGN at single cell level.

3.4.1 General considerations

3.4.1.1 Mouse eye movements

In primates, the purpose of saccadic movements is to bring images of particular areas of the visual field to fall onto the fovea, which is a region representing approximately 1% of the retina (Perry and Cowey, 1985) and critical for resolving objects. Absence of fovea in mice results in head movements being functionally more important than eye movements in viewing specific parts of the visual fields (Huberman and Niell, 2011).

It was found in anesthetized C57Bl/6 wild type mice that eye movements were not a critical problem in quantitative analysis, even though the animals were not paralyzed (Wagor et al., 1980). Earlier studies in mouse LGN and visual cortex (Métin et al., 1988; Grubb and Thompson, 2003) have shown that the magnitude of receptive field shifts due to eye movements but are negligible compared to the average receptive field sizes.

To ensure that there was minimal interference of head movements, all recordings in this study were made from head-fixed animals. Our observation from recordings made from the same site but with different levels of anesthesia revealed that the receptive field locations had little or no shifts over approximately 2hrs of recording. As a result, we consider mouse eye movements to have no confounding impact on cell response characterization and therefore can be spared as a parameter in this study.

3.4.1.2 Electrophysiological recordings from mouse LGN

A few novel aspects in the experimental design played a key role in data acquisition, providing reliable approaches to reveal functional properties of mouse LGN in this study.

Compared with injectable anaesthetics, the inhalation anaesthesia protocols with isoflurane as the main agent greatly improved the success rate of surgery, and maintained stable state of anaesthesia over extended periods of recording. In addition, the specifically designed nose cone (Figure 2.1) featured minimal interference with characterizations of the visual regions recorded from.

The use of MEAs served to record both spikes and LFPs (discussed further in Chapter 4). The MEA's configuration covered the full extent of mouse LGN along dorsal-ventral direction, and therefore allowed a thorough investigation of response properties. Together with the customized designed 16-channel audio splitter (Section 2.4.2), our data acquisition

system also featured real-time monitoring of neuronal activity that was crucial in hand mapping of receptive field.

Moreover, with the development of the LGN targeting protocols based on our stereotaxic apparatus, we were able to maintain and control electrode locations precisely across animals, regardless of LGN's small volume (0.30 ± 0.02 mm^3 in C57Bl/6 wild type) (Seecharan et al., 2003) and deep localization (2.6 ~ 3.2 mm below the pia) (Franklin and Paxinos, 2007) in the mouse brain.

Finally, the use of custom-designed rotatory rail mounted under the monitor (Figure 2.2) enabled its smooth rotation corresponding to receptive field mapped by hand initially and to cover visual fields of as many cells as possible. More importantly, the rail maintained the distance from the monitor to the animal eye at 25 cm.

3.4.2 Single cell response properties in mouse LGN

3.4.2.1 Classical ON-/OFF- centre receptive fields

Section 3.3.2.2 has presented successful extraction of spatial receptive field information from mouse LGN neurons. These neurons could be categorized as ON- or OFF- centre cells according to their increased or decreased firing activities to bright stimuli placed in receptive field centres. Additionally, receptive field size was approximately 6.5 deg in radius. This value was relatively larger than those reported in cat and monkey LGN, but remained comparable with sizes in mouse retina and V1 from earlier studies (Chalupa and Williams, 2008; Niell and Stryker, 2008). These features also paralleled two key studies in mouse LGN (Grubb and Thompson, 2003; Piscopo et al., 2013).

However, in this study, we only included cells that had receptive fields successfully computed from STA technique that comprised approximately 50% of all single units obtained from spike-sorting. Contrastingly, in the recent research on mouse LGN, Piscopo et al. (2013) took advantage of a clustering algorithm, and therefore investigated the entire response profile regardless of cell firing activity and receptive field property. As a result, in addition to the standard ON- and OFF- centre cells that formed the majority, two other subpopulations were revealed in their paper: direction/orientation selectivity and suppressed-by-contrast cells. Interestingly, 7.0% (9/129) cells exhibited direction/orientation selectivity in our dataset. Direction/orientation selectivity will be discussed in more details in the

following section. However, our observation does not support the notion that direction/orientation selectivity and ON-/OFF- receptive fields are entire separable features in mouse LGN as claimed by Piscopo et al. (2013).

On the other hand, we did not record from any cells that fired in a "suppressed-by-contrast" pattern as reported by Piscopo et al. (2013). This rarely encountered response type has been demonstrated in a few other studies, for instance, in monkey LGN (Tailby et al., 2007), cat retina (Rodieck, 1967), and also V1 of behaving mice (Niell and Stryker, 2010). One plausible explanation for its absence in this study is due to the selection criteria applied for cell inclusion, and this particular cell type was excluded from the data pool. Alternatively, given that these cells responded "inversely" compared to the rest of units (the decrease in baseline activity was at the same magnitude as the increase in firing rate seen in other cells) (Piscopo et al., 2013), it is possible that these cells were interneurons and inhibited responses to incoming stimuli.

There was a small number of cells ((4/189, 2.1%)) from 4 separate recordings that displayed the classical receptive field structure, yet could not be driven by any sinusoidal gratings. Looking into the receptive field properties of these cells, no trends were found from the responses to full-field flickers or cell locations in LGN that could be different from the rest of the cells in the dataset. Similar findings were reported in a study on LGN in owl monkeys (Xu et al., 2001), in which 9% of M cells, 6% of P cells and 34% of K cells were not responsive to grating stimuli. Being further quantitatively tested, heterogeneous responses were revealed among these monkey LGN neurons, including those only responding to changes in luminance, or moving bars. It would be interesting to investigate the functionality of these "non-responsive" cells by presenting other forms of stimuli, and study how they contribute to information processing in mouse LGN in future studies.

In conclusion, our dataset, which takes into account of mouse LGN neurons displaying centre-surround receptive fields, highlights the existence of cells with direction/orientation selectivity as well as a small population of "heterogeneous-responsive" cells that could not be triggered by grating stimuli.

3.4.2.2 Direction/orientation selectivity

Section 3.3.2.6 presents results showing a small fraction of cells (7.0% or 9/129) that responded preferably to directions of motion. The OS cell has been initially reported in

monkey LGN (Cheong et al., 2013), and three recent studies have revealed the existence of DS/OS cells in mouse LGN (Marshel et al., 2012, Piscopo et al., 2013, Zhao et al., 2013). Our data echoes these findings and suggests that more sophisticated properties are encoded in LGN than previously thought.

We further compared response features of the DS/OS cells with the overall dataset in Section 3.3.3.2, and explored in Section 3.3.4 whether preferred angles and cell density displayed a regional bias in mouse LGN. Compared with other investigations in this field (Marshel et al., 2012; Piscopo et al., 2013, Zhao et al., 2013), a few properties were of similarity and variance in our dataset that will be explicitly discussed in the following section. These features raise the issue of potential sources for DS/OS response patterns in mouse LGN cells, which mainly include inheriting from DSRGCs, feedback from the superior colliculus and layer 6 in V1 as well as from convergence:

- **Inheriting directly from DSRGCs.** Our results indicated that the LGN DS/OS cells showed a tendency towards higher spatial frequency sensitivity. Furthermore, selectivity was mostly restricted to the four cardinal axes. All these features are consistent with DSRGCs' characteristics (Weng et al., 2005). Therefore, our data supports the assumption that the selectivity in LGN is probably derived from the DSRGCs. From our observation in Section 3.3.4, however, the majority of DS/OS cells located within the middle LGN along the ventral-dorsal axis. This observation might result from the larger sample size in the middle area and did not display significantly higher density within the area where DSRGC axons terminate (posterior and dorsolateral shell of LGN) as reported by Piscopo et al. (2013). These observations on the topography of DS/OS cells imply that there are probably other contributing elements to the source of DS/OS cells in LGN other than the DSRGCs.

- **Feedback from layer 6 in V1 and the superior colliculus.** As introduced in Section 1.2.5, the retinal inputs merely comprise 5%~10% synapses onto the LGN relay neurons (Ahmed et al., 1994; Latawiec, 2000). It is therefore plausible that directional/orientation selectivity in LGN derive from other non-retinal sources. We report that all of the DS/OS cells in this study were non-linear. Along with the fact that DS/OS cells in V1 are primarily simple and linear cells (Niell and Stryker, 2008), such inconsistency did not support the hypothesis that selectivity was superimposed back on LGN from the cortex. Zhao et al. (2013) and Scholl et al. (2013) also tested cortical contribution by silencing cortex

pharmacologically. They found no changes in the selectivity in LGN, therefore ruling out such a possibility. There is also evidence that the superior colliculus exhibit OS receptive fields (Wang et al., 2006). However, together with cortical feedback, these sources of input are more likely to be modulators, unlike retinal inputs that strongly drive depolarization in LGN (Sherman and Guillery, 1998, 2006, 2011; Sincich et al., 2007).

- **From convergence.** In the research conducted by Zhao et al. (2013), one third of OS LGN cells had a single elongated receptive field that could result from the summation of two circular retinal receptive fields with a slight offset in location. This assumption could provide a basis for the selectivity. The other two thirds had circular receptive fields. One possibility could be that LGN cells summed two DSRGCs with opposite preferred direction that leading to orientation selectivity (Marshel et al., 2012). Of the nine DS/OS cells characterized in this study, 33% (3 of 9) of them displayed non-circular receptive fields (receptive field size ratio was out of the range from 0.7 to 1.3, detailed in Section 3.3.2.2). Further connectivity characterization, taking advantage of genetic markers and functional imaging, may be able to clearly distinguish these mechanisms apart.

These DS/OS cells and their characteristics add to the understanding of functionality in mouse LGN. Compared to the standard model in which direction/orientation selectivity was computed anew in the cortex, it has been increasingly recognized that relay cells in LGN could convey information on direction/orientation preference. Further, two mechanisms might contribute to the generation of direction/orientation selectivity in mouse LGN. One is direction/orientation selectivity deriving directly from the DSRGCs, while the other is from elongated receptive fields in LGN due to summation of two retinal receptive fields having spatial offset (Figure 3.20). By taking advantage of the LGN volume (see details in Chapter 5), our results demonstrate that DS/OS cells are prevalent in mouse LGN and are not restricted to the area that DSRGCs projecting to. Although the characterization presented cannot conclusively determine where these DS/OS cells come from, it provides valuable evidence for experimental and computational study in future.

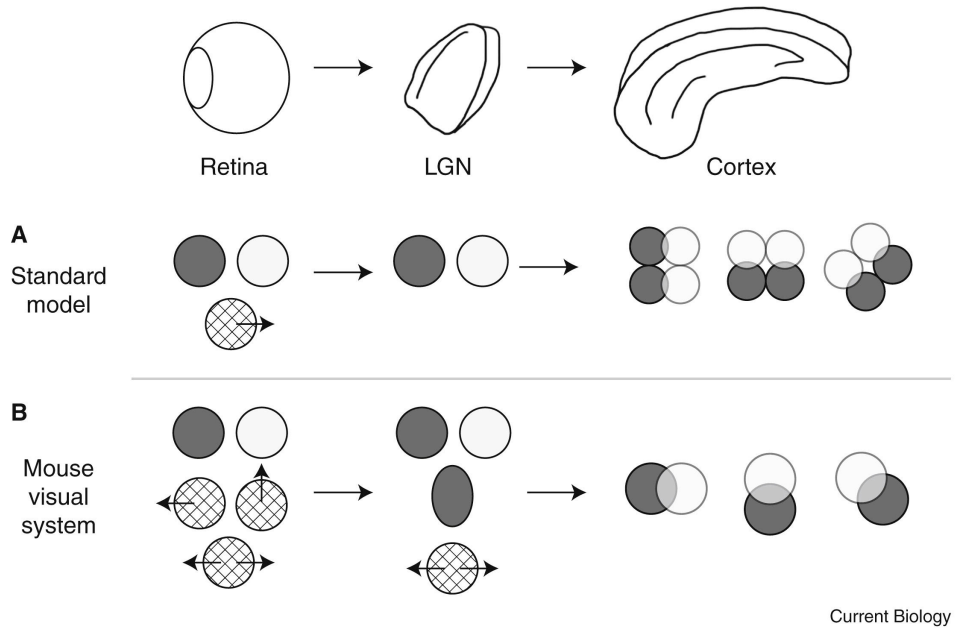

Figure 3.20 Standard and current models of the visual system in direction/orientation selectivity. A. The standard model of Hubel and Wiesel, DSRGCs are present in the retina, however, they do not project to the cortex. The direction/orientation selectivity in the cortex is due to the summation of aligned unturned subcortical inputs. B. Updated models of direction/orientation selectivity in the visual pathway. Two possible mechanisms might contribute to the generation of direction/orientation selectivity in LGN: deriving directly from DSRGCs or summation of two retinal receptive fields that results in an elongated spatial receptive field structure. Thalamic inputs to the cortex is assumed to result from aligned unturned units. This figure is taken from Niell (2013).

3.4.2.3 Other response properties

One goal of this study was to quantitatively compare the functional performance of mouse LGN with previous studies. Table 3.5 summarizes results from this study and other two significant investigations in this field: the classical characterization from Grubb and Thompson (2003) and the other more recent dedicated analysis (Piscopo et al., 2013) (only sustained ON- and sustained OFF- subtypes were included here for simplification). As observed from Table 3.5, some response characterizations were missing from either of the previous studies. From this perspective, our study provides a more thorough quantification of mouse LGN neurons.

Parameters including baseline spontaneous activity, receptive field radius and preferred spatial frequency are comparable to both the earlier studies (Grubb and Thompson, 2003; Piscopo et al., 2013) (Table 3.5). The re-characterization of these properties acted as a reference point in the research of mouse LGN in this study before looking into other parameters and establishing novel response features.

Described in Section 3.3.2.4, a small number of cells (3.5% or 2/57) in our dataset were found to respond preferably to exceptionally low temporal frequency and display a low pass-filtering pattern that had not been previously observed in mouse LGN. These cells were obtained from 2 separate animals, and remained consistent with the population dataset in baseline responsivity and receptive field properties. Although the low-pass cells were sparse in quantity, it is unlikely that their responsivity resulted from spurious recordings. In addition, such low-pass responses in temporal frequency tunings have been reported in visual cortex of monkeys (Foster et al., 1985) and cats (Movshon et al., 1978a) that suggested to represent distinct temporal-frequency-selective mechanisms (Foster et al., 1985).

Interestingly, our results show that these low-pass cells established extremely poor contrast sensitivity (with contrast gain 0.09 spikes/s/% as maximum). A possible hypothesis of this informal observation is that stimuli at non-optimal temporal frequency lead to loss of contrast sensitivity. Similarly, temporal frequency related low contrast sensitivity has been revealed in monkeys (Derrington and Lennie, 1984; Solomon et al., 1999) and cats (Troy, 1983). A future direction might be to perform targeted recordings with stimuli that contain temporal variance in the mouse LGN.

Results in section 3.3.2.5 reveals that for contrast sensitivity measures, although tuning curves differed at single cell level, all cells showed increasing response amplitude with increasing contrast. However, the overall population tended to be notably more responsive (with a mean of contrast gain 0.98 ± 0.04 spikes/s/%) than the data examined by Grubb and Thompson (2003) (with a mean of contrast gain 0.47 ± 0.05 spikes/s/%) that served as the only existing result we could compare to in mouse LGN (Table 3.5). One reason that could possibly lead to the difference is the animals used for electrophysiology: mice from both sexes and older than 3 months were used in Grubb and Thompson's study (2003), whereas the current data was recorded from female mice aged 2~4 months. Alphen et al. (2008) argued that contrast sensitivity of C57Bl/6 mice could vary greatly between sexes and between mice that differed only a few months in age as the responsivity of photoreceptors decrease with aging. Alternatively, different anaesthetics might also be able to account for distinct contrast sensitivity. In primate LGN, Solomon et al. (1999) suggested that contrast sensitivity could be altered by different anaesthetics (isoflurane vs. sufentanil). Similar characteristic might be applicable to mouse LGN as well and could explain contrast

sensitivity difference observed with fentanyl (Grubb and Thompson, 2003) and isoflurane (this study) anaesthetized mice. Hence, from the perspective of contrast performance, it is essential to use groups matched for sex and age, otherwise differences in visual capabilities might influence results. It will also be informative to compare different anaesthetics and investigate their effects on contrast sensitivity in the mouse LGN.

Table 3.5 Comparison of single cell response properties in mouse LGN from two published works (Grubb and Thompson, 2003; Piscopo et al., 2013) and this study.

	Grubb & Thompson (2003) (*)	Piscopo et al. (2013) (**)		Data from this study
		Sustained (ON)	Sustained (OFF)	
No. of cells	133	64	28	185
Spont activity (spikes/s)	3.24 (**)	1.0 ± 0.28	1.7 ± 0.35	2.0 (0.9, 4.3)
Evoked activity (spikes/s)	-	4.0 ± 0.51	4.6 ± 0.83	7.3 (3.7,13.0)
RF radius (deg)	5.6	5.8	8.0	6.5 (5.3, 8.1)
ON cells	62%	-	-	48.6%
Preferred SF (c/deg)	0.027 (**)	0.05 ± 0.006	0.03 ± 0.003	0 (0, 0.04)
SF cutoff (c/deg)	0.18 ± 0.009	-	-	0.19 (0.11, 0.33)
Preferred TF (Hz)	3.95 ± 0.24	-	-	3.4 ± 0.1(*)
TF $high_{50}$ (Hz)	7.26 ± 0.40	-	-	7.1 ± 0.2 (*)
TF low_{50} (Hz)	-	-	-	1.0 ± 0.1 (*)
Contrast gain (spikes/s/%)	0.47 ± 0.05	-	-	0.98 ± 0.04 (*)
Contrast C_{50} (%)	32.53 ± 2.18	-	-	50.1 ± 2.0 (*)
Fraction of linear cells (%)	97%	-	-	14.1%
Fraction of sustained cells (%)	50	-	-	7.3

Spont activity: spontaneous activity; RF radius: receptive field radius; SF: spatial frequency; TF:temporal frequency; Trans/sust:transient/sustained. (*): mean ± SEM. (**): median value. Values from Grubb and Thompson (2013) were all presented as mean ± SE unless specified. Data from this study: (*) shows mean ± S.E.M., the rest are presented in the format of median (25 percentile, 75 percentile).

Overall, compared to data reported by Grubb and Thompson (2003) and Piscopo et al. (2013), single cell response properties characterized in this chapter were obtained from a relatively larger sample size and also provided a more comprehensive investigation of mouse LGN by characterizing more parameters. This broad characterization will consequently contribute to functional modelling of mouse LGN and should also benefit future studies by providing the relevant range of stimulus parameters that are effective in driving the strongest responses. It has also highlighted some crucial experimental considerations for future research, namely that it is important to further investigate cells with exceptional features, including non-responsive cells to gratings and low-pass responses in temporal frequency tunings.

3.4.3 Functional parallel pathways in mouse LGN

Unlike the cat and monkey LGN, which have clear laminar segregation related to the parallel pathways that originate from the retina, mouse LGN is not laminated (introduced in Section 1.2.2). Dataset was divided into a few functional subtypes, including ON-/OFF- centre, transient/sustained and linear/non-linear cells and evidence of parallel pathways within this nucleus was investigated (Section 3.3.3). An overview of the findings will be presented here. I will further relate the results to what has been known about single unit activity in corresponding subtypes in LGN and V1 in mice and other species in this section, and the functional implications of parallel projections will also be discussed.

3.4.3.1 ON-/OFF- centre cells

As detailed in Section 3.3.3.1, our data suggests that ON- and OFF- centre cells were comparable in fractions among the dataset, receptive field size, spontaneous and evoked activities, spatial frequency tuning properties, as well as proportion of linear cells and transient responsive cells (summarized in Table 3.6).

Interestingly, we found that ON- centre cells were more sensitive than their OFF- centre counterparts over both contrast parameters. These differences were in agreement with other ON- and OFF- neuronal comparisons in the primate retina (Chichilnisky and Kalmar, 2002) and mouse LGN (Grubb and Thompson, 2003), and suggest that parallel pathways through ON- and OFF- centre cells is a visual system feature conserved across species and brain regions.

Moreover, our results indicated that OFF-centre cells showed higher degree of selectivity in temporal frequency tuning properties. Specifically, OFF- centre cells possessed significantly higher preferred temporal frequency, broader tuning bandwidth and higher low_{50}s. However, Lanhkeet and colleagues observed that ON- centre cells had faster response kinetics than OFF- counterparts in the primate visual system (Lanhkeet et al. 1998). This might reflect a species difference, as the mouse being nocturnal. It will be of interest to explore whether different characteristics between ON- and OFF- centre cells at the thalamic level have any impact on cortical responses or visual behaviour.

3.4.3.2 Transient/sustained cells

We identified transient/sustained classification from responses to full-field flicker, and this classification applied to both ON- and OFF- centre cells, which was in accordance with the observation of Grubb and Thompson (2003). Further compared with their result (transient cells: n=23, 50%), we report a higher proportion of transient units (92.7% or 114 of 123).

In contrast, Piscopo et al. (2013) demonstrated that transient property was restricted to neurons with OFF- rather than ON- centre receptive fields. They further proposed that the absence of ON-transient type was in correspondence with physiological properties of mouse alpha ganglion cells (Murphy & Rieke, 2006; Margolis & Detwiler, 2007), which provided the primary input to the canonical pathways. However, study performed by Brown et al. (2011) showed that other forms of retinal inputs to LGN, such as rod signals, appeared to own extensive sensory capabilities and could also drive an array of responses in mouse LGN, including transient “ON” and “OFF” excitation.

Comparing the response properties, we observed that for transient neurons, the response latency calculated from spatial frequency stimulus was higher than those of sustained neurons (Section 3.3.3.3). However, the transient and sustained responsive cells overlapped considerably in latencies calculated from the flicker stimuli. Moreover, the cutoff spatial frequency of sustained neurons was far higher than the values observed among transient ones in general (Section 3.3.3.3).

These characteristics may reflect response differences between the transient and sustained neurons to spatial frequency stimulus, specifically, higher spatial resolution correlated with shorter response latency. Although response latency differs greatly between transient and sustained neurons in the visual system among other species (Ikeda and Wright, 1975;

Maunsell et al., 1999; Hooser et al., 2003), there was lack of evidence to support such feature applicable to mouse LGN.

Interestingly, we find that sustained cells exhibit a much higher level of contrast sensitivity than transient neurons (Table 3.2). In contrast, in the population of DS/OS cells, all of cells (100%, 9/9) responded in a transient fashion. It is possible that this higher prevalence is a consequence of more transient (92.7%, 114/123) than sustained (7.3%, 9/123) responsive cells within the entire sample. Alternatively, combined with comparisons noted above in spatial frequency tuning, they might indicate that transient and sustained cells respond to different aspects of visual inputs: transient cells code for direction or orientation selectivity, whereas sustained cells being more involved in spatial and contrast characterization of the visual stimulus, as it has been reported in the cat retina of transient/sustained categorization (Ikeda and Wright, 1972c; Ikeda and Wright, 1975).

In addition, we observed that the percentage of linear and nonlinear cells between transient and sustained cells did not differ significantly (Section 3.3.3.3), which led to our suggestion that transience and nonlinearity were independent properties in mouse LGN. It was suggested from early studies of X- and Y- cells in the cat (e.g. Hochstein and Shapley, 1976a) that response transience and nonlinearity of spatial summation was highly correlated. Nevertheless, evidence from at least two species showed separation between transience and nonlinearity: some magnocellular neurons in macaque monkey (Kaplan and Shapley, 1982) were transient and linear, whereas all sustained neurons in rabbits were nonlinear (Swadlow and Weyand, 1985). These differences together supported the assumption raised by Hooser et al. (2003) that the co-occurrence of transience and nonlinearity can vary greatly from species to species due to waking behaviour or habitat.

3.4.3.3 Linear/non-linear cells

Nonlinearity in LGN has been established in numerous investigations in primates and cats. For example, M- cells in primate LGN, displaying similar spatial nonlinearities as Y- cells of cats (Dhruv et al., 2009), could be characterized by nonlinearities including contrast saturation (Derrington and Lennie, 1984), surround suppression (Cleland et al., 1983; Solomon et al., 2002) and phase advance (Kaplan and Shapley, 1982). However, the nonlinearity in mouse LGN has not been widely accepted: from both the quantitative studies of this nucleus, nearly all units that had centre-surround receptive fields were reported to

respond in linear pattern (Grubb and Thompson, 2003; Piscopo et al., 2013). In contrast to above listed investigations on mouse LGN, we found in the current study that a substantial percentage of cells (85.9% or 79/92) showed nonlinear spatial summation (Section 3.3.2.9 and 3.3.3.3). This high fraction of nonlinear cells in our dataset might be attributeed to the analysis method, in which F0 and F1 were measured as averaged responses across gratings with all the different spatial frequencies from 0.02 c/deg to 0.96 c/deg. In the following work, it might be of interest to re-calculate the F1/F0 index as neuronal responses to the spatial frequency parameter that closest to the preferred value.

Looking into other response features, we notice that properties including response amplitudes, spatial and temporal tuning curves and contrast sensitivity overlapped considerably between the linear and nonlinear cells (Section 3.3.3.3), in contrast to marked differences between X- and Y- cells in cats (e.g. Schwartz and Rieke, 2011). The homogeneity in response property between linear and nonlinear cells has been reported in the mouse retina as well (Stone and Pinto, 1993), where over 10% of RGCs were found to respond non-linearly. One striking feature observed in our characterization is that the nonlinear cells exhibit a higher ratio of DS/OS cells (6.3%) than the linear cells (0%). It leads to the postulation that subcortical nonlinearities in mice are able to represent complex visual patterns such as direction/orientation preference that is indicative of parallel projections. This postulation is supported by a study in the cat visual system, where the principle finding is that Y-cells, but not X-cells in the cat LGN are likely to underlie complex cortical responses to interference patterns including carrier orientation selectivity (Rosenberg et al., 2010). The initial characterization of the nonlinear population in this study also raised several fundamental questions for future investigation, for instance, are there other aspects in response feature to distinguish linear and nonlinear cells? What is the origin of these nonlinear cells and what is their functional impact on V1?

We probed the locations of the linear/nonlinear units with similar protocols applied for Figure 3.19 and did not reveal obvious spatial segregation that could correlate to the morphological X-/Y- like cell distribution noted by Krahe et al. (2012). These authors claimed that X- likes cells resided near the ventral border within LGN, whereas Y- like cells were evenly dispersed throughout a central core. This observation that linked linearity with cell location implies that linearity may not be the appropriate distinguishing criterion that correlates with X-/Y- morphology and spatial segregation.

To sum up, we discussed in this section the comparison of response properties in mouse LGN with previous studies on mice and other species, and proposed possible explanations and implications to differences. We also discussed cell characteristics based on selectivity to direction/orientation, nonlinearity and possible functional parallel projections of mouse LGN. These findings may imply that more elaborate and diverse visual features are encoded in the mouse visual thalamus, which is able to dynamically modulate visual inputs before relaying them to V1.

Appendix

Table 3.6 Response properties of ON- and OFF- cells.

		ON-cells	OFF-cells
No. of cells		90 (48.6%)	95 (51.4%)
Spontaneous firing rate (spikes/s)		2.0 (0.8, 4.4)	1.9 (0.9, 3.9)
Evoked firing rate (spikes/s)		6.4 (3.4, 13.8)	7.6 (3.7, 11.8)
Receptive field radius (deg)		6.7 (5.5, 8.0)	5.9 (4.9, 7.9)
Spatial frequency tuning properties	Preferred	0 (0, 0.04)	0 (0, 0.04)
	Cutoff	0.20 (0.12, 0.34)	0.19 (0.10, 0.31)
Fraction of linear cells		5 (11.9%)	8 (17.7%)
Fraction of transient cells		3 (4.8%)	6 (9.8%)
Contrast	Gain (spikes/s/%)	1.10 ± 0.05	0.87 ± 0.06
	C_{50} (%)	47.3 ± 3.1	56.2 ± 3.3
Temporal frequency tuning properties	Preferred (Hz)	3.1 ± 0.1	3.6 ± 0.2
	Bandwidth (Hz)	4.9 ± 0.3	6.5 ± 0.3
	$High_{50}$ (Hz)	7.2 ± 0.4	7.6 ± 0.3
	Low_{50} (Hz)	0.7 ± 0.1	1.0 ± 0.1

CHAPTER 4

State-dependent neuronal activity in mouse LGN

4.1 Introduction

In this chapter, we investigate LFPs in the LGN and primary visual cortex in mice under different anaesthesia states by adjusting isoflurane concentrations, and also the functional impact of the states on single-cell response properties in LGN.

As introduced in Chapter 1, in a complex environment, animals constantly switch between different behavioural states that are normally associated with prominent changes in cortical circuits to control the way information is being processed (Gervasoni et al., 2004). Measuring electrophysiologically, we now know that the cortical state is a function of the sleep-wake cycle: during non-REM sleep and quiet wakefulness, the cortex operates in a "synchronized" state, characterized by high-amplitude and low-frequency fluctuations in the cortical activity, whereas during REM sleep and alertness, low-frequency LFP power is decreased and the corresponding cortical state is referred to as the "desynchronized" state (Harris and Thiele, 2012).

A growing body of studies has been investigating the state-dependent cortical control of information flow in rodents to answer two fundamental questions: mechanisms controlling cortical states and functional significance of cortical states. Several mechanisms have been implicated in cortical state transitions, including the broad projecting neuromodulatory systems (e.g. those releasing acetylcholine (Ach), norepinephrine (NE), serotonin (5-HT), dopamine (DA)), as well as fast glutamatergic and GABAergic projections from the thalamus and potentially other cortical areas (McCormick and Bal, 1997; Lee and Dan, 2012; Castro-Alamancos, 2004; Poulet et al., 2012). Functionally, it has been demonstrated that desynchronized cortical activity normally observed in attention and arousal states can greatly

enhance sensory processing (Poulet et al., 2012), whereas the synchronized state prevalent in sleep and quiet wakefulness may be more suited for "offline" functions including memory consolidation and synaptic scaling (Marshall et al., 2006; Xu et al., 2012).

At the subcortical level, apart from being a major pathway through which the neuromodulatory inputs regulate cortical function, the thalamus can directly influence cortical states. For instance, it has been suggested that the tonic-firing mode of thalamic neurons (typically observed during alertness and attention) could effectively trigger the desynchronization of the cortical area that received the inputs (McCormick and Bal, 1997; Sherman, 2005; Hirata and Castro-Alamancos, 2010). Interestingly, cortical states, in turn, are able to affect the burst/tonic firing of neurons in the thalamus. Experimental evidence has suggested that thalamic relay neurons tended to fire in the bust mode during the synchronized cortical state (Sherman, 2001).

Several investigations have set out to look into the influence of brain states such as anaesthesia and alertness on single-cell response properties in LGN of monkeys and rabbits, and shifts in neuronal excitability as well as tuning functions have been reported (Cano et al., 2006; Alitto et al., 2011; Hei et al., 2014). In mice, Niell and Stryker (2010) established that the response amplitude in LGN was independent of the still or running state of the animal. In general, however, little is currently known about the functional impact of brain states on single-cell response properties in mouse LGN. We therefore sought to provide a better understanding of this topic in this chapter. Our first aim was to study LFPs in mouse LGN and V1 in distinct states, differentiated by depths of anaesthesia. The second aim was to examine if response properties of single units in LGN were modulated by the states.

The second part in this chapter (Section 4.2) presents a reminder of the experimental procedure and data analysis process. Briefly, simultaneous recordings from LGN and V1 with two separate MEAs were performed on isoflurane-anesthetized mice. A battery of visual stimuli was presented with the same animal at both deep (1.5~2.0% isoflurane) and light levels of anaesthesia (0.3~0.5% isoflurane). In addition, theta/delta (θ/δ) ratio, defined as the ratio of LFP power in 4~8 Hz against 1~4 Hz, was applied to discriminate the state corresponding to the isoflurane concentration.

In Section 4.3, from a sample of four animals, the results firstly indicated that LFPs in V1 exhibited distinct patterns between high and low concentrations of isoflurane, which resembles the synchronized and desynchronized cortical states respectively. We further reported that the θ/δ ratio was able to effectively discriminate the high and low isoflurane states throughout the presentation of various visual stimuli in both V1 and LGN, with the θ/δ ratio obviously higher in the low isoflurane state than the high isoflurane state. In addition, the θ/δ ratio between these two brain areas were correlated, especially in the low isoflurane state. These novel results suggest that changing isoflurane concentration acts as a good model for this "state-dependent" LFPs in general. Additionally, V1 and LGN in mice are strongly and reciprocally interconnected in reflecting brain activity.

Related to the second aim of this chapter, the θ/δ ratio was calculated in 25 recordings obtained from mouse LGN with the animal in either the high or low isoflurane state, and its relationship with single-cell response properties was subsequently investigated. Interestingly, our results show that as the θ/δ ratio going higher (the animal being more lightly anaesthetized), the response latency decreases, and the contrast sensitivity increases, also the neurons tend to be responsive to the gratings moving at higher spatial frequencies as well.

Section 4.4 of this chapter starts with a summary of the findings, followed with a discussion on what has been known about brain states and possible implications and challenges of this study.

4.2 Methods

All recordings were carried out on the same stereotaxic apparatus, and the same preparation and surgery procedures were followed as described in Chapter 2. A larger rubber ring (approximately 4.5 mm in diameter) and craniotomy were applied to achieve a larger area of exposed brain.

The recording was made from two separate 32-channel-MEAs (A1*32-5mm-25s-177 for LGN and A4*8-5mm-100s-200-177 for V1, NeuroNexus). The target coordinate for LGN was set as 2.15 mm lateral and 2.6 mm posterior from the Bregma point (the middle LGN). A second micromanipulator (MM-3, Narishige) was mounted onto a stand (501623, WPI, UK) for the V1 electrode (Figure 4.1). The same set of headstage, electrode adaptor and ground wire as the LGN recording was duplicated. To avoid interference of the second

manipulator, the V1 electrode adaptor was customized to mount onto its manipulator through a bar (Figure 4.1).

The setup for recording from V1 was positioned before craniotomy and the V1 electrode was lowered onto skull surface to confirm the coordinate that was in the monocular region of left V1 according to the brain atlas (Paxinos and Franklin, 2008). We considered placing the V1 electrode as close as possible to the aimed LGN coordinate, and also minimizing interference of the two electrodes or extra tissue damage. Therefore, the V1 electrode was usually inserted at an angle between 25~45 deg to the horizontal plane, and 200~400 μm posterior and lateral compared to the LGN coordinate (Figure 4.1). Precise electrode location was verified from post-hoc histology (procedures and representative results described in Chapter 5). The V1 electrode insertion was performed after the craniotomy and the LGN electrode settling at the desired depth. The electrode tip was aimed for the deep layers of V1 (~ 700 μm below the pia surface) and was also allowed to settle in position for approximately 30 min before the start of recording.

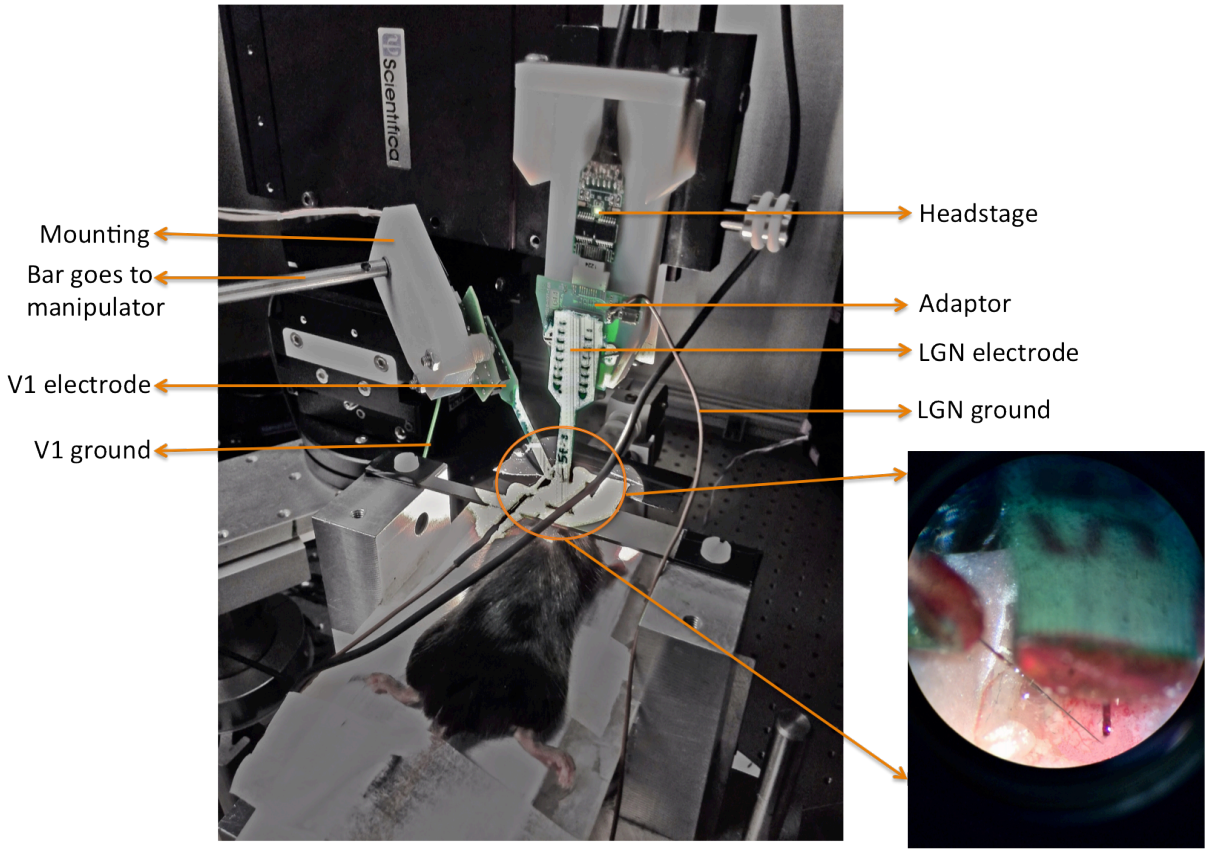

Figure 4.1 Experimental setup of simultaneous recording from LGN and V1 with two separate MEAs in the isoflurane anaesthetized animal. Left. Overview of the two sets of electrodes, headstages, electrode adaptors, ground wires and manipulators during recording while the animal was secured with the headplate under isoflurane anaesthesia. The LGN electrode went vertically into the brain, whereas the V1 electrode was inserted at an angle to avoid physical interference. Right. Magnified view under 40× microscope, showing exposed brain with two electrodes in position.

Signals were amplified and acquired with Grapevine Neural Recording System (Ripple LLC, Salt Lake City, UT). Signals were filtered from 0.3 Hz ~ 7.5 KHz, with sample rate at 30 KHz. Recordings were firstly carried out on animals under relatively high isoflurane concentration (1.5~2.0% isoflurane in O_2). Then the subjects were intraperitoneally injected with 0.02 ml chlorprothixene, at the concentration of 0.5 mg/ml. The isoflurane concentration was subsequently lowered to 0.3~0.5% after 5~10 min of chlorprothixene injection to transfer the animals into the lighter anaesthesia. The same series of visual stimuli as listed in Section 2.4.4 were presented in both high and low isoflurane states. Respiratory rate, paw pinch withdrawal reflexes, body temperature and brain moisture were intensively monitored throughout the recording period. Animals that suffered from issues of corneal quality or respiratory stability were excluded from the database.

At the end of recording, the animal was terminated with overdose of 10% urethane and perfusion, the brain was fixed for histological and imaging procedures to visualize the tracks of both electrodes (Section 5.2.1). Also, the histological LGN model (described in Chapter 5) was applied afterwards to determine the electrode position along the anterior-posterior axis within LGN. Only electrode sites that were histologically confirmed within LGN and V1 were included for subsequent analysis.

Data analysis was performed using custom routines written in Matlab. Chronux toolbox (www.chronux.org) was used to compute the power spectrum of the LFPs for each non-overlapping one-min segment recording. Normality was assessed with D'agostino-Pearson test in datasets. Normal distribution data was described with mean ± S.E.M. and compared with parametric Student's *t* test. Pearson correlation coefficients were computed for correlation test. Non-normal distribution data was presented in the format of median (25 percentile, 75 percentile), and Mann-Whitney-Wilcoxon test was used for comparison within two groups. Nonparametric Spearman correlation was computed for correlation test. The level of significance was set at 0.05 unless specified. **** signifies $P<0.0001$, *** $P<0.001$, ** $P<0.01$, * $P<0.05$.

4.3 Results

This section comprises two major parts. In the first part, based on simultaneous recordings from V1 and LGN, we explored and compared LFPs in the two brain areas with the animal under high or low isoflurane state (Section 4.3.1, 4.3.2 and 4.3.3). In the second part, we assessed whether single-cell response properties in mouse LGN were dependent on the isoflurane state (Section 4.3.4).

4.3.1 Distinct LFP features in high and low isoflurane concentrations

Simultaneous recordings from LGN and V1 under the high as well as low isoflurane concentrations were successfully performed on four mice. The number of penetrations in both V1 and LGN was limited to one to avoid damage to the brain tissue from multiple penetrations. For each of these four subjects, the hand mapping of receptive field in LGN was performed in 2~3 non-adjacent channels to facilitate electrophysiological targeting (see Section 2.4.3 for protocols). The corneal quality and respiratory stability of each individual subject were well maintained, and units from majority of the channels were able to respond

robustly to visual stimuli till the end of 5-hour recording. Histological and confocal imaging procedures were carried out to recover electrode tracks and to indicate laminar position of each electrode site of the V1 probe, and electrode sites that located outside the targeted areas were eliminated from further analysis.

The first interesting feature we noticed was that during recording, the LFP exhibited distinct patterns between the high and low isoflurane states, reflected as changes in the frequency and amplitude. Figure 4.2 demonstrates a representative 10 sec LFP traces in V1 recovered from recording, with the animal presented with a blank screen at the mean luminance (46.93 cd/m^2). Signals were taken from one of the four shanks of the V1 electrode that spanned superficial layers to deep layers in the cortex, and the correspondence between the electrode sites and V1 layers are shown on the left in Figure 4.2 based on the information acquired from confocal imaging.

The LFPs in the high isoflurane state (left panel in Figure 4.2) showed pronounced slow oscillations at high amplitudes (at amplitudes up to nearly 1 mv and frequency <1 Hz), accompanied by high-frequency activity at low amplitudes. By contrast, during the low isoflurane state of the same animal (right panel in Figure 4.2), the LFPs were characterized by higher frequency fluctuations at relatively lower amplitudes, whereas the high-amplitude oscillation at low frequency as seen in the high isoflurane state, was absent. Moreover, in these two states, only blank screen was shown to the animal, the change of LFP features was therefore irrelevant to visual stimuli. It is also revealed in Figure 4.2 that for both isoflurane states, the abovementioned patterns of LFPs display little variance among the eight channels, suggesting that the patterns of neuronal ensemble activity stayed largely consistent across layers in V1.

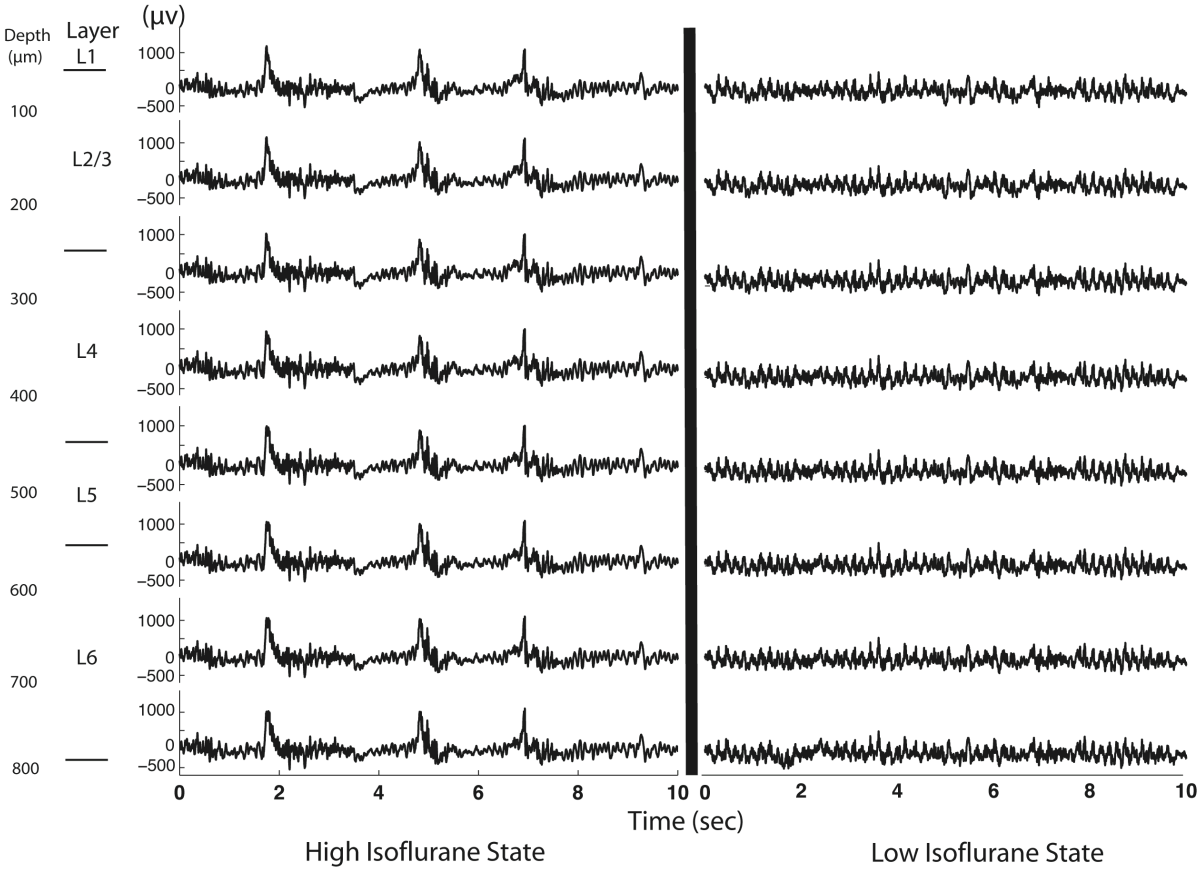

Figure 4.2 A 10 sec example of LFP traces recorded from V1 of the same animal at high (left) and low (right) isoflurane states. The recording was obtained while the animal was presented with a blank screen at the mean luminance. Traces were recovered from one of four shanks of the electrode (A4*8-5mm-100-200-177, NeuroNexus), and the correspondence between the electrode channels and V1 layers were marked on the left according to information obtained from histology and confocal imaging. The amplitudes of two LFP segments were scaled to the same. Right: in the state of high isoflurane concentration (1.5%~2.0%), the LFPs display low-frequency oscillations at high amplitudes (the amplitude peaks around 1 mv and the frequency <1 Hz), separated by high-frequency activity at low amplitudes. Left: in the state of low isoflurane concentration (0.3%~0.5%), the LFPs show high-frequency activity at low amplitudes, and the slow fluctuations at large amplitude are not seen. In both isoflurane states, these LFP patterns stay mostly stable among all the eight channels.

To further compare LFPs between the two states of high and low isoflurane concentrations, we examined the LFPs recorded from one session of the contrast noise movie stimulus (5 min presentation of grey background and 5 min of the movie, see Section 2.4.4 for detailed description of the movie). The difference of LFP power between the two states was measured by subtracting the power of the high isoflurane state from that of the low isoflurane state (ΔPower) in 1~120 Hz frequency range. The difference was further separated into spontaneous (responses to the grey background) and evoked (responses to the movie) conditions and analysed separately in V1 and LGN.

The ΔPower of the population (n=4) is displayed in Figure 4.3, and the pink areas show the variance of the ΔPower across the samples, while the red lines represent the mean values. In both baseline and evoked conditions in LGN (bottom panels), the ΔPower exhibits a tendency of greater variety across the population in the low frequency band (1~2 Hz). On average, compared to that in the high isoflurane state in both V1 (top panels) and LGN, the network fluctuation in the low isoflurane state reveals lower power in 1~4 Hz (delta or δ, light grey areas in Figure 4.3), 8~12 Hz (alpha or α) and 12~30 Hz (beta or β) frequency bands. The low isoflurane state also illustrates higher power in 4~8 Hz (theta or θ, dark grey areas in Figure 4.3) and 30~120 Hz (gamma or γ) frequency bands. Additionally, these characteristics are evident in baseline as well as triggered activities and are not dependent on visual stimuli presented.

Taken together, the comparison of the LFP power spectrum (Figure 4.3), combined with the LFP traces recovered from the recording (Figure 4.2) lead to the indication that LFPs in mouse visual system successfully resembled the features reported in the synchronized and desynchronized cortical states (Lee and Dan, 2012; Harris and Thiele, 2012). In addition to the well-established states including sleep/waking and quietness/alertness, the changes in LFP features could also be effectively realised by adjusting isoflurane concentrations in mice.

Next, we looked for certain frequency bands in LFPs to faithfully differentiate neuronal activities under high and low isoflurane states and avoid perplexing effects from the external stimuli or environment at the same time. Numerous experimental and computational studies have suggested that the synchronized neuronal activity in the gamma band is highly related to stimulus (Fries et al., 2001b, 2008; Gregoriou et al., 2009; Chalk et al., 2010; Tallon-Baudry et al., 2005). Moreover, it has been reported that the beta-band fluctuations are actively involved in the expectation of a forthcoming event or impending change of current state (Engel and Fries, 2010). Also, investigators have found under some brain states, the beta- and gamma-band activities appeared in conjunction and fluctuated simultaneously (Steriade, 2005). Due to these considerations, we applied theta/delta (θ/δ) ratio, defined as the ratio of LFP power in 4~8 Hz against 1~4 Hz, to discriminate neuronal activities under the high and low isoflurane states in this project. Costa-Miserachs and colleagues (2003) has demonstrated the θ/δ ratio, together with ECoG or EMG, could act as a reliable algorithm to assess sleep/awake state.

In the following sections, the goodness of this ratio in differentiating the high and low isoflurane states will firstly be examined. Next, results on characterizing the correlation between V1 and LGN in LFPs using this ratio, and impact of the isoflurane state on single-unit response features in mouse LGN will be presented and discussed.

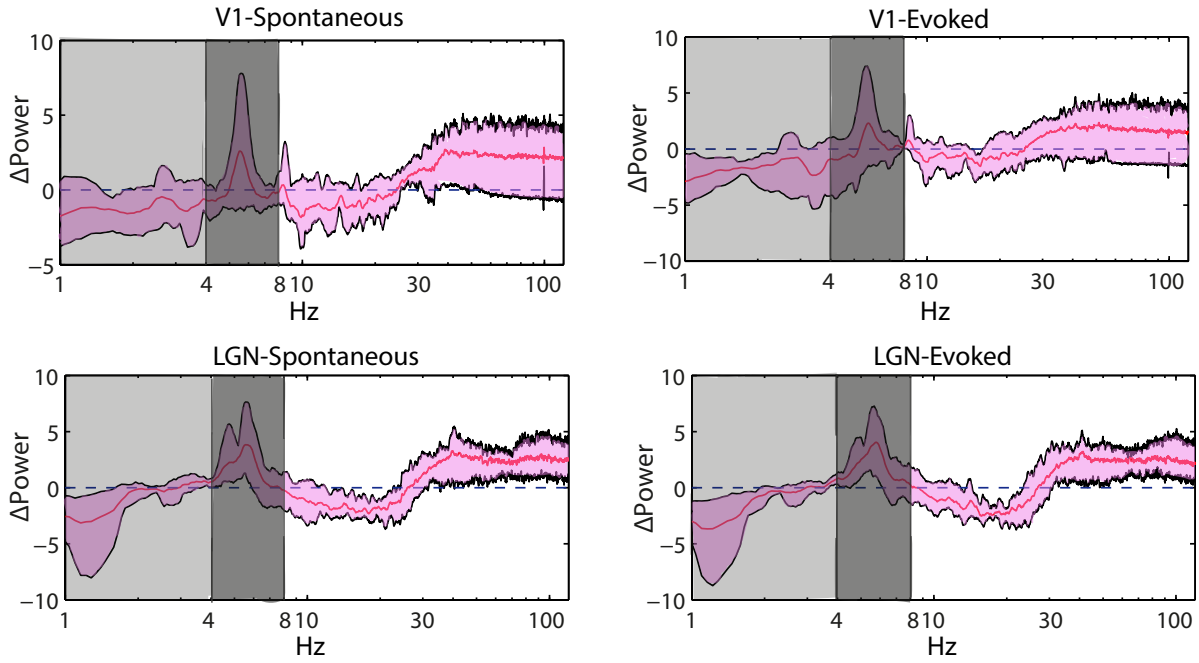

Figure 4.3 The difference of LFP power spectrum between the low and high isoflurane states in V1 and LGN. The LFPs were obtained from a session of recording with the animal presented with the contrast noise movie stimulus (5 min blank screen and 5 min movie) in the high and low isoflurane states. The LFP power difference was measured as subtracting the power in the high isoflurane state from the power in the low isoflurane state (ΔPower, Y-axis) in the 1~120 Hz bandwidth (X-axis) under spontaneous (the left panel) and evoked (the right panel) conditions. Note the logistics scale of the X-axis. The pink areas show the variance of ΔPower across four animals, and the red line represents the mean. In both spontaneous and evoked conditions in the V1 (top panels) and LGN (bottom panels), the network fluctuation in the light anaesthesia state reveals lower power in 1~4 Hz (delta or δ), 8~12 Hz (alpha or α) and 12~30 Hz (beta or β) frequency bands, and also higher power in 4~8 Hz (theta or θ) and 30~120 Hz (gamma or γ) frequency bands. The areas highlighted in light grey and dark grey represent ΔPower in 1~4 Hz (δ) bandwidth and 4~8 Hz (θ) bandwidth respectively.

4.3.2 The θ/δ ratio in high and low isoflurane states

We next moved from one session of the contrast noise movie stimulus to examine the variation in the θ/δ ratio over the entire period of recording. Figure 4.4 presents such an example from one experiment (mouse 4). The main panels show the variation of the θ/δ ratio calculated from V1 (top) and LGN (bottom) over nearly 2-hour recording (X axis) with the same animal in high (black, solid line) and low (red, dashed line) isoflurane states separately. Compared to that in the high isoflurane state, the θ/δ ratio of the low isoflurane state in V1

and also LGN stayed at higher values almost throughout the whole recording session, and this relationship was largely unaffected by the specific visual stimulus presented (the order and approximate start timing of each stimulus session are illustrated in blue in Figure 4.4). Furthermore, our results showed that the θ/δ ratio displayed higher degree of fluctuations in the low than the high isoflurane state in the two brain areas. These features are also reflected in the overall distributions of the θ/δ ratio in the small panels in Figure 4.4, specifically, the θ/δ ratio distributions from the low isoflurane state (red) covered broader ranges than those in the high isoflurane state (black), and its peak greatly shifted towards higher values in the low isoflurane state.

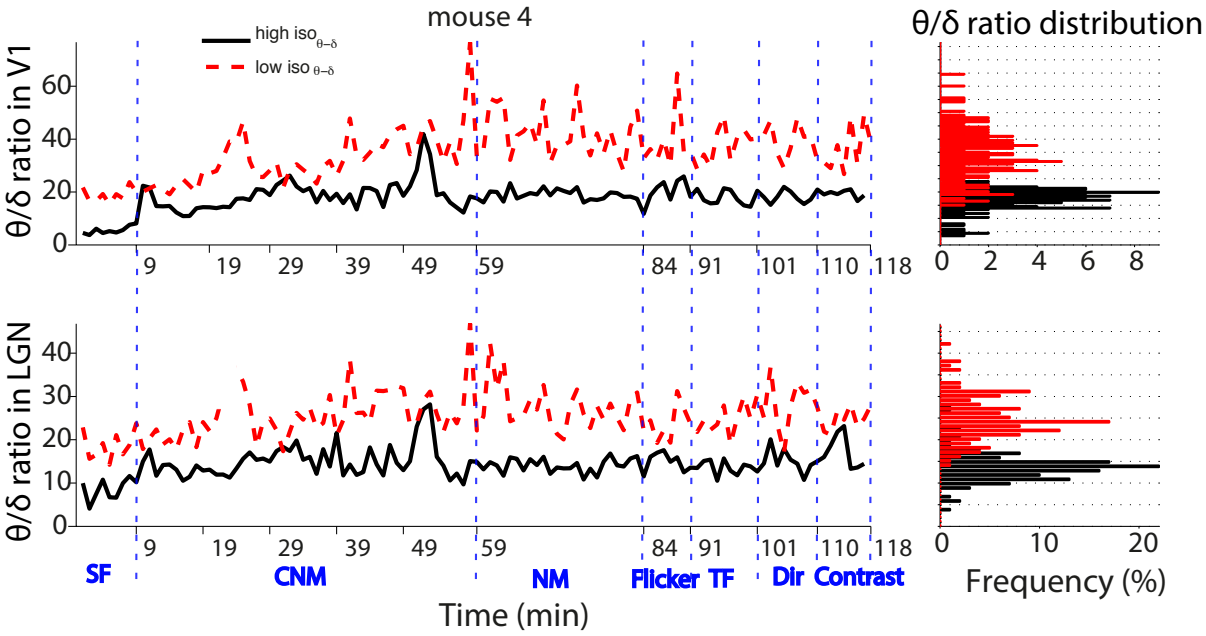

Figure 4.4 The θ/δ ratio across the entire period of recording is higher in the low than the high isoflurane state in V1 and also LGN, and this relationship is unaffected by the presentation of visual stimulus. Representative results from one animal (mouse 4) are shown here. Each value on the X coordinate indicates the starting point in min of each visual stimulus session, and the order of the stimulus presented is illustrated in blue. Main panels show the variances of the θ/δ ratio (the ratio of LFP power in 4~8 Hz against 1~4 Hz) across the entire period of recording in V1 (top) and LGN (bottom). Solid black lines and dashed red lines represent the θ/δ ratios under the high and low isoflurane states respectively in both V1 and LGN. The histograms on the right are distributions of the θ/δ ratio in V1 (top, black in high isoflurane and red in low isoflurane states) and LGN (bottom, black in high isoflurane and red in low isoflurane states). Stimulus information: CNM, contrast noise move; NM, natural movie; SF, TF, Contrast and Dir: sinusoidal monochromatic gratings moving at various spatial frequencies, temporal frequencies, contrasts and directions respectively (see Section 2.4.4 for stimulus parameters).

We then examined the difference of the θ/δ ratio between the high and low isoflurane states in all the subjects. As shown from the cumulative probability plots and the bar charts in Figure 4.5, across the four samples, the θ/δ ratios stay in the comparable range in LGN, while the ratios vary in V1 among the animals, with the largest difference seen between mouse 3 (in the scope of 0 to 8) and mouse 4 (in the scope of 0 to 80). Looking individually into the four animals, the θ/δ ratio of the low isoflurane state was statistically higher than that observed in the high isoflurane state in both the brain areas (Figure 4.5).

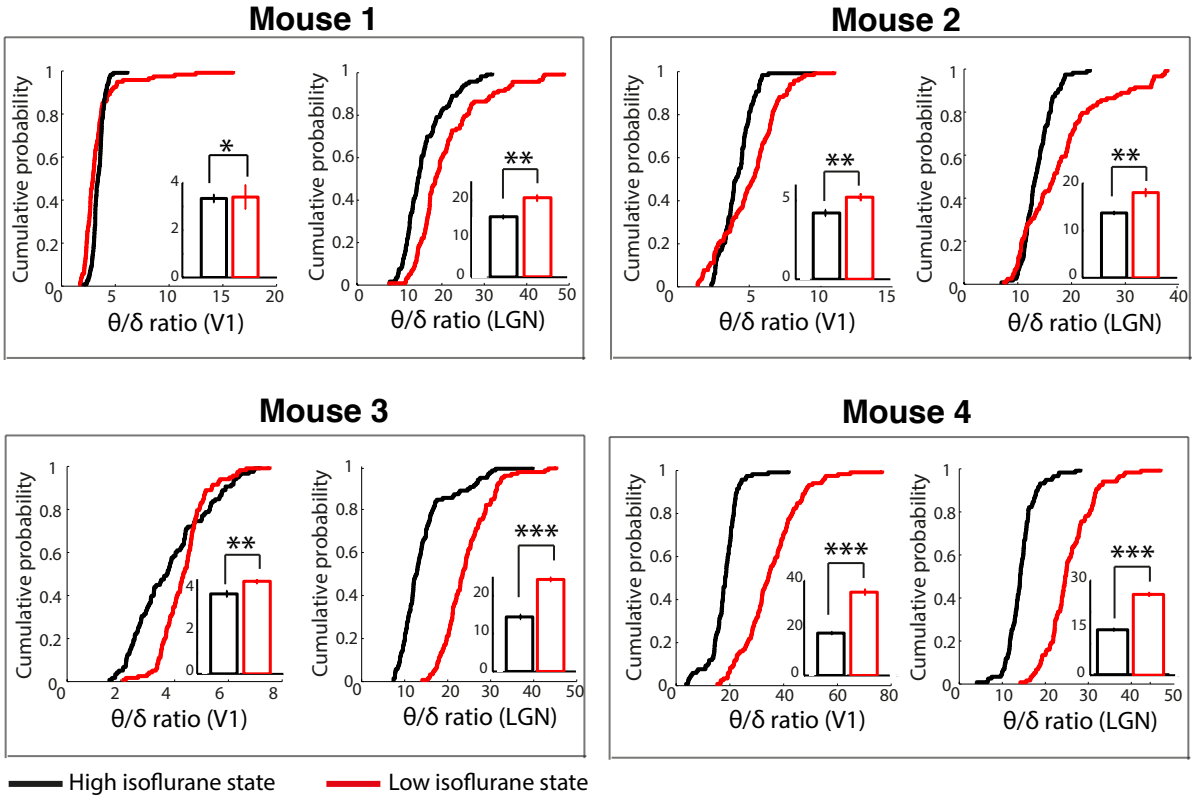

Figure 4.5 The θ/δ ratio is significant higher in the low isoflurane state than the high isoflurane state, in both V1 and LGN across all samples (n=4). The main cumulative probability plots in each panel show marked differences in the distributions of the θ/δ ratio (the ratio of LFP power in 4~8 Hz against 1~4 Hz) between the high (black) and low (red) isoflurane states in V1 (right) as well as LGN (left) in each animal, and the bar plots (inset) show the mean ± SEM of the θ/δ ratio in the two states. (Mouse 1: V1, the high, 3.3 ± 0.3; the low, 3.5 ± 1.0; LGN, the high, 15.8 ± 0.6; the low, 21.6 ± 1.1; Mouse 2: V1, the high, 4.2 ± 0.4; the low, 5.1 ± 0.4; LGN, the high, 13.8 ± 0.3; the low, 18.0 ± 1.1; Mouse 3: V1, the high, 3.7 ± 0.6; the low, 4.4 ± 0.3; LGN, the high, 14.3 ± 1.6; the low, 24.2 ± 1.2; Mouse 4: V1, the high, 17.9 ± 0.8; the low, 35.0 ± 1.4; LGN, the high, 14.6 ± 0.9; the low, 25.9 ± 1.1; Student's *t* test, **P*<0.05; ***P*<0.01; ****P*<0.001).

The results presented in this section showed that the θ/δ ratio was considerably higher in the low isoflurane state than that in the high isoflurane state throughout the recording session, and such relationship was unaffected by any visual stimulus presentation. These observations suggest that the θ/δ ratio could provide an LFP-based measure of anaesthesia depth. Also,

adjusting isoflurane concentrations can effectively lead to distinct LFP features in the mouse brain representing different states. In addition to the cortical area that has been extensively investigated under different brain states, our results indicate that LGN reveals such anaesthesia-state dependency in LFPs as well.

4.3.3 State-dependent correlation between mouse V1 and LGN

Proceeding from looking into LFPs in V1 and LGN separately, the extent of correlation between these two structures in both the high and low isoflurane states was further examined in this section. For each non-overlapping one-min segment of the LFP across the same period of recording, we calculated the θ/δ ratio in both V1 and LGN and assessed the correlation between these two areas under the high and low isoflurane states separately.

Figure 4.6 illustrates the θ/δ ratio of V1 and LGN from both high (black) and low (red) isoflurane states. Across all the four subjects, the θ/δ ratio of the two brain areas over the same period displayed a higher tendency of centralization in the low isoflurane state, whereas more variability was noticed in the high isoflurane state. Evaluated with correlation test, the correlation of the θ/δ ratio in mouse 1 (ρ=0.3), 2 (ρ=0.82) and 4 (ρ=0.81) were positively correlated in the low isoflurane state except for mouse 3 (ρ=-0.11). The same positive-correlation trend was observed in the high isoflurane state for mouse 3 (ρ=0.62) and 4 (ρ=0.81), the θ/δ ratio between LGN and V1 in mouse 1 (ρ=0.022) and 2 (ρ=-0.0074) did not demonstrate a strong correlation.

Combined with location of each recording site within the V1 laminar organization reconstructed from histology and confocal imaging, we further investigated relationship of the θ/δ ratio between LGN and different layers of V1 separately and no layer-dependent correlation pattern was observed.

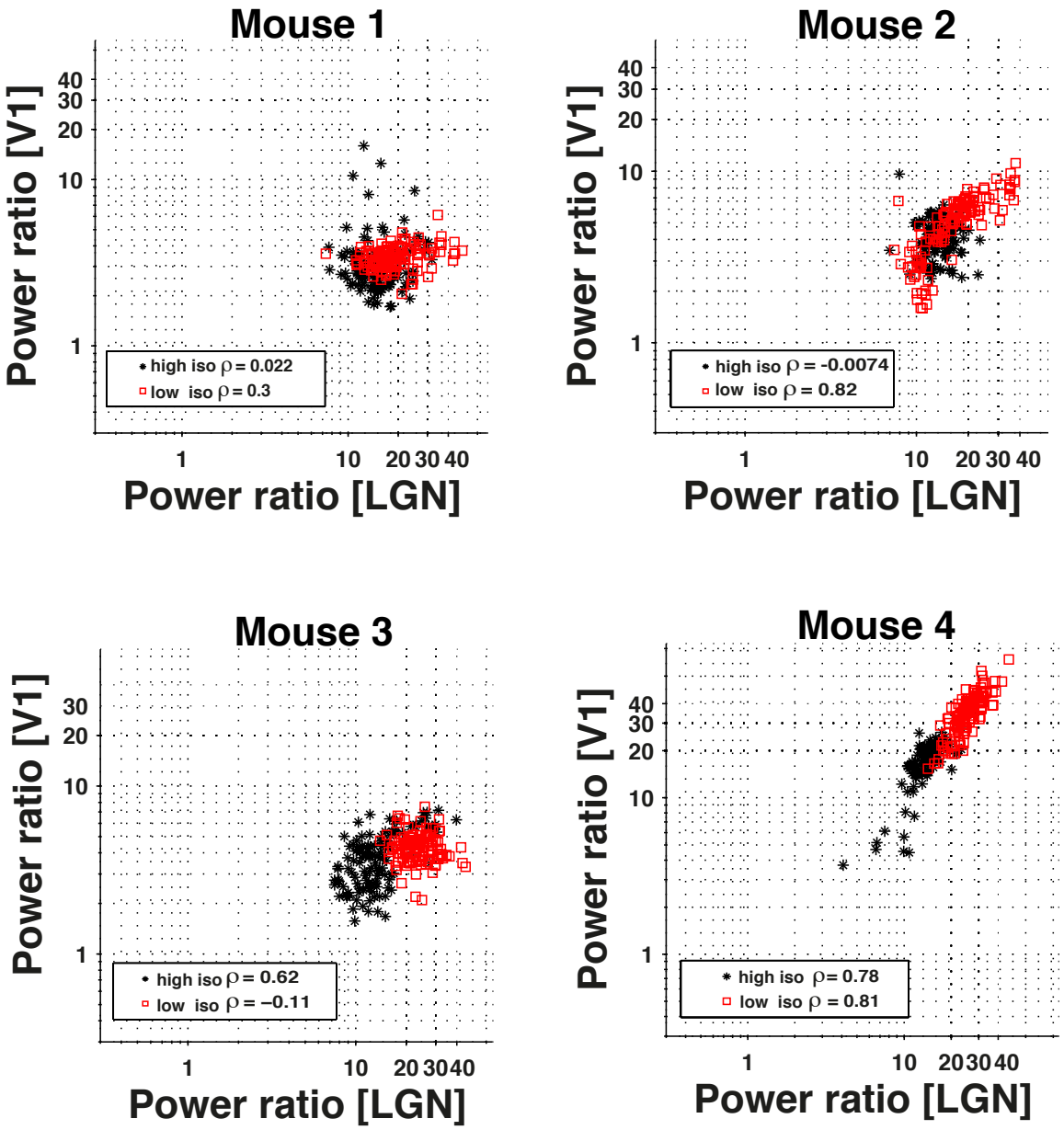

Figure 4.6 Correlation index (ρ) of the θ/δ ratio between V1 and LGN over the same period of recording in the high as well as low isoflurane states across samples (n=4). For each non-overlapping one-min segment of the LFP across the entire period of recording, the θ/δ ratio (the ratio of LFP power in 4~8 Hz against 1~4 Hz) between LGN and V1 was assessed and plotted in both high (black stars) and low (red squares) isoflurane states. The correlation index (ρ) is illustrated in the bottom left of each panel.

4.3.4 Comparisons of single-unit response properties in LGN between high and low isoflurane states

Results presented previously showed that LFPs in mouse LGN exhibited distinct power spectrums in the 1~120 frequency bands between high and low isoflurane states. We then sought to investigate whether response properties at single cell level in LGN showed any state dependency.

Recordings were made from LGN in 20 adult (age 2~4 months) female mice, using 16-channel-MEAs (A1x16-Poly2-5mm-50s-177-A16, NeuroNexus). Of the 20 subjects, 5 were recorded under both the high (1.5~2.0% isoflurane in O_2) and low (0.3~0.5% isoflurane in O_2) isoflurane states, 11 were recorded only under the high isoflurane state, while 4 were recorded only under the low isoflurane state. This resulted in 25 recordings in total, 16 in the high and 9 in the low isoflurane state respectively. Data acquisition was the same as stated in Section 2.3.3. Both LFPs and action potentials were recorded from all these recordings. The extracellular signals were filtered from 0.1 to 9000 Hz for channels to record LFPs, and from 300 to 9000 Hz for channels to record action potentials.

From 25 recordings, we obtained 157 single units that were histologically confirmed within LGN and displayed classical centre-surround receptive fields. Individual recording sessions consisted of simultaneous recordings of 4 to 11 - isolated single units across the 16 sites of the MEA. Of these units, 98.7% (155 of 157) were responsive to at least one episodic sinusoidal grating visual stimulus. Nonresponsive units were not included in the data analysis.

We first assessed LFPs in different isoflurane states by measuring the θ/δ ratio and examining its fluctuation during visual stimulus presentation (contrast noise movie and all sinusoidal gratings). Figure 4.7 shows that the θ/δ ratio is in the range of 5 to 25 for all the 25 recordings. Importantly, the θ/δ ratio displays low level of fluctuation throughout stimulus presentation in most cases, and the degree of fluctuation is free from modulation of the stimulus (Figure 4.7). These observations are in accordance with previous results demonstrated in Section 4.3.2 where the θ/δ ratio was largely unaffected by the specific visual stimulus presented.

Next, the relationship between the θ/δ ratio and the isoflurane state was explored. We first examined the normality of the θ/δ ratio distribution with D'agostino-Pearson test, and found that except for one recording under the low isoflurane state, the θ/δ ratio of the rest 24 of 25 recordings was normally distributed (Figure 4.8A). We therefore measured the mean (normally distributed data) or the median (non-normally distributed data) of the θ/δ ratio and took the value as representative of the θ/δ ratio of each recording for further analysis. The 25 recordings were subsequently re-ordered according to the θ/δ ratio, from the minimum to the maximum (Figure 4.8B). Figure 4.8A and B show that compared to that in the high isoflurane state, the θ/δ ratios from the low isoflurane state reveal the tendency towards larger values. However, the ratios of the low isoflurane state also displays higher degree of variability. Statistically, the θ/δ ratio from all recordings in the low isoflurane state was considerably higher than that from all recordings in the high isoflurane state (Student's t test, $P<0.0001$) (Figure 4.8C).

These results accord well with observations from simultaneous recordings made from V1 and LGN (Section 4.3.2). They suggest that the θ/δ ratio is a reliable index to differentiate LFPs in mouse LGN under different isoflurane concentrations, with the higher θ/δ ratio corresponding to the state with lower isoflurane concentration. We therefore evaluated the 25 recordings based on the θ/δ ratio as shown in Figure 4.8B and examined the relationship between the θ/δ ratio and response properties of single LGN cells in the following sections.

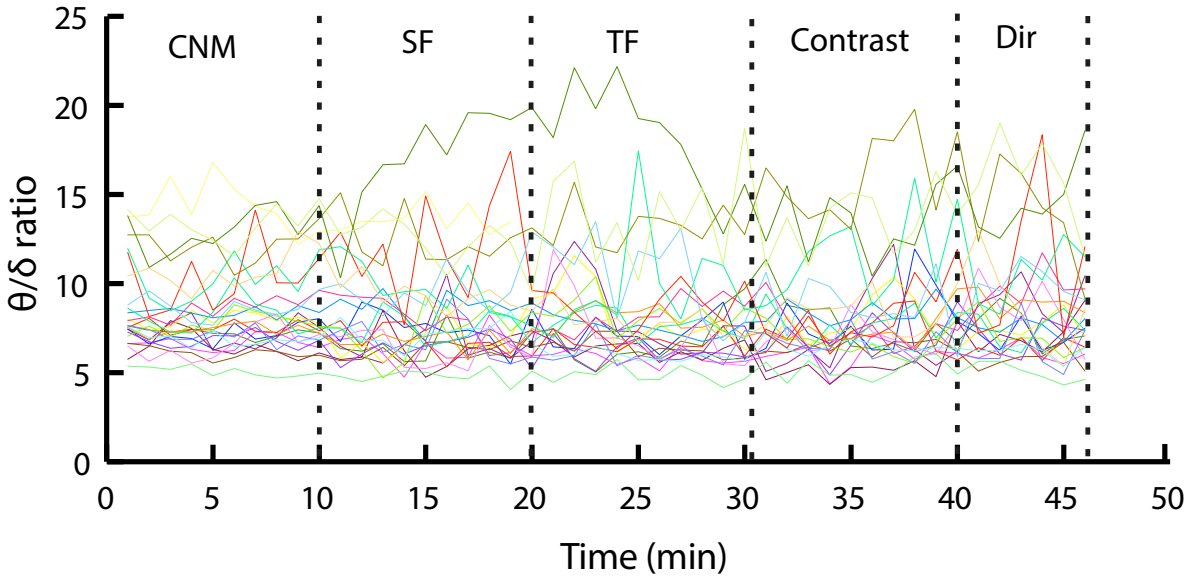

Figure 4.7 The fluctuation of the θ/δ ratio during visual stimulus presentation of 25 recordings from mouse LGN. The θ/δ ratio (Y-axis) of each recording was coded in a different colour. The timing of each stimulus (X-axis) was separated with dashed lines. The θ/δ ratio of the contrast noise movie (CNM) was averaged from 4 or 5 repetitions of presentation. Stimulus information: CNM: contrast noise movie; SF, TF, Contrast and Dir: sinusoidal monochromatic gratings moving at various spatial frequencies, temporal frequencies, contrasts and directions respectively (see Section 2.4.4 for stimulus parameters).

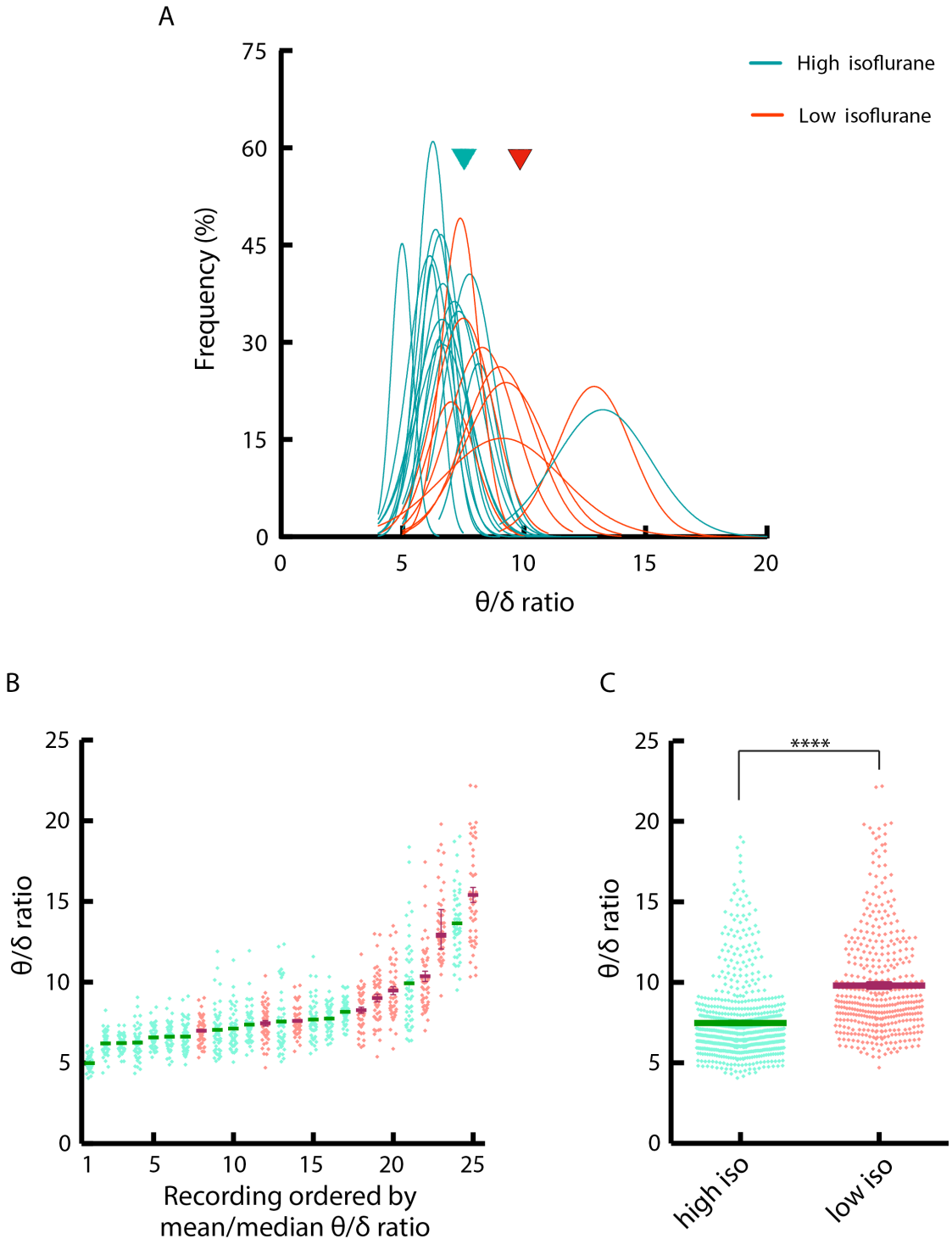

Figure 4.8 The relation between the θ/δ ratio and the high/low isoflurane state. A. Distributions of the θ/δ ratio from all recordings, with green and red representing recordings made under high and low isoflurane states respectively. Assessed with D'agostino-Pearson test, the θ/δ ratios of 24 out of 25 recordings are normally distributed, except one from the low isoflurane state. The arrows represent the overall mean values from the two separate states. B. The 25 recordings are ordered by the mean ± S.E.M. (θ/δ ratio normally distributed) or median with interquartile ranges (θ/δ ratio non-normally distributed) of their θ/δ ratios, from the minimum to the maximum. The distribution of the θ/δ ratio within each recording is also shown. C. The overall distributions of the θ/δ ratio from all recordings in the high (green) versus the low (red) isoflurane state. The mean ± S.E.M. of the deep is 7.48 ± 0.08, and the mean ± S.E.M. of the light is 9.81 ± 0.16, Student's *t* test, **** $P<0.0001$.

4.3.4.1 State dependent single-cell response properties in mouse LGN

It has been found that neurons in rat V1 exhibited shorter response latency while the animals were vigilant, as reflected by cortical desynchronization (Wang et al., 2014). In addition, investigators have reported that some response properties, including firing rates and spatial/temporal frequency tunings in macaque LGN varied significantly between the alert and anaesthetized subjects, whereas the contrast sensitivity was not modulated by brain states (Alitto et al., 2011). Considering the fact that little is currently known about the impact of brain states on response features in mouse LGN cells, we aimed to study the correlation between the high/low isoflurane state and response properties as explored in other species (Alitto et al., 2011).

The same series of visual stimuli as listed in Section 2.4.4 was presented to all subjects over the 25 recordings, including the contrast noise movie, full-field flicker and sinusoidal gratings. Also, the same analysis protocol as described in Section 2.5.2 was applied here. We explored the variation of firing rates, spatial frequency tuning properties, contrast sensitivity, response latency under the high and low isoflurane states, and evaluated the correlation between these properties and states (summarized in Table 4.1). In this section, response properties of mouse LGN neurons that were found to depend on the isoflurane state will be described, and properties that were independent from the isoflurane state will be presented in the following section.

Table 4.1 The relationship among the θ/δ ratio and response properties of mouse LGN neurons tested with Spearman correlation test.

Response properties		Spearman correlation test	
		r value	*P* value
Firing rate (spikes/s)	Spontaneous	-0.12	0.56
	Evoked	-0.06	0.74
Spatial frequency tuning (c/deg)	Preferred	0.33	0.11
	Cutoff	0.55	<0.01
Contrast sensitivity	Gain (spikes/s/%)	0.82	<0.0001
	C_{50} (%)	-0.41	<0.05
Response latency (msec)		-0.93	<0.0001

We first sought to study the correlation between the isoflurane state and response latency. Latency was measured from responses to sinusoidal gratings moving at various spatial frequencies (Section 2.5.2). 82 single units across 25 recordings were successfully fitted with a curve generated from the DoG equation (Rodieck, 1965; So and Shapley, 1981) (Section 2.5.2) and included in this latency analysis, and 1~6 - isolated single units were acquired from individual recording sessions. The latency of these single units varied from 19 msec up to nearly 250 msec, and overlapped among recordings (Figure 4.9 left and Table 4.2). Our results also showed that the response latency on average was negatively correlated with the θ/δ ratio (Spearman correlation test, r=-0.93, $P<0.0001$) (Figure 4.9 right), which meant that the response latency decreased as the animal became lightly anaesthetized. It is interesting to note that the latency from the six recordings that had the highest θ/δ ratio (illustrated in pink in Figure 4.9) stayed within a relatively comparable range from 64 to 78 msec, and did not decrease further as the θ/δ ratio increased. This indicates that the latency of single units might reach a "threshold" as the isoflurane concentration being lower.

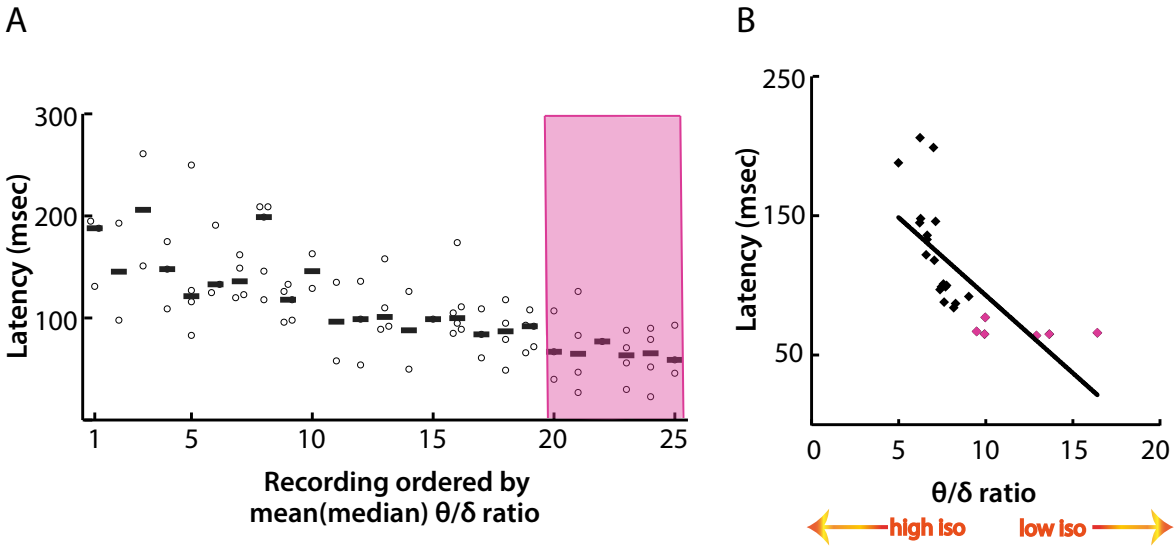

Figure 4.9 The response latency to sinusoidal gratings of LGN neurons decreases as the isoflurane concentration being lower. Left, the distribution of response latency to gratings (Y-axis) of 25 recordings, with the recordings ordered based on their θ/δ ratios from the minimum to the maximum (X-axis). The latency of each single cell is shown as an open circle, and the median of each recording is presented as a bar. Right, the correlation between the θ/δ ratio (X-axis) and the response latency (Y-axis) that assessed with Spearman correlation test, r=-0.93, P<0.0001. The pink shaded area and pink dots represent data from the six recordings that have the highest θ/δ ratio.

Subsequently, the correlation between the isoflurane state and contrast sensitivity was investigated. Contrast sensitivity was measured from single-cell responses to gratings at varying contrasts (see Section 2.4.4 for stimulus parameters). 148 single units from 24 of 25 recordings were successfully fitted with a hyperbolic function (Albrecht and Hamilton, 1982), except from one recording (mean of the θ/δ ratio was 7.38, ranked 11 of 25 in the θ/δ ratio order). 3 to 11 units were included from individual recordings for contrast sensitivity analysis. The contrast gain of single cells across recordings displayed a notable increase while the θ/δ ratio became higher, from around 0.7 spikes/s/% in the higher isoflurane state to 1.2 spikes/s/% in the lower isoflurane state (Figure 4.10A and Table 4.2). Correspondingly, the correlation test revealed that the contrast gain and the θ/δ ratio was positively correlated (Spearman correlation test, r=0.82, P<0.0001) (Figure 3.10B).

On the other hand, the contrast C_{50} showed a higher degree of recording-to-recording fluctuations compared to the contrast gain. Despite this variability, the contrast C_{50} reduced with increase in the θ/δ ratio among the recordings (Figure 4.10C and Table 4.2). Moreover, the C_{50} was negatively dependent on the isoflurane state with statistical significance (Spearman correlation test, r=-0.41, P<0.05) (Figure 4.10D). These differences in the contrast gain as well as in C_{50} relating to the anaesthesia state support the interesting

discovery that the contrast response characteristics in mouse LGN are dependent on the subject's isoflurane state. Specifically, LGN neurons are more sensitive in the low than the high isoflurane state over both contrast parameters.

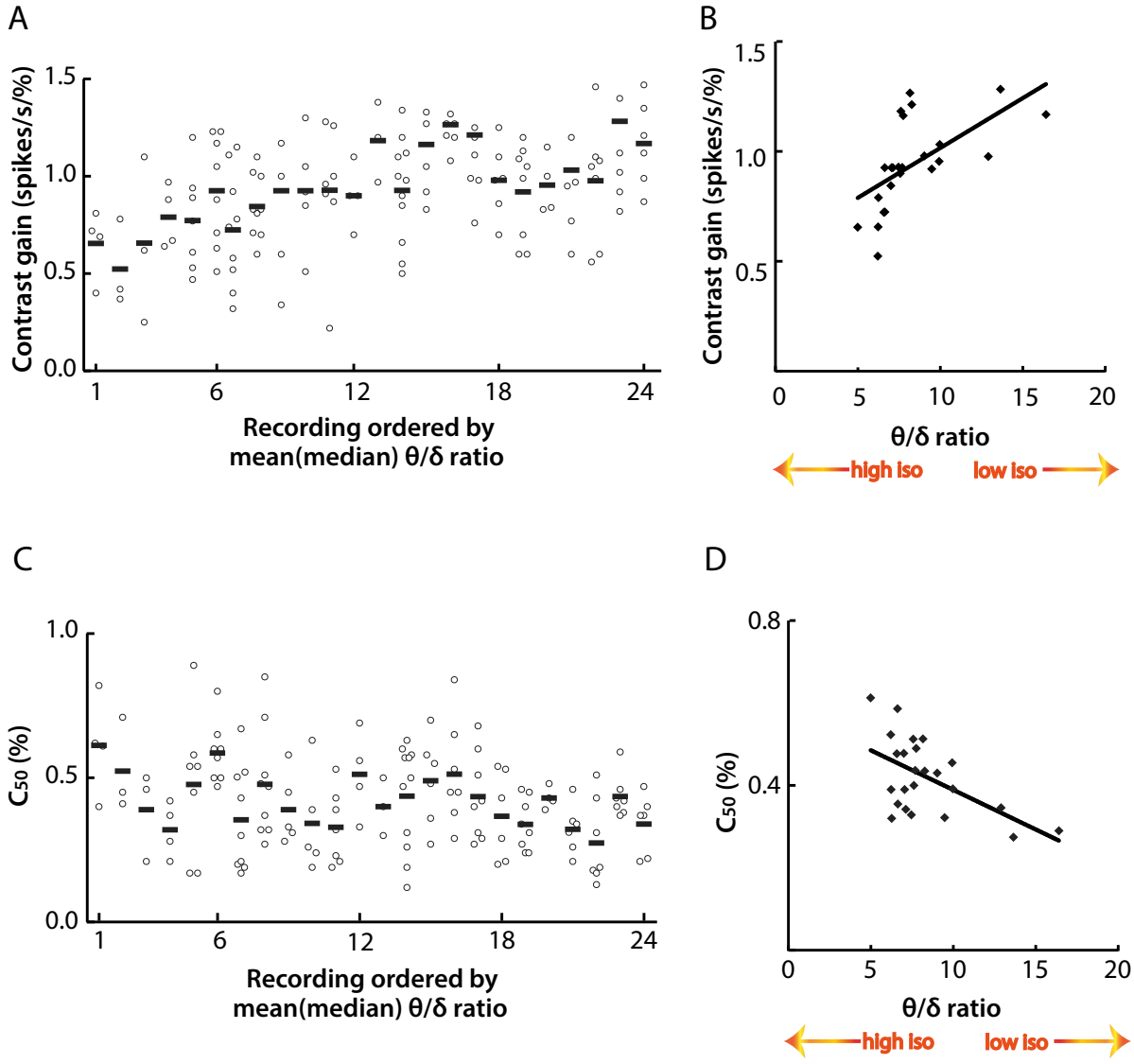

Figure 4.10 The contrast gain increases and contrast C_{50} decreases as the isoflurane concentration becomes lower. A and C. Distributions of contrast gain (A) and contrast C_{50} (C) of 24 recordings, with the recordings ordered based on their θ/δ ratios from the minimum to the maximum (X-axis). The contrast gain (A) and contrast C_{50} (C) of each single cell is shown as an open circle, and the median of each recording is presented as a bar. B. The correlation between the θ/δ ratio (X-axis) and the contrast gain (Y-axis), significance assessed with Spearman correlation test, r=0.82, $P<0.0001$. D. The correlation between the θ/δ ratio (X-axis) and the C_{50} (Y-axis), significance assessed with Spearman correlation test, r=-0.41, $P<0.05$.

We further compared the contrast response tunings between the two isoflurane states (Figure 4.11). Responses of all single units to drifting gratings at varying contrast were firstly extracted. Contrast response characteristics in the high and low isoflurane states were taken as the normalized responses (the responses at the maximal contrast was set as 1) from the first five and last five recording sessions respectively based on the minimum-to-maximum θ/δ ratio of all 24 recordings. Compared to those of the high isoflurane state, the contrast gain was higher and the contrast C_{50} was lower in the low isoflurane state that were in accordance with the correlation tests presented in Figure 4.10 (Contrast gain, high: 0.67 spikes/s/%; low: 1.08 spikes/s/%; Contrast C_{50}, high: 46%; low: 35%.). The tunings were then acquired by fitting the normalized responses to a hyperbolic function (Albrecht and Hamilton, 1982) (see Section 2.5.2 for detail). The differences over both contrast parameters between the isoflurane states were also reflected in the tunings, with the tuning of the lower isoflurane state (red) showing a sharper slope than that of the higher isoflurane state (black) (Figure 4.11).

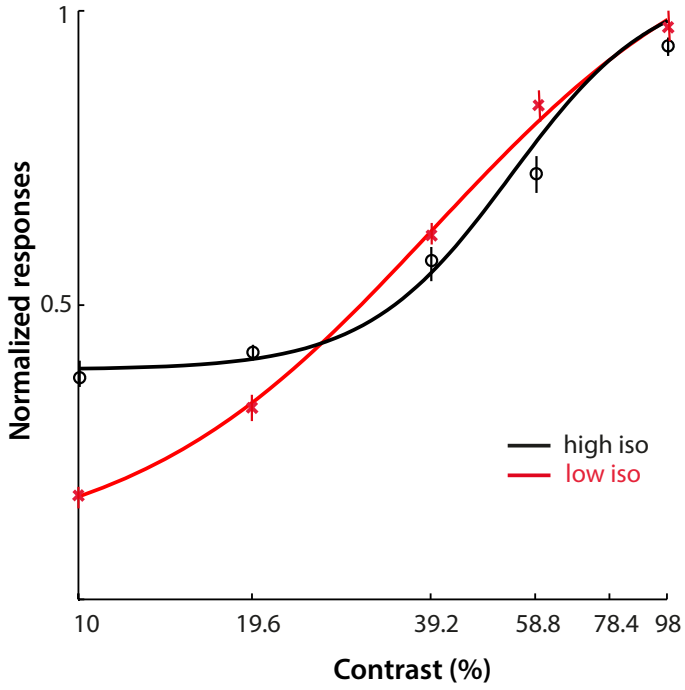

Figure 4.11 Normalized single-cell contrast response tunings in the high and low isoflurane states. The contrast response features were firstly extracted from single-cell responses to drifting gratings at various contrasts (X axis). The contrast responses with S.E.M. of the high (black circle) and low (red cross) isoflurane states were then normalized from the first five and last five recordings respectively according to the minimum-to-maximum θ/δ ratio of all 24 recordings. The contrast tunings were obtained by fitting the responses to a hyperbolic function (Albrecht and Hamilton, 1982), with the high and low isoflurane states represented in black and red lines respectively. Contrast gain, high: 0.67 spikes/s/%; low: 1.08 spikes/s/%; Contrast C_{50}, high: 46%; low: 35%.

The impacts of isoflurane state on spatial frequency tunings were subsequently studied. Preferred and cutoff spatial frequencies were computed from responses to drifting gratings at varying spatial frequencies, and fitted with a curve generated from the DoG equation (Rodieck, 1965; So and Shapley, 1981) (see Section 2.4.4 for stimulus information and Section 2.5.2 for equation details). Of the 25 recordings, 82 isolated single neurons were included in this spatial frequency tuning analysis, and 1 to 6 neurons were obtained from the individual recording sessions.

Our results showed that the median preferred spatial frequency of more than half of the recordings (17 of 25) were between 0 to 0.01 c/deg ("lower"), and the median from the rest were in the range of 0.02 to 0.05 c/deg ("higher"). The last two recording sessions with the highest θ/δ ratio also displayed the highest preferred spatial frequency among recordings (0.05 and 0.04 c/deg separately). In general, however, recordings with "lower" and "higher" preferred spatial frequencies were free from notable influence of the θ/δ ratio (Figure 4.12A and Table 4.2). No strong correlation was found between the isoflurane state and preferred spatial frequency from the 25 recordings (Spearman correlation test, $r=0.33$, $P>0.05$) (Figure 4.12B).

On the other hand, the cutoff spatial frequency, taken as the high spatial frequency at which response amplitude reached 1% of its maximum (Grubb and Thompson, 2003) was more tightly related to the θ/δ ratio than the preferred spatial frequency. Explicitly, the median cutoff spatial frequency covered the range from 0.08 to 0.49 c/deg across recordings, and it exhibited a trend towards higher values with increase of the θ/δ ratio, in spite of fluctuations among separate recording sessions (Figure 4.12C and Table 4.2). Statistical testing also confirmed that the cutoff spatial frequency and θ/δ ratio was positively correlated (Spearman correlation test, $r=0.55$, $P<0.01$) (Figure 4.12D). To summarize, these results on the influence of the isoflurane state on both spatial frequency parameters lend support to the indication that the peak spatial frequency that evoked the highest firings in mouse LGN neurons stayed largely consistent under the high and low isoflurane states. Interestingly, the neurons exhibited a higher degree of responsiveness to gratings moving at higher spatial frequencies as the animal in the low isoflurane state.

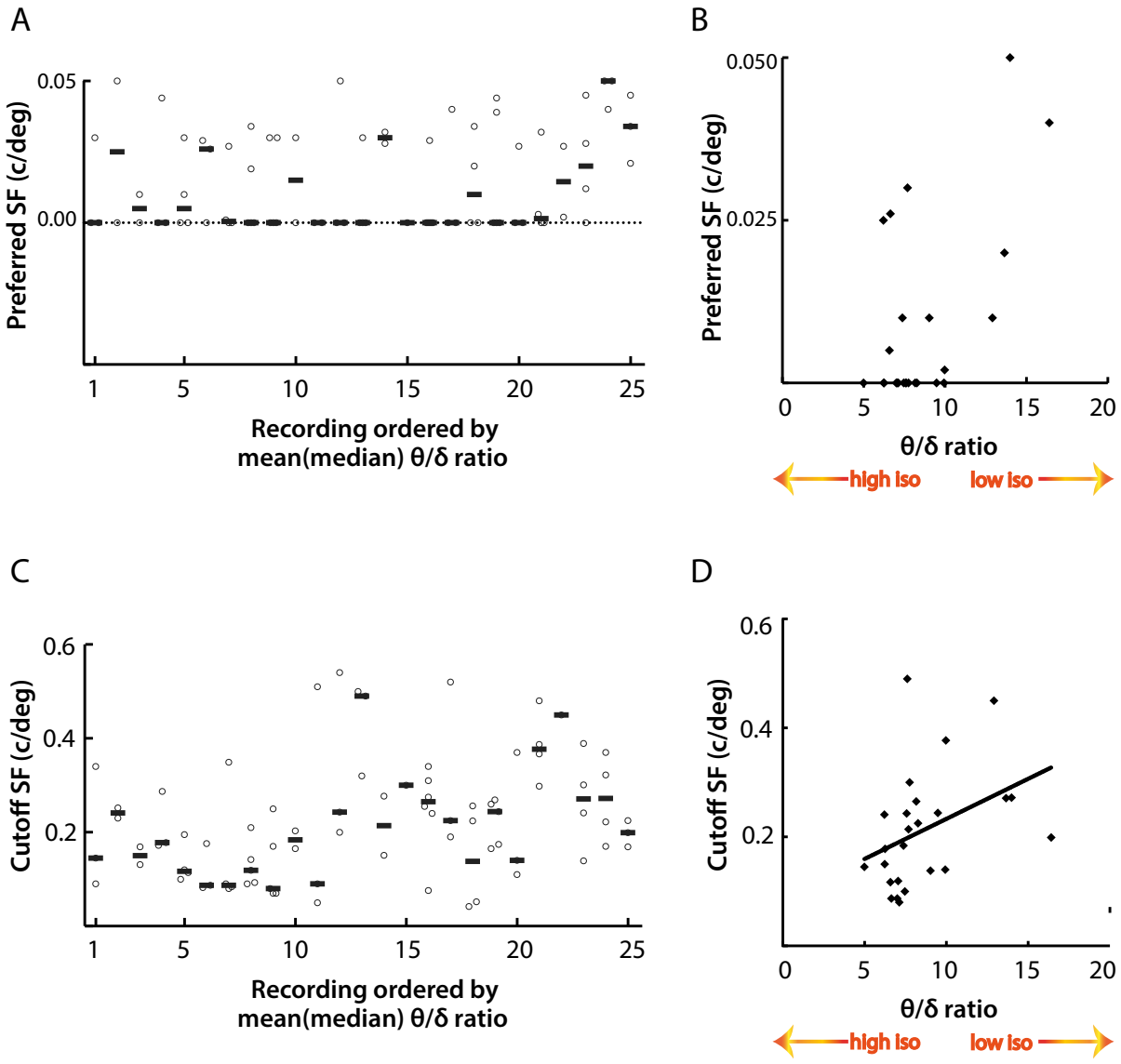

Figure 4.12 The preferred spatial frequency stays consistent while the high cutoff increases as the isoflurane concentration becomes lower. A and C. Distributions of preferred SF (spatial frequency) (A) and high cutoff SF (spatial frequency) (C) of 25 recordings, with the recordings ordered based on their θ/δ ratios from the minimum to the maximum (X-axis). The preferred spatial frequency (A) and cutoff spatial frequency (C) of each single cell is shown as an open circle, and the median of each recording is presented as a bar. B. The correlation between the θ/δ ratio (X-axis) and the preferred spatial frequency (Y-axis), significance assessed with Spearman correlation test, r=0.33, $P>0.05$. D. The correlation between the θ/δ ratio (X-axis) and the cutoff spatial frequency (Y-axis), and significance was assessed with Spearman correlation test, r=0.55, $P<0.01$.

We next decided to explore and compare the spatial frequency tunings of single cells under the high and low isoflurane states. To do so, response of all cells to gratings drifting at multiple spatial frequencies were firstly extracted. We defined the spatial frequency features from the high and low isoflurane states as the normalized responses from the first five and last five recordings separately, ranked by the minimum-to-maximum θ/δ ratio of all 25 recordings.

Compared to those from the high isoflurane state, the value of cutoff spatial frequency was larger in low isoflurane state (high: 0.17 c/deg; low: 0.31 c/deg), in accordance with the overall relationship observed from the 25 recordings (Figure 4.12C and D). By contrast, the value of preferred spatial frequency normalized from responses in the low isoflurane state was significantly larger than those in the high isoflurane state (high: 0.01 c/deg; low: 0.03 c/deg; Mann-Whitney test $P<0.0001$). The significant difference between the states was in contrary to the finding that took the data from all the 25 recordings into consideration (Figure 4.12A and B). This resulted from the preferred spatial frequency remained comparable within the entire dataset, although statistical differences existed between the extreme high and low isoflurane states.

The spatial frequency tuning curves from the two states were ascertained by fitting the normalized responses to a DoG equation (Rodieck, 1965; So and Shapley, 1981) (detailed in Section 2.5.2). In addition to the peak spatial frequency shifting towards higher values, the tuning curve from the lower isoflurane state (red) showed responses to a broader range of spatial frequencies than that from the higher isoflurane state (black) before decreasing rapidly as spatial frequency increased further (Figure 4.13). This was a reflection of the positive correlation between the isoflurane state and cutoff spatial frequency displayed in Figure 4.12C and D.

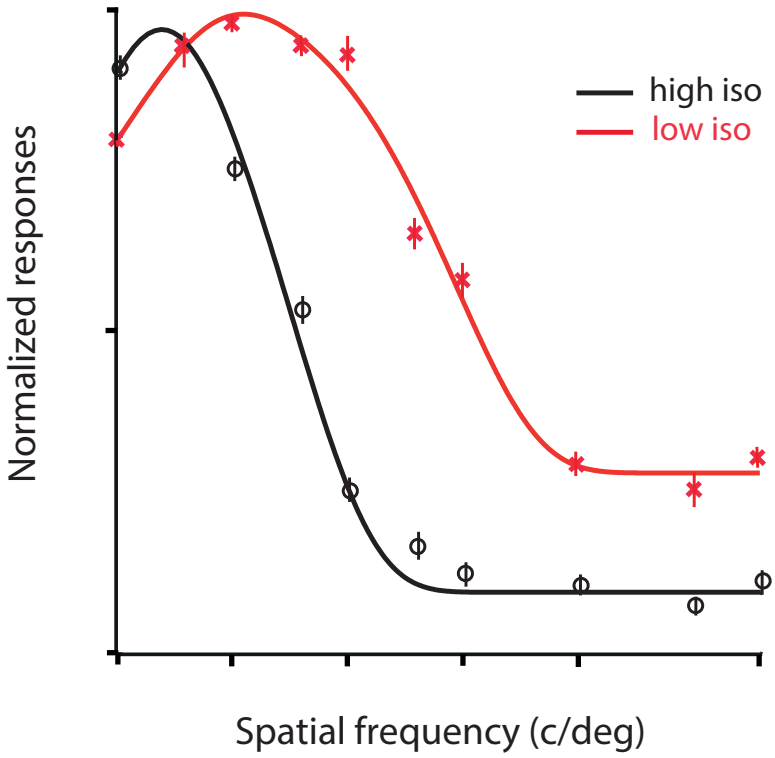

Figure 4.13 Normalized single-cell spatial frequency tunings in the high and low isoflurane states. The spatial frequency response features were extracted from single-cell responses to drifting gratings at various spatial frequencies (X axis). The spatial frequency parameters with S.E.M. of the high (black circle) and low (red cross) isoflurane states were then normalized from the first five and last five recordings respectively according to the minimum-to-maximum θ/δ ratio of all 25 recordings. The spatial frequency tunings were obtained by fitting the responses with a DoG equation (Rodieck, 1965; So and Shapley, 1981), with the high and low isoflurane states represented in black and red lines respectively. Preferred spatial frequency, high: 0.01 c/deg; low: 0.03 c/deg; spatial frequency cutoff, high: 0.17 c/deg; low: 0.31 c/deg.

4.3.4.2 Non- state dependent single-cell response properties in mouse LGN

It has been established in macaque LGN that neurons in the alert subjects responded to visual stimuli with significantly higher firing rate than the anaesthetized subjects (Alitto et al., 2011). We therefore sought to examine whether the firing rate of mouse LGN neurons were regulated by the high/low isoflurane state. To do so, we measured the spontaneous and evoked firing rates from responses to screens at mean luminance without visual stimuli and the maximal responses to different sinusoidal gratings, and evaluated their relationships with the isoflurane state. 155 single units across 25 recordings were included in the firing rate analysis, and 4 to 11 single units were obtained from individual recording sessions. The median spontaneous firing rate from the 25 recordings varied from 2.2 to 7.3 spikes/s (Figure 4.14A and Table 4.2), while in the evoked condition, the medians of firing rate displayed higher level of variability and went as high as 15.9 spikes/s (Figure 4.14C and Table 4.2).

The firing rates from both the spontaneous and evoked conditions were lightly correlated with the θ/δ ratio (Spearman correlation test, P>0.05) (Figure 4.14B and D). These results imply that the firing rates of mouse LGN neurons, regardless of the presentation of visual stimuli, are not regulated by the high or low isoflurane state.

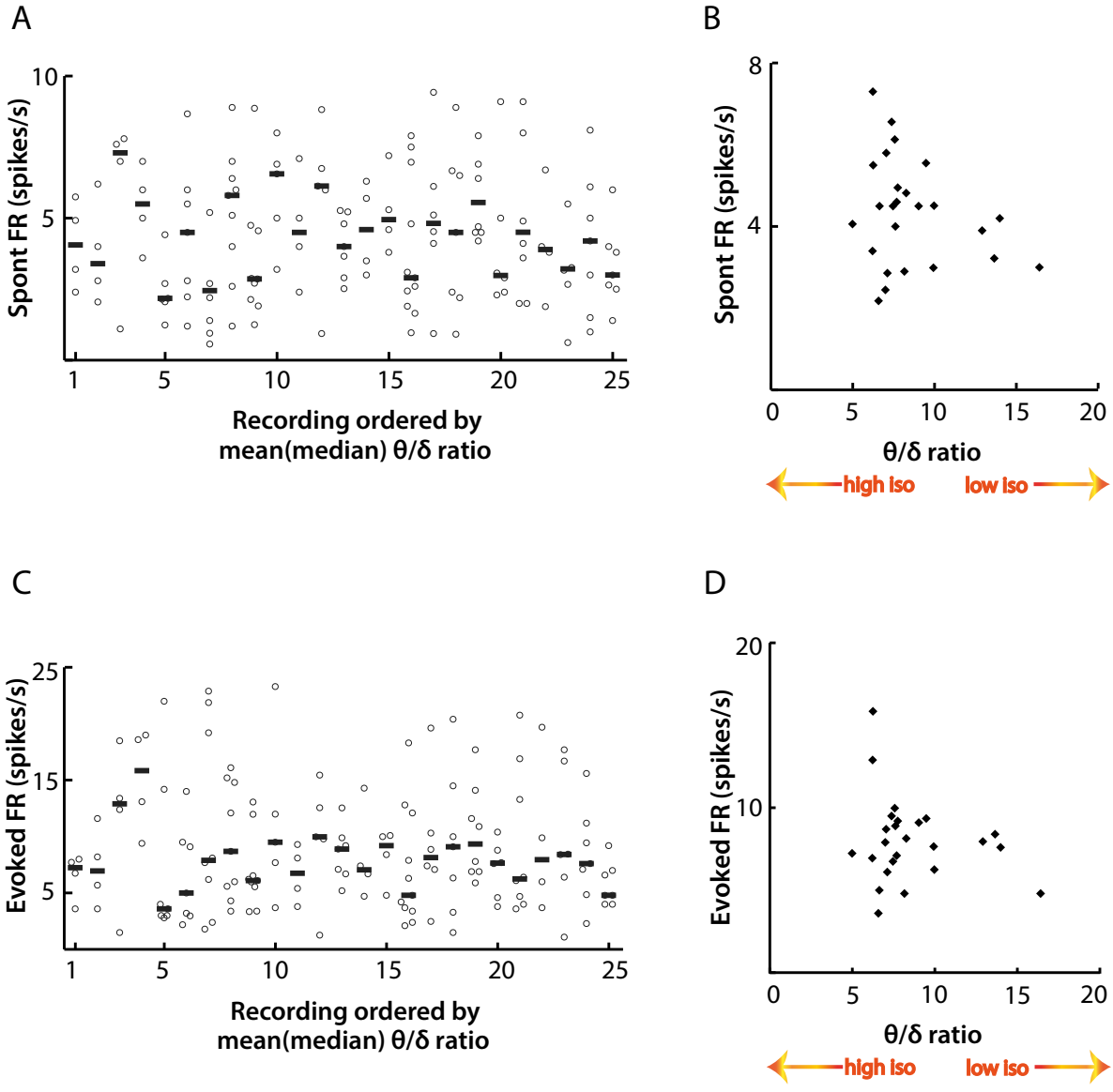

Figure 4.14 The spontaneous and evoked firing rates of mouse LGN neurons are not modulated by the high/low isoflurane state. A and C. Distributions of spontaneous FR (firing rate) (A) and evoked FR (firing rate) (C) of 25 recordings, with the recordings ordered based on their θ/δ ratios from the minimum to the maximum (X-axis). The spontaneous firing rate (A) and evoked firing rate (C) of each single cell is shown as an open circle, and the median of each recording is presented as a bar. B. The correlation between the θ/δ ratio (X-axis) and the spontaneous firing rate (Y-axis) that assessed with Spearman correlation test, r=-0.12, P=0.56. D. The correlation between the θ/δ ratio (X-axis) and the evoked firing rate (Y-axis), significance assessed with Spearman correlation test, r=-0.06, P=0.74.

Table 4.2 Response properties of neurons from 25 recordings in mouse LGN.

	Cell No.	Latency (mesec)	Spont FR (spikes/s)	Evoked FR (spikes/s)	Contrast Gain (spikes/s/%)	Contrast C_{50} (%)	Peak SF (c/deg)	Cutoff SF (c/deg)
1	4	188 (131, 195)	4.1 (2.6, 5.5)	7.2 (4.4, 7.9)	0.7 (0.5, 0.8)	0.6 (0.5, 0.8)	0.00 (0.00, 0.03)	0.15 (0.09,0.34)
2	4	146 (98, 193)	3.4 (2.2, 5.7)	7.0 (4.1, 10.8)	0.4 (0.4, 0.8)	0.5 (0.4, 0.7)	0.03 (0.00, 0.05)	0.24 (0.23,0.25)
3	4	206 (151, 261)	7.3 (2.6, 7.8)	12.9 (4.2, 17.2)	0.6 (0.3, 1.1)	0.5 (0.2, 0.5)	0.01 (0.00. 0.01)	0.15 (0.13, 0.17)
4	4	148 (109, 175)	5.5 (4.0, 6.8)	15.9 (10.3, 18.9)	0.8 (0.6, 0.9)	0.3 (0.2, 0.4)	0.00 (0.03, 0.04)	0.18 (0.17, 0.29)
5	7	122 (91, 219)	2.2 (2.1, 4.4)	3.6 (3.0, 14.2)	0.8 (0.5, 0.9)	0.5 (0.2, 0.6)	0.01 (0.00, 0.03)	0.12 (0.10,0.18)
6	7	133 (125, 191)	4.5 (2.2, 6.0)	5.0 (3.0, 9.5)	0.9 (0.7, 1.2)	0.6 (0.5, 0.6)	0.03 (0.00, 0.03)	0.09 (0.08, 0.18)
7	8	136 (120, 159)	7.9 (3.4, 21.1)	5.3 (2.1, 19.5)	0.7 (0.5, 1.0)	0.3 (0.2, 0.5)	0.00 (0.00, 0.02)	0.09 (0.08, 0.28)
8	9	199 (132, 209)	8.7 (5.0, 15.0)	14.8 (5.6, 16.1)	0.8 (0.7, 1.0)	0.5 (0.3, 0.6)	0.00 (0.00, 0.03)	0.12 (0.09,0.18)
9	9	118 (97, 130)	6.1 (4.5, 9.3)	6.2 (3.3, 12.2)	1.0 (0.5, 1.3)	0.3 (0.3, 0.5)	0.00 (0.00, 0.03)	0.08 (0.07, 0.21)
10	5	146 (129, 163)	6.6 (4.1, 7.5)	9.5 (5.7, 17.7)	0.9 (0.7, 1.2)	0.3 (0.2, 0.5)	0.02 (0.00, 0.03)	0.18 (0.17,0.20)

Table 4.2. (2) Response properties of neurons from 25 recordings in mouse LGN.

	Cell No.	Latency (mesec)	Spont FR (spikes/s)	Evoked FR (spikes/s)	Contrast Gain (spikes/s/%)	Contrast C_{50} (%)	Peak SF (c/deg)	Cutoff SF (c/deg)
11	4	97 (58, 135)	4.5 (2.8, 6.6)	6.8 (4.2, 9.0)	–	–	0.00 (0.00, 0.00)	0.09 (0.05,0.51)
12	5	99 (54, 136)	6.1 (3.5, 7.8)	10.0 (5.5, 14.0)	1.0 (0.9, 1.3)	0.3 (0.2, 0.4)	0.00 (0.00, 0.05)	0.24 (0.20, 0.54)
13	7	101 (90, 146)	4.0 (2.9, 5.2)	8.9 (6.7, 9.9)	0.9 (0.8, 1.1)	0.5 (0.4, 0.7)	0.00 (0.00. 0.02)	0.49 (0.32,0.50)
14	4	88 (50, 126)	4.6 (3.1, 6.2)	7.1 (5.2, 12.6)	1.2 (1.0, 1.4)	0.4 (0.3, 0.5)	0.03 (0.03, 0.03)	0.21 (0.15, 0.28)
15	4	99	5.0 (4.0, 6.7)	9.2 (5.7, 10.1)	1.0 (0.7, 1.1)	0.5 (0.3, 0.6)	0.00 (0.00, 0.00)	0.30
16	11	100 (88, 127)	2.9 (1.9, 7.0)	4.8 (3.4, 12.1)	1.2 (0.9, 1.4)	0.5 (0.3, 0.6)	0.00 (0.00, 0.01)	0.27 (0.20, 0.32)
17	6	84 (61, 109)	4.8 (3.3, 6.9)	8.1 (5.9, 12.7)	1.3 (1.2, 1.3)	0.5 (0.4, 0.7)	0.00 (0.00, 0.04)	0.23 (0.19, 0.52)
18	7	87 (57, 112)	4.5 (2.2, 6.7)	9.1 (3.3, 14.5)	1.2 (1.0, 1.5)	0.4 (0.3, 0.6)	0.01 (0.00, 0.03)	0.14 (0.05,0.25)
19	8	92 (69, 101)	5.6 (4.5, 7.7)	9.4 (6.9, 13.5)	1.0 (0.8, 1.1)	0.4 (0.2, 0.5)	0.00 (0.00, 0.04)	0.24 (0.17,0.26)
20	6	67 (40, 107)	3.0 (2.4, 6.0)	7.7 (4.4, 9.2)	1.0 (0.6, 1.1)	0.3 (0.2, 0.4)	0.00 (0.00, 0.03)	0.14 (0.11,0.37)

Table 4.2. (3) Response properties of neurons from 25 recordings in mouse LGN.

	Cell No.	Latency (msec)	Spont FR (spikes/s)	Evoked FR (spikes/s)	Contrast Gain (spikes/s/%)	Contrast C_{50} (%)	Peak SF (c/deg)	Cutoff SF (c/deg)
21	8	65 (32, 115)	4.5 (2.4, 8.8)	6.3 (4.2, 16.0)	0.9 (0.8, 1.1)	0.4 (0.4, 0.5)	0.00 (0.00, 0.02)	0.38 (0.32, 0.46)
22	4	77	3.9 (2.4, 6.0)	8.0 (4.3, 17.3)	1.0 (0.7, 1.3)	0.3 (0.2, 0.4)	0.01 (0.00,0.03)	0.45
23	6	64 (37, 84)	3.2 (2.2, 6.7)	8.4 (5.1, 17.0)	1.1 (0.6, 1.1)	0.2 (0.2, 0.4)	0.02 (0.00,0.04)	0.27 (0.16,0.37)
24	7	66 (30, 87)	4.2 (1.5, 6.1)	7.6 (4.9, 11.2)	1.1 (0.9, 1.8)	0.4 (0.4, 0.5)	0.05 (0.04,0.06)	0.27 (0.18,0.36)
25	7	59 (46, 93)	3.0 (2.5, 4.0)	4.8 (4.0, 7.0)	1.2 (1.0, 1.4)	0.4 (0.2, 0.4)	0.03 (0.02,0.05)	0.20 (0.17,0.23)

4.4 Summary and discussion

The primary intension of the study, as highlighted at the start of this chapter, was to examine neuronal activity in mouse LGN under high and low isoflurane concentrations. We have provided convincing evidence in Section 4.3 to demonstrate the following: 1). Adjusting levels of anaesthesia generates a controllable experimental model to study state-dependent activity in the mouse. 2). The θ/δ ratio could provide an LFP-based measurement of anaesthesia depth. 3). Response properties of single cells in mouse LGN, including response latency, contrast sensitivity and spatial frequency tuning properties are dependent on the subject's isoflurane state.

In the following discussion we relate our findings to previous studies, and also provide speculations on potential sources and functional implications of the properties we have characterized.

4.4.1 LFPs under high and low isoflurane states

It is already known that the cortical state is a functional reflection of the sleep-wake cycle, with the cortex operating in the synchronized and desynchronized states during non-REM sleep/quiet wakefulness and REM sleep/vigilance respectively (Harris and Thiele, 2012). Emerging evidence suggests that the synchronized and desynchronized states are characterized by distinct response patterns, and most work have focused on the contribution of cortical states in information processing at cortical level (reviewed in Lee and Dan, 2012; Harris and Thiele, 2012). However, the functional significance of subjective state in mouse LGN has not been comprehensively studied.

Here, we firstly examined the LFP in mouse LGN and compared with those in V1 under high and low isoflurane states. Simultaneous recording from mouse LGN and V1 with two separate MEAs was the first novel feature of experimental design in this study. As illustrated in Figure 4.1, the custom designed V1 recording setup successfully overcame the limitation of small brain volume, and also minimized undesirable interference/damage to brain tissues. In addition, the linear configuration of 32-channel MEA enabled us to record from the full extent of LGN along the dorsal-lateral axis, whilst the 4-shank MEA for the cortex featured the cover of all layers as well as a broad range in mid-lateral direction from V1.

The second unique feature was the attempt to differentiate brain states on the same animal by adjusting isoflurane concentrations. Isoflurane is an inhalational anaesthetic and functions as both promoting inhibitory GABAergic and reducing excitatory glutamatergic neurotransmissions (Franks, 2006; Thompson and Wafford, 2001). In addition, isoflurane, due to its lower blood solubility, allows faster induction and recovery than its related isomers such as halothane and enflurane (Eger, 1981). The application of isoflurane therefore allows response comparison under different anaesthesia levels on the same subject, in contrast to the widely used urethane anaesthesia protocol that has been widely applied in rodent brain state studies (Curto et al., 2009; Renart et al., 2010; Clement et al., 2008; Pagliardini et al., 2013).

To maximally differentiate the state, isoflurane concentrations ranging from 0.1%~3.0% have been tested in preliminary experiments. We found that 1.5%~2.0% and 0.3%~0.5% isoflurane in O_2 were the optimum highest and lowest concentrations applicable to the mouse, whilst maintaining satisfactory anesthetized conditions and triggering visual responses over long periods of recording. Therefore, these concentrations were applied during the current study.

We established that LFP in mouse V1 exhibited distinct patterns between the high and low isoflurane states. The LFP captures aggregate electrical activity generated by various neural processes, such as voltage-gated membrane oscillations (Kamondi et al., 1998) and synchronized synaptic potentials (Mitzdorf, 1985), in a cell ensemble around the electrode tip. In the present study, the LFPs in the high isoflurane state showed pronounced slow oscillations at high amplitudes, and were separated by high-frequency activity at low amplitudes. Contrastingly, the LFPs in the low isoflurane state featured higher frequency fluctuations at relatively low amplitudes, whereas the high-amplitude oscillation at low frequency as seen in the high isoflurane state was absent. Moreover, these changes were not related to visual stimulus presentation (Figure 4.2). These LFP characteristics reveal that high and low isoflurane states are in agreement with features demonstrated in the synchronized and desynchronized cortical states respectively (Lee and Dan, 2012; Harris and Thiele, 2012).

Furthermore, the cortical spread of LFP has been addressed by numerous studies, and the conclusion varies greatly from 250 μm to a few millimetres (Katzber et al., 2009; Berens et al., 2008). Despite the discrepancy in spatial extent, Kohn and colleagues proposed that LFP power display laminar variations within the cortex (Smith et al., 2012). However, with

electrode tracks recovered from histology and confocal imaging, we did not observe from the traces that LFP vary substantially among cortical layers.

Subsequently, we showed that the isoflurane state also had strong impacts on LFPs in different frequency bands. Compared to the high isoflurane state in both V1 and LGN, the low isoflurane state was linked to an increase in the power of theta (4~8 Hz, θ) and gamma (30~120 Hz, γ) frequency oscillations, as well as a decrease in the power of delta (1~4 Hz, δ), alpha (8~12 Hz, α) and beta (12~30 Hz, β) frequency oscillations (Figure 4.3). Related to previous studies, the gamma band activity has been most extensively assessed under distinct cortical states among these frequency bands. Gamma band activity is able to strongly assemble neurons into synchronous groups (Fries, 2009). Numerous investigations have demonstrated a notable increase of gamma LFP power in the cortical desynchronization in rodents (Metherate et al., 1992; Munk et al., 1996; Niell and Stryker, 2010), and this current study supports this notion.

Taken together, these observations imply that adjusting isoflurane concentration is an effective approach to induce distinct and controllable LFP fluctuations in the visual areas of mouse brain. In addition, differences in both the LFP trace and power spectrum in the cortex under the two isoflurane states raises the speculation that high and low isoflurane states mimic, in some respects, the synchronized and desynchronized cortical states. Also, the similarity in LFP power spectrum between V1 and LGN indicates that the brain state transition is likely to be a global effect that exists at various stages along the visual pathway. Results to test this hypothesis will be discussed in the following section.

4.4.2 State-dependent LFPs in V1 and LGN

The θ/δ ratio was applied in our current study to examine LFPs under high and low isoflurane states. This was supported by a previously defined algorithm that used the θ/δ ratio, together with ECoG or EMG, to score sleep/awake states (Costa-Miserachs et al., 2003). We firstly showed from one representative recording, unaffected by visual stimulus, the θ/δ ratio in V1 and also LGN persisted at statistically larger values in the low than the high isoflurane state throughout the recording (Figure 4.4). This result was in agreement with the higher θ/δ ratio observed in REM sleep than non-REM sleep in the sleep/waking score algorithm (Costa-Miserachs et al., 2003).

Importantly, this capability of θ/δ ratio in differentiating LFPs in relevance to the isoflurane state was verified from all the samples (n=4), in V1 as well as LGN (Figure 4.5). Next, looking into the correlation of the θ/δ ratio between V1 and LGN within individual animals, we demonstrate that these two brain areas are positively correlated, with a higher degree in the low isoflurane state (Figure 4.6). These results suggest that the increase of θ/δ ratio is beyond modulatory influence of visual stimulus presented, whilst isoflurane concentration change from deep-to-light. Such state-dependent activity exists in both subcortical and cortical areas in the mouse visual system, indicative of a global interconnection of neuronal activity along the visual pathway. Collectively, observations summarized in Section 4.4.1 and 4.4.2 demonstrate that adjusting levels of anaesthesia generates a controllable experimental model to study state-dependent activity in the mouse.

Supported by the findings described above, we investigated single-unit response properties in mouse LGN as isoflurane concentration varied from high to low, which was defined by the θ/δ ratio. From 25 recordings made from mouse LGN with animals anaesthetized with high/low isoflurane concentration, we show that their θ/δ ratios are unaffected by visual stimulus (Figure 4.7). Moreover, the θ/δ ratio shows significant increase in the low than high isoflurane state in general, in spite of some variations from individual recordings (Figure 4.8). These observations are in agreement with results described in Figure 4.4 and provide supporting evidence to uncover the link between state and response features of mouse LGN neurons.

4.4.3 State-dependent single-unit response property in LGN

In spite of the spreading interest in understanding state-dependent visual processing at the cortical level, relatively little attention has been focused on quantifying neuronal response features that provide inputs to V1. We evaluated the variations of response properties in mouse LGN under high-to-low isoflurane state transitions. To our knowledge, this study is the first in-depth report to characterize the role of subjective state on single-cell response properties in the visual thalamus of mice.

Isoflurane states vs. Response latency

From 155 single units made from 25 recordings in mouse LGN, we identified that the response latency was highly correlated with the isoflurane state, with the latency decreasing

as the animal transited to lightly anaesthetized state (Figure 4.9). Recent work by Wang et al. (2014) in rats appears to be most closely associated with the results we described here. Recording simultaneously from V1 and LGN, these authors broadly classify brain states based on desynchronization and synchronization evaluated by a cluster analysis of LFP power spectrum and measure response latency from temporal profile of receptive fields. Compared to the synchronized state, they showed that neurons in both V1 and LGN displayed shorter latency in the desynchronized state. Interestingly, they also observed that the latency advance accumulated along visual stages, from LGN to V1 and across successive V1 layers. Our results are in agreement with this finding, which suggest that fast sensory processing is pivotal for animal's efficient adaptation to the changing environment.

Wang and colleagues (2014) further reported that firing rates increased in the desynchronized state in LGN. This might lead to elevated membrane potential and increased conductance, and could contribute to the latency advance of LGN neurons. However, our results show that firing rates in mouse LGN are independent of isoflurane state. Therefore, an alternative contribution may originate from the RGCs, where response latency has been proved to be state-dependent (Galambos et al., 2001), through the "latency advance accumulation" along visual pathways.

Isoflurane states vs. Contrast sensitivity

To explore whether the isoflurane state had an influence on contrast sensitivity, we analysed the contrast gain and C_{50} of 148 single units and assessed their correlations with isoflurane states. Our results indicate that contrast gain significantly increase whilst C_{50} decrease as the animal under the state of low isoflurane, as indicated in the θ/δ ratio (Figure 4.10). This state-dependent contrast sensitivity was confirmed by normalized individual contrast response tunings (Figure 4.11), which showed a sharper slope in the low isoflurane state.

However, disparities exist in earlier studies in this field. It has been demonstrated that contrast sensitivity remained comparable in awake rabbits as they shifted between alert and non-alert states (Cano et al., 2006). Similar results have been reported from macaque LGN neurons in alert/anaesthetized states (Alitto et al., 2011). These findings could be largely explained by a scaled multiplicative gain change (Cano et al., 2006). Consistent with this hypothesis, a modeling study suggests that the multiplicative gain modulation might result from alterations in the membrane potential of cortical neurons (Murphy and Miller, 2003).

There are two possible reasons that might explain the differences between previous literature and our results. The first is the influence from anaesthetic agent. It has been demonstrated that many anaesthetic agents including isoflurane can alter membrane potentials and current in thalamocortical neurons through alterations of ions (Ries and Puil, 1999). This alteration might influence the multiplicative gain modulation as a consequence. Moreover, Funke and colleagues (Zhao et al., 2001) established that small amount of DA can facilitate contrast sensitivity in cat LGN, and extracellular DA concentration can be modulated by isoflurane administration (Votaw et al., 2003).

The other important aspect is that some state-dependent effects might go beyond multiplicative gain modulation. A recent experimental observation made from V1 neurons in awake rabbits detected contrast C_{50} of simple neurons in layer 4 cortex to be preserved in alert and non-alert states (Zhuang et al., 2014). Interestingly, these authors also identified that alertness selectively suppressed the simple cell responses to high-contrast stimuli. Such selective suppression could not be explained by multiplicative gain modulation, and subsequent modeling implied that it played a critical role in the speed of cortical feature detection (Zhuang et al., 2014).

Our result suggests that contrast sensitivity in mouse LGN is negatively correlated with isoflurane concentration. It requires further validation on whether this observation is a consequence of anaesthetic choice and/or reflects "untraditional" state-dependent information processing features, or attributes to other potential sources.

Isoflurane states vs. Firing rates and spatial frequency tuning properties

We examined the variation of spatial frequency properties from the high to low anaesthesia states. From a dataset of 82 isolated single neurons, we showed that preferred spatial frequency was free from modulation by isoflurane concentration. Interestingly, cutoff spatial frequency increased as the subject entered low isoflurane state (Figure 4.12), which was also verified from normalized individual spatial frequency tunings with enhanced responsiveness to a broader range of spatial frequencies (Figure 4.13).

We further evaluated whether spontaneous and evoked activities of mouse LGN neurons were under modulation of isoflurane concentration. Analysing from 155 cells, we found that the anaesthetic concentration did not have a modulatory effect on the spontaneous or evoked

firing rates (Figure 4.14).

Related to previous literature, it has been shown that macaque LGN neurons responded to visual stimuli at notably higher firing rates and followed stimuli drifting at higher spatial and temporal frequencies as the animal transited from anaesthetized to alert state (Alitto et al., 2011). In another study on rabbit V1, Zhuang et al. (2014) established that alertness increased the firing rate and temporal frequency bandwidth but preserved spatial frequency selectivity. A plausible explanation to these differences can be in the definition of "brain state". The state of the thalamus in inattentive/non-alert subjects may not directly be equivalent to that during deep anaesthesia or even sleep (Bezdudnaya et al., 2006), while both the desynchronized and synchronized states exist in the awake as well as anaesthetized states (Wang et al., 2014). Our results were based on the θ/δ ratio measured from LFP power, and therefore provided a more quantitative differentiation of brain state. Future work to record from awake animals and compare results to that under anaesthesia may provide further insights on the influence of brain states in response properties.

Additionally, in contrast to the findings stated above, increasingly experimental work has pointed out that a general increase in vigilance such as task engagement or behavioral arousal did not always show enhanced responses (Fanselow and Nicolelis, 1999; Castro-Alamancos, 2004; Otazu et al., 2009). A study in mouse V1 added more complexity by claiming that responses to drifting gratings significantly increased when the subject was behaviorally active (running) than inactive (standing still) (Niell and Stryker, 2010). An important aspect that might contribute to the discrepancy among these investigations was the selection of sustained (drifting gratings) versus transient (tactile stimulus) stimulation parameters, which can potentially evoke distinct levels of neuronal adaptation (Harris and Thiele, 2011). This mechanism may help to illustrate the higher sensitivity in spatial and temporal frequency reported by Alitto et al. (2011), in which drifting gratings were presented for 4 sec to anaesthetized animals and 3 sec to alert animals.

Isoflurane states vs. Direction/orientation selectivity

We mainly focused on evaluating averaged single-cell response properties from one recording and relating to those from other recordings in this study. However, a future direction could involve comparing response properties under different isoflurane states recorded from the same individual cell. It has been recently reported that the directional

selectivity of DS neurons in rabbit LGN was strongly regulated by alertness, which increased responses in the preferred direction whilst suppressed responses in the null direction, thereby enhancing the directional selectivity of these neurons (Hei et al., 2014). Consequently, it may be interesting to compare the directional/orientation selectivity of individual neurons in mouse LGN recorded from both high and low isoflurane states. In addition, this improvement may also help to provide insight into the variation of contrast response tuning properties and spatial frequency tuning properties that have been reported to depend on the anaesthesia state (Section 4.3.4).

CHAPTER 5

Localisation of recording sites and histological reconstruction of mouse LGN

5.1 Introduction

Histological recovery of recording sites plays a fundamental role in electrophysiological studies of the brain. Specifically, electrode localization serves as a prerequisite to characterize response patterns in mouse LGN, as this nucleus is located deep in the brain (2.6~3.2 mm below the pia) and occupies a small volume (0.30 ± 0.02 mm^3 in C57Bl/6 wild type mouse) (Seecharan et al., 2003).

Compared to traditional electrolytic lesion protocols for histological electrode reconstruction (Grubb and Thompson, 2003), fluorescent staining and confocal microscopy has two primary advantages that lead to its increased popularity in recent research endeavours (Piscopo et al., 2013; Zhao et al., 2013): one obvious advantage is that fluorescent dyes stain nuclei near electrodes, and therefore avoid the issue of balancing between obvious lesion size and brain integrality that is crucial for localizing recorded cell regions; the other advantage is that fluorescent nuclei staining is far more efficient in processing than nissl staining, which is the most commonly used protocol for evaluation of lesions.

In the second part of this chapter (Section 5.2.1), new approaches developed and improved from recent mouse LGN researches (Piscopo et al., 2013; Zhao et al., 2013) will be introduced. These techniques enabled confirmation of electrode location with the use of fluorescent dye and subsequent confocal imaging for both electrophysiological recordings in LGN as well as for simultaneous recordings in V1 (Section 5.3.1).

Additionally, we attempted to record from the full range of mouse LGN and make comparisons on response properties across different locations after characterizing as many

parameters as possible, including direction/orientation selectivity. To clarify location of different electrodes, a precise and straightforward approach is required, and a standardized LGN model needs to be established at the outset.

Numerous studies have been exploring protocols towards 3D visualizations of the mouse brain. For instance, magnetic resonance imaging (MRI) and positron emission tomography combined with computed tomography have been employed for imaging of the entire brain. However, these techniques often lack the resolution or contrast required to visualize small-volume anatomic nuclei like that encountered in the mouse brain. Microscopic techniques, such as two-photon laser microscopy, are capable of achieving cellular resolution but lack adequate resolution in depth (Lemmens et al., 2010; Truong et al., 2011). Traditional histological sectioning approaches, such as sectioning with freezing microtome or paraffin, are able to obtain cellular resolution over large volumes, but section alignment is time-consuming and difficult due to distortions that occur during slicing.

For these reasons, the development of 3D visualization techniques that operate on a mesoscopic scale, over relatively large field of view, with at least 50 μm resolution, is highly demanded. In Section 5.2.2, we show, for the first time, the protocols to section and image the mouse brain at 5 μm resolution with histocutter. Subsequently, we describe the LGN volume visualization with Amira. Histocutter is a purpose-built robotic device for high-throughput 3D tissue visualization, whereby, multi-spectral signals can be imaged from thousands of aligned tissue slices, with thickness as thin as 1 μm. Amira (http://www.vsg3d.com/amira/overview) is a commercial software, specifically designed for reconstruction and analysis of volumetric 3D data with a wide array of applications.

The 3D LGN model obtained in this way displays a close to perfect alignment and satisfactory match to original images, and is also able to identify subtle neuroanatomical changes of mouse LGN (Section 5.3.3). With this model, we were able to map confocal-imaged electrode tracks based on morphological features and could define electrode location within LGN with reasonable accuracy (Section 5.3.4).

In Section 5.4, we conclude this chapter with a summary of findings, and draw on a wider context of previous studies.

5.2 Methods

5.2.1 Visualisation of electrode track

5.2.1.1 Staining electrode with fluorescent dye

At the end of a recording session, the electrode position in X, Y, and Z axes were recorded from the micromanipulator, then the electrode was withdrawn and soaked into DiI (42364, Sigma Aldrich) /DMSO (Dimethyl sulfoxide, Sigma Aldrich) solution (20 mg DiI in 300 microliter DMSO) for a few seconds, and left to dry.

The electrode was then inserted quickly to the same recorded coordinate in the brain, taking about 5~10 seconds to reach a depth of 3.0 mm. Prompt insertion was crucial here, to lower the risk of dye being absorbed by cells before reaching the target location in LGN. The electrode was then taken out slowly after having settled in brain for approximately 25 min, for DiI to fully spread among neurons near the electrode.

Additionally, another simplified approach for electrode track visualization was developed for experiments with simultaneous V1 recoding. Staining solution was made with DiI in 100% ethanol (Sigma-Aldrich, UK), at the concentration of 3 mg/ml. Before recording, the back of the electrode was painted with the staining solution using a small brush under a microscope. Then the V1 electrode was positioned to the targeted depth at the speed of 10~15 μm/sec.

5.2.1.2 Perfusion and nuclei staining

The probe was taken out of the brain after staining, and the animal was sacrificed with an overdose of 10% urethane (Sigma-Aldrich, UK), and perfused intracardially with PBS (Life Technologies, UK) and fixed with 4% paraformaldehyde (PFA) (Sigma-Aldrich, UK) solution. The brain was dissected out and placed in 4% PFA at 4˚C overnight, and then transferred to PBS for stock at 4˚C until further processing.

On the day of imaging, an incision was first made in the contralateral brain with blade to help with site localization. Then the brain was embedded with 2% agarose (Sigma Aldrich, UK), and sectioned coronally at 200 μm with a vibratome (Leica VT 1000 S), at a speed 0.65 mm/s and a frequency of 50 Hz.

The slices were then mounted on positively charged slides (Thermo Scientific, UK), and PBS around and on slices was dried out with soft tissue to prevent further dye concentration

from diluting. Following incubation with DAPI (Fluoroshield with DAPI, Sigma Aldrich) for 15~20 min to stain nuclei, slices were covered with coverslips (Thermo Scientific, UK). Afterwards, slides were kept away from the light for a few hours for DAPI to dry. Coverslip was sealed with nail polish before imaging.

5.2.1.3 Confocal imaging and post-processing

Images were taken on Leica TCS SP5. The LAS_AF (Leica Application Suite_Advanced Fluorescence) acquisition software was used to process the images with the following beam path settings: for DAPI and DiI, UV and 543 nm laser were powered at no more than 50% and 80% respectively. Two sequential scans were conducted at spectral range of 419~473 nm for DAPI (sequential scan 1), and 554~607 nm for DiI (sequential scan 2). Focus was achieved by adjusting Z position. To perform the best balance between contrast and brightness, Smart Gain was increased until a few single blue dots appeared, while Smart Offset was decreased till a few green dots emerged. Images were taken with 10×objective lens with size settings of 1024×1024 pixels, line average of 4 and frame average of 4. For tile scan, images were obtained with 5×objective lens with size settings of 512×512 pixels, line average of 4 and frame average of 1. Image post-processing was carried out with ImageJ and Amira.

Next, the outlines of LGN and the electrode track from confocal microscopy were traced manually. The boundaries of the LGN were readily visible from DAPI staining: the optic tract indicates the dorsal-lateral LGN borders, and the medial boarders of LGN are illustrated by a small but obvious gap in soma density between LGN and the latero-posterior nucleus. This gap reveals the major site of afferent and efferent LGN fibers comprising the internal capsule and remains constant throughout the anterior-posterior axis of LGN (Piscopo et al., 2013; Cruz-Martin et al., 2014).

5.2.2 3D LGN reconstruction and electrode localization

5.2.2.1 Specimen preparation

The animal was perfused (the same protocol as mentioned in Section 5.2.1.2), and the brain was taken out and kept in PBS at 4˚C until further processing. For brain staining, Sudan Blue II (Sigma-Aldrich, UK) was selected. Sudan Blue II is a member of the Sudan family and is known for masking fluorescent structures (Baschong et al., 2001). Sudan Blue II was

weighted and mixed with 2% paraffin wax (Fisher Scientifica Ltd), and then kept in oven (Genlab, UK) at 60˚C till the wax fully melted. At this stage, wax was stirred thoroughly for a few times so that Sudan Blue II could dissolve in wax completely and evenly to avoid crystal accumulation that could degrade the quality of the sections and subsequent imaging.

The brain sample, went through dehydration, staining and embedding procedures, according to the following protocol.

Day1:

1) Dehydration:

70% ethanol (Sigma-Aldrich, UK) 30 min

90% ethanol 30 min

100% ethanol 45 min

100% ethanol 45 min

100% ethanol 30min

2) Cleaning:

Histoclear (Fisher Scientific Ltd, UK) 30 min

Histoclear 30 min

3) Cleaning combined with the first stage of dye infiltration:

Histoclear + 3% Sudan Blue II (0.3 g Sudan Blue II in 10 ml histoclear) 2~3 hours at room temperature.

4) Dye infiltration:

2% Sudan Blue II in paraffin wax inside embedding oven (TAAB MK II) at 60˚C with a pressure of 600 m Bar for overnight.

Day 2:

5) Embedding:

Using a pre-warmed KD-BM Tissue Embedding Center (Jinhua Kedi Co Ltd), brain specimen was embedded in 2% Sudan Blue II in paraffin wax, in embedding ring (Fisher Scientific Ltd, UK), and was left to cool down and mould.

After waiting for at least 4 hours for the specimen to fully settle in wax, specimen block was trimmed with microtome (Leica 2655) at speed 3 with thickness of 10 μm/slice until specimen position could be recognized and smooth wax surface could be obtained. The wax around the specimen was manually trimmed with a blade, leaving the specimen area sticking out, and finally, the specimen module was ready to be processed with the histocutter.

5.2.2.2 The histocutter

The histocutter and its corresponding Java-based CutterMaster software used in this project (originally developed by J. Crawford and J. Reynaud at Devers Eye Institute) was a duplicated system bought by Professor Ross Ethier (head of Medical Engineering Solutions in Osteoarthritis Center of Excellence at Imperial College London) and under development and maintenance of Amanda Wilson (High Throughput Histology Technician in Bioengineering, Imperial College London).

As illustrated in Figure 5.1, main components of this system consist of rotary microtome, cutting head with clamp for tissue block, arc lamp, objective lens, filter wheel (fluorescein isothiocyanate (FITC), Rhodamine (RHOD) and diamidino-2-phenylindole (DAPI) etc.), camera with high resolution at 4096×4096 pixels, as well as a computer with CutterMaster software that was responsible for image-capturing, reconstruction and analysis.

On the histocutter, firstly the specimen module was mounted in the block holder, trimmed for a few sections with the microtome for blade alignment. Lens position was then adjusted to observe the specimen appropriately. Focus position was decided under the facilitation of the objective lens on the microscope and real-time updating of images from Streaming function on the CutterMaster. Finally, after air puffers placed in position (one each on the objective lens, the specimen block and the blade), the microtome was switched to the continuous section mode, with number of slices set to 300 on the CutterMaster. The system was left for processing overnight.

Parameters and settings used on the histocutter are:

Cutting speed: 3

Knife angle: 2.5

Lamp intensity: 100

Channel No.: Channel 2 (Excitation at 560 nm, Emission at 645 nm)

Thickness: 5 µm/slice

Focus exposure(s): 5

Thumbnail Exposure(s): 20

Objective lens and zoom: AZ Plan Fluor 2×, Zoom 2× from Nikon, resulting in a working distance of 45mm. Field of view (FOV) (mm): 4.585, microns per pixel: 1.119.

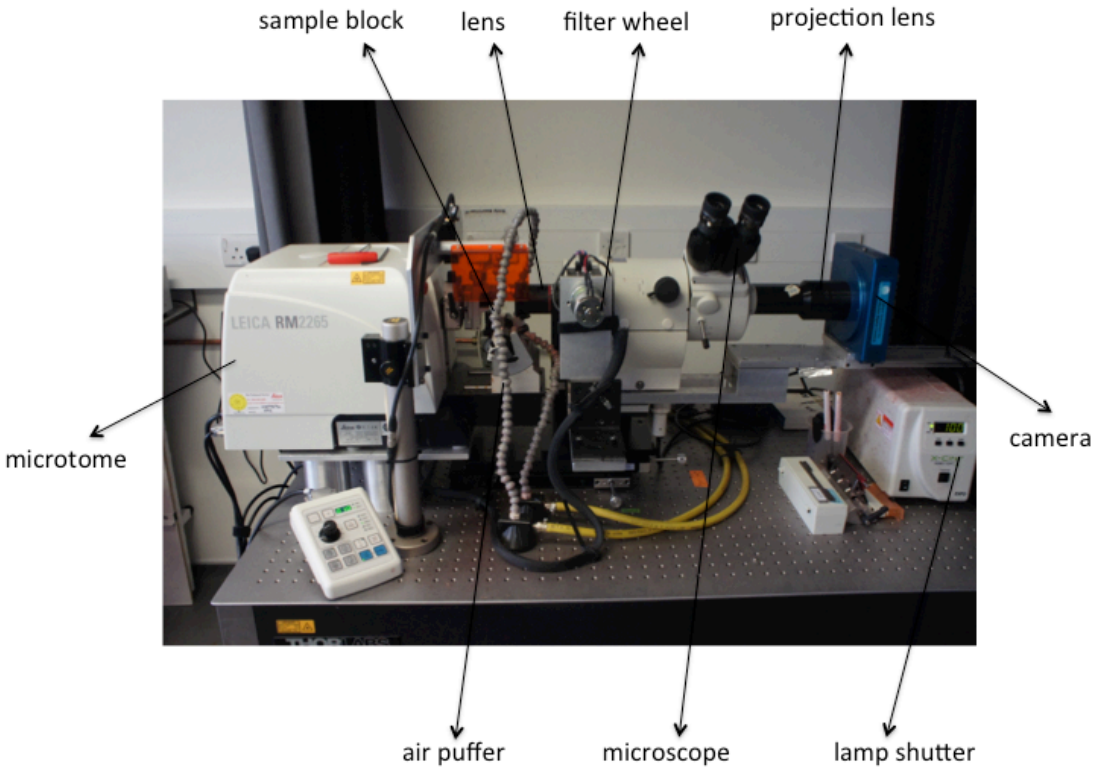

Figure 5.1 Image of the histocutter used in this project. Each main component is marked. Together with image capturing computer (not shown in this image), these components make the histocutter system function as an automatic device for high quality imaging of aligned fixed tissue.

5.2.2.3 Post-image processing with the Amira

After image-capturing, the image stack was downscaled to 1024×1024 pixels and processed with ImageJ. A sub-stack of 512×512 pixels containing the relevant brain areas was chosen, the remaining brain areas not of interest were chopped out. This modified image stack was then reopened on Amira (version 5.2.2), with voxel size: x: 4.476; y: 4.476; z: 5. The voxel size was decided according to settings on the objective lens and slice thickness.

The outline of LGN boundary was manually segmented every 5~10 voxels with Intuos Pro touch pen (Wacom, UK) that connected to the Amira computer. Starting from the anterior specimen, once any two voxels were selected, Amira conducted automatic analyses of their morphological features such as shape, size, and orientation. Based on that, a volume between those two selected voxels could be created. Advancing such analyses from the anterior to the posterior allowed an entire LGN volume in 3D to be initially reconstructed.

Afterwards, each image within the LGN volume was eye-inspected at corresponding level. Any image that either failed to match with original image or had inconsistent shapes, sizes or orientations to adjacent images was ruled out. Procedures including segmentation and eye-inspection were repeated until 3D LGN volume with satisfying smooth edge was obtained. The LGN volume was evenly divided into three sub-locations along the anterior-posterior axis and named as the anterior, the middle and the posterior LGN respectively. This 3D LGN was utilized for further comparison with confocal images from each recording, to categorize the electrode track location and single cell location that the relevant site recorded from.

For the image taken with confocal microscopy after each recording, it was adjusted to same resolution as the 3D LGN on ImageJ, and imported to Amira at voxel size: x: 4.476; y: 4.476; z: 1. A continuous comparison between the confocal image and the 3D LGN along the anterior-posterior axis was conducted in terms of morphological features, until the best match was found throughout the LGN volume. Based on its relative location within the 3D LGN, electrode location categorized as the anterior/middle/posterior could be determined.

5.3 Results

The results are presented in three parts. The first part describes the electrode track visualization within mouse LGN and V1 by confocal microscopy, with protocol improved from previous studies (Piscopo et al., 2013; Zhao et al., 2013) (Section 5.3.1). The second

part presents the original reconstruction of mouse LGN in 3D with histological approach (Section 5.3.2 and 5.3.3), and the final Section 5.3.4 shows results on mapping the confocal image with the LGN volume and determining electrode location accordingly.

5.3.1 Electrode track visualization

The staining and confocal imaging were performed across all subjects, for recordings from LGN alone as well as simultaneously from V1. Results to recover electrode tracks from the two brain areas are presented separately in this section, and their contributions to the electrophysiological characterization and implications on recording quality are also shown. Overall, the protocol introduced in Section 5.2.1 provided satisfactory visualization of electrode tracks, in addition to brain areas that electrodes were recorded from.

In all of the cases to retrieve electrode penetration tracks in LGN, the contralateral brain was cut off before staining to help with registration. In the post-processing of the confocal image with ImageJ, the electrode track dyed with DiI was displayed in red, whilst the brain stained with DAPI was shown in green, and the LGN boundary was manually traced in white. At the thickness of 200 μm per slice, the entire electrode track was restricted to only one slice in most cases. As a consequence, it saved the trouble of image alignment and registration in post-processing (Figure 5.2A).

First of all, the tile scan, which demonstrated an overview of the brain condition and electrode track, acted as the primary filter for electrophysiological data pool to be subsequently looked into in this project. This resulted in 28 penetrations across 20 mice in total for single-unit characterization in LGN (Chapter 3), and 4 penetrations across 4 subjects with simultaneous recordings from LGN and V1 (Chapter 4). Additionally, according to the location of the electrode tip, positions of each electrode site became readily available. As a result, signals recorded from sites that were outside the LGN boundary were excluded from subsequent analysis.

Moreover, as seen from the representative tile scan image in Figure 5.2A, the electrode track was parallel to the brain's midline, suggesting that the electrode was lowered vertically into brain as desired and both eyes of the mouse were maintained at the same horizontal plane successfully throughout the surgery and recording. Also, as observed from tile scans of all 24 animals, the depth of LGN spanned from 2.4 mm to 3.2 mm below the pia, in accordance

with mouse brain anatomy and other mouse LGN studies (Paxinos and Franklin, 2008; Grubb and Thompson, 2003; Psicopo et al., 2013).

Secondly, confocal images with higher magnification are capable of providing more detailed histological information in terms of electrode locations. Figure 5.2B-D illustrate such examples from three individual subjects. Images were obtained from the same protocol as the tile scan, except with 10× objective lens and higher resolution resulting in higher magnification and better image quality. Electrodes were recorded from the anterior (Figure 5.2B), middle (Figure 5.2C) and posterior (Figure 5.2D) LGN individually. This location classification was decided based on both the aimed coordinates during surgery (2.2 mm, 2.6 mm and 3.0 mm posterior from Bregma point respectively) and the morphological mapping of electrode tracks visualized by confocal microscopy with the 3D LGN model (see Section 5.3.4 for more details).

The 16 (A1x16-Poly2-5mm-50s-177-A16) or 32 (A1*32-5mm-25s-177-A32) - channel electrode for the LGN characterization spanned 750 μm along the vertical axis. On the basis of these specifications as well as anatomy of mouse LGN, the electrode was aimed at the middle LGN in the coronal plane, instead of being either too lateral or medial. This was done under consideration to record as many cells as possible from LGN. Like illustrative images shown in Figure 5.2, most electrodes recorded from the middle LGN in the coronal plane as required.

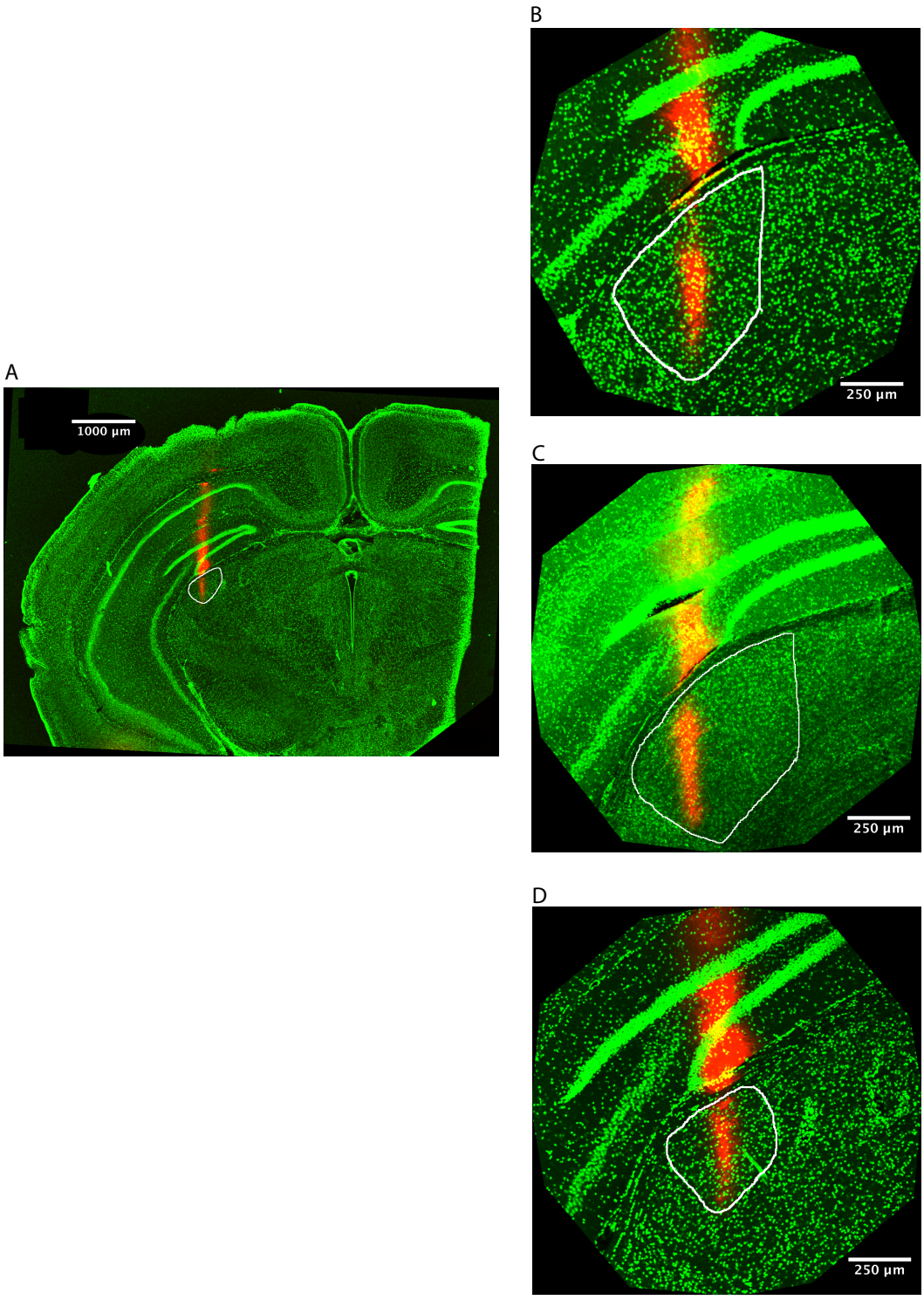

Figure 5.2 Confocal imaging of coronal sectioned brain slices to recover electrode tracks in mouse LGN. Electrodes were dyed with DiI/DMSO solutions (red track), and slices were stained with DAPI (displayed as green on these images). LGN boundaries are manually outlined in white here. A: Tile scan obtained with 5× objective lens, displays the coronal section and electrode track as a whole; B-D: Imaged with 10× objective lens, show electrode penetration tracks in the anterior, the middle and the posterior LGN from three different subjects.

For subjects with simultaneous recordings from V1 and LGN, the V1 electrode was painted with DiI in ethanol before insertion, followed by the same histological protocol and confocal imaging process as for the LGN electrode. The confocal imaging of the V1 electrode served four basic purposes:

1). It directly indicated the distances between the two electrodes along the anterior-posterior axis when slicing the brain, which was difficult to precisely assess during surgery. In most instances, the V1 electrode was 1~2 slices more posterior to the LGN electrode, which meant that they were approximately 200~400 μm apart. We targeted to place the two electrodes as close as possible, to record from the corresponding anatomical thalamocortical connection, and 200~400 μm was the shortest distance achievable in recording to minimize physical interference as well as maintain the projection aimed for.

2). The tile scan of the brain section with the V1 electrode, as exemplified in Figure 5.3A, provided a straightforward idea of brain tissue integrity. This overview was of special importance in recordings when two electrodes were closely placed in the brain. Any extra mechanical shift or damage may lead to recording quality degradation.

3). More importantly, it ensured histologically that the electrode was correctly placed in V1. If electrode sites were located outside V1 area, corresponding recordings were excluded from further analysis.

4). Tile scan accounted for the electrode angle. The V1 electrode was designed to penetrate at 25 to 45 deg to minimize interference of the two electrodes. Figure 5.3A demonstrates that in this specific recording, the electrode was lowered at approximately 30 deg from the middle line. In addition, under higher magnification taken with 10× objective lens, the location of the electrode tip location was easily obtained. From the evidence of the electrode angle and tip location, it is straightforward to infer the correspondence between electrode sites and layers of V1 (Figure 5.3B). This information is of significance in studying functional connectivity between LGN and V1.

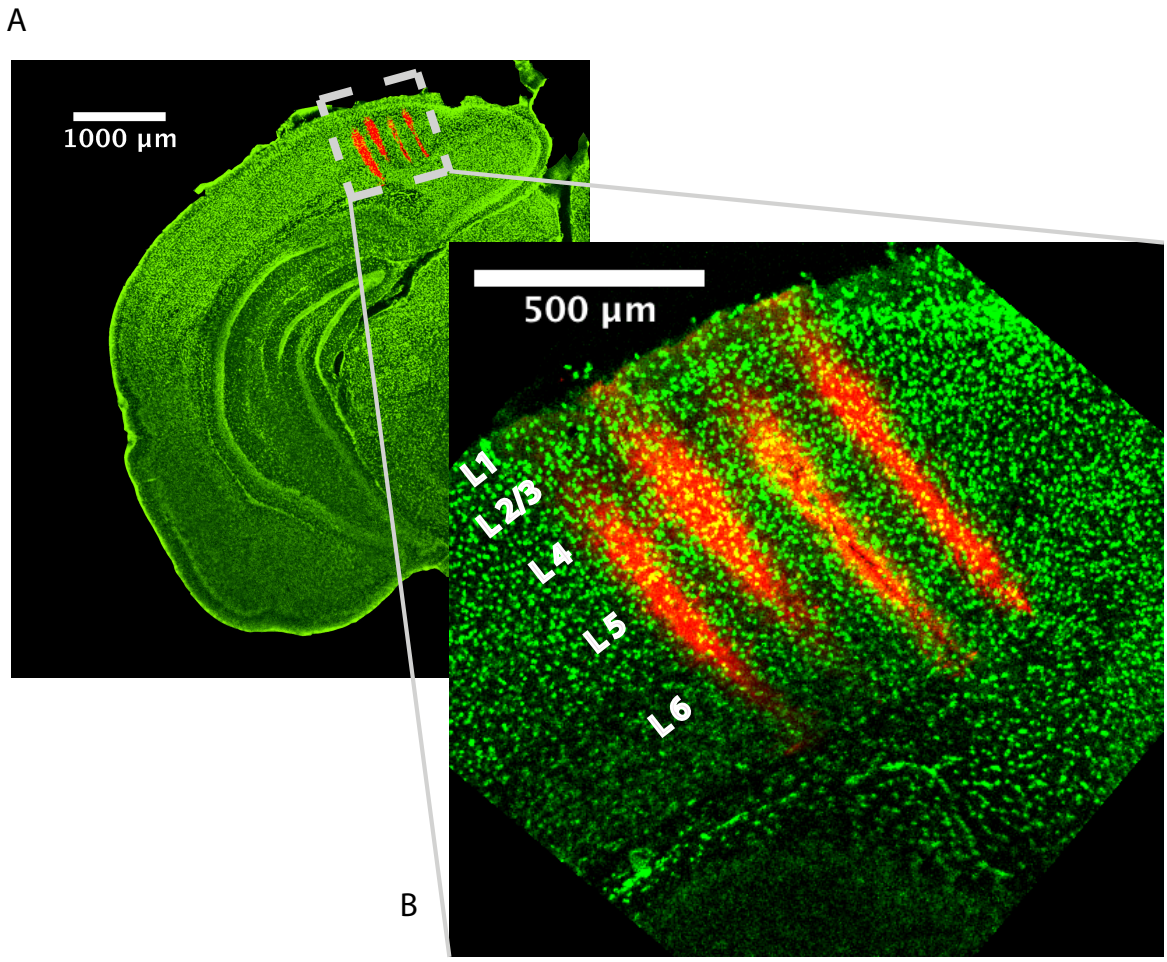

Figure 5.3 Images obtained with confocal microscopy of coronal sections to recover electrode tracks in mouse V1. The brain specimen was taken from experiments with simultaneous recordings in LGN and V1. The V1 electrode was painted with DiI in ethanol (3 mg/ml) (red track), and brain sections were stained with DAPI at thickness of 200 µm (displayed in green here). A: Tile scan taken with 5× objective lens, provides a general idea of depth and angle of the electrode penetration, with the contralateral cortex being cutoff. B: Zoom in image of the electrode within V1 area, taken with 10× objective lens, displays correspondence between electrode sites and V1 layers.

5.3.2 Histocutter sectioning of Sudan Blue stained mouse brain

We successfully developed the protocol to section Sudan Blue II stained mouse brain with the histocutter for the first time.

We started with the optimization of specimen preparation protocols. Sudan dyes were applied because they make blocks opaque. Therefore, they are capable of blocking out of focus light and resulting in better resolution in Z-axis. Staining protocols including Sudan Black, Sudan Purple, and different concentrations of Sudan Blue II were tested. Generally, Sudan Black produced over-strong dye infiltration. Both Sudan Purple and Sudan Blue II were capable of maintaining endogenous fluorescence and limiting out-of-plane fluorescence.

Compared with Sudan Purple and higher concentrations (2.5% and 3% in paraffin wax) of Sudan Blue II, the current protocol described in Section 5.2 had better performance in obtaining sufficient contrast in imaging.

As shown in Figure 5.4, the raw images obtained with the optimized protocol displayed clearly the cortex and the hippocampus. The boundary of LGN could be defined based on the optic tract for dorsal and lateral boarders, while different soma densities marked the medial and ventral boarders among adjacent nuclei. Although it was difficult to delineate at the single cell level within LGN, the well-defined borders of LGN provided sufficient information for further investigation.

At the thickness of 5 μm per section, we were able to gradually track the slightest changes in morphology of LGN along anterior-posterior axis, which fundamentally support the reconstruction of this nucleus. In total, 290 coronal sections were obtained from one mouse brain that spanned the entire LGN. Figure 5.4A-C illustrates three individual examples (No. 45, 140 and 235 respectively) out of the 290 coronal sections captured by the histocutter system. The images were maintained at the same brightness and contrast level and perfectly aligned, benefiting from the histocutter and CutterMaster's automated continuous processing specifications.

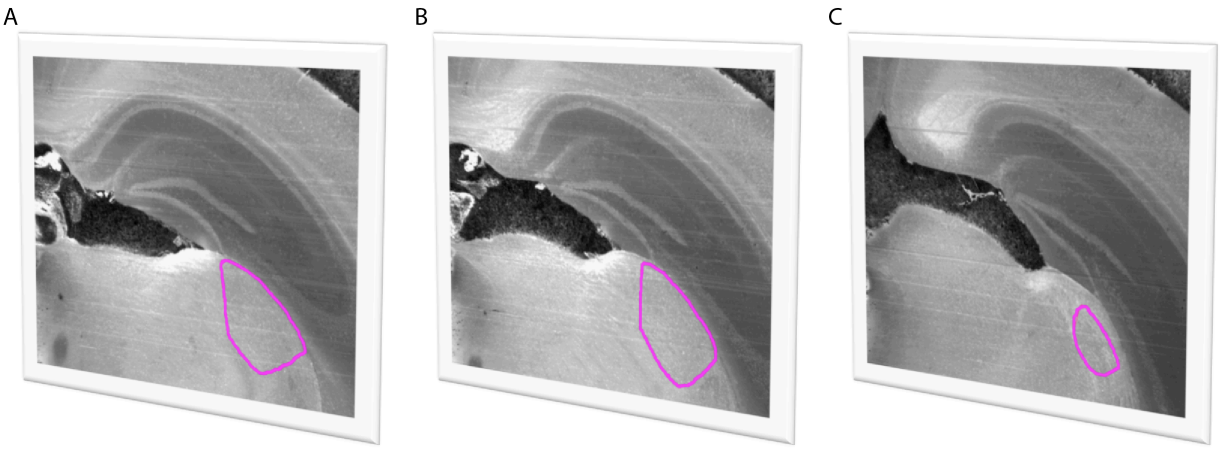

Figure 5.4 The mouse brain specimen that embedded with 2% Sudan Blue II in paraffin wax after dehydration and being processed on the histocutter at thickness of 5 μm/slice. Images were captured and saved automatically by data capturing computer of the histocutter system. 290 coronal sections that spanned the entire LGN were obtained. Post-imaging processing was carried out on ImageJ. A-C shows section No. 45, 140 and 235 respectively out of 290 coronal sections, with the LGN boundary highlighted in pink.

5.3.3 The 3D LGN reconstruction with Amira

After obtaining successive brain images, the next step was to reconstruct the LGN volume from them. The image stack containing 290 coronal sections was processed further with Amira after downscaling via ImageJ. 280 out of 290 sections were included for reconstruction. Remaining 10 sections were too vague to outline the LGN boundary both at the beginning of the anterior LGN and towards the end of the posterior LGN. As seen in Figure 5.5, the LGN volume was preliminarily reconstructed with segmentation throughout 280 sections, with the volume colored in green and other parts of brain in grey. In general, the reconstructed LGN in Figure 5.5 adapted morphological features from the original results. However, the reconstruction procedure at this stage was totally dependent on manual segmentation every 5~10 voxels that might have led to unsmooth border or mismatch with original images.

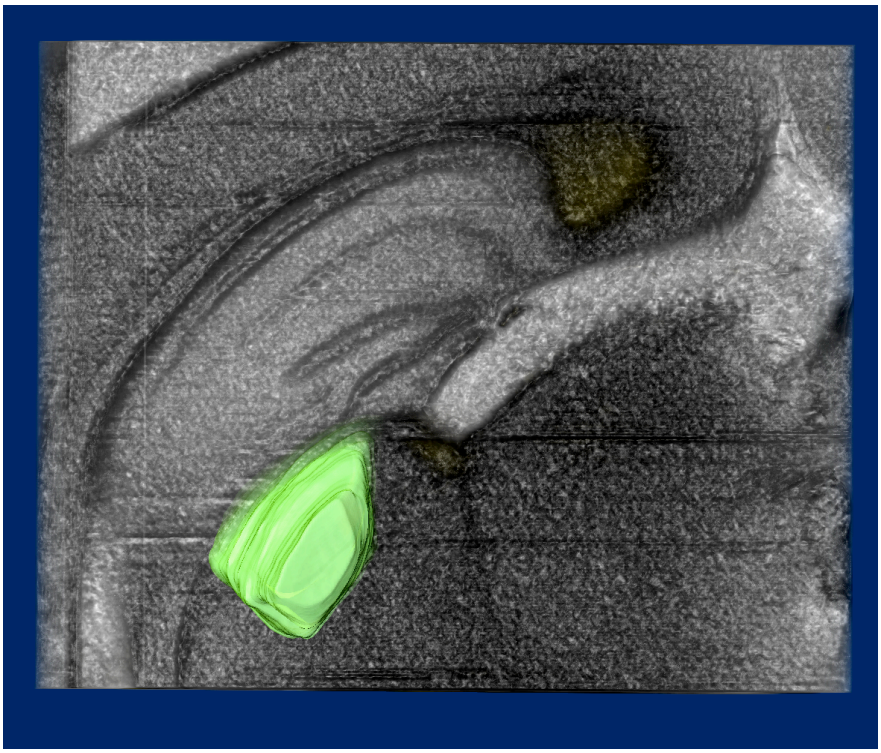

Figure 5.5 Initial reconstructed 3D LGN with Amira. By manual segmentation of the LGN boundary every 5~10 voxels, a volume LGN in 3D was initially created (green). Other brain areas remained grey.

To further improve the raw volume, each voxel was compared with its corresponding original section through eye-inspection and re-segmentation was performed on poorly matched voxels until edge smoothness was optimized to a satisfying level along with maintaining the original outline of each section. Figure 5.6A-C showed the finalized version of the LGN volume. Its back view (Figure 5.6A), front view (Figure 5.6B), and side view (Figure 5.6C) demonstrated a consistent transition in morphology among voxels with polished boarders. This was taken as the standard histological model of the 3D LGN.

The ultimate aim of the development of the LGN volume was to classify locations of electrode tracks accordingly. To accomplish this aim, the LGN volume was evenly divided into three sub-locations along the anterior-posterior axis and named as the anterior, the middle and the posterior LGN respectively (displayed as blue, green and magenta in Figure 5.6D). Also, a representative voxel taken out from each of the sub-location is shown on the right in Figure 5.6D, which manifests distinct morphological features in terms of size, orientation, and boundary, especially medial and ventral boarders. This 3D LGN based categorization together with targeted coordinates in recording were the criteria in determining electrode location.

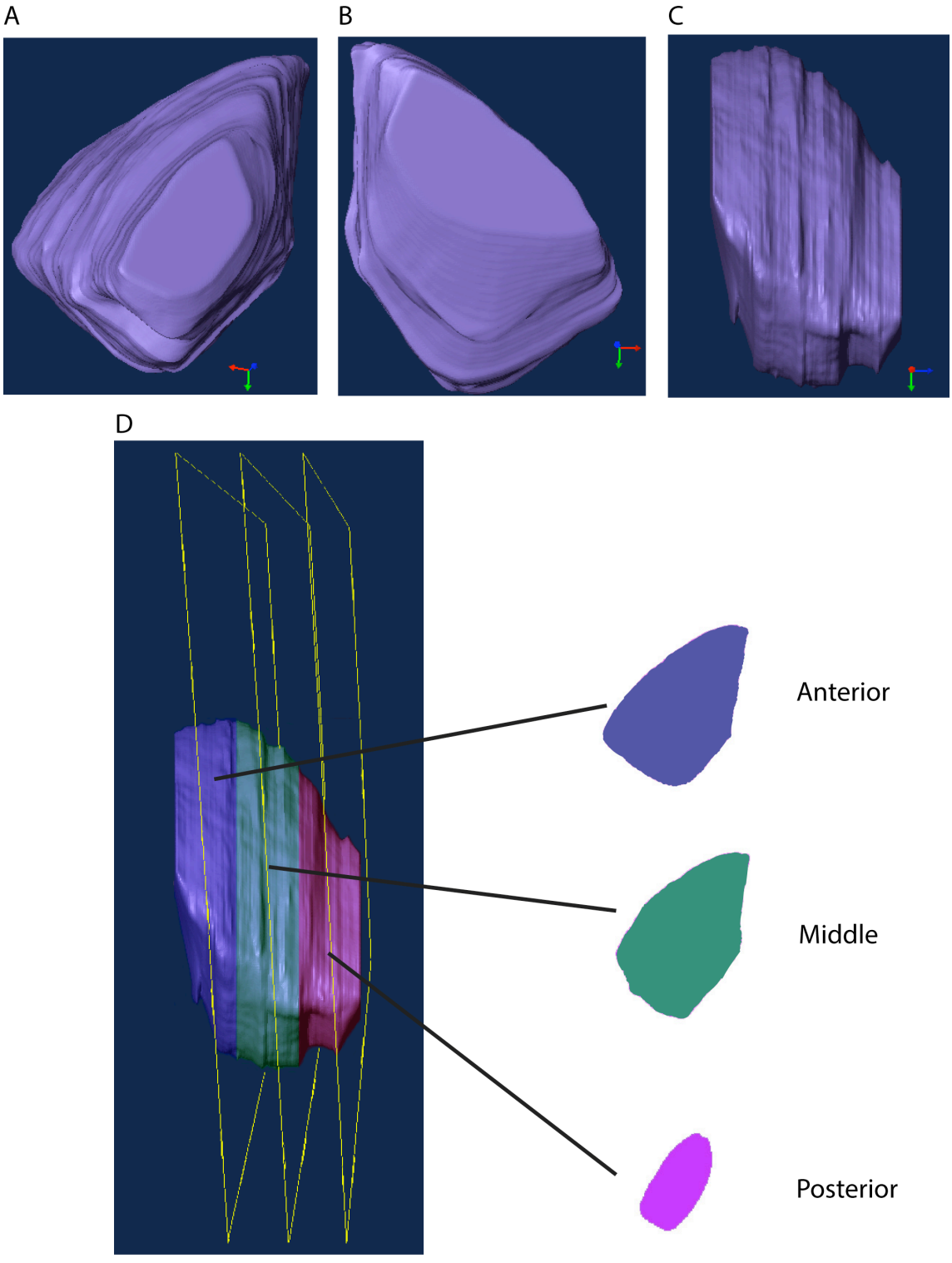

Figure 5.6 The 3D LGN model. Back (A), front (B) and side view (C) of the separated out LGN volume from the same specimen in Figure 5.5. They display a more polished edge, more consistent progression in morphology following further processing on Amira (eye-inspection and re-segmentation). D: The LGN volume was evenly divided into three subdivisions along the anterior-posterior axis and named as the anterior (blue), the middle (green) and the posteior (magenta) LGN respectively. A representative voxel is taken out from each of the subdivision and is shown on the right.

5.3.4 The 3D LGN based electrode track localization

This section presents results on the utilization of the 3D LGN in electrode track localization. Figure 5.7 presents a representative of mapping brain slice obtained from confocal imaging of actual recording with the 3D LGN model. Confocal image was analyzed with Amira at the same voxel size as the standard LGN model except that the thickness on Z-axis was taken as 1μm. Although not illustrated in Figure 5.7, from the 3D model, it is feasible to trace morphological relationship of LGN with other brain areas including V1 and the hippocampus. This feature offers more comparable factors between the model and confocal images, thus providing better accuracy in categorizing electrode locations.

In Figure 5.7, the volume LGN was changed into transparent color for better visualization of electrode penetration (red trace) and LGN boundary delineation (outlined as white) from the confocal image. The front view (Figure 5.7A) indicated almost identical matching of the confocal image with the individual voxel from the LGN model, whilst the back view (Figure 5.7B) showing an even better correspondence concerning size and orientation. From the side view (Figure 5.7C), it is clearly noticeable that the electrode was located in the middle LGN. All of the confocal-imaged electrode tracks from 24 subjects could be well matched with the 3D LGN model. Moreover, no ambiguous situations, such as electrode track slice felling into adjacent locations (e.g. in the anterior and middle LGN or the middle and posterior LGN) were observed.

The mouse brain that was used to create the LGN model was selected from animals of the same sex, age and weight matched to minimize individual variance. In addition, during the actual mapping of 24 mice that were included in data analysis, we found that all of them fitted well with the LGN model morphologically, including features in size, orientation and shape. There was no significant impact from individual variance on data presented here.

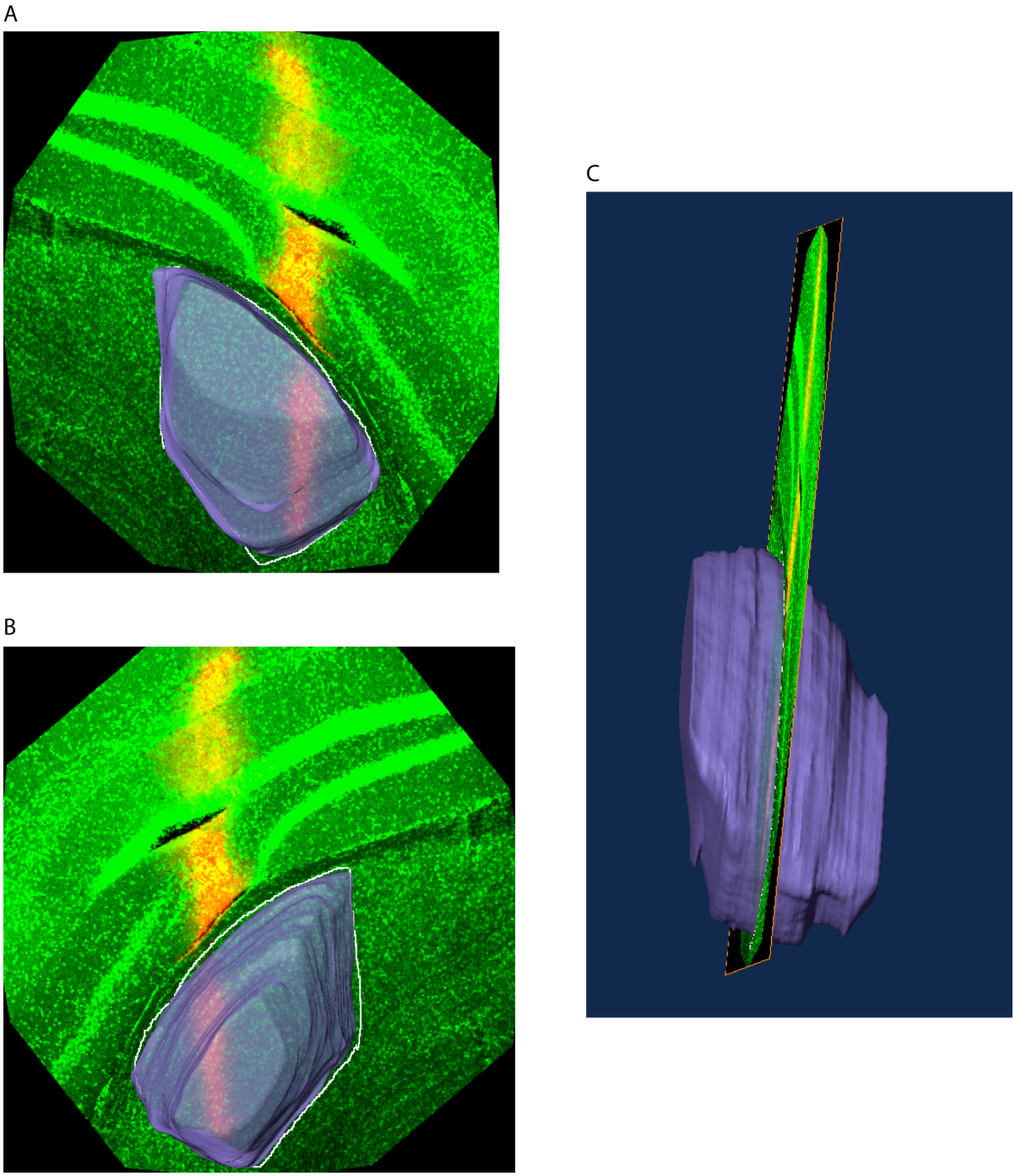

Figure 5.7 A representative matching the slice from an actual recording with the standard LGN volume to determine electrode location. The LGN volume was made transparent to visualize electrode track. Front (A) and back (B) views show the LGN boundary (outlined in white) from confocal imaging is in accordance with the 3D LGN. The side view (C) indicates that in this specific recording, the electrode was located in the middle LGN.

5.4 Summary and discussion

The protocols and results presented in this chapter describe a novel histological technique to reconstruct the mouse LGN volume. Along with the electrode track location confirmation through fluorescent dye and confocal microscopy, we are able to investigate the relationship between neuroanatomical structures and response features at single cell level. This section mainly involves three parts that relate to the results in Section 5.3. Firstly, discussions on improved protocols of electrode track visualization from previous studies are described in Section 5.4.1; secondly, technical considerations in the LGN volume reconstruction are presented in Section 5.4.2; thirdly, enhanced accuracy compared to earlier studies on mapping electrode locations owing to the LGN volume are evaluated in Section 5.4.3.

5.4.1 Confocal microscopy for electrode track confirmation

According to the pioneering mouse LGN research from Grubb and Thompson (2003), electrolytic lesions were performed at the end of experiments, and coronal sectioning with freezing microtome was carried out on the brain, followed by nissl staining. We tried a similar protocol previously in this study, however, it brought difficulties in controlling lesion current to generate obvious lesion track while maintaining integrity of LGN, which was crucial in determining electrode tip position and electrode track location involving the anterior/middle/posterior LGN. Moreover, in another very recent report by Piscopo et al. (2013), DiI/DiO was coated onto electrode before the first insertion. Without verifying neuronal responses by hand mapping of receptive fields, this protocol raised the risk of labeling mis-targeted brain areas other than LGN.

In this study, by coating the electrode with DiI and inserting it back to the same coordinate at the end of recording (Section 5.2.1), we were able to trace only penetrations that were electrophysiologically proven to be within LGN. In addition, under precise control of micro-drive and with the mouse's head being fixed during experiment, the electrode could be inserted back to the exact same coordinates used during the recording session.

Fluorescent dye and confocal microscopy based histological electrode visualization served three significant purposes in this study. Firstly, it provided a straightforward confirmation of the electrode track, thereby helping to exclude electrode sites that fell outside LGN or V1 from subsequent electrophysiological analysis. Secondly, it formed the precondition in

classifying electrode track location by mapping the result with the LGN volume. Thirdly, in simultaneous recordings from both LGN and V1, we were able to trace back the correspondence between electrode sites and V1 layers with precise histological location. This enabled us to study feedback and feedforward connectivity of LGN and V1 with confidence.

5.4.2 The 3D mouse LGN reconstruction

Reconstructing a 3D volume of the mouse brain has gained widespread attention in recent years, especially with developmental techniques for manipulating an animal's genome that bridges the divide between genomics and neuroanatomy.

The typical technique applied in most recent investigations has focused on appropriate registration algorithm for aligning 2D histological consecutive slices (Maheswaran et al., 2006; Yushkevich et al., 2006). The 2D consecutive slice histology had problems such as distortion that did not occur with 3D histocutter technique. Due to this drawback, studies in 2D consecutive slicing involved considerable mathematical and computational procedures.

In the study presented here, we exhibit, for the first time to our knowledge, a protocol to reconstruct 3D volume of mouse LGN with the histocutter. The histocutter serves as an automated and histology-based system for imaging and 3D reconstruction. It has gained widespread application in tissues such as bone and cartilage (Murienne et al., 2011). However, its usage in mouse brain reconstruction is unique. As a result, a few considerations in the protocol setting are discussed in this section, for the purpose of further optimization and application in brain volume reconstruction.

We started with testing effects of various specimen preparation approaches on the mouse brain. Given the small volume of the specimen size and soft neuronal tissue involved, we report that Sudan Blue dye at relatively high concentration at the first stage of dye infiltration (3%) and lower concentration (2%) in embedding could effectively achieve the balance between avoidance of dye crystallization in specimens and obtaining satisfactory image contrast (Section 5.2.2).

In parameter setting-up, cutting speed was set as 3, whereas focus exposure was 5 sec and thumbnail exposure was 20 sec. These parameters were decided in attempting to balance between section quality and time consumption. Thickness of each section was set as 5 μm, in

order to be consistent with voxel resolution on x- and y- axes, both of which were 4.476 μm. Apart from these, we used 2× objective lens at zoom 2, representing 1.119 microns/pixel with overall resolution of 4096×4096 pixels. These parameters were the best compromise between resolution and field of view (Figure 5.5). Improved from the original LGN volume (Figure 5.5) with Amira, the standard LGN model (Figure 5.6) adapts morphological features from the sample brain and exhibits satisfactory smooth borders.

A few recent studies have been investigating optimized specimen preparation protocol that is a critical step affecting imaging quality. Among them, Gleave et al. (2012) reported that lighter fixation, with 1% PFA, could provide greater detail in the mouse brain imaging than the standard 4% PFA fixation. The trade-off between too little fixation and compromised specimen quality should be taken into consideration. It is therefore of interest in the future work to experiment with alternative specimen preparations that may lead to enhanced imaging quality.

Above all, we demonstrate primarily a histological approach to reconstruct mouse LGN in 3D. It captures and displays morphological features at the resolution of 5 μm, thus providing visualization of continuous transition through the entire LGN. Moreover, this protocol can potentially be applicable to reconstruct other brain areas from other species, for the purpose of visualization and structural characterization.

5.4.3 Electrode localization with the 3D LGN model

In the electrophysiological characterization of this study (Chapter 3 and 4), electrodes were designed to target the middle LGN along the mid-lateral axis to record as many neurons as possible. Therefore, to investigate anatomical-dependent response properties, we aimed to record from various coordinates along the anterior-posterior axis, and electrode location determination related to this axis provided the rationale to use the 3D LGN model in this project.

We separated the LGN model evenly into three in the anterior-posterior axis and named them as the anterior, middle and posterior subdivisions separately (Figure 5.6D). To map the electrode track into one of the three subdivisions, we firstly aligned the confocal electrode track with the anterior 3D LGN, and then moved the confocal image along the anterior-posterior axis while comparing its morphological features with the model until the best

match was obtained (Figure 5.7). This procedure was successfully carried out on all 24 animals.

Compared to the simplified planes used by Piscopo et al. (2013), in which a 2D LGN template was used to represent each anterior/middle/posterior subdivision, our 3D model recovered the morphological features of the entire LGN. Thus, this LGN volume provides a more direct and precise technique in electrode localization. Additionally, moving a step forward from the 2D LGN diagrammatic sketches (Piscopo et al., 2013), we provide the innovative feasibility to retrace single unit location in 3D with higher accuracy (see Chapter 3 for an example of mapping the location of each DS/OS unit in the LGN volume), which links electrophysiology characterization with anatomical structure.

To sum up, the LGN volume allows spatial localization of electrode penetrations as well as single unit in fine detail, thus providing a fascinating opportunity to look into the relationship between anatomy and functional properties.

CHAPTER 6

Discussion

6.1 Single-cell response characterization in mouse LGN

An increasing number of investigations have indicated that LGN is strategically positioned to dynamically modulate visual inputs before they reach V1 (Saalmann and Kastner, 2011; Guillery and Sherman, 2002). Additionally, highly developed techniques of genetic manipulations in mice provide powerful tools to address many open questions to elucidate visual information processing (Brecht et al., 2004; Luo et al., 2008). Nevertheless, till now, our knowledge on response properties of mouse LGN mostly came from two studies (Grubb and Thompson, 2003; Piscopo et al., 2013) and a comprehensive characterization is therefore very much needed, to cover a broad range of response features as well as the full extent of the anatomy. A thorough characterization of mouse LGN neurons will shed new light on our understanding of this "smart-gating" operator in the mouse visual pathway.

6.1.1 Implications of findings

We performed comprehensive response characterizations on mouse LGN neurons in this study, from the perspectives of response parameters as well as volumes. Our dataset included 189 single units that displayed centre-surround receptive fields, made from 28 recordings that were histologically confirmed to be located within LGN. We firstly identified several response properties that paralleled the two key electrophysiological studies in this field (Grubb and Thompson, 2003; Piscopo et al., 2013), including receptive field properties, baseline spontaneous response amplitudes, spatial tuning curves and sustained/transient responses of cells.

In addition, our results revealed a few exceptional response features of mouse LGN neurons. Specifically, 2.1% (4/189) neurons displayed the classical receptive field structure that could not be driven by any sinusoidal gratings. Moreover, there were 2 out of 57 cells (3.5%) that

responded as “low-pass” filters, while 3 cells (5.3%) responded as “high-pass” filters in temporal frequency tuning curves.

Our results also showed cells (7.0% or 9/129) responded preferably to directions of motion. The selective direction/orientation was mostly restricted to the four cardinal axes. Comparing response properties of these DS/OS cells with the rest of population, it revealed that the LGN DS/OS cells showed a preference for higher spatial frequency. Furthermore, all of the DS/OS cells in this study were non-linear (6/6). Confirming the locations of these DS/OS cells by mapping cell location onto the LGN volume, we found that DS/OS cells were free to restrict to the area where DSRGCs project as previously demonstrated (Piscopo et al., 2013).

We further investigated parallel pathways in mouse LGN by comparing response properties between the ON-/OFF- centre cells. Our results indicated that ON- and OFF- centre cells were comparable in fractions among the dataset, receptive field size, as well as spontaneous and evoked activities. Interestingly, ON- centre cells were more sensitive than their OFF-centre counterparts over both contrast parameters, whereas OFF-centre cells showed higher degree of selectivity in temporal frequency tuning properties.

Along the line to look for evidence of parallel processing, we also explored response features between transient and sustained responsive cells, with transient responsive cells representing a far higher proportion in our dataset (92.7%, 114/123). It was revealed that compared to the cells firing in the sustained mode, the transient cells had longer response latency, and also tended to prefer lower cutoff spatial frequency and poorer contrast sensitivity.

6.1.2 Future directions

Our current work has provided characterizations on neurons that displayed centre-surround receptive fields, and future work could focus on the LGN cells with exceptional properties, as well as exploring functional significance of these cells in information processing. It would therefore be essential to:

- Include a larger sample in LGN, by applying quality analysis in single-unit clustering (Schmitzer-Torbert et al., 2005), regardless of receptive field structures. This improvement will potentially enable response characterization on non-typical cells and uncover a distinct set of visual features carried by these cells.

- Introduce on-line single-unit clustering. This will be beneficial in cases where unusual response characteristics are encountered, and targeting these single units with specific visual stimuli will help to further characterize their properties.

- Take advantage of genetic techniques. Targeted genetic manipulation allows cell-type specific perturbation of firing patterns (Zhang et al., 2007) and cellular signalling (Karpova et al., 2005) at single cell resolution (Brecht et al., 2004). These powerful techniques provide precise approaches to assess functional impact of specific retinal projections on LGN and subsequent cortical processing, and also help to elucidate the origins of some response properties within LGN, such as selectivity to direction/orientation and nonlinearity.

6.1.3 Conclusion

To sum up, we re-characterized and confirmed several response properties established from previous studies. Our current work featured a larger sample size and also more characterized properties. It will therefore benefit future work from both experimental and computational perspectives. Furthermore, the novel findings of exceptional response properties and evidence of parallel projections in mouse LGN indicate that sophisticated features are encoded at subcortical level.

6.2 State-dependent characterization in mouse LGN

Animals constantly switch between different states in the changing environment, which is typically associated with changes in brain activity. When numerous references in mechanisms and functionality of state dependence have emerged in the cortex (Harris and Thiele, 2012), these issues remain vague in mouse LGN. We therefore aimed in this work to study the modulation of states on response properties in mouse LGN, through a controllable state model.

6.2.1 Implications of findings

In this study, simultaneous recordings from LGN and V1 with two separate MEAs were made on four isoflurane-anesthetized mice, with the same animal at both high (1.5%~2.0% isoflurane) and low (0.3%~0.5% isoflurane) isoflurane concentrations. We first observed during recording that the LFP during the high isoflurane concentration was dominated by low-amplitude fast frequency activity, while during the low isoflurane concentration, the LFP showed high-amplitude slow waves. These distinct activities were in accordance with the essential features as classically seen during the desynchronized and synchronized cortical states (Lee and Dan, 2012).

We then explored the θ/δ ratio during high and low isoflurane concentrations. The θ/δ ratio, defined as the ratio of LFP power in 4~8 Hz against 1~4 Hz, has served as an algorithm to score sleep/awake states (Costa-Miserachs et al., 2003). Our results showed that the θ/δ ratio, independent from visual stimulus presentation, was significantly higher in low than the high isoflurane concentration, in both V1 and LGN. In addition, the θ/δ ratio between these two brain areas were correlated, especially in the low isoflurane concentration. These results indicate that adjusting isoflurane concentration is an effective approach to lead to controllable state model in the mouse.

Subsequent analysis was to characterize the impact of high/low isoflurane states on single-cell response properties of mouse LGN neurons. We first confirmed that the θ/δ ratio was statistically different corresponding to the isoflurane concentration from 25 recordings made from mouse LGN, consistent to what we have established earlier. From 157 single units isolated from the 25 recordings, we demonstrated that as the animal changing from higher to lower isoflurane state, the response latency decreased, and the contrast sensitivity increased.

Additionally, the LGN neurons had the tendency to be responsive to the gratings moving at higher spatial frequencies. By contrast, the spontaneous and evoked activities were free from modulation of the isoflurane concentration.

6.2.2 Future directions

We introduced in this study a controllable state model by changing isoflurane concentration and investigated the state-dependent activity in mouse LGN. Up till now, we have characterized single-cell response properties from different animals in either high or low isoflurane state. To fully interpret the role of brain state, it would be of interest in the following work to:

- Include a "global" measurement of cortical activity. For instance, the use of ECoG or EMG during recording may help to ascertain an animal as being in wake, or REM/non-REM sleep state (Costa-Miserachs et al., 2003). This approach, in combination with the θ/δ ratio measured from LFP activity, will provide indices of increased accuracy in brain state classification.

- Compare the response property of the same individual cell recoded from different states. The major challenge to this improvement was faithful spike-detecting and manual spike-sorting to extract information from MEA recordings, considering issues including neuronal response stability during approximate 5-hour recording from two states on the same animal. We have started to apply a more powerful cluster analysis algorithm that was newly developed by researchers from Harris's group (Kadir et al., 2014), which featured time-efficient clustering of high-channel-count neuronal data. We thus expect to advance this work by incorporating the individual cell comparison into the state-dependent response characterization.

- Characterize cell activities with the animal in the waking state and compare with those under anaesthesia, as anaesthesia may disrupt integration of information across brain regions through decreasing long-range coherence (John and Prichep, 2005). This direction will therefore expand current topic, and also add weight to relate with previous literatures, as numerous studies have focused on waking/alertness states in other species.

- Probe the multi-neuron firing patterns in mouse visual system. Neural activity displays striking interactions, and the collective function of a neural circuit is typically not predictable on the basis of single-unit recordings. With the data made from large-scale multi-electrode recordings available in this study, it is of interest to probe the neural interactions and how they contribute to information processing through approaches established by earlier studies (reviewed in Shlens et al., 2008).

6.2.3 Conclusion

To sum up, we show that adjusting isoflurane concentration is able to provide a reliable and manageable model to explore the state-dependent neural activity in mouse visual system. Our findings also demonstrate that properties, including response latency, contrast sensitivity and spatial frequency properties are modulated by the isoflurane concentration, highlighting state-dependent response features in mouse LGN.

6.3 Electrode track visualization and LGN reconstruction

LGN, locates deep and occupies a small volume in mouse brain (Seecharan et al., 2003). It is therefore essential to ascertain electrode location before studying response properties. Furthermore, for the purpose to characterize response features from the full extent of mouse LGN, a straightforward morphological volume to classify neuronal location is highly demanded. Numerous studies have been exploring protocols towards 3D visualizations of the mouse brain by aligning 2D histological consecutive slices, which involved extensive computational procedures due to slicing distortion (Maheswaran et al., 2006; Yushkevich et al., 2006). Consequently, we aimed in this study to establish a LGN volume that individual sections were in satisfactory alignment and could explicitly capture morphological features to determine neuronal locations.

6.3.1 Implications of findings

In this work, we optimized the protocol from previous studies (Piscopo et al., 2013; Zhao et al., 2013) to recover electrode track from each experiment. By coating the electrode with DiI/DMSO solution and inserting it back promptly to the same coordinate at the end of recording, our approach featured the capability to trace only penetrations that were electrophysiologically proven to be within LGN. In addition, under precise control of micro-drive and with the mouse's head being fixed, we were able to ascertain the electrode being inserted back to the exact same coordinate as during the recording. This protocol, together with subsequent confocal imaging, help to exclude electrode sites that fell outside targeted areas from further analysis. Importantly, it also acted as the precondition in confirming single cell location within the 3D LGN.

Next, we established, for the first time, a series of procedures to reconstruct LGN volume with the histocutter and Amira. By testing different combinations in specimen preparation and parameter setting-up, we reported that Sudan Blue dye at relatively higher concentration in the dye infiltration (3%) and lower concentration (2%) in embedding, with focus exposure of 5 sec and thumbnail exposure of 20 sec, could generate the best outcome in specimen imaging. Moreover, at the resolution of 5 μm/slice, the LGN volume presents a visualization of continuous morphological transition of this structure, which provides a high degree of accuracy in mapping neuronal location.

The ultimate application of this LGN volume is to classify the location of single neuron recorded from MEA. In doing so, we aligned the confocal-imaged electrode track with the LGN volume and looked for their best match in morphology, followed by categorizing cell location as in the anterior/middle/posterior LGN. Compared to the simplified LGN diagrammatic sketches in the previous literature (Piscopo et al., 2013), our results demonstrated neuronal location mapping with enhanced preciseness and provided a straightforward link between the response characterization and anatomical structure.

6.3.2 Future directions

As we have shown the accuracy to classify single-cell location to be in the anterior/middle/posterior mouse LGN according to the 3D LGN model, future work will focus on developing the LGN model and expanding its appliance in neuronal localization. To do so, it would be necessary to improve on:

- A more generalized mouse LGN volume by averaging from a larger sample size of mouse brains, considering factors such as sex dimorphism (Shah et al., 2004; Spring et al., 2007) might influence the model morphologically.

- Alternative specimen preparation protocol that may lead to enhanced imaging quality. For instance, lighter fixation, with 1% PFA, has been reported to provide greater detail in mouse brain imaging than the standard 4% PFA fixation (Gleave et al., 2012).

- Exploring regional preference of certain response property within the entire volume, without limiting to the manually defined anterior/middle/posterior categorization of mouse LGN. As revealed from the investigation by Krahe et al. (2011), the X-like, W-like and Y-like cells were more concentrated in the ventral border, along the boundary and around the central core respectively of the mouse LGN.

6.3.3 Conclusion

In conclusion, we present the first 3D mouse LGN reconstruction with the histocutter and Amira. The protocol is potentially applicable to reconstruct other brain areas from other species, for the purpose of visualization and structural characterization. In addition, together with the confocal-visualized electrode tracks, we are able to determine single cell position in

the 3D LGN with high level of accuracy, and thus provide a direct link between neuroanatomical structures and response properties in mouse LGN.

6.4 Afterword

In light of the recent findings of morphological X-/Y-/W- like cells and direction/orientation selectivity in mouse LGN, we revisited the issue of response properties of this nucleus through electrophysiological approach. Moving a step forward from earlier studies, we provide a reliable morphological link to response properties of neurons in mouse LGN. Also, we looked into the dependency of response features on isoflurane concentrations. Our current work suggests that the mouse LGN can dynamically regulate information transmission to the cortex using numerous mechanisms, including responding mode, modulation of neuronal responses according to subjective states. These results add to the increasing awareness of the active role of the visual thalamus in information processing, although subsequent work is needed to fully characterize response properties and uncover potential parallel projections in mouse LGN. Together with the availability of modern genetic tools in mice, response characterization in LGN will assist scientists to functionally target visual neurons, by doing so, unify anatomy, physiology and perception.

Bibliography

Adjamian P, Holliday IE, Barnes GR, Hillebrand A, Hadjipapas A, Singh KD (2004) Induced visual illusions and gamma oscillations in human primary visual cortex. The European journal of neuroscience 20:587-592.

Ahmed B, Anderson JC, Douglas RJ, Martin KA, Nelson JC (1994) Polyneuronal innervation of spiny stellate neurons in cat visual cortex. The Journal of comparative neurology 341:39-49.

Albrecht DG, Hamilton DB (1982) Striate cortex of monkey and cat: contrast response function. Journal of neurophysiology 48:217-237.

Albright TD (1984) Direction and orientation selectivity of neurons in visual area MT of the macaque. Journal of neurophysiology 52:1106-1130.

Alitto HJ, Moore BDt, Rathbun DL, Usrey WM (2011) A comparison of visual responses in the lateral geniculate nucleus of alert and anaesthetized macaque monkeys. The Journal of physiology 589:87-99.

Alitto HJ, Weyand TG, Usrey WM (2005) Distinct properties of stimulus-evoked bursts in the lateral geniculate nucleus. The Journal of neuroscience : the official journal of the Society for Neuroscience 25:514-523.

Alkire MT, Hudetz AG, Tononi G (2008) Consciousness and anesthesia. Science 322:876-880.

Alonso JM (2002) Neural connections and receptive field properties in the primary visual cortex. The Neuroscientist : a review journal bringing neurobiology, neurology and psychiatry 8:443-456.

Alonso JM, Usrey WM, Reid RC (1996) Precisely correlated firing in cells of the lateral geniculate nucleus. Nature 383:815-819.

Andolina IM, Jones HE, Wang W, Sillito AM (2007) Corticothalamic feedback enhances stimulus response precision in the visual system. Proceedings of the National Academy of Sciences of the United States of America 104:1685-1690.

Angelucci A, Bressloff PC (2006) Contribution of feedforward, lateral and feedback connections to the classical receptive field center and extra-classical receptive field surround of primate V1 neurons. Progress in brain research 154:93-120.

Arcelli P, Frassoni C, Regondi MC, De Biasi S, Spreafico R (1997) GABAergic neurons in mammalian thalamus: a marker of thalamic complexity? Brain research bulletin 42:27-37.

Bal T, Debay D, Destexhe A (2000) Cortical feedback controls the frequency and synchrony of oscillations in the visual thalamus. The Journal of neuroscience : the official journal of the Society for Neuroscience 20:7478-7488.

Baschong W, Suetterlin R, Laeng RH (2001) Control of autofluorescence of archival formaldehyde-fixed, paraffin-embedded tissue in confocal laser scanning microscopy (CLSM). The journal of histochemistry and cytochemistry : official journal of the Histochemistry Society 49:1565-1572.

Bastos AM, Briggs F, Alitto HJ, Mangun GR, Usrey WM (2014) Simultaneous recordings from the primary visual cortex and lateral geniculate nucleus reveal rhythmic interactions and a cortical source for gamma-band oscillations. The Journal of neuroscience : the official journal of the Society for Neuroscience 34:7639-7644.

Bauer M, Oostenveld R, Peeters M, Fries P (2006) Tactile spatial attention enhances gamma-band activity in somatosensory cortex and reduces low-frequency activity in parieto-occipital areas. The Journal of neuroscience : the official journal of the Society for Neuroscience 26:490-501.

Berens P, Keliris GA, Ecker AS, Logothetis NK, Tolias AS (2008) Feature selectivity of the gamma-band of the local field potential in primate primary visual cortex. Frontiers in neuroscience 2:199-207.

Bertini G, Buffalo EA, De Weerd P, Desimone R, Ungerleider LG (2004) Visual responses to targets and distracters by inferior temporal neurons after lesions of extrastriate areas V4 and TEO. Neuroreport 15:1611-1615.

Bezdudnaya T, Cano M, Bereshpolova Y, Stoelzel CR, Alonso JM, Swadlow HA (2006) Thalamic burst mode and inattention in the awake LGNd. Neuron 49:421-432.

Blasdel GG, Lund JS (1983) Termination of afferent axons in macaque striate cortex. The Journal of neuroscience : the official journal of the Society for Neuroscience 3:1389-1413.

Boley TJ, Popek EJ (1993) Parvovirus infection in pregnancy. Seminars in perinatology 17:410-419.

Brecht WJ, Harris FM, Chang S, Tesseur I, Yu GQ, Xu Q, Dee Fish J, Wyss-Coray T, Buttini M, Mucke L, Mahley RW, Huang Y (2004) Neuron-specific apolipoprotein e4 proteolysis is associated with increased tau phosphorylation in brains of transgenic mice. The Journal of neuroscience : the official journal of the Society for Neuroscience 24:2527-2534.

Bressler SL, Coppola R, Nakamura R (1993) Episodic multiregional cortical coherence at multiple frequencies during visual task performance. Nature 366:153-156.

Briggs F, Usrey WM (2007) A fast, reciprocal pathway between the lateral geniculate nucleus and visual cortex in the macaque monkey. The Journal of neuroscience : the official journal of the Society for Neuroscience 27:5431-5436.

Briggs F, Usrey WM (2008) Emerging views of corticothalamic function. Current opinion in neurobiology 18:403-407.

Briggs F, Usrey WM (2011) Corticogeniculate feedback and visual processing in the primate. The Journal of physiology 589:33-40.

Brown TM, Wynne J, Piggins HD, Lucas RJ (2011) Multiple hypothalamic cell populations encoding distinct visual information. The Journal of physiology 589:1173-1194.

Bruns A, Eckhorn R (2004) Task-related coupling from high- to low-frequency signals among visual cortical areas in human subdural recordings. International journal of psychophysiology : official journal of the International Organization of Psychophysiology 51:97-116.

Buzsaki G, Anastassiou CA, Koch C (2012) The origin of extracellular fields and currents--EEG, ECoG, LFP and spikes. Nature reviews Neuroscience 13:407-420.

Buzsaki G, Bickford RG, Ponomareff G, Thal LJ, Mandel R, Gage FH (1988) Nucleus basalis and thalamic control of neocortical activity in the freely moving rat. The Journal of neuroscience : the official journal of the Society for Neuroscience 8:4007-4026.

Callaway EM (2005) Structure and function of parallel pathways in the primate early visual system. The Journal of physiology 566:13-19.

Cano M, Bezdudnaya T, Swadlow HA, Alonso JM (2006) Brain state and contrast sensitivity in the awake visual thalamus. Nature neuroscience 9:1240-1242.

Casagrande VA, Norton TT (1991) The lateral geniculate nucleus: A review of its physiology and function. The Neural Basis of Visual Function. London: MacMillan Press pp. 41–84.

Castelo-Branco M, Neuenschwander S, Singer W (1998) Synchronization of visual responses between the cortex, lateral geniculate nucleus, and retina in the anesthetized cat. The Journal of neuroscience : the official journal of the Society for Neuroscience 18:6395-6410.

Castro-Alamancos MA (2004a) Absence of rapid sensory adaptation in neocortex during information processing states. Neuron 41:455-464.

Castro-Alamancos MA (2004b) Dynamics of sensory thalamocortical synaptic networks during information processing states. Progress in neurobiology 74:213-247.

Cetin A, Komai S, Eliava M, Seeburg PH, Osten P (2006) Stereotaxic gene delivery in the rodent brain. Nature protocols 1:3166-3173.

Chalk M, Herrero JL, Gieselmann MA, Delicato LS, Gotthardt S, Thiele A (2010) Attention reduces stimulus-driven gamma frequency oscillations and spike field coherence in V1. Neuron 66:114-125.

Chalupa LM, Williams R (2008) Eye, Retina, and Visual System of the Mouse. MIT Press.

Cheong SK, Tailby C, Solomon SG, Martin PR (2013) Cortical-like receptive fields in the lateral geniculate nucleus of marmoset monkeys. The Journal of neuroscience : the official journal of the Society for Neuroscience 33:6864-6876.

Chichilnisky EJ, Kalmar RS (2002) Functional asymmetries in ON and OFF ganglion cells of primate retina. The Journal of neuroscience : the official journal of the Society for Neuroscience 22:2737-2747.

Cleland BG, Lee BB, Vidyasagar TR (1983) Response of neurons in the cat's lateral geniculate nucleus to moving bars of different length. The Journal of neuroscience : the official journal of the Society for Neuroscience 3:108-116.

Clement EA, Richard A, Thwaites M, Ailon J, Peters S, Dickson CT (2008) Cyclic and sleep-like spontaneous alternations of brain state under urethane anaesthesia. PloS one 3:e2004.

Constantinople CM, Bruno RM (2011) Effects and mechanisms of wakefulness on local cortical networks. Neuron 69:1061-1068.

Contreras D, Steriade M (1997) Synchronization of low-frequency rhythms in corticothalamic networks. Neuroscience 76:11-24.

Costa-Miserachs D, Portell-Cortes I, Torras-Garcia M, Morgado-Bernal I (2003) Automated sleep staging in rat with a standard spreadsheet. Journal of neuroscience methods 130:93-101.

Cruz-Martin A, El-Danaf RN, Osakada F, Sriram B, Dhande OS, Nguyen PL, Callaway EM, Ghosh A, Huberman AD (2014) A dedicated circuit links direction-selective retinal ganglion cells to the primary visual cortex. Nature 507:358-361.

Cudeiro J, Sillito AM (2006) Looking back: corticothalamic feedback and early visual processing. Trends in neurosciences 29:298-306.

Curto C, Sakata S, Marguet S, Itskov V, Harris KD (2009) A simple model of cortical dynamics explains variability and state dependence of sensory responses in urethane-anesthetized auditory cortex. The Journal of neuroscience : the official journal of the Society for Neuroscience 29:10600-10612.

Dacey DM, Petersen MR (1992) Dendritic field size and morphology of midget and parasol ganglion cells of the human retina. Proceedings of the National Academy of Sciences of the United States of America 89:9666-9670.

Dacey DM, Peterson BB, Robinson FR, Gamlin PD (2003) Fireworks in the primate retina: in vitro photodynamics reveals diverse LGN-projecting ganglion cell types. Neuron 37:15-27.

Demiralp T, Bayraktaroglu Z, Lenz D, Junge S, Busch NA, Maess B, Ergen M, Herrmann CS (2007) Gamma amplitudes are coupled to theta phase in human EEG during visual perception. International journal of psychophysiology : official journal of the International Organization of Psychophysiology 64:24-30.

Denning KS, Reinagel P (2005) Visual control of burst priming in the anesthetized lateral geniculate nucleus. The Journal of neuroscience : the official journal of the Society for Neuroscience 25:3531-3538.

Derrington AM, Lennie P (1984) Spatial and temporal contrast sensitivities of neurones in lateral geniculate nucleus of macaque. The Journal of physiology 357:219-240.

Deschenes M, Roy JP, Steriade M (1982) Thalamic bursting mechanism: an inward slow current revealed by membrane hyperpolarization. Brain research 239:289-293.

Destexhe A, Contreras D, Steriade M (1999) Cortically-induced coherence of a thalamic-generated oscillation. Neuroscience 92:427-443.

Dhruv NT, Tailby C, Sokol SH, Majaj NJ, Lennie P (2009) Nonlinear signal summation in magnocellular neurons of the macaque lateral geniculate nucleus. Journal of neurophysiology 102:1921-1929.

Drager UC (1975) Receptive fields of single cells and topography in mouse visual cortex. The Journal of comparative neurology 160:269-290.

Eckhorn R, Bauer R, Jordan W, Brosch M, Kruse W, Munk M, Reitboeck HJ (1988) Coherent oscillations: a mechanism of feature linking in the visual cortex? Multiple electrode and correlation analyses in the cat. Biological cybernetics 60:121-130.

Eger EI (1981) Isoflurane: A Review. Anesthesiology, 55, 559-576.

Engel AK, Fries P (2010) Beta-band oscillations--signalling the status quo? Current opinion in neurobiology 20:156-165.

Engel AK, Fries P, Singer W (2001) Dynamic predictions: oscillations and synchrony in top-down processing. Nature reviews Neuroscience 2:704-716.

Engel AK, Konig P, Kreiter AK, Singer W (1991) Interhemispheric synchronization of oscillatory neuronal responses in cat visual cortex. Science 252:1177-1179.

Erskine L, Herrera E (2014) Connecting the Retina to the Brain. ASN neuro 6.

Fanselow EE, Nicolelis MA (1999) Behavioral modulation of tactile responses in the rat somatosensory system. The Journal of neuroscience : the official journal of the Society for Neuroscience 19:7603-7616.

Fanselow EE, Sameshima K, Baccala LA, Nicolelis MA (2001) Thalamic bursting in rats during different awake behavioral states. Proceedings of the National Academy of Sciences of the United States of America 98:15330-15335.

Fell J, Klaver P, Elfadil H, Schaller C, Elger CE, Fernandez G (2003) Rhinal-hippocampal theta coherence during declarative memory formation: interaction with gamma synchronization? The European journal of neuroscience 17:1082-1088.

Fell J, Klaver P, Lehnertz K, Grunwald T, Schaller C, Elger CE, Fernandez G (2001) Human memory formation is accompanied by rhinal-hippocampal coupling and decoupling. Nature neuroscience 4:1259-1264.

Fontanini A, Katz DB (2008) Behavioral states, network states, and sensory response variability. Journal of neurophysiology 100:1160-1168.

Foster KH, Gaska JP, Nagler M, Pollen DA (1985) Spatial and temporal frequency selectivity of neurones in visual cortical areas V1 and V2 of the macaque monkey. The Journal of physiology 365:331-363.

Franks NP (2006) Molecular targets underlying general anaesthesia. British journal of pharmacology 147 Suppl 1:S72-81.

Frederick A, Bourget-Murray J, Chapman CA, Amir S, Courtemanche R (2014) Diurnal influences on electrophysiological oscillations and coupling in the dorsal striatum and cerebellar cortex of the anesthetized rat. Frontiers in systems neuroscience 8:145.

Fries P (2009) Neuronal gamma-band synchronization as a fundamental process in cortical computation. Annual review of neuroscience 32:209-224.

Fries P, Neuenschwander S, Engel AK, Goebel R, Singer W (2001a) Rapid feature selective neuronal synchronization through correlated latency shifting. Nature neuroscience 4:194-200.

Fries P, Reynolds JH, Rorie AE, Desimone R (2001b) Modulation of oscillatory neuronal synchronization by selective visual attention. Science 291:1560-1563.

Fries P, Roelfsema PR, Engel AK, Konig P, Singer W (1997) Synchronization of oscillatory responses in visual cortex correlates with perception in interocular rivalry. Proceedings of the National Academy of Sciences of the United States of America 94:12699-12704.

Fries P, Scheeringa R, Oostenveld R (2008) Finding gamma. Neuron 58:303-305.

Galambos R, Szabo-Salfay O, Szatmari E, Szilagyi N, Juhasz G (2001) Sleep modifies retinal ganglion cell responses in the normal rat. Proceedings of the National Academy of Sciences of the United States of America 98:2083-2088.

Gandhi SP, Yanagawa Y, Stryker MP (2008) Delayed plasticity of inhibitory neurons in developing visual cortex. Proceedings of the National Academy of Sciences of the United States of America 105:16797-16802.

Gervasoni D, Lin SC, Ribeiro S, Soares ES, Pantoja J, Nicolelis MA (2004) Global forebrain dynamics predict rat behavioral states and their transitions. The Journal of neuroscience : the official journal of the Society for Neuroscience 24:11137-11147.

Gieselmann MA, Thiele A (2008) Comparison of spatial integration and surround suppression characteristics in spiking activity and the local field potential in macaque V1. The European journal of neuroscience 28:447-459.

Gleave JA, Lerch JP, Henkelman RM, Nieman BJ (2013) A method for 3D immunostaining and optical imaging of the mouse brain demonstrated in neural progenitor cells. PloS one 8:e72039.

Gray CM, Konig P, Engel AK, Singer W (1989) Oscillatory responses in cat visual cortex exhibit inter-columnar synchronization which reflects global stimulus properties. Nature 338:334-337.

Gray CM, Singer W (1989) Stimulus-specific neuronal oscillations in orientation columns of cat visual cortex. Proceedings of the National Academy of Sciences of the United States of America 86:1698-1702.

Gregoriou GG, Gotts SJ, Zhou H, Desimone R (2009) High-frequency, long-range coupling between prefrontal and visual cortex during attention. Science 324:1207-1210.

Grubb MS, Thompson ID (2003) Quantitative characterization of visual response properties in the mouse dorsal lateral geniculate nucleus. Journal of neurophysiology 90:3594-3607.

Grubb MS, Thompson ID (2005) Visual response properties of burst and tonic firing in the mouse dorsal lateral geniculate nucleus. Journal of neurophysiology 93:3224-3247.

Guillery RW (1995) Anatomical evidence concerning the role of the thalamus in corticocortical communication: a brief review. Journal of anatomy 187 (Pt 3):583-592.

Guillery RW, Sherman SM (2002) Thalamic relay functions and their role in corticocortical communication: generalizations from the visual system. Neuron 33:163-175.

Harris KD, Bartho P, Chadderton P, Curto C, de la Rocha J, Hollender L, Itskov V, Luczak A, Marguet SL, Renart A, Sakata S (2011) How do neurons work together? Lessons from auditory cortex. Hearing research 271:37-53.

Harris KD, Henze DA, Csicsvari J, Hirase H, Buzsaki G (2000) Accuracy of tetrode spike separation as determined by simultaneous intracellular and extracellular measurements. Journal of neurophysiology 84:401-414.

Harris KD, Thiele A (2011) Cortical state and attention. Nature reviews Neuroscience 12:509-523.

Harvey AR (1978) Characteristics of corticothalamic neurons in area 17 of the cat. Neuroscience letters 7:177-181.

Hei X, Stoelzel CR, Zhuang J, Bereshpolova Y, Huff JM, Alonso JM, Swadlow HA (2014) Directional selective neurons in the awake LGN: response properties and modulation by brain state. Journal of neurophysiology 112:362-373.

Hendrickson AE, Wilson JR, Ogren MP (1978) The neuroanatomical organization of pathways between the dorsal lateral geniculate nucleus and visual cortex in Old World and New World primates. The Journal of comparative neurology 182:123-136.

Hendry SH, Reid RC (2000) The koniocellular pathway in primate vision. Annual review of neuroscience 23:127-153.

Hendry SH, Yoshioka T (1994) A neurochemically distinct third channel in the macaque dorsal lateral geniculate nucleus. Science 264:575-577.

Henrie JA, Shapley R (2005) LFP power spectra in V1 cortex: the graded effect of stimulus contrast. Journal of neurophysiology 94:479-490.

Hirata A, Castro-Alamancos MA (2010) Neocortex network activation and deactivation states controlled by the thalamus. Journal of neurophysiology 103:1147-1157.

Hobson JA (2005) Sleep is of the brain, by the brain and for the brain. Nature 437:1254-1256.

Hochstein S, Shapley RM (1976) Quantitative analysis of retinal ganglion cell classifications. The Journal of physiology 262:237-264.

Hoogenboom N, Schoffelen JM, Oostenveld R, Parkes LM, Fries P (2006) Localizing human visual gamma-band activity in frequency, time and space. NeuroImage 29:764-773.

Hubel DH, Wiesel TN (1959) Receptive fields of single neurones in the cat's striate cortex. The Journal of physiology 148:574-591.

Hubel DH, Wiesel TN (1961) Integrative action in the cat's lateral geniculate body. The Journal of physiology 155:385-398.

Hubel DH, Wiesel TN (1962) Receptive fields, binocular interaction and functional architecture in the cat's visual cortex. The Journal of physiology 160:106-154.

Hubel DH, Wiesel TN (1965) Receptive Fields and Functional Architecture in Two Nonstriate Visual Areas (18 and 19) of the Cat. Journal of neurophysiology 28:229-289.

Hubel DH, Wiesel TN (1968) Receptive fields and functional architecture of monkey striate cortex. The Journal of physiology 195:215-243.

Huberman AD, Manu M, Koch SM, Susman MW, Lutz AB, Ullian EM, Baccus SA, Barres BA (2008) Architecture and activity-mediated refinement of axonal projections from a mosaic of genetically identified retinal ganglion cells. Neuron 59:425-438.

Huberman AD, Niell CM (2011) What can mice tell us about how vision works? Trends in neurosciences 34:464-473.

Huberman AD, Wei W, Elstrott J, Stafford BK, Feller MB, Barres BA (2009) Genetic identification of an On-Off direction-selective retinal ganglion cell subtype reveals a layer-specific subcortical map of posterior motion. Neuron 62:327-334.

Humphrey AL, Sur M, Uhlrich DJ, Sherman SM (1985) Projection patterns of individual X- and Y-cell axons from the lateral geniculate nucleus to cortical area 17 in the cat. The Journal of comparative neurology 233:159-189.

Ikeda H, Wright MJ (1972) Receptive field organization of 'sustained' and 'transient' retinal ganglion cells which subserve different function roles. The Journal of physiology 227:769-800.

Ikeda H, Wright MJ (1975a) The latency of visual cortical neurones in area 17 in the cat to visual stimuli with reference to the sustained (X) and transient (Y) and 'simple' and 'complex' cell classification. The Journal of physiology 245:114P-115P.

Ikeda H, Wright MJ (1975b) The relationship between the 'sustained-transient' and the 'simple-complex' classifications of neurones in area 17 of the cat. The Journal of physiology 244:58P-59P.

Irvin GE, Casagrande VA, Norton TT (1993) Center/surround relationships of magnocellular, parvocellular, and koniocellular relay cells in primate lateral geniculate nucleus. Visual neuroscience 10:363-373.

Jacobs GH (2008) Primate color vision: a comparative perspective. Visual neuroscience 25:619-633.

Jacobs GH, Birch DG, Blakeslee B (1982) Visual acuity and spatial contrast sensitivity in tree squirrels. Behavioural processes 7:367-375.

Jeffries AM, Killian NJ, Pezaris JS (2014) Mapping the primate lateral geniculate nucleus: a review of experiments and methods. Journal of physiology, Paris 108:3-10.

John ER, Prichep LS (2005) The anesthetic cascade: a theory of how anesthesia suppresses consciousness. Anesthesiology 102:447-471.

Jones HE, Sillito AM (1991) The length-response properties of cells in the feline dorsal lateral geniculate nucleus. The Journal of physiology 444:329-348.

Kaas JH, Guillery RW, Allman JM (1972) Some principles of organization in the dorsal lateral geniculate nucleus. Brain, behavior and evolution 6:253-299.

Kadir SN, Goodman DF, Harris KD (2014) High-dimensional cluster analysis with the masked EM algorithm. Neural computation 26:2379-2394.

Kamondi A, Acsady L, Wang XJ, Buzsaki G (1998) Theta oscillations in somata and dendrites of hippocampal pyramidal cells in vivo: activity-dependent phase-precession of action potentials. Hippocampus 8:244-261.

Kaplan E (2004) The M, P, and K pathways of the primate visual system. In: The visual neurosciences. Cambridge, MA: MIT Press, pp 481– 493.

Kaplan E, Shapley RM (1982) X and Y cells in the lateral geniculate nucleus of macaque monkeys. The Journal of physiology 330:125-143.

Karpova AY, Tervo DG, Gray NW, Svoboda K (2005) Rapid and reversible chemical inactivation of synaptic transmission in genetically targeted neurons. Neuron 48:727-735.

Katzner S, Nauhaus I, Benucci A, Bonin V, Ringach DL, Carandini M (2009) Local origin of field potentials in visual cortex. Neuron 61:35-41.

Kim IJ, Zhang Y, Meister M, Sanes JR (2010) Laminar restriction of retinal ganglion cell dendrites and axons: subtype-specific developmental patterns revealed with transgenic markers. The Journal of neuroscience : the official journal of the Society for Neuroscience 30:1452-1462.

Kim IJ, Zhang Y, Yamagata M, Meister M, Sanes JR (2008) Molecular identification of a retinal cell type that responds to upward motion. Nature 452:478-482.

Kirk IJ, Mackay JC (2003) The role of theta-range oscillations in synchronising and integrating activity in distributed mnemonic networks. Cortex; a journal devoted to the study of the nervous system and behavior 39:993-1008.

Knyazev GG (2007) Motivation, emotion, and their inhibitory control mirrored in brain oscillations. Neuroscience and biobehavioral reviews 31:377-395.

Kolev V, Yordanova J, Schurmann M, Batar E (1999) Event-related alpha oscillations in task processing. Clinical neurophysiology : official journal of the International Federation of Clinical Neurophysiology 110:1784-1792.

Krahe TE, El-Danaf RN, Dilger EK, Henderson SC, Guido W (2011) Morphologically distinct classes of relay cells exhibit regional preferences in the dorsal lateral geniculate nucleus of the mouse. The Journal of neuroscience : the official journal of the Society for Neuroscience 31:17437-17448.

Kreiter AK, Singer W (1996) Stimulus-dependent synchronization of neuronal responses in the visual cortex of the awake macaque monkey. The Journal of neuroscience : the official journal of the Society for Neuroscience 16:2381-2396.

Lankheet MJ, Lennie P, Krauskopf J (1998) Distinctive characteristics of subclasses of red-green P-cells in LGN of macaque. Visusal Neuroscience 15:37-46.

Latawiec D, Martin KA, Meskenaite V (2000) Termination of the geniculocortical projection in the striate cortex of macaque monkey: a quantitative immunoelectron microscopic study. The Journal of comparative neurology 419:306-319.

Lee CC, Sherman SM (2009) Glutamatergic inhibition in sensory neocortex. Cerebral cortex 19:2281-2289.

Lee SH, Dan Y (2012) Neuromodulation of brain states. Neuron 76:209-222.

Lemmens MA, Steinbusch HW, Rutten BP, Schmitz C (2010) Advanced microscopy techniques for quantitative analysis in neuromorphology and neuropathology research: current status and requirements for the future. Journal of chemical neuroanatomy 40:199-209.

Lennie P (1981) The physiological basis of variations in visual latency. Vision research 21:815-824.

LeVay S, Gilbert CD (1976) Laminar patterns of geniculocortical projection in the cat. Brain research 113:1-19.

Leventhal AG, Rodieck RW, Dreher B (1981) Retinal ganglion cell classes in the Old World monkey: morphology and central projections. Science 213:1139-1142.

Levitt JB, Schumer RA, Sherman SM, Spear PD, Movshon JA (2001) Visual response properties of neurons in the LGN of normally reared and visually deprived macaque monkeys. Journal of neurophysiology 85:2111-2129.

Li CY, Poo MM, Dan Y (2009) Burst spiking of a single cortical neuron modifies global brain state. Science 324:643-646.

Livingstone MS, Hubel DH (1981) Effects of sleep and arousal on the processing of visual information in the cat. Nature 291:554-561.

Livingstone MS, Hubel DH (1982) Thalamic inputs to cytochrome oxidase-rich regions in monkey visual cortex. Proceedings of the National Academy of Sciences of the United States of America 79:6098-6101.

Llinas R, Jahnsen H (1982) Electrophysiology of mammalian thalamic neurones in vitro. Nature 297:406-408.

Luo L, Callaway EM, Svoboda K (2008) Genetic dissection of neural circuits. Neuron 57:634-660.

Maheswaran S, Barjat H, Bate ST, Aljabar P, Hill DL, Tilling L, Upton N, James MF, Hajnal JV, Rueckert D (2009) Analysis of serial magnetic resonance images of mouse brains using image registration. NeuroImage 44:692-700.

Mangini NJ, Pearlman AL (1980) Laminar distribution of receptive field properties in the primary visual cortex of the mouse. The Journal of comparative neurology 193:203-222.

Margolis DJ, Detwiler PB (2007) Different mechanisms generate maintained activity in ON and OFF retinal ganglion cells. The Journal of neuroscience : the official journal of the Society for Neuroscience 27:5994-6005.

Marshall L, Helgadottir H, Molle M, Born J (2006) Boosting slow oscillations during sleep potentiates memory. Nature 444:610-613.

Marshel JH, Kaye AP, Nauhaus I, Callaway EM (2012) Anterior-posterior direction opponency in the superficial mouse lateral geniculate nucleus. Neuron 76:713-720.

Martin PR, White AJ, Goodchild AK, Wilder HD, Sefton AE (1997) Evidence that blue-on cells are part of the third geniculocortical pathway in primates. The European journal of neuroscience 9:1536-1541.

Maunsell JH, Ghose GM, Assad JA, McAdams CJ, Boudreau CE, Noerager BD (1999) Visual response latencies of magnocellular and parvocellular LGN neurons in macaque monkeys. Visual neuroscience 16:1-14.

McCormick DA, Bal T (1997) Sleep and arousal: thalamocortical mechanisms. Annual review of neuroscience 20:185-215.

Metherate R, Cox CL, Ashe JH (1992) Cellular bases of neocortical activation: modulation of neural oscillations by the nucleus basalis and endogenous acetylcholine. The Journal of neuroscience : the official journal of the Society for Neuroscience 12:4701-4711.

Metin C, Godement P, Imbert M (1988) The primary visual cortex in the mouse: receptive field properties and functional organization. Experimental brain research 69:594-612.

Miltner WH, Braun C, Arnold M, Witte H, Taub E (1999) Coherence of gamma-band EEG activity as a basis for associative learning. Nature 397:434-436.

Mitzdorf U (1985) Current source-density method and application in cat cerebral cortex: investigation of evoked potentials and EEG phenomena. Physiological reviews 65:37-100.

Montgomery SM, Buzsaki G (2007) Gamma oscillations dynamically couple hippocampal CA3 and CA1 regions during memory task performance. Proceedings of the National Academy of Sciences of the United States of America 104:14495-14500.

Movshon JA, Thompson ID, Tolhurst DJ (1978) Spatial summation in the receptive fields of simple cells in the cat's striate cortex. The Journal of physiology 283:53-77.

Mukherjee P, Kaplan E (1995) Dynamics of neurons in the cat lateral geniculate nucleus: in vivo electrophysiology and computational modeling. Journal of neurophysiology 74:1222-1243.

Muller MM, Keil A (2004) Neuronal synchronization and selective color processing in the human brain. Journal of cognitive neuroscience 16:503-522.

Munk ME, Madison MS, Robb EW (1996a) The neural network as a tool for multispectral interpretation. Journal of chemical information and computer sciences 36:231-238.

Munk MH, Roelfsema PR, Konig P, Engel AK, Singer W (1996b) Role of reticular activation in the modulation of intracortical synchronization. Science 272:271-274.

Murienne BJ, Girard MJ, Loerup L, Boussommier-Calleja A, Shefelbine SJ, Marenzana M, Either CR (2011) An automated histologic system for 3D histotmorphometry of the mouse knee. Proceedings of the ASME Summer Bioengineering Conference, June 22-25, Farmington, Pennsylvania, USA.

Murphy BK, Miller KD (2003) Multiplicative gain changes are induced by excitation or inhibition alone. The Journal of neuroscience : the official journal of the Society for Neuroscience 23:10040-10051.

Murphy GJ, Rieke F (2006) Network variability limits stimulus-evoked spike timing precision in retinal ganglion cells. Neuron 52:511-524.

Murphy PC, Sillito AM (1987) Corticofugal feedback influences the generation of length tuning in the visual pathway. Nature 329:727-729.

Neuenschwander S, Singer W (1996) Long-range synchronization of oscillatory light responses in the cat retina and lateral geniculate nucleus. Nature 379:728-732.

Niell CM (2013) Vision: more than expected in the early visual system. Current biology : CB 23:R681-684.

Niell CM, Stryker MP (2008) Highly selective receptive fields in mouse visual cortex. The Journal of neuroscience : the official journal of the Society for Neuroscience 28:7520-7536.

Niell CM, Stryker MP (2010) Modulation of visual responses by behavioral state in mouse visual cortex. Neuron 65:472-479.

Nunez P (1995) Neocortical dynamics and human EEG rhythms. Oxford University Press, New York – Oxford.

Okun M, Naim A, Lampl I (2010) The subthreshold relation between cortical local field potential and neuronal firing unveiled by intracellular recordings in awake rats. The Journal of neuroscience : the official journal of the Society for Neuroscience 30:4440-4448.

Oram MW, Xiao D, Dritschel B, Payne KR (2002) The temporal resolution of neural codes: does response latency have a unique role? Philosophical transactions of the Royal Society of London Series B, Biological sciences 357:987-1001.

Orban GA (1984) Neuronal Operations in the Visual Cortex. Berlin, Springer-Verlag.

Otazu GH, Tai LH, Yang Y, Zador AM (2009) Engaging in an auditory task suppresses responses in auditory cortex. Nature neuroscience 12:646-654.

Ouellette BG, Casanova C (2006) Overlapping visual response latency distributions in visual cortices and LP-pulvinar complex of the cat. Experimental brain research 175:332-341.

Pagliardini S, Gosgnach S, Dickson CT (2013) Spontaneous sleep-like brain state alternations and breathing characteristics in urethane anesthetized mice. PloS one 8:e70411.

Palva S, Palva JM (2007) New vistas for alpha-frequency band oscillations. Trends in neurosciences 30:150-158.

Paxinos G, Franklin KBJ (2008) The mouse brain in stereotaxic coordinates. Academic Press, 3rd edition.

Perry VH, Cowey A (1985) The ganglion cell and cone distributions in the monkey's retina: implications for central magnification factors. Vision research 25:1795-1810.

Perry VH, Oehler R, Cowey A (1984) Retinal ganglion cells that project to the dorsal lateral geniculate nucleus in the macaque monkey. Neuroscience 12:1101-1123.

Pesaran B, Pezaris JS, Sahani M, Mitra PP, Andersen RA (2002) Temporal structure in neuronal activity during working memory in macaque parietal cortex. Nature neuroscience 5:805-811.

Piscopo DM, El-Danaf RN, Huberman AD, Niell CM (2013) Diverse visual features encoded in mouse lateral geniculate nucleus. The Journal of neuroscience : the official journal of the Society for Neuroscience 33:4642-4656.

Poulet JF, Fernandez LM, Crochet S, Petersen CC (2012) Thalamic control of cortical states. Nature neuroscience 15:370-372.

Reese BE (1988) 'Hidden lamination' in the dorsal lateral geniculate nucleus: the functional organization of this thalamic region in the rat. Brain research 472:119-137.

Reid RC, Shapley RM (2002) Space and time maps of cone photoreceptor signals in macaque lateral geniculate nucleus. The Journal of neuroscience : the official journal of the Society for Neuroscience 22:6158-6175.

Reinagel P, Godwin D, Sherman SM, Koch C (1999) Encoding of visual information by LGN bursts. Journal of neurophysiology 81:2558-2569.

Remtulla S, Hallett PE (1985) A schematic eye for the mouse, and comparisons with the rat. Vision research 25:21-31.

Ries CR, Puil E (1999) Ionic mechanism of isoflurane's actions on thalamocortical neurons. Journal of neurophysiology 81:1802-1809.

Rochefort NL, Narushima M, Grienberger C, Marandi N, Hill DN, Konnerth A (2011) Development of direction selectivity in mouse cortical neurons. Neuron 71:425-432.

Rodieck RW (1965) Quantitative analysis of cat retinal ganglion cell response to visual stimuli. Vision research 5:583-601.

Rodieck RW (1967) Receptive fields in the cat retina: a new type. Science 157:90-92.

Rodieck RW, Watanabe M (1993) Survey of the morphology of macaque retinal ganglion cells that project to the pretectum, superior colliculus, and parvicellular laminae of the lateral geniculate nucleus. The Journal of comparative neurology 338:289-303.

Rols G, Tallon-Baudry C, Girard P, Bertrand O, Bullier J (2001) Cortical mapping of gamma oscillations in areas V1 and V4 of the macaque monkey. Visual neuroscience 18:527-540.

Roopun AK, Middleton SJ, Cunningham MO, LeBeau FE, Bibbig A, Whittington MA, Traub RD (2006) A beta2-frequency (20-30 Hz) oscillation in nonsynaptic networks of somatosensory cortex. Proceedings of the National Academy of Sciences of the United States of America 103:15646-15650.

Rosenberg A, Husson TR, Issa NP (2010) Subcortical representation of non-Fourier image features. The Journal of neuroscience : the official journal of the Society for Neuroscience 30:1985-1993.

Saalmann YB (2014) Intralaminar and medial thalamic influence on cortical synchrony, information transmission and cognition. Frontiers in systems neuroscience 8:83.

Saalmann YB, Kastner S (2011) Cognitive and perceptual functions of the visual thalamus. Neuron 71:209-223.

Salinas E, Sejnowski TJ (2001) Correlated neuronal activity and the flow of neural information. Nature reviews Neuroscience 2:539-550.

Saul AB, Humphrey AL (1990) Spatial and temporal response properties of lagged and nonlagged cells in cat lateral geniculate nucleus. Journal of neurophysiology 64:206-224.

Schiller PH, Sandell JH, Maunsell JH (1986) Functions of the ON and OFF channels of the visual system. Nature 322:824-825.

Schmitzer-Torbert N, Jackson J, Henze D, Harris K, Redish AD (2005) Quantitative measures of cluster quality for use in extracellular recordings. Neuroscience 131:1-11.

Scholl B, Tan AY, Corey J, Priebe NJ (2013) Emergence of orientation selectivity in the Mammalian visual pathway. The Journal of neuroscience : the official journal of the Society for Neuroscience 33:10616-10624.

Schwartz G, Rieke F (2011) Perspectives on: information and coding in mammalian sensory physiology: nonlinear spatial encoding by retinal ganglion cells: when 1 + 1 not equal 2. The Journal of general physiology 138:283-290.

Sederberg PB, Gauthier LV, Terushkin V, Miller JF, Barnathan JA, Kahana MJ (2006) Oscillatory correlates of the primacy effect in episodic memory. NeuroImage 32:1422-1431.

Sederberg PB, Kahana MJ, Howard MW, Donner EJ, Madsen JR (2003) Theta and gamma oscillations during encoding predict subsequent recall. The Journal of neuroscience : the official journal of the Society for Neuroscience 23:10809-10814.

Seecharan DJ, Kulkarni AL, Lu L, Rosen GD, Williams RW (2003) Genetic control of interconnected neuronal populations in the mouse primary visual system. The Journal of neuroscience : the official journal of the Society for Neuroscience 23:11178-11188.

Shah NM, Pisapia DJ, Maniatis S, Mendelsohn MM, Nemes A, Axel R (2004) Visualizing sexual dimorphism in the brain. Neuron 43:313-319.

Sherman SM (2001) Tonic and burst firing: dual modes of thalamocortical relay. Trends in neurosciences 24:122-126.

Sherman SM (2004) Interneurons and triadic circuitry of the thalamus. Trends in neurosciences 27:670-675.

Sherman SM (2005) Thalamic relays and cortical functioning. Progress in brain research 149:107-126.

Sherman SM, Guillery RW (1998) On the actions that one nerve cell can have on another: distinguishing "drivers" from "modulators". Proceedings of the National Academy of Sciences of the United States of America 95:7121-7126.

Sherman SM, Guillery RW (2001) Exploring the thalamus. London: Academic Press.

Sherman SM, Guillery RW (2002) The role of the thalamus in the flow of information to the cortex. Philosophical transactions of the Royal Society of London Series B, Biological sciences 357:1695-1708.

Sherman SM, Guillery RW (2011) Distinct functions for direct and transthalamic corticocortical connections. Journal of neurophysiology 106:1068-1077.

Sherman SM, Spear PD (1982) Organization of visual pathways in normal and visually deprived cats. Physiological reviews 62:738-855.

Shlens J, Rieke F, Chichilnisky E (2008) Synchronized firing in the retina. Current opinion in neurobiology 18:396-402.

Siegert S, Scherf BG, Del Punta K, Didkovsky N, Heintz N, Roska B (2009) Genetic address book for retinal cell types. Nature neuroscience 12:1197-1204.

Sillito AM, Jones HE (2002) Corticothalamic interactions in the transfer of visual information. Philosophical transactions of the Royal Society of London Series B, Biological sciences 357:1739-1752.

Sillito AM, Jones HE, Gerstein GL, West DC (1994) Feature-linked synchronization of thalamic relay cell firing induced by feedback from the visual cortex. Nature 369:479-482.

Simpson JI (1984) The accessory optic system. Annual review of neuroscience 7:13-41.

Sincich LC, Adams DL, Economides JR, Horton JC (2007) Transmission of spike trains at the retinogeniculate synapse. The Journal of neuroscience : the official journal of the Society for Neuroscience 27:2683-2692.

Singer W, Gray CM (1995) Visual feature integration and the temporal correlation hypothesis. Annual review of neuroscience 18:555-586.

Sireteanu R, Hoffmann KP (1979) Relative frequency and visual resolution of X- and Y-cells in the LGN of normal and monocularly deprived cats: interlaminar differences. Experimental brain research 34:591-603.

Sirota A, Montgomery S, Fujisawa S, Isomura Y, Zugaro M, Buzsaki G (2008) Entrainment of neocortical neurons and gamma oscillations by the hippocampal theta rhythm. Neuron 60:683-697.

Skottun BC, De Valois RL, Grosof DH, Movshon JA, Albrecht DG, Bonds AB (1991) Classifying simple and complex cells on the basis of response modulation. Vision research 31:1079-1086.

Smith MA, Jia X, Zandvakili A, Kohn A (2013) Laminar dependence of neuronal correlations in visual cortex. Journal of neurophysiology 109:940-947.

Smith SL, Hausser M (2010) Parallel processing of visual space by neighboring neurons in mouse visual cortex. Nature neuroscience 13:1144-1149.

So YT, Shapley R (1981) Spatial tuning of cells in and around lateral geniculate nucleus of the cat: X and Y relay cells and perigeniculate interneurons. Journal of neurophysiology 45:107-120.

Solomon SG, Lennie P (2007) The machinery of colour vision. Nature reviews Neuroscience 8:276-286.

Solomon SG, White AJ, Martin PR (1999) Temporal contrast sensitivity in the lateral geniculate nucleus of a New World monkey, the marmoset Callithrix jacchus. The Journal of physiology 517 (Pt 3):907-917.

Solomon SG, White AJ, Martin PR (2002) Extraclassical receptive field properties of parvocellular, magnocellular, and koniocellular cells in the primate lateral geniculate nucleus. The Journal of neuroscience : the official journal of the Society for Neuroscience 22:338-349.

Spreafico R, Frassoni C, Arcelli P, De Biasi S (1994) GABAergic interneurons in the somatosensory thalamus of the guinea-pig: a light and ultrastructural immunocytochemical investigation. Neuroscience 59:961-973.

Spring S, Lerch JP, Henkelman RM (2007) Sexual dimorphism revealed in the structure of the mouse brain using three-dimensional magnetic resonance imaging. NeuroImage 35:1424-1433.

Stanford LR, Friedlander MJ, Sherman SM (1981) Morphology of physiologically identified W-cells in the C laminae of the cat's lateral geniculate nucleus. The Journal of neuroscience : the official journal of the Society for Neuroscience 1:578-584.

Steriade M (1997) Synchronized activities of coupled oscillators in the cerebral cortex and thalamus at different levels of vigilance. Cerebral cortex 7:583-604.

Steriade M (1999) Brainstem activation of thalamocortical systems. Brain research bulletin 50:391-392.

Steriade M (2001) Impact of network activities on neuronal properties in corticothalamic systems. Journal of neurophysiology 86:1-39.

Steriade M (2005) Sleep, epilepsy and thalamic reticular inhibitory neurons. Trends in neurosciences 28:317-324.

Steriade M (2006) Grouping of brain rhythms in corticothalamic systems. Neuroscience 137:1087-1106.

Steriade M, McCarley RW (2005) Brain control of wakefulness and sleep. Kluwer Academic/Plenum, New York.

Steriade M, McCormick DA, Sejnowski TJ (1993) Thalamocortical oscillations in the sleeping and aroused brain. Science 262:679-685.

Stoelzel CR, Bereshpolova Y, Swadlow HA (2009) Stability of thalamocortical synaptic transmission across awake brain states. The Journal of neuroscience : the official journal of the Society for Neuroscience 29:6851-6859.

Stokes EL, Flecknell PA, Richardson CA (2009) Reported analgesic and anaesthetic administration to rodents undergoing experimental surgical procedures. Laboratory animals 43:149-154.

Stone C, Pinto LH (1993) Response properties of ganglion cells in the isolated mouse retina. Visual neuroscience 10:31-39.

Sur M, Sherman SM (1982) Linear and nonlinear W-cells in C-laminae of the cat's lateral geniculate nucleus. Journal of neurophysiology 47:869-884.

Swadlow HA, Gusev AG (2001) The impact of 'bursting' thalamic impulses at a neocortical synapse. Nature neuroscience 4:402-408.

Swadlow HA, Weyand TG (1985) Receptive-field and axonal properties of neurons in the dorsal lateral geniculate nucleus of awake unparalyzed rabbits. Journal of neurophysiology 54:168-183.

Swadlow HA, Weyand TG (1987) Corticogeniculate neurons, corticotectal neurons, and suspected interneurons in visual cortex of awake rabbits: receptive-field properties, axonal properties, and effects of EEG arousal. Journal of neurophysiology 57:977-1001.

Szczesny G, Veihelmann A, Massberg S, Nolte D, Messmer K (2004) Long-term anaesthesia using inhalatory isoflurane in different strains of mice-the haemodynamic effects. Laboratory animals 38:64-69.

Tailby C, Solomon SG, Peirce JW, Metha AB (2007) Two expressions of "surround suppression" in V1 that arise independent of cortical mechanisms of suppression. Visual neuroscience 24:99-109.

Tailby C, Szmajda BA, Buzas P, Lee BB, Martin PR (2008) Transmission of blue (S) cone signals through the primate lateral geniculate nucleus. The Journal of physiology 586:5947-5967.

Tallon-Baudry C, Bertrand O, Henaff MA, Isnard J, Fischer C (2005) Attention modulates gamma-band oscillations differently in the human lateral occipital cortex and fusiform gyrus. Cerebral cortex 15:654-662.

Tallon-Baudry C, Bertrand O, Peronnet F, Pernier J (1998) Induced gamma-band activity during the delay of a visual short-term memory task in humans. The Journal of neuroscience : the official journal of the Society for Neuroscience 18:4244-4254.

Tauchi M, Morigiwa K, Fukuda Y (1992) Morphological comparisons between outer and inner ramifying alpha cells of the albino rat retina. Experimental brain research 88:67-77.

Taylor K, Mandon S, Freiwald WA, Kreiter AK (2005) Coherent oscillatory activity in monkey area v4 predicts successful allocation of attention. Cerebral cortex 15:1424-1437.

Thatcher RW, Krause PJ, Hrybyk M (1986) Cortico-cortical associations and EEG coherence: a two-compartmental model. Electroencephalography and clinical neurophysiology 64:123-143.

Thatcher RW, Walker RA, Giudice S (1987) Human cerebral hemispheres develop at different rates and ages. Science 236:1110-1113.

Thompson SA, Wafford K (2001) Mechanism of action of general anaesthetics--new information from molecular pharmacology. Current opinion in pharmacology 1:78-83.

Troy JB (1983) Spatio-temporal interaction in neurones of the cat's dorsal lateral geniculate nucleus. The Journal of physiology 344:419-432.

Truong TV, Supatto W, Koos DS, Choi JM, Fraser SE (2011) Deep and fast live imaging with two-photon scanned light-sheet microscopy. Nature methods 8:757-760.

Usrey WM, Reid RC (2000) Visual physiology of the lateral geniculate nucleus in two species of new world monkey: Saimiri sciureus and Aotus trivirgatis. The Journal of physiology 523 Pt 3:755-769.

van Alphen B, Winkelman BH, Frens MA (2009) Age- and sex-related differences in contrast sensitivity in C57BL/6 mice. Investigative ophthalmology & visual science 50:2451-2458.

Van Essen DC, Anderson CH, Felleman DJ (1992) Information processing in the primate visual system: an integrated systems perspective. Science 255:419-423.

Van Hooser SD, Heimel JA, Nelson SB (2003) Receptive field properties and laminar organization of lateral geniculate nucleus in the gray squirrel (Sciurus carolinensis). Journal of neurophysiology 90:3398-3418.

Van Horn SC, Erisir A, Sherman SM (2000) Relative distribution of synapses in the A-laminae of the lateral geniculate nucleus of the cat. The Journal of comparative neurology 416:509-520.

Varela C (2014) Thalamic neuromodulation and its implications for executive networks. Frontiers in neural circuits 8:69.

Varela F, Lachaux JP, Rodriguez E, Martinerie J (2001) The brainweb: phase synchronization and large-scale integration. Nature reviews Neuroscience 2:229-239.

Votaw J, Byas-Smith M, Hua J, Voll R, Martarello L, Levey AI, Bowman FD, Goodman M (2003) Interaction of isoflurane with the dopamine transporter. Anesthesiology 98:404-411.

Wagor E, Mangini NJ, Pearlman AL (1980) Retinotopic organization of striate and extrastriate visual cortex in the mouse. The Journal of comparative neurology 193:187-202.

Wang L, Sarnaik R, Rangarajan K, Liu X, Cang J (2010) Visual receptive field properties of neurons in the superficial superior colliculus of the mouse. The Journal of neuroscience : the official journal of the Society for Neuroscience 30:16573-16584.

Wang P, Nikolic D (2011) An LCD Monitor with Sufficiently Precise Timing for Research in Vision. Frontiers in human neuroscience 5:85.

Wang XD, Chen C, Zhang D, Yao H (2014) Cumulative latency advance underlies fast visual processing in desynchronized brain state. Proceedings of the National Academy of Sciences of the United States of America 111:515-520.

Webb BS, Tinsley CJ, Vincent CJ, Derrington AM (2005) Spatial distribution of suppressive signals outside the classical receptive field in lateral geniculate nucleus. Journal of neurophysiology 94:1789-1797.

Weng S, Sun W, He S (2005) Identification of ON-OFF direction-selective ganglion cells in the mouse retina. The Journal of physiology 562:915-923.

Wiesel TN, Hubel DH (1966) Spatial and chromatic interactions in the lateral geniculate body of the rhesus monkey. Journal of neurophysiology 29:1115-1156.

Wilson JR (1993) Circuitry of the dorsal lateral geniculate nucleus in the cat and monkey. Acta anatomica 147:1-13.

Wolfart J, Debay D, Le Masson G, Destexhe A, Bal T (2005) Synaptic background activity controls spike transfer from thalamus to cortex. Nature neuroscience 8:1760-1767.

Womelsdorf T, Fries P (2006) Neuronal coherence during selective attentional processing and sensory-motor integration. Journal of physiology, Paris 100:182-193.

Womelsdorf T, Fries P (2007) The role of neuronal synchronization in selective attention. Current opinion in neurobiology 17:154-160.

Worgotter F, Nelle E, Li B, Funke K (1998) The influence of corticofugal feedback on the temporal structure of visual responses of cat thalamic relay cells. The Journal of physiology 509 (Pt 3):797-815.

Xu S, Jiang W, Poo MM, Dan Y (2012) Activity recall in a visual cortical ensemble. Nature neuroscience 15:449-455, S441-442.

Xu X, Bosking W, Sary G, Stefansic J, Shima D, Casagrande V (2004) Functional organization of visual cortex in the owl monkey. The Journal of neuroscience : the official journal of the Society for Neuroscience 24:6237-6247.

Xu X, Ichida JM, Allison JD, Boyd JD, Bonds AB, Casagrande VA (2001) A comparison of koniocellular, magnocellular and parvocellular receptive field properties in the lateral geniculate nucleus of the owl monkey (Aotus trivirgatus). The Journal of physiology 531:203-218.

Yushkevich PA, Piven J, Hazlett HC, Smith RG, Ho S, Gee JC, Gerig G (2006) User-guided 3D active contour segmentation of anatomical structures: significantly improved efficiency and reliability. NeuroImage 31:1116-1128.

Zhang F, Aravanis AM, Adamantidis A, de Lecea L, Deisseroth K (2007) Circuit-breakers: optical technologies for probing neural signals and systems. Nature reviews Neuroscience 8:577-581.

Zhao X, Chen H, Liu X, Cang J (2013a) Orientation-selective responses in the mouse lateral geniculate nucleus. The Journal of neuroscience : the official journal of the Society for Neuroscience 33:12751-12763.

Zhao X, Liu M, Cang J (2013b) Sublinear binocular integration preserves orientation selectivity in mouse visual cortex. Nature communications 4:2088.

Zhao Y, Kerscher N, Eysel U, Funke K (2001) Changes of contrast gain in cat dorsal lateral geniculate nucleus by dopamine receptor agonists. Neuroreport 12:2939-2945.

Zhou Z, Bernard MR, Bonds AB (2008) Deconstruction of spatial integrity in visual stimulus detected by modulation of synchronized activity in cat visual cortex. The Journal of neuroscience : the official journal of the Society for Neuroscience 28:3759-3768.

Zhuang J, Bereshpolova Y, Stoelzel CR, Huff JM, Hei X, Alonso JM, Swadlow HA (2014) Brain state effects on layer 4 of the awake visual cortex. The Journal of neuroscience : the official journal of the Society for Neuroscience 34:3888-3900.